

NORTHWESTERN UNIVERSITY

Solution-Processable Molecular and Polymeric Semiconductors for Ambient-Stable Organic Field-Effect Transistors

A DISSERTATION

**SUBMITTED TO THE GRADUATE SCHOOL
IN PARTIAL FULFILLMENT OF THE REQUIREMENTS**

for the degree

DOCTOR OF PHILOSOPHY

Field of Chemistry

by

Hakan Usta

EVANSTON, ILLINOIS

December 2008

© Copyright by Hakan Usta 2008

All Rights Reserved

ABSTRACT

Solution-Processable Molecular and Polymeric Semiconductors for Ambient-Stable Organic Field-Effect Transistors

Hakan Usta

π -Conjugated oligomeric and polymeric semiconductors have been the focus of intense research over the past few decades as alternatives to inorganic semiconductors for low-cost electronic applications such as organic field-effect transistors (OFETs). These materials enable vapor- or solution-phase fabrication of large-area, light-weight electronic devices, and are compatible with plastic substrates for mechanically flexible, conformable, and wearable electronics. Two primary challenges to realizing these applications are the ambient stability of organic thin films and solution-processability. Although several synthetic and device processing strategies have led to air-stable semiconductors having charge mobilities ranging from 10^{-5} to $> 0.1 \text{ cm}^2/\text{V}\cdot\text{s}$, there are still very few *p*-type polymeric and *n*-type or ambipolar molecular/polymeric semiconductors exhibiting truly high performance (charge mobility $\geq 0.1 \text{ cm}^2/\text{V}\cdot\text{s}$, $I_{\text{on}}/I_{\text{off}}$ ratio of $>10^5$). Thus, the development of new solution-processable, π -conjugated semiconductors exhibiting high field-effect carrier mobility and good stability under ambient conditions is of great interest. Furthermore, the fundamentals governing device environmental stability and FET performance with respect to the molecular/polymeric structure should be understood in greater depth.

This study addresses these challenges via theory-aided rational design, synthesis, and characterization of novel hole- and electron transporting molecules and polymers as air-stable

and solution-processable semiconductors for high performance *p*-channel, *n*-channel, and ambipolar OFETs. Significant correlations are established between molecular/polymeric structures, physicochemical properties, and OFET device performance, providing detailed insight into charge transport characteristics and ambient stability. In the first part, a series of dibenzosilole- and dithienosilole-based homo- and copolymers were developed for air-stable solution-cast *p*-channel FETs with high hole mobilities up to $0.08 \text{ cm}^2/\text{V}\cdot\text{s}$ and current modulations of $10^5 - 10^6$. In the second part, a new family of carbonyl-/dicyanovinylene-functionalized bis(indenofluorene) compounds and their corresponding homo- and copolymers were synthesized and characterized. Thin films of these semiconductors yield OFETs with high electron mobility (up to $0.16 \text{ cm}^2/\text{V}\cdot\text{s}$) and high $I_{\text{on}}/I_{\text{off}}$ ratio ($10^7 - 10^8$), one of the highest to date for a solution-cast air-stable *n*-channel semiconductor. Additionally, we reported the first examples of polymeric and molecular ambipolar semiconductors to function in air. Detailed analysis of the operational air-stabilities of a series of thin-films shows that air stability is principally governed by LUMO energetics with minimal contribution from thin film microstructure. The onset LUMO energy for carrier electron stabilization is estimated as $-4.1 - -4.0 \text{ eV}$. Density functional theory calculations provide detailed insight into molecule/polymer physicochemical and charge transport characteristics. These results, in total, affirm the possibility of achieving low-cost microelectronic devices through organic materials that enable simple solution fabrication processes under ambient conditions.

ACKNOWLEDGEMENTS

I am indebted to many people during this thesis work. This work could not be done without help of my professors, colleagues, friends and family. First and foremost, I would like to express my gratitude to Prof. Tobin J. Marks for his advisory and support. He has been a great professor, advisor and example for me. He worked untiringly to create the best research environment for his students. Prof. Antonio Facchetti has always been a part of my scientific development, sharing his knowledge, experience and wisdom throughout my graduate life. I would like to thank him for his advisory, guideness, and believing in me. Prof. Chad A. Mirkin, Prof. Michael R. Wasielewski, and Prof. Mark A. Ratner deserve a special thanks as my thesis committee members. I appreciate their sincere interest in my progress toward my Ph.D. and scientific development.

There are many highly talented people that I have to thank in the Marks group. Among these, special thanks to Dr. Gang Lu, Dr. Zhiming Wang, Dr. Chad Risko, Dr. Hui Huang and summer intern students Murat Kadir Deliomeroğlu and Aleksandr Zhukhovitskiy for their contributions to these projects; each are talented scientists and I am honored to have the opportunity to work with them. I also would like to thank to Dr. Myung-Han Yoon, Choongik Kim, Alex Hains, Dr. Matt Russell, Sara Dibenedetto, Dr. Brooks Jones, Dr. Joseph Letizia, Michael Irwin, Jun Liu, Jangdae Youn, Young-geun Ha, Myung-gil Yoon, Dr. Shinji Ando, Dr. Roberto Macchi, Dr. Michele Schiavo, Dr. Selvaggia Landi, Fabio Silvestri, Dave Frattarelli, Alma Dzudza, Dr. Paul Byrne, Hyun-Jin Choi for being great colleagues and for inspiring me in research and life through our interactions during the long hours in the lab. In addition, I am indebted to my dear friends Dr. Bilal Gokpinar, Huseyin Karaca, Dr. Mustafa Guler, Harun Taha Hayvaci, Gokhan Barin,

and Yasin Ozcan for being true friends while we were sharing the same house over the past four years. Thanks guys for making me feel like I am with my own family. I also would like to thank Ahmet Uysal, Dr. Ozgur Yazaydin, Dr. Tarek Zeidan, Dr. Ibrahim Eryazici, Dr. Rasim Ozcan, Dr. Cemil Selcuk, Isa Yildirim, Dr. Ali Coskun, Murat Sunbul, Yunus Emre Turkmen, Seraphine Wegner, Serhan Uslubas, M. Hayri Tongarlak, and Cengiz Senol for their great friendships, which makes Northwestern University and Chicago an enjoyable place.

I would like to acknowledge Northwestern University, Department of Chemistry, the Office of Naval Research (ONR), the NSF-MRSEC program through the Northwestern University Materials Research Science and Engineering Center, and Polyera for providing both financial support and characterization facilities.

I wish to thank my entire extended family for their invaluable love and support. Particularly, Uncles Ali, Sukru, Mustafa, Selahattin, their wives, Grandpa, Mahmut Kocyigit, and innumerable cousins have always been supportive during my graduate school years.

Finally, and most importantly, my deepest gratitude goes to my parents, Hakim and Sukran, my brother, Arif and my sister, Dilek for their endless love and support, who have done everything they possibly could to give me the opportunity to pursue my dreams. I dedicate my thesis to my family.

DEDICATION

To My Parents, Arif, and Dilek

Table of Contents

Copyright.....	2
Abstract.....	3
Acknowledgements.....	5
Dedication.....	7
List of Figures.....	11
List of Schemes.....	15
List of Tables.....	16
Chapter 1. Introduction.....	18
Chapter 2. Synthesis, Characterization, and Transistor Response of Semiconducting Silole Polymers with Substantial Hole Mobility and Air Stability.....	31
2.1. Introduction.....	32
2.2. Experimental.....	37
2.2.1. Materials and Methods.....	37
2.2.2. Synthesis and Characterizations.....	38
2.2.3. Device Fabrication and Thin-Film Characterization.....	47
2.2.4. Electrochemistry.....	48
2.2.5. Computational Methodology.....	48
2.3. Results.....	49
2.3.1. Synthesis.....	49
2.3.2. Thermal Properties.....	55
2.3.3. Optical Properties.....	57
2.3.4. Electrochemical Properties.....	61
2.3.5. Thin-Film X-ray Diffraction (XRD) Analysis.....	64

	9
2.3.6. Transistor Fabrication and Optimization.....	66
2.3.7. Device Air-Stability	74
2.4. Discussion.	77
2.4.1. Polymer Architecture vs. FET Performance	77
2.4.2. Electrochemical and Optical Properties as a Function of Electronic Structure	82
2.4.3. Role of the Injection Barrier.....	89
2.5. Conclusions.	92
Chapter 3. Design, Synthesis and Characterization of Ladder-Type Molecules and Polymers. Air-Stable, Solution-Processable <i>n</i>-Channel Semiconductors for Thin-Film Transistors via Experiment and Theory.....	93
3.1. Introduction	94
3.2. Experimental	102
3.2.1. Materials and Methods.....	102
3.2.2. Synthesis and Characterizations.....	102
3.2.3. Single-Crystal Structure Determination	122
3.2.4. Device Fabrication and Thin-Film Characterization.....	122
3.2.5. Electrochemistry.....	123
3.2.6. Computational Methodology	123
3.3. Results	124
3.3.1. Synthesis.....	124
3.3.2. Thermal Properties	131
3.3.3. Optical Properties.....	136
3.3.4. Electrochemical Characterization	144
3.3.5. Single-Crystal Structures	148
3.3.6. Thin Film Morphology.....	151
3.3.7. Thin Film Transistor Device Characterization.....	157
3.4. Discussion.	162

	10
3.4.1. Electrochemical and Optical Properties as a Function of Electronic Structure	162
3.4.2. Molecular Architecture and HOMO/LUMO Energetics vs. FET Performance and Air Stability.....	165
3.5. Conclusions.....	172
References.....	215
Curriculum Vitae.....	234

List of Figures

Figure 1.1. Schematic of a top-contact, bottom-gate field-effect transistor (FET), and <i>p</i> - and <i>n</i> -channel device operations.	21
Figure 1.2. Representative current-voltage characteristics of an organic field-effect transistor: A. Output plot showing linear and saturation regimes. B. Transfer plot in the saturation regime indicating threshold voltage (V_T) and current on/off ratio (I_{on}/I_{off}). . .	23
Figure 2.1. Structures of P3HT and air-stable thiophene-based polymeric semiconductors.	33
Figure 2.2. Schematic of the lamellar π -stacking in polymers P3HT, PQT, and PBTTT.	34
Figure 2.3. Structures of silole-thiophene polymers 5-10, fluorene-thiophene polymers 11 and 12.	36
Figure 2.4. Thermogravimetric analysis (TGA) of polymers 5-12.	55
Figure 2.5. Differential Scanning Calorimetry (DSC) of the polymers 6 (A), 7 (B), 9(C), 10 (D), 11 (E), and 12 (F) at a scanning speed of 10 °C/min under N ₂	56
Figure 2.6. UV-Vis absorption spectra of polymers 5-12 in THF solution (A), as thin films on glass substrate (B), and photoluminescence spectra in THF solution (C).	58
Figure 2.7. Cyclic voltammograms of polymers 5-12 as thin films in 0.1 M Bu ₄ N ⁺ PF ₆ ⁻ solution in acetonitrile at a scan rate of 100 mV/s. In all experiments, ferrocene is used as the internal standard.	61
Figure 2.8. θ -2 θ X-ray diffraction (XRD) scans of drop-cast films of polymers 5-10 on silicon substrates.	64
Figure 2.9. θ -2 θ X-ray diffraction (XRD) scans of drop-cast films of polymers 11(A) and 12 (B) on silicon substrates.	65

Figure 2.10. OTFT response plots of devices fabricated with polymers 7 and 10. A. Transfer plot of polymer 7 at $V_{SD} = -100V$, and output plot of polymer 7, B. Transfer plot of polymer 10 at $V_{SD} = -100V$, and output plot of polymer 10.	67
Figure 2.11. Transfer characteristics of OTFT devices fabricated with polymers 6 (A), 9 (C) at $V_{SD} = -100V$. Output characteristics of OTFT devices fabricated with polymers 6 (B), 9 (D) for various gate voltages.	68
Figure 2.12. Transfer characteristics of OTFT devices fabricated with polymers 11 (A), and 12 (C) at $V_{SD} = -100V$. Output characteristics of OTFT devices fabricated with polymers 11 (B), and 12 (D) for various gate voltages.	69
Figure 2.13. AFM Images of the spin-coated thin-films (25-30 nm) of polymer 10.	71
Figure 2.14. Evolution of field effect mobility and I_{on}/I_{off} ratio with annealing temperature in OTFTs of polymer 7 (A) and 10 (B).	73
Figure 2.15. OTFT transfer (A) (at $V_{SD} = -40 V$) and output (B) plots of a gravure printed device fabricated with polymer 10 and a printed dielectric.	74
Figure 2.16. Transfer characteristics of OTFT devices fabricated with polymers 7 (A), 10 (C), and P3HT (E) as a function of storage time in the air. The on-off cycles (0.03 Hz) under ambient conditions for the annealed devices of polymers 7 (B) and 10 (D) at $V_{SD} = -50 V$ were measured for the different gate biases indicated ...	76
Figure 2.17. Schematic models of layered and π - π stacked silole copolymer structures 7 and 10: DFT-calculated molecular dimensions (A), no side chain interdigitation model (B), and minimal free volume model (C).	81

Figure 2.18. Chemical structures of model polymer building blocks for electronic structure calculations.....	83
Figure 2.19. Pictorial representations of B3LYP/6-31G**,-derived selected valence molecular orbitals for the present silole-based polymer building blocks (A), and carbon-based polymer building blocks (B).....	84
Figure 2.20. A. Comparison of theoretical (AIP, —) and experimentally-estimated (IP^{ox} , —) ionization potentials using eq. 1; differences in the ionization potentials for each species arise from a comparison of a model monomer (theoretical) versus the full polymer (experimental) measurements and neglect solvent dielectric effects in the gas-phase calculations. B. Experimental mobility as a function of hole injection barrier. Note that for polymers 5 and 8 negligible mobilities were measured.....	91
Figure 3.1. Structures of air-stable <i>n</i> -channel semiconductors.....	97
Figure 3.2. Structures of ladder-type (bis)indenofluorene-based compounds 1-12	100
Figure 3.3. Structures of ladder-type (bis)indenofluorene-based homo- and copolymers P1-P14	100
Figure 3.4. A. Differential scanning calorimetry (DSC) of the compounds 1-12 at a temperature ramp of 5 °C/min under N ₂ . B. Optical images of compounds 7 and 10 , taken under 90° cross-polarization conditions as a function of temperature. Scale bars denote 100 μm	133
Figure 3.5. DFT-calculated molecular structures of 1 , 2 , and 7-10	134
Figure 3.6. Optical absorption (solid lines) and photoluminescence (dashed lines) spectra of molecules 1-12 and polymers P2-P4 , P6-P8 , and P12-P14 as THF solutions.....	137

- Figure 3.7. Optical absorption and photoluminescence spectra of molecules **1** (A, B) and **6** (C) in cyclohexane, THF, and ethanol solutions..... 139
- Figure 3.8. Cyclic voltammograms of compounds **1-12** in THF (A and B) and polymers **P3**, **P5**, and **P8** as thin films in acetonitrile (C) in 0.1 M Bu₄N⁺PF₆⁻ at a scan rate of 100 mV/s...144
- Figure 3.9. Single crystal X-ray structures of A. bisindenofluorenediketone compound **7**, B. indenofluorenedicyanovinylene monomer **M2**, and C. bisindenofluorenedicyanovinylene compound **M4**..... 151
- Figure 3.10. θ -2 θ X-ray diffraction (XRD) scans of spin-cast films of compounds **1-12** on silicon substrates. 154
- Figure 3.11. A. Electron mobilities measured in ambient for TFTs fabricated with spin-coated **10** and annealed at the indicated temperatures (80 °C – 150 °C) vs storage time of the devices in air without excluding light or ambient humidity (25% – 40 %). B. θ – 2 θ X-ray diffraction (XRD) scans of spin-coated **10** thin films at different annealing temperatures (Note that peak intensities are not normalized for comparison purposes). C. Tapping mode AFM images of **10** thin films at different annealing temperatures. Scale bars denote 1 μ m.....156
- Figure 3.12. Schematic model of the layered and π - π stacked thin-film microstructure of **10**. The gray region shows the interdigitated alkyl chains forming an insulating barrier between conducting π -conjugated backbones (blue region). Note that the tilt angle (θ) strongly depends on the extent of alkyl-chain interdigitation for a given d-spacing 157
- Figure 3.13. OTFT data for devices fabricated with compounds **6** and **10**. A. Output and transfer ($V_{SD} = 100$ V) plots for films of **6**, B. Output and transfer ($V_{SD} = 100$ V) plots for films of **10**. The general structure of an OTFT device is given in the inset..... 159

Figure 3.14. Transfer curves of compounds 10 (A) and 6 (B) under vacuum (red curves) and in ambient (blue curves). Note that the transfer curve for 10 was recorded after 5 months of storage in ambient. Below: the band lineups of LUMO energies of 10 and 6 with respect to the O ₂ /H ₂ O electrochemical redox couple at air-thin film interface.....	160
Figure 3.15. HOMO and LUMO pictorial representation for the present carbonyl- (1 , 3 , 5 , 7 , 9 , and 11) and dicyanovinylene-substituted (2 , 4 , 6 , 8 , 10 , and 12) semiconductors	165
Figure 3.16. (A) Schematic of a Schottky-type injection barrier between a metal electrode and an organic semiconductor, showing electron/hole injection barriers. The energy diagram for compounds 1-12 , and polymers P2 , P3 , P6 , P7 , P8 , and P12-P14 showing experimentally estimated (B and C) and theoretical (D) HOMO/LUMO energy levels, and charge carrier polarity. Blue region indicates TFT devices with ambient stability. The dashed lines indicate the Fermi level of the gold electrode and the air-stability limit.. The dashed lines indicate the Fermi level of the gold electrode and the air-stability limit.....	168

List of Schemes

Scheme 2.1. Synthesis of dibenzosilole and dithienosilole monomers.	49
Scheme 2.2. Synthesis of dibenzosilole-based and dithienosilole-based homo- and copolymers.	51
Scheme 3.1. Synthesis of indenofluorene-based compounds 1-4 and monomers	125
Scheme 3.2. Synthesis of bisindenofluorene-based compounds 5-8 and monomers.....	126
Scheme 3.3. Synthesis of bisindenofluorene-based compounds 9-12 and monomers.....	128
Scheme 3.4. Synthesis of (bis)indenofluorene-based homo- and copolymers P1-P15	131

List of Tables

Table 2.1. Physicochemical Properties (Molecular Weight (Mw, KD), polydispersity (PD), melting temperature (T _m), crystallization temperature (T _c), onset decomposition temperature (T _d), solution (in THF) and film optical absorption maxima, emission maxima (in THF), (λ, nm), energy gaps (E _{g,op} , eV),) and FET performance summary (OFET charge carrier mobilities (μ, cm ² V ⁻¹ s ⁻¹), and current On/Off ratios (I _{on} /I _{off}) in air) of polymers 5-12	54
Table 2.2. Electrochemical properties of polymers 5-12	63
Table 2.3. Computed adiabatic ionization potentials and electron affinities (eV), selected valence molecular orbital energies (eV), HOMO-LUMO gaps (eV), and low-lying excited-state energies (eV and nm, in parentheses), oscillator strengths, and excited-state configurations as determined at the B3LYP/6-31G** level. (^a Computed using ΔSCF methods)	88
Table 3.1. Summary of Thermal, Optical Absorption/Emission, and Electrochemical Properties of Compounds 1-12 , and Corresponding Estimated Frontier Molecular Orbital Energies.....	174
Table 3.2. Majority charge carrier types, field-effect mobilities (μ), threshold voltages (V _T), and current I _{on} /I _{off} ratios for thin-films of compounds 1-12 fabricated by spin-coating/vacuum-deposition on OTS-treated Si/p ⁺ -SiO ₂ substrates. ^a The mobility values, threshold voltages, and I _{on} /I _{off} ratios given are the average values for 10 devices with the standard deviations less than 5%.	175
Table 3.3. Physicochemical Properties (Molecular Weight (Mw, KD), polydispersity (PD), melting temperature (T _m), crystallization temperature (T _c), onset decomposition temperature	

(T _d), solution (in THF) and film optical absorption maxima, energy gaps (E _{g,op} , eV), and FET performance summary (OFET charge carrier mobilities and current on/off ratios of polymers P1-P14	176
Table 3.4. XRD reflections and d-spacings calculated from the (100) reflection for vacuum-deposited and solution-cast films of compounds 1-12	177
Table 3.5. Computed vertical and adiabatic electron affinity (VEA, AEA) and ionization potential (VIP, AIP) energies (eV), intermolecular relaxation energies (λ ₁ , λ ₂), and total intermolecular reorganization energy (λ _i) as determined at the B3LYP/6-31G** level.....	178
Table 3.6. Selected molecular orbital energies (eV), HOMO-LUMO gap (eV), and low-lying excited-state energies (eV and nm), oscillator strengths, and excited-state configurations as determined at the B3LYP/6-31G** level.....	179
Tables 3.7. - 3.18. Low-lying excited-state energies (eV and nm), oscillator strengths, and excited-state configurations for 1-12 as determined at the B3LYP/6-31G** level.....	180 - 187

Chapter One

Introduction

π -Conjugated organic molecules and polymers have been the focus of extensive scientific and technological research over the past few decades as active materials in organic electronics.^{1,2} These structures are composed of π -conjugated molecular or polymeric units with highly delocalized π -orbitals, which give them unique electrical and optical features that can be easily tuned through structural modifications.^{3,4} In contrast to inorganic-based materials where atoms are held together with strong covalent or ionic bonds, organic structures exhibit relatively weak van der Waals, dipole-dipole and π - π interactions, and usually produce polycrystalline or amorphous thin-films that are capable of transporting charge and interacting with light.⁵ Among the diverse applications of organic materials as conducting, semiconducting, insulating, and light-absorbing/-emitting layers in new generation electronic devices, organic semiconductors have been widely studied during the past two decades as the main component of field-effect transistors (FETs).⁶ In the solid-state of organic semiconductors, due to the presence of weak intermolecular interactions, charge delocalization occurs along the backbone of a molecule/polymer chain or between the π -orbitals of the neighboring molecules/monomeric units, resulting in localized states with negligible band formations.⁷ Hence, charge transport mechanism is mainly thought to be a hopping process between these localized states where electrons or holes migrate through the lowest unoccupied molecular orbitals (LUMOs) or highest occupied molecular orbitals (HOMOs), respectively.⁸ Generally, organic semiconductors exhibit lower performances compared to most inorganic semiconductors, nevertheless they have numerous advantages such as low-temperature processing on flexible (rollable) substrates, large area coverage, low-cost and high-speed fabrication, and facile synthetic modifications.^{1-4,9} These features facilitate the realization of new generation electronic products such as low-power

consumption flexible displays, inexpensive plastic RFID tags, smart cards, electronic papers, sensors and plastic solar cells, which have been previously limited due to the mechanical properties of the traditional solid-state electronic materials.¹⁰ The solubility, stability, and rheological properties of organics enable printing, patterning, and spin-coating of the active materials over large areas in ambient conditions, which is a great improvement over the fabrication of current silicon-based chips that require advanced lithography techniques.^{11, 12} The utilization of conventional printing techniques (ink-jet printing, screen printing) enables high device fabrication throughput (100 – 10,000 m²/h) and quick device design optimizations. In addition, molecular structures can be easily tailored through exploratory synthetic chemistry resulting in new materials with desirable chemical, optical, and electrical properties, which allow quick screening of a series of structures to meet the required criteria for any particular application.¹

Among the various applications of organic semiconductors in electronic devices such as field-effect transistors (OFETs),^{1, 2} light-emitting diodes (OLEDs),¹³ and photovoltaic cells (OPVs),¹⁴ FETs are the central logic unit in modern electronic circuits, where they usually function as either a switch or an amplifier. As it is shown in Figure 1.1, in a typical top-contact/bottom-gate FET device structure, a semiconductor layer is deposited as a thin-film (30 nm – 100 nm) on top of a dielectric layer (usually 300 nm of SiO₂) with an underlying gate electrode (*p*- or *n*-doped Si). Charge-injecting source (S) and drain (D) electrodes (thermally grown 50 nm thick Au) are deposited on top of the semiconductor layer through a shadow mask giving channel lengths (*L*) of 25 – 100 μm and channel widths (*W*) of 500 – 5000 μm. A field-effect transistor can be depicted as a three terminal device in which the current flowing through

the semiconducting layer between two terminals (S and D) is controlled by an external voltage (V_G , gate voltage) applied at the third terminal (gate). The general device operation is as follows: when no gate voltage is applied, the number of charge carriers, and consequently the current flowing through the semiconducting layer, is minimal ($\leq 10^{-8} - 10^{-9}$ A), which is defined as the *off-state*. Upon the application of a bias at gate electrode ($V_G < 0$ for *p*-type and $V_G > 0$ for *n*-type, Figure 1.1), an electrical field is induced through the dielectric layer resulting in the accumulation of charge carriers at semiconductor-dielectric interface along with an increase in S \rightarrow D current (*on-state*). OFETs are commonly classified as *p*-type (hole-conducting) or *n*-type (electron-conducting) depending on which type of charge carrier is induced and transported. In a few cases, OFETs can operate as both *p*-type and *n*-type, and the semiconductor is called ambipolar.

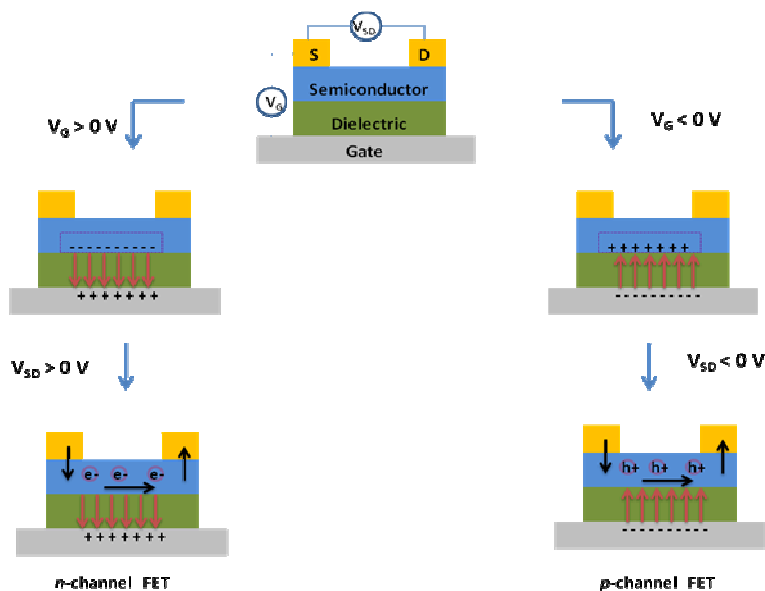


Figure 1.1. Schematic of a top-contact/bottom-gate field-effect transistor (FET), and *p*- and *n*-channel device operations.

The typical transfer and output curves obtained by the electrical characterization of a FET are shown in Figure 1.2. In an output plot, which resembles real device operation, there are two regimes; the linear regime is observed at low source-drain voltage ($V_{SD} < V_G$) where the current increases linearly by source-drain biases, and the saturation regime is observed when the source-drain current is independent of the source-drain voltage. As the initial characterization of organic semiconductors, electrical measurements are usually carried out in the saturation regime,¹⁵ and transistor characteristics are calculated using Eq. 1:¹⁶

$$I_{SD} = (W/2L)\mu C_i(V_G - V_T)^2 \quad (1)$$

where W and L are the FET channel width and length, respectively, C_i is the capacitance per unit area of the dielectric, μ is the field-effect mobility, and V_G and V_T are the gate and threshold voltages, respectively. Three important figures of merit for organic transistors are the charge carrier mobility (μ), on/off ratio (I_{on}/I_{off}), and the threshold voltage (V_T).^{2, 17} Mobility is defined as the drift velocity of the charge carriers per unit of electrical field and shows how efficiently the charge carriers can move along the conduction channel from S to D. The ratio between the currents in the *on-state* and the *off-state* is called I_{on}/I_{off} ratio, indicative of the switching behavior of the device. Threshold voltage is defined as the voltage where the device turns on, corresponding to the x-axis intercept in the plot of $(I_{SD})^{1/2}$ vs V_G (Figure 1.2B). The overall device performance of a FET is evaluated by the combination of these three parameters, and for organic materials, in order to be realized in the aforementioned low-performance applications and to be competitive with hydrogenated amorphous silicon, charge carrier mobilities of ≥ 0.1 $\text{cm}^2/\text{V}\cdot\text{s}$, I_{on}/I_{off} ratios of $\geq 10^5$, and $V_T \sim 0$ V are required.¹⁸

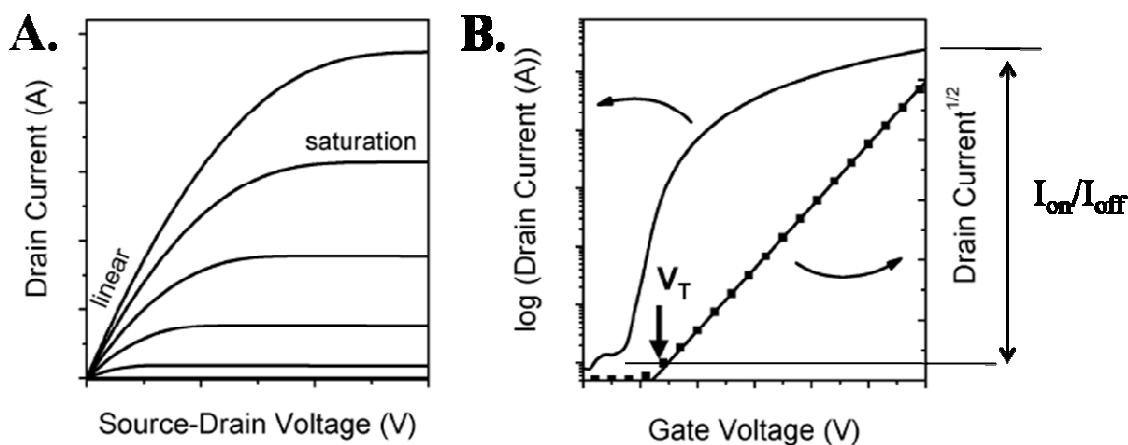


Figure 1.2. Representative current-voltage characteristics of an organic field-effect transistor: A. Output plot showing linear and saturation regimes. B. Transfer plot in the saturation regime indicating threshold voltage (V_T) and current on/off ratio (I_{on}/I_{off}).¹⁹

The electronic and structural criteria governing the charge transport characteristics of semiconductors in OFETs have been widely studied, mainly elucidating the relationship between molecular/solid-state properties and device performance.²⁰ Although some fundamental aspects still remain unclear, the general charge transport mechanism is accepted to occur in two subsequent parts: first, the charge-injection from S electrode into the semiconductor film, and second, the charge transport from S to D through the conduction channel, which is described as the first 2 – 3 nm of the film in proximity to the dielectric-semiconductor interface.²¹ In a zero level vacuum picture, the relative position of molecular energy levels (HOMO/LUMO) versus the Fermi level of source/drain electrodes determines the hole/electron charge injection barriers, which are found to have profound effects on charge-carrier polarity (*p*- vs. *n*-type), threshold voltage, and field-effect mobility.²² The correlations between these parameters have been

successfully explained through a Schottky-type injection barrier model.²³ The charge transport from S to D is mainly controlled by the semiconductor thin-film microstructure, which is generally investigated by in-plane/out-of-plane X-ray diffraction (XRD), AFM, and SEM methods. For polycrystalline organic thin-films at temperatures ≥ 25 K, charge transport is mainly found to be thermally-activated as a result of hopping process occurring between individual molecules or molecular stacks.²⁴ The preferential orientation is with the molecular long axes parallel to the substrate normal with sufficient overlap between molecular frontier π -orbitals. This orientation ensures that intermolecular π - π stacks are in the charge transport direction from S to D, maximizing the electronic coupling between adjacent molecules and lowering charge transfer activation energies, which leads to higher mobilities.²⁵ The crystalline domain size is also crucial in determining the ultimate device performance. The individual grains (determined by AFM/SEM) are accepted as trap-free single-crystal like regions, whereas grain boundaries are known to act as deep charge traps limiting the overall charge transport.²⁶ Hence, crystalline domains should cover as large area as possible between S and D contacts to reduce the possible charge trap densities and enhance charge transport.

There are several aspects of research on OFETs including syntheses of new organic materials as semiconductors, dielectrics, and conductors, device structure optimizations, and studies of dielectric-semiconductor/semiconductor-electrode interfaces. Among these, the development of high performance semiconducting materials with desired chemical and physical characteristics is not fully established yet. New materials are critical both for better understanding of molecular structure-charge transport relationships and for the realization of truly all-organic electronic devices. Since the report of the first OFET (*p*-type) based on electrochemically grown

polythiophene film in 1986, intensive research on the design and synthesis of new materials has resulted in a series of *p*-type, *n*-type, and ambipolar semiconductors over the past two decades.²⁷ Today, *p*-type organic compounds represent the leading family among these three types of semiconductors, mainly due to the synthetic accessibility of the structures and relatively air-stable charge transport characteristics. However, through rational designs and synthetic approaches, many *n*-type semiconductors have been realized via functionalizations of the known *p*-type cores (acene, arylene, thiophene, phenylene, and fluorene-based π -conjugated structures) with electron-deficient units and substituents such as perfluoralkyl ($-\text{C}_n\text{F}_{2n+1}$), $-\text{CN}$, $-\text{F}$, perfluorophenyl (C_6F_5-), carbonyl ($-\text{C}=\text{O}$), and imide ($-\text{C}(\text{O})\text{NHC}(\text{O})-$).²⁸ Additionally, ambipolar FETs have recently been realized from bilayers or blends of *p*- and *n*-type semiconductors, or from low band gap donor-acceptor compounds.¹⁹ The development of both *n*-channel and *p*-channel devices are important for *p-n* junction diodes, organic photovoltaic devices, and complementary organic circuits (CMOS) that have the advantages of low power dissipation, low noise, and greater operational stability.²⁹ Despite the realization of many semiconductors from different researches, there are still only a few semiconductors that fully meet the performance requirements for real applications, and the main challenges remain to be solution-processibility and ambient stability. For *p*-type semiconductors, unintentional *p*-doping of the active layer with ambient species (O_2 and H_2O) result in an increase of the charge carriers (i.e. holes) in the *off-state* that eventually reduces the $I_{\text{on}}/I_{\text{off}}$ ratio of the device.³⁰ Ambient stability is a more prominent issue for *n*-type materials, since organic anions are known to be very reactive with O_2 and H_2O . In general, devices fabricated with most *n*-type semiconductors only operate under vacuum/inert atmosphere, and become totally inactive upon exposure to

ambient.³¹ Although several different strategies such as reducing frontier molecular orbital energies or kinetic barrier formation have been developed to enhance ambient stability of devices, the number of materials with desired properties is still inadequate, and the fundamentals governing the ambient stability are not fully established.³² On the other hand, strong π -interactions and the rigidity of conjugated backbones render the molecules insoluble in most common solvents, which introduces extra synthetic challenges towards new structures with highly balanced solid-state packing and solubility. Molecular and polymeric *n*-type semiconductors combining ambient stability, solution-processibility and high performance still remain to be fully realized. Additionally, no ambient stability has been reported for molecular and polymeric ambipolar materials, and only recently an inorganic coordination compound is reported to operate in ambient as an ambipolar semiconductor with a moderate device performance.³³

The aforementioned considerations prompted this thesis research to realize new organic molecules and polymers as air-stable and solution-processable semiconductors for high-performance *p*-channel, *n*-channel, and ambipolar OFETs, and to gain detailed insight into the charge transport characteristics revealing the correlations between molecular properties and device performances. Throughout the design and synthesis of new semiconductors, along with synthetic accessibility, the following key structural parameters are considered: (i) a highly π -conjugated planar backbone for efficient charge delocalization/transport and high thin-film crystallinity, (ii) alkyl chains to enhance the solubility in conventional organic solvents and to promote molecular self-assembly in thin-film phase without disrupting the backbone π -conjugation/planarity, (iii) electron-deficient substituents and functionalities to lower HOMO

and LUMO energies to facilitate electron transport and to enhance ambient stability, (iv) bromo/boronic ester/trialkyltin functionalities at molecular termini for step-growth polymerization reactions. In each research project, a series of polymers and molecules is synthesized and fully characterized. Along with high device performances observed for the new materials, some of which are among the best in the literature, we observe significant correlations between structural properties, thermal/optical/electrochemical features, thin-film microstructures and FET device characteristics. Without any doubt, the present findings not only introduce new high-performance materials, but also provide key structural information which is of critical importance for the future design of new semiconductors and for detailed understanding of the fundamental aspects of organic electronics. To that end, this thesis is arranged in the following order.

Chapter 2 demonstrates the design, synthesis and characterization of a new class of dithienosilole and dibenzosilole-based homo- and copolymers as air-stable and solution-processable high performance *p*-type semiconductors. Previously, several different strategies have been pursued to suppress unintentional p-doping of high mobility thiophene-based polymeric systems, such as introducing electron-withdrawing side-chains, or modulating the effective π -conjugation length via introduction of rotational degrees of freedom, geometric twists, or less π -conjugated subunits into the polymer backbone.³¹ Although these strategies have led to many air-stable semiconducting polymers having mobilities ranging from 10^{-5} $\text{cm}^2/\text{V}\cdot\text{s}$ to > 0.1 $\text{cm}^2/\text{V}\cdot\text{s}$, there are still few polymers exhibiting truly high performance (≥ 0.1 $\text{cm}^2/\text{V}\cdot\text{s}$, $I_{\text{on}}/I_{\text{off}}$ ratio of $>10^5$).³² This work shows that introduction of silole (silacyclopentadiene) cores into thiophene- and fluorene-based polymeric backbones is a new promising approach to

obtaining air-stable devices since in a silole core, the exo-cyclic Si-C σ^* -orbital effectively hybridizes with the π^* -orbital of the butadiene fragment to afford low-lying LUMO and HOMO energy levels.³² By using this approach, high *p*-channel mobilities up to 0.08 cm²/V·s and current modulations of 10⁵ – 10⁶ are achieved along with air stability. In the present contribution, we report a broad synthetic/characterization/theoretical investigation aimed at better understanding of the relationships between the chemical structures and electrical properties of this novel silole-containing polymeric class. The interrelationships between molecular structure, solution/thin-film phase photophysical and redox properties, and frontier molecular orbital energy positioning on TFT performance are elucidated, and TFT device performances are optimized in terms of solvent selection and film processing methodology. Furthermore, density functional theory (DFT) calculations are done to investigate the effect of silole and thiophene units on the polymer physicochemical and charge transport characteristics. Solution-cast thin-films of all polymers exhibit high degree of crystallinities and the preferential “edge-on” orientation relative to the substrate which leads to layered structure formation with the π - π stacking direction parallel to the substrate plane, which is known to favor in-plane source-to-drain (S \rightarrow D) charge transport. A direct correlation between the hole injection barrier and both TFT turn-on voltage and TFT polymer hole mobility is discovered for the first time and discussed, in combination with thin-film morphological characteristics, to explain the observed OTFT performance trends across the present silole-based series. These results, in total, affirm the possibility of achieving low-cost microelectronic devices through polymeric organic materials that enable simple solution fabrication processes under ambient conditions.

Chapter 3 depicts the discovery of a new highly electron-deficient class of indeno[1,2-b]fluorene-6,12-dione, 2,2'-(indeno[1,2-b]fluorene-6,12-diylidene) dimalononitrile, bisindenofluorene-12,15-dione, and 2,2'-(bisindenofluorene-12,15-diylidene) dimalononitrile-based ladder-type building blocks and their corresponding homo- and copolymers, and examine in detail the effects of core size, thiophene vs. core regiochemistry, carbonyl vs. dicyanovinylene functionality, and alkyl chain orientation on the physicochemical properties, thin-film microstructures, and OFET device performance. New compounds are characterized by DSC, TGA, melting point, single-crystal X-ray diffraction (XRD), solution/thin-film optical, PL, and cyclic voltammetry measurements to evaluate frontier molecular orbital energetics and intermolecular cohesive forces. Thin films are grown by vacuum deposition and spin-coating, and investigated by X-ray diffraction (XRD) and AFM, which indicates the presence of well-organized lamellar microstructures with the common preferential molecular/chain “edge-on” orientation relative to the substrate with short π - π stacking distances of 3.1 – 3.4 Å. Exceptionally, some of these thin-films exhibit very large plate-like highly crystalline grains (\sim 3 – 5 μ m) with terraces of \sim 2.8 nm, corresponding to the d-spacings along the lamellar layer, which introduces the possibility of the fabrication of grain boundary free, single-crystal like solution-cast FETs. By tuning the HOMO/LUMO energetics of the present materials over a 1.0 eV range, *p*-type, *n*-type, or ambipolar charge transport characteristics can be observed, thus identifying the MO energetic windows governing majority carrier polarity and air stability. One of these systems, thiophene-terminated indenofluorenedicyanovinylene exhibits an electron mobility of 0.16 cm²/V·s and an $I_{\text{on}}/I_{\text{off}}$ ratio of 10^7 – 10^8 , one of the highest to date for a solution-cast air-stable *n*-channel semiconductor. Here we also report solution-processed

ambipolar films of a thiophene-based molecule and two new copolymers which exhibit electron and hole mobilities of $1 \times 10^{-3} - 2 \times 10^{-4}$ and $I_{\text{on}}/I_{\text{off}}$ ratios of $\sim 10^4$, representing the first examples of molecular and polymeric ambipolar semiconductors to function in air. Analysis of the operational air-stabilities of a series of thin-films having different crystallinities, orientations, and morphologies suggest that operational air-stability for thermodynamically-predicted (i.e., no kinetic barrier contribution) air-stable semiconductors is principally governed by LUMO energetics with minimal contribution from thin-film microstructure. The onset LUMO for stabilization of carrier electrons is estimated as $-4.0 - -4.1$ eV, indicating an overpotential of $0.9 - 1.0$ eV. Density functional theory calculations provide detailed insight into molecule/polymer physicochemical and charge transport characteristics.

Chapter Two

**Synthesis, Characterization, and Transistor Response
of Semiconducting Silole Polymers with Substantial
Hole Mobility and Air Stability**

2.1 Introduction

π -Conjugated oligomeric and polymeric semiconductors have been the focus of intense research over the past few decades as alternatives to inorganic semiconductors for low-cost electronic applications such as organic thin-film transistors (OTFTs),¹⁻⁴ light-emitting diodes (OLEDs),^{5, 6} and photovoltaics (OPVs).⁷⁻¹⁰ These materials enable vapor- or solution-phase fabrication of large-area, light-weight electronic devices, and are compatible with plastic substrates for mechanically flexible, conformable, and wearable electronics. OTFTs can be used in low-performance memory elements, sensors, and drive electronics for active-matrix displays.^{11, 12} OLEDs are envisioned as cheap, energy-efficient alternatives to liquid crystal displays and solid-state lighting sources. Flat-panel displays based on OLEDs are emerging in commercial portable electronic devices and novel textiles.

Among the organic semiconductor classes used for OTFTs, (oligo, poly)-thiophenes have been among the most extensively investigated. The hole transporting properties of α -sexithiophene (α -6T) were first disclosed in 1988,¹³ and p-type OTFTs fabricated from thermally evaporated α -6T thin films were reported one year later.^{14, 15} High-performance electron-transporting (n-type) oligothiophenes have also been developed to fully realize the potential of organic electronics via complementary circuits.¹⁶⁻¹⁸ Unfortunately, OTFTs based on oligothiophenes usually exhibit lower mobilities when films are grown from solution,¹⁹ presumably reflecting difficulties in creating high levels of long-range structural order. This lack of solution processibility, along with the intrinsic inefficiency of alternative vacuum vapor-phase film growth processes, limits the appeal of oligothiophenes as active channel materials in OTFTs.

For taking full advantage of the efficiencies of solution processing methodologies such as spin-coating,²⁰ stamping,²¹ or inkjet printing,²² polymeric organic semiconductors offer excellent candidate materials. Among the polythiophenes, soluble regioregular polythiophenes such as poly(3-hexylthiophene) (P3HT, Figure 2.1) and variants thereof,²³⁻²⁵ are among the most commonly used in OTFTs due to large charge carrier mobilities and synthetic accessibility.²⁶⁻²⁹ Despite recent design advances, a major drawback of commonly used polythiophenes is poor air stability –a shortcoming that is particularly acute when these materials are used as the active layers in OTFTs. Unintentional doping of polythiophenes by ambient O₂ often results in large off-currents, leading to low current on/off ratios ($I_{\text{on}}/I_{\text{off}}$) and positive threshold voltage shifts.^{23, 30} Consequently, precautions must be taken during synthesis and device fabrication to exclude O₂.^{31, 32} These constraints thus render polythiophene-based OTFTs less attractive as cheap alternatives to silicon-based electronics. Thus, there is a continued need to develop semiconducting polymers with both high carrier mobility and air stability.

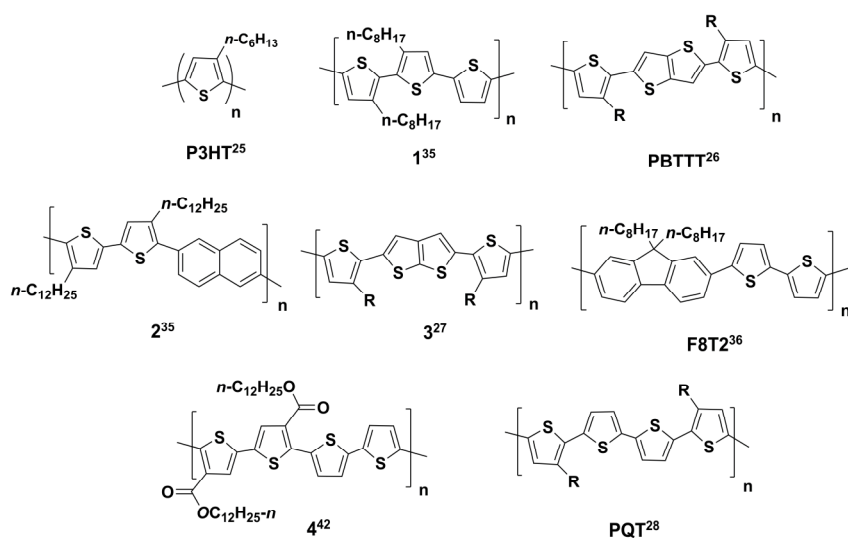


Figure 2.1. Structures of P3HT and air-stable thiophene-based polymeric semiconductors.

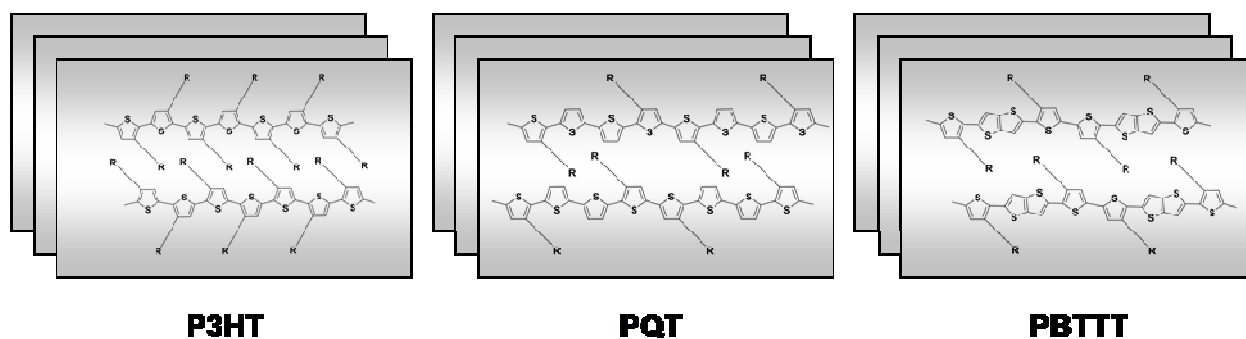


Figure 2.2. Schematic of the lamellar π -stacking in polymers **P3HT**, **PQT**, and **PBTTT**.

To a first approximation, the ambient air stability of organic semiconducting polymers towards oxidative doping is governed principally by the ionization potential³³ – or in terms of simple Koopmans' theorem³⁴ metrics, the energy of the highest-occupied molecular orbital (HOMO). Generally, increasing the ionization potential of organic semiconducting polymers improves environmental stability by minimizing the p-doping level achievable with ambient O_2 . At the molecular level, the HOMO can be modified either by tailoring the effective conjugation length and/or by varying the electron density in the conjugated π -system. The effective conjugation length in polymers can be modulated by introducing rotational degrees of freedom, geometric twists, or less conjugated groups into the macromolecule backbone. For example, a polythiophene containing adjacent, twisted 3-octyl thiophene rings exhibits greater air stability than its regioregular head-to-tail counterpart (**1**, Figure 2.1).³⁵ Similarly, incorporation of either a thieno[3,2-b]thiophene (PBTTT, Figure 2.1), naphthalene (**2**, Figure 2.1) or thieno[2,3-b]thiophene (**3**, Figure 2.1) into the polymer backbone affords greater environmental stability,^{26, 27, 35} and copolymers of thiophene with fluorene are reported to have good air stability and hole mobilities up to $0.01 \text{ cm}^2/\text{V}\cdot\text{s}$ – $0.02 \text{ cm}^2/\text{V}\cdot\text{s}$ (F8T2, Figure 2.1).³⁶ An

alternative approach to reducing the HOMO energy is to incorporate electron-withdrawing substituents. Reports of polythiophenes with electron-withdrawing substituents are rare, doubtless due to synthetic challenges.^{37, 38} For example, polythiophenes bearing carboxylate groups at the 3-position have been synthesized using Ullmann,^{39, 40} Kumada,⁴¹ and Stille coupling reactions.⁴² (e.g., **4**, Figure 2.1) These polymers exhibit increased oxidation potentials due to the presence of the electron-withdrawing substituents; as a result, OTFT devices based on these polymers are reported to exhibit air stability superior to that of P3HT-based devices.⁴² PBTTT²⁶ and PQT²⁸ also exhibit enhanced FET performance with good ambient stabilities due to their highly organized film microstructures and larger ionization potentials in comparison to P3HT; highly ordered, lamellar π -stacks of these polymers are oriented normal to the substrate and lead to high OTFT mobilities (Figure 2.2).⁴³⁻⁴⁵

Silicon substituents have long been known to stabilize adjacent carbanionic centers due to the effective hyperconjugation between negatively charged carbon and the adjacent silyl group.⁴⁶ Among the various silicon-containing π -conjugated systems, silole (sila-2,4-cyclopentadiene, Figure 2.3)-containing polymers have attracted recent attention as novel systems in which the exo-cyclic Si-C σ^* -orbital effectively mixes with the π^* -orbital of the butadiene fragment to afford a low-lying lowest-unoccupied molecular orbital (LUMO) and a relatively small band gap.⁴⁷⁻⁴⁹ Additionally, silicon introduction stabilizes the diene HOMO level compared to the carbon counterparts,⁴⁸ which should, *a priori*, enhance the ambient stability of silole-polymer-derived TFTs. To date, however, the use of polymeric silole derivatives has been limited to electron-transporting materials in OLEDs⁵⁰⁻⁵⁴ and solar cells.^{55, 56} Only recently have silole-containing polymers been investigated as the active layer in OTFTs.⁵⁷⁻⁵⁹ Nevertheless, the

performance of the reported materials is generally modest in regard to carrier mobility and $I_{\text{on}}/I_{\text{off}}$, probably because non-bonded repulsions between the large substituents at the silole 3- and 4-positions interfere with the close π - π stacking requisite for efficient charge transport.⁶⁰

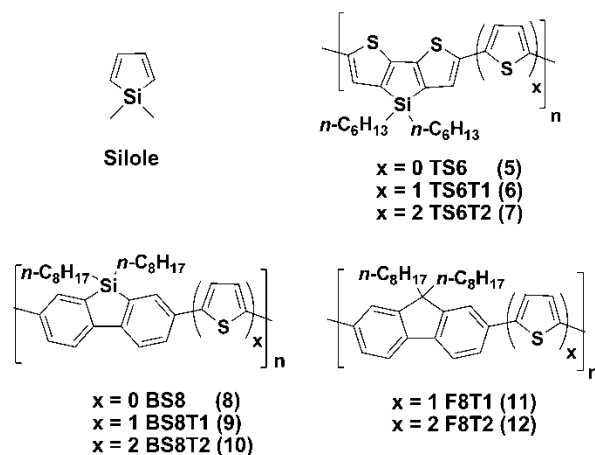


Figure 2.3. Structures of silole-thiophene polymers **5-10**, fluorene-thiophene polymers **11** and **12**.

In this contribution, we describe the synthesis and characterization of new silole-based polymers, **5 – 10** (Figure 2.3) to explore architecture–electronic structure relationships in silole-based polymers and their impact on OTFT performance.⁶¹ Electrical measurements revealed the surprising result *that each of these new polymers is a p-type semiconductor*, and despite the depressed LUMO energies, no evidence of n-channel transport was found. We furthermore provided evidence that these polythiophenes exhibit excellent air and thermal stability. The silole-containing polythiophenes exhibit useful FET properties after thermal annealing, and the devices are stable upon exposure to air for extended storage without protective encapsulation. It will be seen that materials having hole mobilities approaching $0.1 \text{ cm}^2/\text{V}\cdot\text{s}$ with $I_{\text{on}}/I_{\text{off}} > 10^6$ are obtained with devices fabricated in ambient atmosphere using simple spin-coating techniques.

TFT devices based on polymers **5** – **10** are optimized in terms of solvent selection and film processing methodology. Furthermore, the first example of TFT fabrication with a gravure printed semiconductor on a gravure printed dielectric is reported. Finally, the silole polymer electronic structures are analyzed using density functional theory (DFT). The result is a detailed representation of the electronic structures of polymers **5-10** that, when combined with the experimental characterization data, provides clear insight into the OTFT performance and reveals the basis of the hole-transporting characteristics. Two new fluorene-containing copolymers, **11** and **12** (F8T2), are also synthesized and characterized. TFTs based on **11**, **12**, and **P3HT** are fabricated and evaluated for comparative purposes.

2.2 Experimental

2.2.1 Materials and Methods.

All reagents were purchased from commercial sources and used without further purification unless otherwise noted. Anhydrous THF was distilled from Na/benzophenone. Conventional Schlenk techniques were used, and reactions were carried out under N₂ unless otherwise noted. Optical spectra were recorded on a Cary Model 1 UV-Vis spectrophotometer. Fluorescence measurements were recorded on a Photon Technology International model QM-2 fluorimeter. NMR spectra were recorded on a Varian Unity Plus 500 spectrometer (¹H, 500 MHz; ¹³C, 125 MHz). GPC analyses of polymer samples were performed on a Waters Alliance GPCV 2000 (3 columns, Waters Styragel HT 6E, HT 4, HT 2; operation temperature, 150 °C; mobile phase, 1,2,4-trichlorobenzene; flow rate, 1 mL/min) and are reported relative to polystyrene standards purchased from Aldrich. Electrospray mass spectrometry was performed with a Thermo Finnegan model LCQ Advantage mass spectrometer. Electrochemistry was performed on a C3

Cell Stand electrochemical station equipped with BAS Epsilon software (Bioanalytical Systems, Inc., Lafayette, IN).

2.2.2 Synthesis and Characterization.

Synthesis of 3,3',5,5'-tetrabromo-2,2'-bithiophene (13). Bromine (19.6 g, 122.6 mmol) was added dropwise over 1.5 h to a solution of 2,2'-bithiophene (5.57 g, 33.5 mmol) in the mixed solvent glacial acetic acid (20 mL) and chloroform (45 mL) at 5-15 °C. The mixture was subsequently stirred at room temperature for 5 h and then under reflux for 24 h. After cooling to room temperature, the reaction was quenched by addition of 50 mL of 10% KOH aqueous solution. The mixture was then extracted with CHCl₃ (2×100 mL), the combined extracts were washed with water, dried over anhydrous MgSO₄, filtered, and the solvent removed by evaporation. Recrystallization from ethanol afforded off-white crystals in 77% yield. ¹H NMR (CDCl₃): δ 7.06 (s, 2H) ppm; ¹³C NMR (CDCl₃): δ 112.32, 115.31, 133.17 ppm.

Synthesis of 3,3'-dibromo-2,2'-bithiophene (14). Bithiophene **13** (12.5 g, 25.9 mmol) was added in portions within 0.5 h to a refluxing dispersion of Zn powder (6.5 g, 0.10 mol) in 130 mL of ethanol containing 13 mL of water, 31 mL of glacial acetic acid, and 2.6 mL of 3 M HCl. After refluxing for an additional 2 h and then cooling to room temperature, the mixture was filtered and the residue washed three times with ethanol, and the combined filtrate collected. The solvent was then removed by evaporation, and 60 mL of H₂O was added. The mixture was then extracted with diethyl ether, and the combined extracts were washed with water, dried over anhydrous MgSO₄, and filtered. The solvent was removed by evaporation, and the crude product was recrystallized from hexane to give colorless crystals (7.6 g, yield 90% yield). ¹H NMR

(CDCl₃): 7.41 (d, J = 5.3 Hz, 2H), 7.09 (d, J = 5.3 Hz, 2H) ppm; ¹³C NMR (CDCl₃): δ 112.84, 127.73, 129.07, 131.01 ppm.

Synthesis of 3,3'-di-*n*-hexylsilylene-2,2'-bithiophene (15). To a solution of *n*-BuLi in hexane (60 mmol, 24 mL) in anhydrous THF (500 mL) at -78°C was added dropwise over the course of 30 min under vigorous stirring a solution of **14** (30 mmol, 9.720 g) in anhydrous THF (100 mL). The mixture was then stirred at -78°C for 1 h, resulting in a white suspension. Next, a solution of dichlorodihexylsilane (30 mmol, 8.070 g) in THF (100 mL) was added dropwise. The reaction mixture was stirred at -78°C for an additional 5 h, allowed to warm to room temperature, and stirred overnight. The reaction was next quenched by adding saturated aqueous NH₄Cl solution (300 mL). The aqueous layer was extracted with ether (3×100 mL). The organic phases were then combined and washed with water and dried over MgSO₄. After filtration, the solvent was removed, and the crude product was purified by column chromatography to yield a light yellow liquid (6.8 g, 68% yield). ¹H NMR (CDCl₃): δ 0.85-0.93 (m, 10H), 1.24-1.41 (m, 16H), 7.06 (d, 2H, J = 5.0 Hz), 7.21 (d, 2H, J = 5.0 Hz) ppm; ¹³C NMR (CDCl₃): δ 12.07, 14.29, 22.80, 24.37, 31.65, 33.07, 125.17, 126.85, 141.81, 149.37 ppm.

Synthesis of 5,5'-dibromo-3,3'-di-*n*-hexylsilylene-2,2'-bithiophene (16). To a solution of **15** (1.84 g, 5.0 mmol) in DMF (40 mL) was added NBS (1.98 g, 11.0 mmol) in one portion. The mixture was stirred at room temperature for 10 min and water (50 mL) was then added. The mixture was next extracted with ether (3×50 mL). The combined organic phase was washed with water (50 mL) and dried over MgSO₄. After filtration, the ether was removed, and the product was purified by column chromatography using hexane as eluent to give a green liquid (2.38 g,

91% yield). ^1H NMR (CDCl_3): δ 0.86-0.88 (m, 10H), 1.32-1.22 (m, 16H), 7.00 (s, 2H) ppm; ^{13}C NMR (CDCl_3): δ 11.85, 14.29, 22.75, 24.19, 31.58, 33.00, 111.62, 132.35, 141.19, 149.13 ppm.

Synthesis of 5,5'-Bis(trimethyltin)-3,3'-di-*n*-hexylsilylene-2,2'-bithiophene (17). To a solution of **16** (0.40g, 0.77 mmol) in THF (20 mL) was added *n*-BuLi (1.85 mmol, 0.74 mL, 2.5 M in hexanes) dropwise at -78°C . The mixture was stirred at -78°C for 1 h. Chlorotrimethyltin (2.4 mmol, 2.4 mL, 1.0 M in hexanes) was then added, and the mixture was next allowed to warm up to room temperature and stirred for 2 h. The volatiles were removed under vacuum. This preparation is used for the polymerization reaction.

Synthesis of 4,4'-Dibromo-2,2'-dinitrophenyl (18). To a stirring solution of 2,5-dibromonitrobenzene (24.0 g, 85.4 mmol) in DMF (110 mL) was added copper powder (12.0 g, 188.9 mmol), and the reaction mixture was heated at 125°C . After 3 h, the mixture was allowed to cool to room temperature. After most of the DMF was evaporated under high vacuum at 60°C , the residue was dissolved in benzene (400 mL) and the insoluble inorganic salts and excess copper next removed by filtration through Celite. The filtrate was washed with water and 10% NaHCO_3 and evaporated to dryness to yield the crude product as yellow crystals (15.6 g, 91%). The crude product was next recrystallized from isopropanol to yield 11.0 g of pure product. After evaporating the mother liquid to one-fourth of its volume, an additional 3.9 g of pure product was recovered, affording a total yield of 14.9 g (87 % yield). ^1H NMR (CDCl_3): δ 7.17 (2H, d, $J = 8.0$), 7.84 (2H, dd, $J = 8.0, 2.0$), 8.39 (2H, d, $J = 2.0$) ppm; ^{13}C NMR (CDCl_3): δ 123.0, 128.2, 131.8, 132.0, 136.4, 147.5 ppm; m.p. $148-149^\circ\text{C}$.

Synthesis of 4,4'-Dibromobiphenyl-2,2'-diamine (19). To a solution of **18** (11.0 g, 27.4 mmol) in 135 mL of absolute ethanol was added 32 % w/w aqueous HCl (78.0 mL). Tin powder

(13.0 g, 108.5 mmol) was then added in portions over 10 min, and the reaction mixture was heated to reflux at 100 °C for 2 h. After cooling, the mixture was poured into ice water (400 mL) and then made alkaline with 20% w/w aqueous NaOH solution until pH = 9.0. The product was next extracted with diethyl ether, and the organic layer was washed with brine, dried over anhydrous Na₂SO₄, filtered, and then evaporated to dryness to give pure product as light-brown crystals that could be used without further purification (8.6 g, 92% yield). ¹H NMR (CDCl₃): δ 6.92 (6H, s), 3.78 (4H, br s, NH₂) ppm; ¹³C NMR (CDCl₃): δ 118.2, 121.9, 122.1, 122.8, 132.4, 145.3 ppm; m.p. 118-119 °C.

Synthesis of 4,4'-Dibromo-2,2'-diiodobiphenyl (20). A solution of **19** (16.0 g, 46.8 mmol) and concentrated HCl (56.0 mL) in water (64.0 mL) was cooled to 0 °C. Next, 8.0g (0.106 mmol) of NaNO₂ in 40 mL of water was added dropwise to the diamine solution over a period of 30 min, keeping the temperature at 0 °C. After the addition of NaNO₂ was complete, the resulting mixture was stirred for an additional 30 min. and an aqueous solution of KI (77.7 g in 150 mL of water) at -5 °C was added dropwise over 30 min. The reaction mixture was then stirred (by mechanical stirrer) for 1 h at r.t and 3 h at 60 °C, giving a dark brown solution. The solution was then cooled to 25 °C and the brown precipitate was collected by filtration. The crude brown solid was then purified by column chromatography (silica gel, hexane) yielding the title compound as a white solid (7.4 g, 28 % yield). Anal. Calcd. for C₁₂H₆Br₂I₂: C, 25.6; H, 1.1; I, 45.0; found: C, 26.1; H, 1.2; I, 46.2; ¹H NMR (CDCl₃): δ 7.04 (2H, d, *J* = 8.0), 7.57 (2H, d, *J* = 8.0), 8.11 (2H, s) ppm; ¹³C NMR (CDCl₃): δ 99.9, 122.4, 130.8, 131.3, 141.2, 146.6 ppm; m.p. 91-92 °C.

Synthesis of 2,7-Dibromo-9,9'-di-*n*-octyldibenzosilole (21). *n*-Butyllithium (17.0 mL, 42.5 mmol, 2.5 M in hexane) was added in portions over 2 h to a stirring solution of **20** (6.0 g, 10.64

mmol) in dry THF (120 mL) at $-78\text{ }^{\circ}\text{C}$, under a nitrogen atmosphere. The mixture was next stirred for an additional 1 h at $-78\text{ }^{\circ}\text{C}$. Dichlorodioctylsilane (7.4 mL, 21.37 mmol) was subsequently added and the temperature of the mixture was raised to room temperature and the mixture was stirred overnight. The reaction mixture was then quenched with distilled water (30.0 mL), and the solvent was removed under vacuum. The product was then dissolved in diethyl ether and the organic layer washed with brine, dried over anhydrous MgSO_4 , filtered, and evaporated *in vacuo* giving 8.5 g of crude product as brownish oil. Purification by column chromatography (silica gel, hexane) yielded the title compound as colorless oil (4.2 g, 70 % yield) Anal. Calcd. for $\text{C}_{28}\text{H}_{40}\text{Br}_2\text{Si}$: C, 59.6; H, 7.1. Found: C, 60.4; H, 7.4; ^1H NMR (CDCl_3): δ 0.91 (6H, t, CH₃), 0.98 (4H, t, CH₂), 1.23-1.38 (24H, m, CH₂), 7.53 (2H, dd, $J = 8.0, 1.5$), 7.63 (2H, d, $J = 8.0$), 7.68 (2H, d, $J = 1.5$) ppm; ^{13}C NMR (CDCl_3): δ 12.2, 14.3, 22.9, 23.9, 29.2, 29.4, 32.0, 33.5, 122.4, 122.6, 133.2, 136.0, 140.6, 146.2 ppm; ^{29}Si NMR (CDCl_3): δ 4.4 ppm.

Synthesis of 2,7-Bis(4,4,5,5-tetramethyl-1,3,2-dioxaborolan-2-yl)-9,9'-di-*n*-octyldibenzosilole (22). *t*-BuLi (4.6 mL, 7.81 mmol, 1.7 M in pentane) was added over 30 min to a solution of **21** (1.05 g, 1.86 mmol) in dry THF (15 mL) at $-78\text{ }^{\circ}\text{C}$ under N_2 . The mixture was stirred at $-78\text{ }^{\circ}\text{C}$ for a further 15 minutes, and 2-isopropoxy-4,4,5,5-tetramethyl[1,3,2]dioxaborolane (0.95 mL, 4.65 mmol) was subsequently added dropwise to the mixture and stirring continued at $25\text{ }^{\circ}\text{C}$ overnight. The reaction was then quenched with distilled water, and THF was removed under vacuum. The product was then extracted into diethyl ether and the organic layer washed with brine, dried over MgSO_4 , filtered, and evaporated *in vacuo* giving 8.5 g of pure product as a white solid (0.97g, 80% yield). ^1H NMR (CDCl_3): δ 0.92 (6H, t,

CH_3), 0.96 (4H, t, CH_2), 1.22-1.38 (24H, m, CH_2), 1.38 (24H, s, CH_3), 7.82 (2H, d, $J = 7.0$), 7.85 (2H, d, $J = 7.0$), 8.08 (2H, s) ppm; ^{29}Si NMR ($CDCl_3$): δ 3.3 ppm.

Synthesis of TS6 (5). A solution of 5,5'-dibromo-3,3'-dihexyldithienosilole (**16**) (0.40 g, 0.77 mmol) and the catalyst $Pd(PPh_3)_2Cl_2$ (55 mg) in THF (20 mL) was combined under inert nitrogen atmosphere and the reaction mixture was refluxed for 8 days, resulting in dark suspension. The mixture was then cooled to room temperature and water (30 mL) added. The aqueous layer was extracted with CH_2Cl_2 (2×30 mL). The combined organic layer was then washed with water (40 mL) and dried over $MgSO_4$. After filtration, the solvent was removed and the residue was dissolved in THF. Boiling methanol was added dropwise, resulting a black suspension. The precipitate was then collected via filtration, redissolved in THF, and precipitated with methanol again to give a black, chunky solid (0.37 g, 66% yield). GPC: $M_w = 26$ KD, PDI = 2.9; NMR: 1H ($CDCl_2CDCl_2$): δ 7.06 (br, 2H), 1.35 (m, 4H), 1.17 (m, 16H), 0.80 (s, 6H); ^{13}C ($CDCl_2CDCl_2$): δ 146.92, 142.53, 138.01, 125.40, 32.44, 30.92, 23.60, 22.07, 13.61, 11.34; Anal. Calcd. for $(C_{20}H_{28}S_2Si)_n$, C 66.61; H 7.83; found C 66.14, H 7.08.

Synthesis of TS6T1 (6). The reagent 2,5-bis(trimethylstannyl)thiophene (0.614 g, 1.5 mmol), **16** (0.78 g, 1.5 mmol), and $Pd(PPh_3)_2Cl_2$ (50 mg) in anhydrous THF (50 mL) were heated at reflux with stirring under nitrogen for 7 days. The heating was then discontinued, the reaction mixture was allowed to cool to room temperature, and was poured into methanol (800 mL). The nearly black precipitate was collected via filtration, and was further purified by precipitation twice from methanol/THF to yield a deep purple solid (0.52 g, 81% yield). GPC: $M_w = 30$ KD, PDI = 2.9; 1H NMR ($Cl_2CDCDCl_2$): δ 0.81 (br, 6H), 1.20-1.36 (br, 20H), 7.02-7.08 (br, 4H) ppm; ^{13}C NMR ($CDCl_3$): δ 12.04, 14.57, 22.98, 24.45, 31.73, 33.26, 124.43, 126.29, 126.74,

138.52, 143.60, 147.84 ppm; Anal. Calcd. for $(C_{24}H_{30}S_3Si)_n$: C, 65.10; H, 6.83; found: C, 65.11; H, 6.90.

Synthesis of TS6T2 (7). The reagent 2,5'-bis(trimethylstannyl)-2,2'-bithiophene (0.74 g, 1.5 mmol), **16** (0.78 g, 1.5 mmol), and $Pd(PPh_3)_2Cl_2$ (50 mg) in anhydrous THF (50 mL) were heated at reflux under nitrogen for 7 days. The heating was then discontinued; the reaction mixture was allowed to cool to room temperature and was then poured into methanol (800 mL). The black precipitate was collected via filtration, and was further purified by precipitation twice from methanol/THF twice to yield a deep purple solid (0.65 g, 83% yield). GPC: $M_w = 41$ KD, PDI = 3.0; 1H NMR ($Cl_2CDCDCl_2$): δ 0.80-0.87 (br, 6H), 1.19-1.34 (br, 20H), 7.02-7.08 (br, 6H); ^{13}C NMR ($CDCl_3$): δ 12.07, 14.59, 22.98, 24.46, 31.73, 33.26, 124.64, 126.82, 135.85, 143.94 ppm; Anal. Calcd. for $(C_{28}H_{32}S_4Si)_n$: C, 64.07; H, 6.14; found: C, 65.04, H, 6.08.

Synthesis of BS8 (8). A mixture of **22** (315.0 mg, 0.478 mmol), **21** (270.0 mg, 0.478 mmol), and Aliquat 336 (0.040 g) was degassed 3 times with N_2 before 2.5 ml of dry toluene was added. Next, tetrakis(triphenylphosphine)palladium (7.3 mg, 0.007 mmol) and 2M aqueous sodium carbonate solution (0.95 ml) which had been deaerated for 2 h was added under N_2 . The mixture was stirred vigorously and heated at reflux for 2 days. The highly viscous reaction mixture was then poured into boiling methanol (15 mL), precipitating a pale-green polymer. The polymer was collected by filtration and washed with acetone, methanol, water, and dried in vacuum at 70 °C overnight. The polymer was then dissolved in boiling THF (400 mg in 20 ml of THF), filtered, and reprecipitated with 80 mL of methanol to give 300 mg of final pure pale green polymer (76% yield). GPC: $M_w = 32$ KD, PDI = 3.4; 1H NMR ($Cl_2CDCDCl_2$): δ 0.6-1.6 (34 H, br, CH_2+CH_3), 6.3-7.0(6 H, m, ArH), 7.5-8.0(m, ArH) ppm; ^{13}C NMR ($CDCl_3$): δ 13.32, 21.75(br),

23.02, 29.67(br), 31.37, 32.14, 120.16, 123.26, 125.48, 133.52, 141.35, 143.24 ppm; Anal. calcd. for $(C_{28}H_{40}Si)_n$: C, 83.10; H, 9.96. Found: C, 82.68; H, 10.44.

Synthesis of BS8T1 (9). A mixture of **21** (564.5 mg, 1.0 mmol), 2,5-bis(4,4,5,5-tetramethyl-1,3,2-dioxaborolan-2-yl)thiophene (336.0 mg, 1.0 mmol), and Aliquat 336 (0.084 g) was degassed 3 times with N_2 before 7.0 mL of dry toluene was added. Next, tetrakis(triphenylphosphine)palladium (15.0 mg, 0.014 mmol) and 2M aqueous sodium carbonate solution (1.95 mL), which had been deaerated for 2 h, was added under N_2 . The mixture was stirred vigorously and heated at reflux for 2 days. The highly viscous reaction mixture was then poured into boiling acetone (13 mL), precipitating an orange polymer. The polymer was collected by filtration and washed with acetone, methanol, water, and dried under vacuum at 60 °C overnight. The polymer was next dissolved in boiling trichlorobenzene and reprecipitated twice with 100 mL of methanol to give 292 mg of final pure green polymer (60% yield). GPC: $M_w = 112$ KD, PDI = 3.1; 1H NMR ($CDCl_3$): δ 7.41-7.73 (8H, br, ArH), 0.86-1.40 (34H, m, CH_2+CH_3) ppm; ^{13}C NMR ($CDCl_3$): δ 14.32, 22.85(br), 24.02, 29.46(br), 30.27, 32.04, 120.06, 120.39, 124.16, 124.88, 133.52, 140.53, 144.34, 152.01 ppm; Anal. Calcd. for $(C_{32}H_{42}SSi)_n$: C, 78.95; H, 8.70; found: C, 78.58; H, 8.97.

Synthesis of BS8T2 (10). A mixture of **21** (193.0 mg, 0.354 mmol), 2,5'-bis(4,4,5,5-tetramethyl-1,3,2-dioxaborolan-2-yl)bithiophene (148.0 mg, 0.354 mmol) and Aliquat 336 (0.03 g) was degassed three times with N_2 before 2.5 mL of dry toluene was added. Tetrakis(triphenylphosphine)palladium (5.3 mg, 0.005 mmol) and 2M aqueous sodium carbonate solution (0.7 mL) which had been deaerated for 2 h was then added under N_2 . The mixture was stirred vigorously and heated at reflux for 2 days. The highly viscous reaction

mixture was then poured into boiling acetone (13 mL), precipitating an orange polymer. The polymer was collected by filtration and washed with acetone, methanol, water, and dried in vacuum at 60 °C overnight. The polymer was next dissolved in boiling trichlorobenzene (170 mg in 9 mL of TCB) and reprecipitated twice with 40 mL of methanol to give 140 mg of final pure orange polymer (45% yield). GPC: $M_w = 127$ KD, PDI = 3.7; ^1H NMR ($\text{Cl}_2\text{CDCDCl}_2$): δ 7.01-7.85 (10H, br, ArH), 0.86-1.45 (34H, m, CH_2+CH_3) ppm; ^{13}C NMR (CDCl_3): δ 14.34, 22.83, 23.62(br), 29.46(br), 29.96, 32.06, 120.47, 123.55, 124.62, 128.25, 130.55, 131.54, 136.75, 140.65, 144.02, 152.08 ppm. Anal. Calcd. for $(\text{C}_{36}\text{H}_{44}\text{S}_2\text{Si})_n$: C, 76.00; H, 7.79; found: C, 75.68; H, 7.84.

Synthesis of F8T1 (11). A mixture of 2,2'-(9,9-dioctyl-9H-fluorene-2,7-diyl)bis(4,4,5,5-tetramethyl-1,3,2-dioxaborolane) (530.0 mg, 1.0 mmol), 2,5-dibromothiophene (242.0 mg, 1.0 mmol), and Aliquat 336 (0.084 g) was degassed three times with N_2 before 7 mL of dry toluene was added. Tetrakis(triphenylphosphine)palladium (15.0 mg, 0.014 mmol) and 2M aqueous sodium carbonate solution (1.95 mL) which had been deaerated for 2 h was then added under N_2 . The mixture was stirred vigorously and heated at reflux for 2 days. The reaction mixture was next poured into boiling acetone (20 mL), precipitating a green polymer. The polymer was collected by filtration and washed with acetone, methanol, water, and dried in vacuum at 60 °C overnight. The polymer was dissolved in boiling toluene and reprecipitated three times with 40 mL of methanol to give 260 mg of final pure green polymer (55% yield). GPC: $M_w = 17$ KD, PDI = 2.6; ^1H NMR (CDCl_3): δ 7.05-7.80 (8H, brm, ArH), 2.10 (4H, br, CH_2), 0.72-1.21 (30H, m, CH_2+CH_3); ^{13}C NMR (CDCl_3): δ 14.62, 23.85(br), 24.12, 29.49(br), 30.47, 32.08, 56.15,

120.26, 121.28, 124.36, 125.00, 132.52, 141.23, 143.94, 151.01 ppm; Anal. Calcd. for $(C_{33}H_{42}S)_n$: C, 84.20; H, 8.99; found: C, 84.31; H, 9.41.

Synthesis of F8T2 (12). A mixture of 2,2'-(9,9-dioctyl-9H-fluorene-2,7-diyl)bis(4,4,5,5-tetramethyl-1,3,2-dioxaborolane) (800.0 mg, 1.5 mmol) and 5,5'-dibromo-2,2'-bithiophene (489.0 mg, 1.5 mmol), and Aliquat 336 (0.12 g) was degassed three times with N_2 before 10 mL of dry toluene was added. Tetrakis(triphenylphosphine)palladium (23.0 mg, 0.021 mmol) and 2M aqueous sodium carbonate solution (2.95 mL) which had been deaerated for 2 h was next added under N_2 . The mixture was stirred vigorously and heated at reflux for 2 days. The highly viscous reaction mixture was next poured into boiling methanol (30 mL), precipitating a yellow fibrous polymer. The polymer was collected by filtration and washed with acetone, methanol, water, and dried in vacuum at 60 °C overnight. The polymer was next dissolved in boiling toluene and reprecipitated three times with 50 mL of methanol to give 660 mg of yellow fibrous polymer (79% yield). GPC: $M_w = 80$ KD, PD = 3.3; 1H NMR ($CDCl_3$): δ 6.85-7.85 (10H, brm, ArH), 2.02 (4H, br, CH_2), 0.74-1.20 (30H, m, CH_2+CH_3); ^{13}C NMR ($CDCl_3$): δ 14.14, 23.00, 23.42(br), 29.55(br), 30.01, 32.26, 56.45, 120.50, 123.62, 125.00, 128.15, 130.35, 131.42, 137.01, 141.01, 143.92, 152.25 ppm; Anal. Calcd. for $(C_{37}H_{44}S_2)_n$: C, 80.38; H, 8.02; found: C, 80.68; H, 8.14.

2.2.3 Device Fabrication and Thin Film Characterization.

Prime grade n-doped silicon wafers (100) having a 300 nm thermally grown oxide layer (Process Specialties Inc.) were used as device substrates. These were rinsed with water, methanol, and acetone before film deposition. Trimethylsilyl functionalization of the Si/SiO₂ surface was carried out by exposing the silicon wafers to hexamethyldisilazane (HMDS) vapor at

room temperature in a closed container under nitrogen overnight. Polymer films were spin-coated from 5 mg/mL solutions in THF or 1,2,4-trichlorobenzene and then annealed under nitrogen at various temperatures from 100 °C to 300 °C for 30 min. Spin-coated films were 25-30 nm-thick as assessed by profilometry. For FET device fabrication, top-contact electrodes (500 Å) were deposited by evaporating gold (pressure < 10^{-5} Torr); channel dimensions were 25/50/100 μm (L) by 0.2/1.0/2.5/5.0 mm (W). The capacitance of the insulator is 1×10^{-8} F/cm² for 300 nm SiO₂. TFT device measurements were carried out in a customized vacuum probe station (8×10^{-5} Torr) or in air. Coaxial and/or triaxial shielding was incorporated into Signaton probes to minimize the noise level. TFT characterization was performed with a Keithley 6430 subfemtoammeter and a Keithley 2400 source meter, operated by a locally written Labview program and GPIB communication. Thin films were analyzed by wide-angle X-ray film diffractometry (WAXRD) on a Rikagu ATX-G instrument with Cu K α radiation and a monochromator using standard θ - 2θ techniques. All θ - 2θ scans were calibrated in situ with the reflection of the Si (100) substrates.

2.2.4 Electrochemistry.

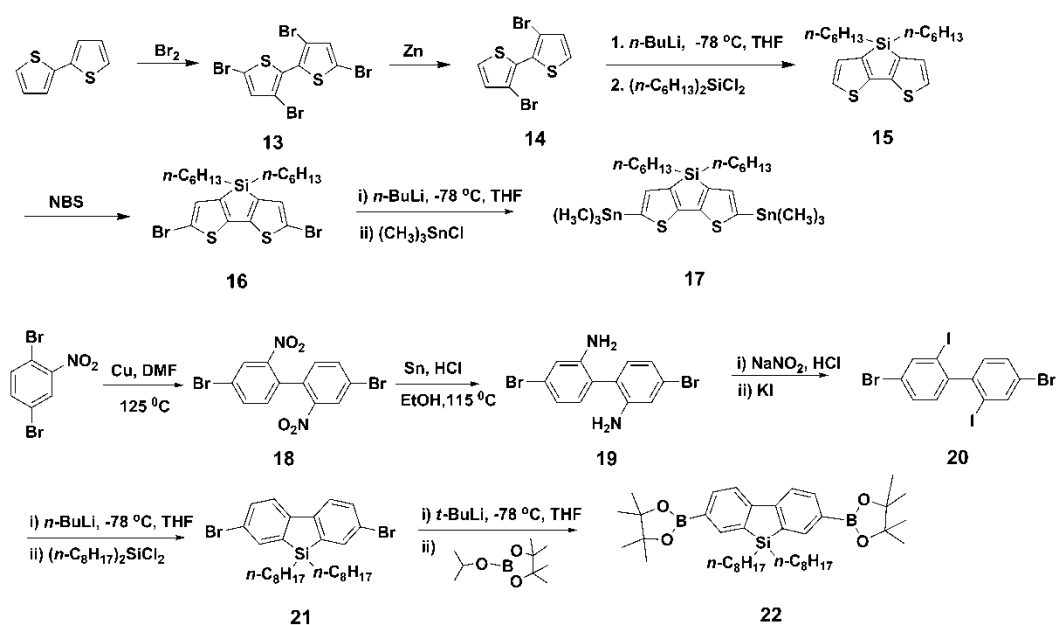
Cyclic voltammetry was performed in an electrolyte solution of 0.1 M tetrabutylammonium hexafluorophosphate (Bu₄N⁺PF₆⁻) in dry acetonitrile. Platinum wire electrodes were used as both working and counter electrodes, and Ag wire was used as the pseudo-reference electrode. A ferrocene/ferrocenium redox couple was used as an internal standard and potentials obtained in reference to a silver electrode were converted to the saturated calomel electrode (SCE) scale. Thin films of the polymers were coated onto the Pt working electrode by drop casting from 0.5 wt % – 1.0 wt % THF solutions and dried under vacuum at 80 °C for 2 h.

2.2.5 Computational Methodology.

Geometry optimizations for the gas-phase neutral, radical-anion, and radical-cation states of the theoretical model structures were carried out at the density functional theory level using the B3LYP functionals and a 6-31G** split valence plus double polarization basis set. Excitation energies of the low-lying excited states have been calculated at the time-dependent DFT (TDDFT) level. All calculations were carried out with QChem (Version 2.1).

2.3 Results

2.3.1 Synthesis.

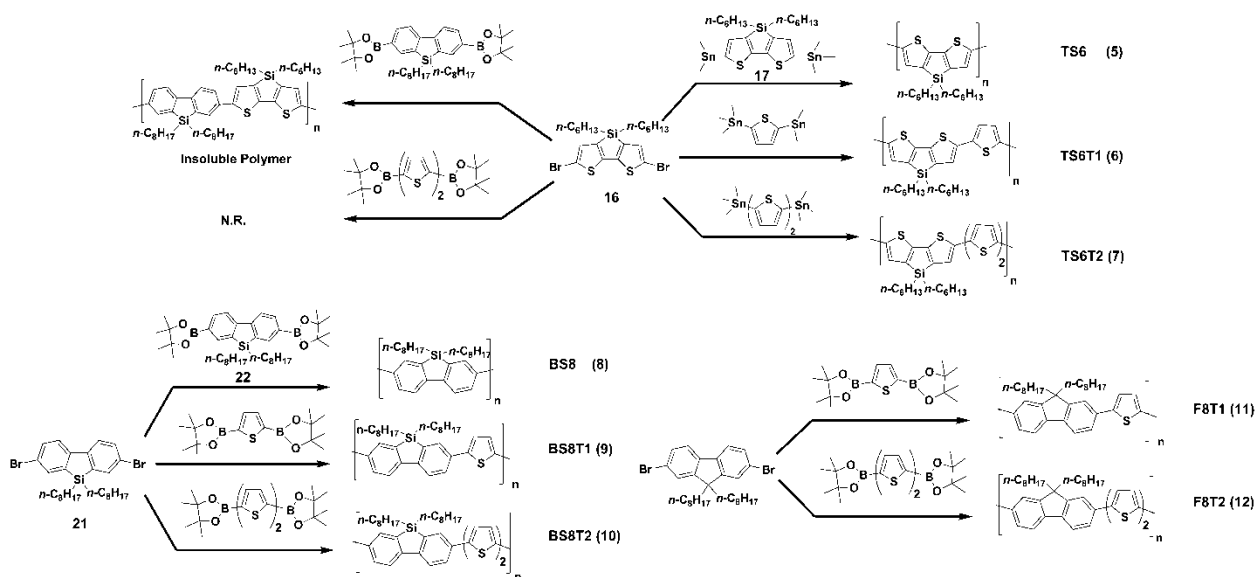


Scheme 2.1. Synthesis of dibenzosilole and dithienosilole monomers.

As shown in Scheme 2.1, dibromo-functionalized dithienosilole- and dibenzosilole-based building blocks **16** and **21** were prepared from commercially-available bithiophene and 2,5-dibromonitrobenzene, respectively. To synthesize the polymers **5-12**, Suzuki and Stille coupling polymerization reactions were conducted as shown in Scheme 2. The building block 3,3'-di- n -

hexylsilylene-2,2'-bithiophene (**15**) was prepared via a reported procedure⁶³ in which bithiophene is first brominated to give 3,5,3',5'-tetrabromobithiophene (**13**) that is then selectively debrominated with Zn to give 3,3'-dibromobithiophene (**14**). Double lithiation of **14** with *n*-butyllithium followed by subsequent cyclization with di-*n*-hexyldichlorosilane yields dithienosilole monomer **15**. Dibromo-functionalized monomer **16** is then prepared by bromination with NBS in DMF. The overall yield for monomer **16** is 43%. Dithienosilole monomer **16** is transformed into distannyl reagent **17** by treatment of **16** with *n*-BuLi followed by trimethyltin chloride. Building block 2,7-dibromo-9,9-dioctyldibenzosilole (**21**) is prepared by a known procedure.⁵⁰ Ullmann coupling product **18** is reduced to the corresponding diamine **19**, and Sandmeyer reaction of **19** with sodium nitrite in concentrated HCl, followed by the addition of a 10-fold excess of concentrated KI solution, gives biphenyl **20** in 28 % yield. Conventional Sandmeyer reactions with stoichiometric amounts of KI result in lower yields of 10 % – 15 % for **20**. The low yield is presumably the result of intramolecular cyclization of the initial mono-iodo substituted product via attack of the iodo substituent on the neighboring 2'-position with decomposition of the second diazonium substituent to give dibenzoiodonium iodide.⁶⁴ Selective translithiation of the 2,2'-iodo-substituents of **20** with *n*-BuLi in THF followed by subsequent cyclization with di-*n*-octyldichlorosilane affords dibenzosilole monomer **21**. The overall yield for monomer **21** is 16%. Since pinacolato boronic esters are reported to be significantly more stable than boronic acids and are frequently used in Suzuki coupling reactions to prepare biaryl compounds and polymers,^{65, 66} compound **21** was converted to pinacolato ester **22** by treatment with *t*-BuLi, followed by 4,4,5,5-tetramethyl-[1,3,2]dioxaborolane, for use as the co-monomer in the homopolymerization with monomer **21**.

Polymers **5-12** were synthesized according to Scheme 2.2. Dithienosilole-based polymers **5-7** were synthesized via a Stille polycondensation between reagents **16** and **17**, 2,5-bis(trimethylstannyl)thiophene, and 2,5'-bis(trimethylstannyl)bithiophene, respectively, in good yields (See Supporting Information). Dibenzosilole-based polymers **8-10** were prepared via a Suzuki polycondensation protocol between reagents **21** and **22**, 2,5-bis(4,4,5,5-tetramethyl-1,3,2-dioxaborolan-2-yl)thiophene, and 2,5'-bis(4,4,5,5-tetramethyl-1,3,2-dioxaborolan-2-yl)bithiophene, respectively, in moderate to good yields (See Supporting Information). The syntheses of the fluorene-thiophene copolymers **11** and **12** were performed by reported procedures.^{67, 68} The physicochemical properties of polymers **5-12** are summarized in Table 1. The molecular weights (M_w s) of **5-7** determined by high-temperature GPC were 26 KD (PDI = 2.9), 30 KD (PDI = 2.9), and 41 KD (PDI = 3.0), respectively.



Scheme 2.2. Synthesis of dibenzosilole-based and dithienosilole-based homo- and copolymers.

These macromolecules are freely soluble in common non-protic organic solvents such as THF, toluene, xylenes, chloroform, methylene chloride, chlorobenzene, o-dichlorobenzene (DCB), and 1,2,4-trichlorobenzene (TCB). GPC-derived molecular weights (M_w) of the dibenzosilole-based polymers **8-10** are 32 KD (PDI = 3.4), 112 KD (PDI = 3.1), and 127 KD (PDI = 3.7), respectively. Polymer **8** is very soluble in common non-protic organic solvents, but the solubilities of **9** and **10** are lower than dithienosilole-based polymers **5-7**. They are only soluble in chlorinated aromatic solvents such as warm chlorobenzene, DCB, and TCB; this is probably a consequence of the higher molecular weights of **9** and **10**. Fluorene-based copolymers **11** and **12** have GPC-derived molecular weights of 17 KD (PDI = 2.6) and 80 KD (PDI = 3.3), respectively. They are soluble in hot toluene, xylene, and chlorobenzene. Each of the new polymers was fully characterized by ^1H and ^{13}C NMR, optical spectroscopy, PL, GPC, TGA, DSC, and elemental analysis.

In order to optimize the molecular weights of polymers **5-7**, a Suzuki polycondensation protocol was investigated. However, all attempts under typical Suzuki polymerization conditions produced low-molecular weight oligomers, and negligible polymeric products were obtained. This is presumably due to deboration side reactions that occur prior to aryl-aryl coupling, thus limiting formation of the desired products. These types of side reactions are well-documented.^{35, 69, 70-74} In contrast, thiophene-phenylene copolymers with satisfactory molecular weights have previously been synthesized using Suzuki polycondensation,^{70, 75, 76} consistent with the present syntheses of dibenzosilole-thiophene copolymers. A copolymer containing dithienosilole and dibenzosilole units was also synthesized via Suzuki polycondensation (Scheme 2.2). However, the polymer was not soluble in the aforementioned solvents, hindering further purification,

characterization, and device fabrication. Halting the polymerization processes at early stages of reaction (reducing the reaction time), in hope of obtaining lower molecular weight polymers, yielded no soluble polymeric products. In order to observe the effect of end-capping process to the physicochemical properties and FET performances of the final polymers reactions with endcapping reagents such as bromobenzene, benzenboronic acid pinacol ester, and 2-tributylstannylthiophene were performed on the highest mobility polymers of each polymer series (compounds **7** and **10**). However, the purified polymers exhibited no difference in electronic/device properties. Eventually, we decided to avoid additional end-capping steps and therefore reported the experimental procedures without the endcapping steps.

Table 2.1. Physicochemical Properties (Molecular Weight (M_w, KD), polydispersity (PD), melting temperature (T_m), crystallization temperature (T_c), onset decomposition temperature (T_d), solution (in THF) and film optical absorption maxima, emission maxima (in THF), (λ, nm), energy gaps (E_{g,op}, eV), and FET performance summary (OFET charge carrier mobilities (μ, cm² V⁻¹ s⁻¹), and current On/Off ratios (I_{on}/I_{off}) in air) of polymers **5-12**.

Polymer	Polymerization Protocol	M _w (PD)	T _m , T _c ^a (°C)	T _d ^c (°C)	λ _{sol} ^d (E _{g,op}) ^d (nm, eV)	λ _{film} (E _{g,op}) ^d (nm, eV)	λ _{em} (nm)	FET μ _h (cm ² /V s)	FET I _{on} :I _{off}
TS6 (5)	Stille	26 (2.9)	- ^b	250	533 (1.9)	535 (1.8)	601	- ^b	- ^b
TS6T1 (6)	Stille	30 (2.9)	257, 230	480	521 (2.0)	574 (1.8)	611	0.05	1×10 ⁵
TS6T2 (7)	Stille	41 (3.0)	300, - ^b	445	544 (1.9)	545 (1.9)	620	0.08	5×10 ⁴
BS8 (8)	Suzuki	32 (3.4)	- ^b	410	377 (3.0)	401 (2.9)	455	- ^b	- ^b
BS8T1 (9)	Suzuki	112 (3.1)	253, - ^b	420	471 (2.5)	484 (2.5)	488	6×10 ⁻⁵	3×10 ⁴
BS8T2 (10)	Suzuki	127 (3.7)	340, 295	430	503 (2.3)	493 (2.3)	528	0.006	4×10 ⁶
F8T1 (11)	Suzuki	17 (2.6)	267, - ^b	415	427 (2.6)	440 (2.5)	469	9×10 ⁻⁵	2×10 ⁵
F8T2 (12)	Suzuki	80 (3.3)	259/277, 196	425	456 (2.4)	460 (2.4)	496	0.006	2×10 ⁵

^a Melting temperature (T_m) and crystallization temperature (T_c) determined by DSC. ^b Not observed. ^c Onset decomposition temperature measured by TGA under nitrogen. ^d Optical band gap estimated from the low energy band edge in the optical spectrum.

2.3.2 Thermal Properties.

Thermogravimetric analysis (TGA, heating ramp rate of 10 °C/min under N₂) was used to determine the thermal stability of polymers **5-12** (Figure 2.4). A 5 % mass loss is defined as the thermolysis threshold. The thermolysis onset temperature for polymer **5** is ~250 °C, while polymers **6-12** all have onset temperatures above 400 °C, indicative of good thermal stability.

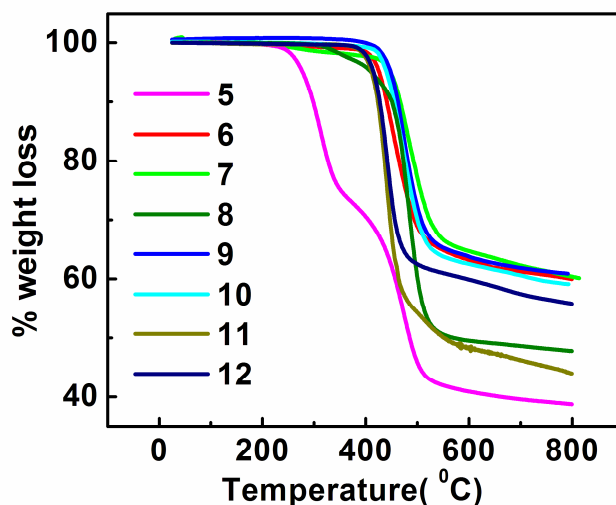


Figure 2.4. Thermogravimetric analysis (TGA) of polymers **5-12**.

The thermal properties of the present polymers were also examined by differential scanning calorimetry (DSC) at a scanning speed of 10 °C/min (Figure 2.5). Polymer **6** exhibits a single endotherm/exotherm around 250 °C on heating/cooling, while **7** exhibits one broad endotherm near 300 °C. For both polymers, the endotherms and exotherms are reversible over many cycles. Polymer **9** exhibits a broad transition at 253 °C in the heating cycle, and an exotherm is not observed in the cooling cycle; similar observations are made for polymer **11**, which exhibits a single endotherm around 267 °C. For polymer **10**, there is an endothermic melting feature at 340

°C in the heating cycle that is tentatively attributed to backbone melting. Upon cooling, an exothermic recrystallization peak is observed at 295 °C. Both the melting and recrystallization peaks are completely reversible over four cycles. The DSC of polymer **12** exhibits two endotherms at 259 °C and 277 °C, and one exotherm at 196 °C upon cooling, consistent with a previous report.⁷⁷

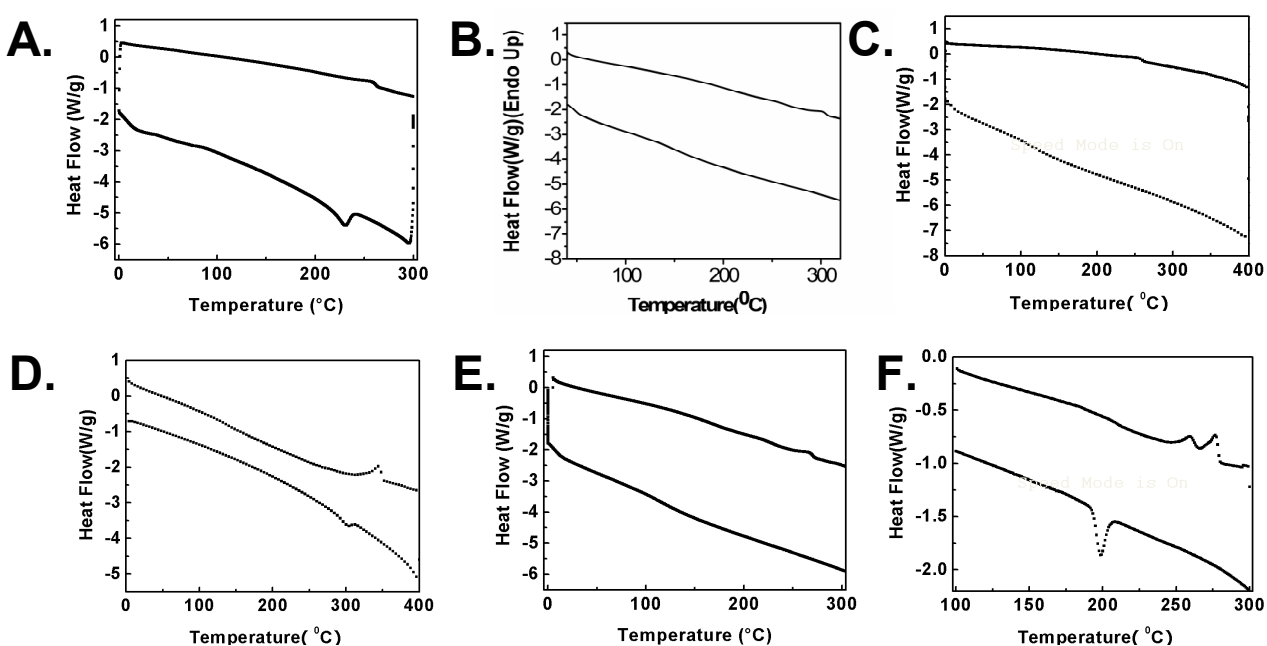


Figure 2.5. Differential Scanning Calorimetry (DSC) of the polymers **6** (A), **7** (B), **9** (C), **10** (D), **11** (E), and **12** (F) at a scanning speed of 10 °C/min under N₂.

On average, the polymers containing bithiophene units have higher melting temperatures, suggesting closer packing in the solid state. The melting temperatures of pair **6** and **9** and pair **7**

and **10** are rather comparable. Silicon substitution lowers T_m for **9** by ~ 15 °C compared to **11**, but increases the T_m and T_c of **10** by 60 °C – 100 °C compared to polymer **12**.

2.3.3 Optical Properties.

Solution and thin-film UV-Vis absorption spectra for polymers **5-12** are shown in Figure 2.6 and data are collected in Table 2.1. Note that the differences in the optical properties of these polymers reflect the differences in the chemical structures since the number-average degree of polymerizations (DP) are sufficiently large (>15) making negligible contribution of the molecular weights.

In THF, polymer **5** exhibits a single absorption maximum at 533 nm, while the solution-cast thin film, which is discontinuous on glass substrates, shows a similar absorption maximum at 535 nm. The absorption maxima for **6** and **7** are located at 521 nm and 544 nm, respectively, in THF. Polymers **6** and **7** form smooth and shiny thin films when solutions are cast on silicon wafers and exhibit absorption maxima at 574 nm for polymer **6** and at 545 nm for polymer **7**. Polymers **5** and **7** exhibit little difference in absorption maxima upon going from solution to thin film; however, the absorption maximum red-shift of approximately 50 nm for polymer **6** in the thin film vs. solution suggests a high degree of macromolecular organization in the thin film phase.

The optical absorption spectra of dibenzosilole-based polymers **8-10** have absorption maxima that are blue-shifted compared to those of dithienosilole-based polymers **5-7**. The absorption maximum for the homopolymer **8** occurs at 377 nm, corresponding to the largest π - π^* transition energy in the silole-based polymer series. Polymers **9** and **10** exhibit two absorption maxima located at 444 nm and 471 nm for **9**, and 473 nm and 503 nm for **10**. These transitions likely

correspond to predominantly local transitions of the constituent dibenzosilole and thiophene units.

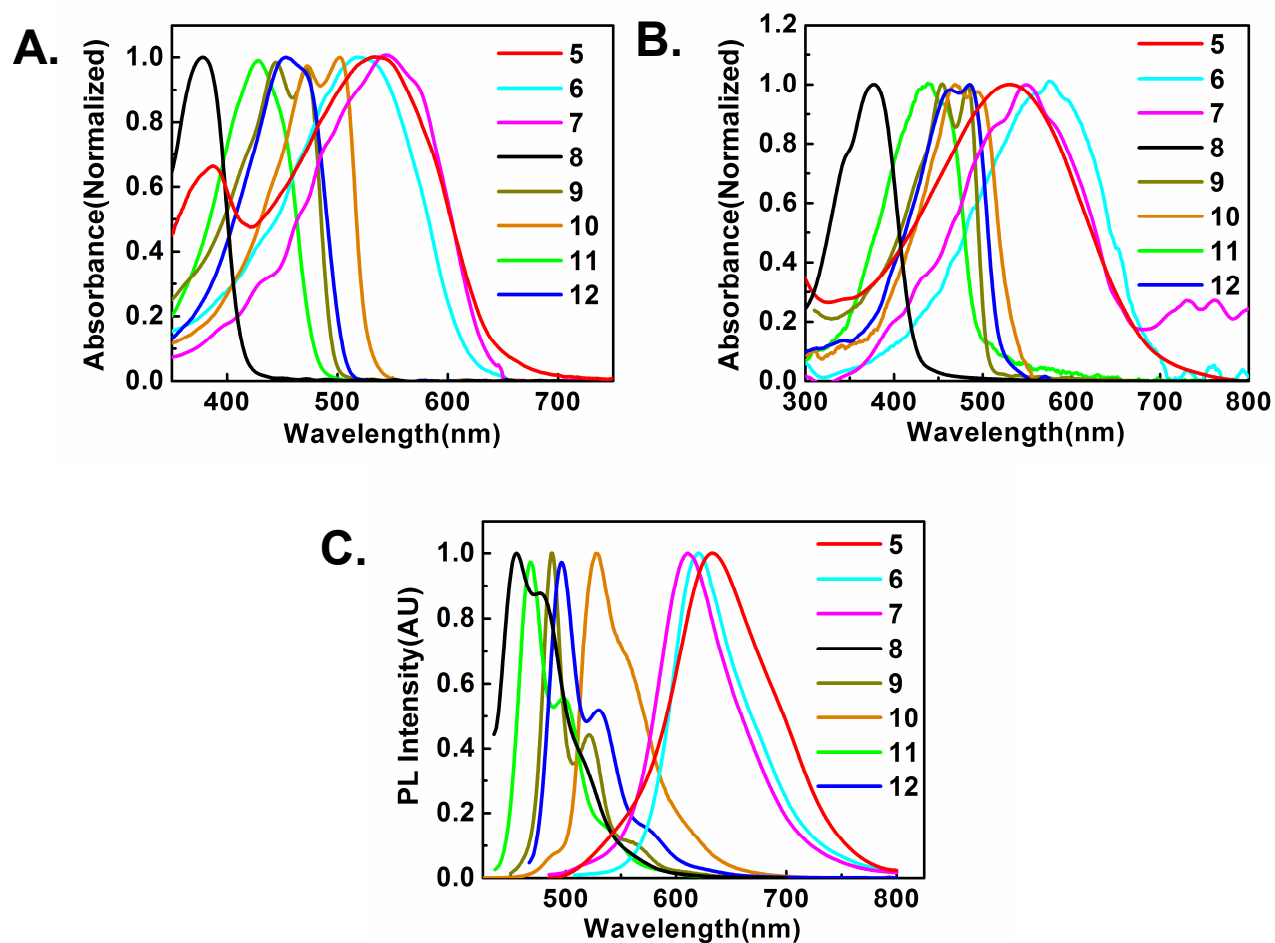


Figure 2.6. UV-Vis absorption spectra of polymers **5-12** in THF solution (A), as thin films on glass substrate (B), and photoluminescence spectra in THF solution (C).

The absorption maxima of polymers **8-10** cast as thin films are 401 nm (**8**), 484 nm (**9**), and 493 nm (**10**). The fluorene-based copolymers exhibit maxima at 427 nm in solution and 440 nm as a thin film for **11**, and 456 nm in solution (with a strong shoulder at 502 nm) and 460 nm as a thin film for **12**. Dibenzosilole-based copolymers **9** and **10** exhibit significant bathochromic shifts of *ca.* 30 nm – 50 nm compared to the fluorene-based polymers **11** and **12**. In both cases, annealing has little impact on the film absorption maxima. Additionally, on proceeding from **8** to **5**, **9** to **6**, and **10** to **7**, the large bathochromic shifts (40-60 nm in THF, 50-130 nm in thin film) in the absorption maximum trends reflect effects from both the π -electron-donating S atom vs. the C=C- linkage and the more planar conformation of five-five vs. five-six inter-ring linkages.

Band gaps for the present polymer series are estimated from the low-energy band edges of the thin-film optical spectra, taking 10% of the maximum as the band edge (see Table 2.1). The optical band gaps of polymers **5**, **6**, and **7** are estimated to be 1.8 eV, 1.8 eV, and 1.9 eV, respectively, and are similar to that of P3HT (1.9 eV).⁷⁸ These small band gaps likely reflect the appreciable planarity of these macromolecules (*vide infra*) and the backbone similarity to polythiophenes. Larger band gaps are observed for the dibenzosilole-based polymers vs. dithienosilole-based polymers – the optical band gaps of polymers **8**, **9**, and **10** are estimated to be 2.9 eV, 2.5 eV, and 2.3 eV, respectively. The optical band gaps for materials **11** and **12** are estimated to be 2.5 eV and 2.4 eV, respectively. Similarities in the optical band gaps of pair **10** and **12** and pair **9** and **11** suggest similarly-extended π -conjugation.

The solution PL emission spectra are shown in Figure 2.6 and data collected in Table 2.1. The dithienosilole-based polymers emit orange-red light with maxima of 601 nm, 611 nm, and 620 nm for **5**, **6**, and **7**, respectively. The dibenzosilole-based polymers exhibit well-resolved vibronic

structures for the shorter-wavelength emission maxima. While homopolymer **8** emits blue light with a maximum at 455 nm, copolymers **9** and **10** show green-yellow emission with maxima at 488 and 528 nm, respectively; these transitions are assigned to the 0-0 transition in dilute solutions. The 0-1 and 0-2 transitions in the PL emission spectra are observed at 477 nm and 512 nm for **8**, and at 521 nm and 561 nm for **9**. Polymer **10** exhibits a 0-1 transition at 555 nm. The 100-150 nm red-shift of emission maxima for **5-7** vs. the dibenzosilole-based polymers **8-10** likely indicates weaker π -conjugation in the latter systems. Fluorene-based polymers **11** and **12** exhibit hypsochromic shifts vs. the dibenzosilole-based polymers with emission maxima at 469 nm and 496 nm, respectively. Polymers **9** and **10** exhibit emissions which are ~20 nm – 30 nm red-shifted compared to those of fluorene-based polymers **11** and **12**. The dithienosilole-based polymers **5-7** and homopolymer **8** show large Stokes' shifts of ~70 nm – 90 nm, which are not unusual for silicon-containing polymers, and may be possibly due to the excimer emission. Polymers **9** and **10** exhibit modest Stokes shifts of ~20 nm between the absorption and emission maxima, which are smaller than those of polymers **11** and **12** (~40 nm); this suggests a greater rigidity in the dibenzosilole-based polymers.

2.3.4 Electrochemical Properties.

Oxidation and reduction potentials for the present polymer series were obtained with cyclic voltammetry (CV). Cyclic voltammograms of the polymer thin films are shown in Figure 2.7, and electrochemical data are summarized in Table 2.2.

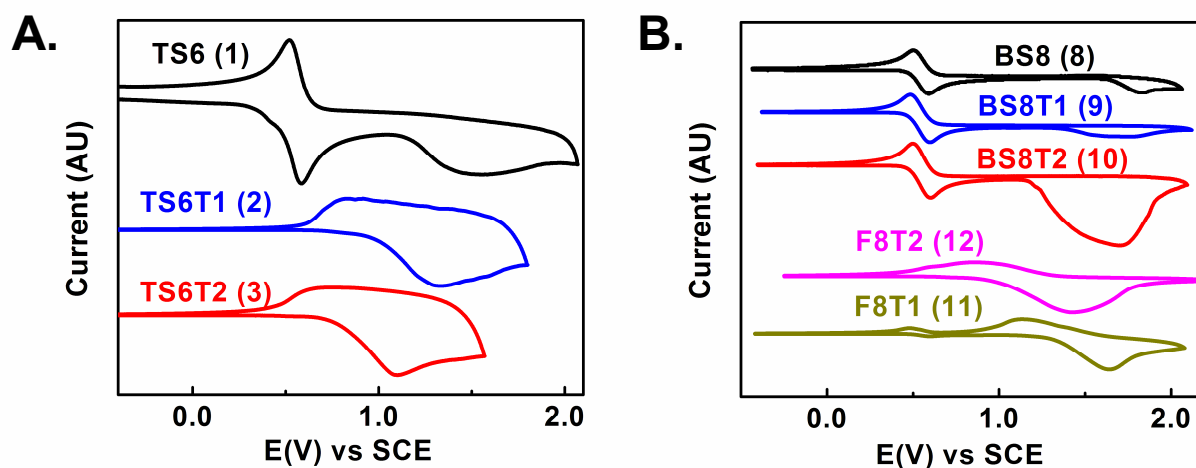


Figure 2.7. Cyclic voltammograms of polymers **5-12** as thin films in 0.1 M $\text{Bu}_4\text{N}^+\text{PF}_6^-$ solution in acetonitrile at a scan rate of 100 mV/s. In all experiments, ferrocene is used as the internal standard.

The dithienosilole-based polymers **5**, **6**, and **7** exhibit oxidation onset potentials of 1.2 V, 0.9 V, and 0.8 V, respectively (vs SCE), with formal oxidation potentials in the range of 1.1 V – 1.5 V (vs SCE). The onset oxidation potentials for the dibenzosilole-based polymers are 1.6 V, 1.4 V, and 1.2 V (vs SCE) for **8**, **9**, and **10**, respectively, which are $\sim 0.4\text{V} - 0.5\text{V}$ greater than for the dithienosilole-based polymers, and suggest higher stability with respect to oxidative doping. The formal oxidation potentials for **8-10** are determined to be in the range of 1.7 V – 1.8 V (vs

SCE). Electrochemical characterization of the fluorene-based copolymers gives onset and formal oxidation potentials of 1.3 V and 1.6 V, respectively, for **11**, and 1.0 V and 1.4 V, respectively, for **12**. None of the polymers exhibit obvious reduction peaks, suggesting that they are intrinsically more suitable for p-type charge conduction vs. n-type conduction.⁷⁹

From these oxidation potentials, the ionization potentials ($IP^{ox} \approx -HOMO^{ox}$, assuming that Koopmans' theorem holds) for the present polymers can be estimated by taking the SCE energy level to be -4.4 eV below the vacuum level and using the relation of eq. 1.⁸⁰

$$HOMO^{ox} = -E_{ox-onset} - 4.4 \quad (1)$$

Using this relationship, the $HOMO^{ox}$ values for the dithienosilole-based polymers are estimated to lie at -5.6 eV, -5.3 eV, and -5.2 eV for **5**, **6**, and **7**, respectively, indicative of larger ionization energies vs. P3HT (~ -4.9 eV).⁸¹ The introduction of the silole core into the thiophene backbone thus stabilizes the system with respect to ionization with no significant compromise of the effective π -conjugation vs. P3HT, as observed in the similar optical band gaps (*vide supra*). The solid state $HOMO^{ox}$ s of the dibenzosilole-based polymers are similarly estimated to lie at -6.0 eV, -5.8 eV, and -5.6 eV for polymers **8**, **9**, and **10**, respectively, suggesting that introduction of the electron-deficient dibenzosilole unit into the thiophene backbone dramatically depresses the HOMO level. For comparison, electrochemical characterization of fluorene-based copolymers **11** and **12** gives $HOMO^{ox}$ energies of -5.7 eV and -5.4 eV, respectively. Dibenzosilole-thiophene copolymers **9** and **10** have electrochemically-estimated ionization energies ~ 0.1 eV – 0.2 eV greater than those of the analogous carbon versions of the same polymers, **11** and **12**, in agreement with the effects deduced from electronic structure

calculations (*vide infra*).⁸²⁻⁸⁴ The electrochemical measurements suggest marked destabilization of the HOMO levels and lesser stabilization of the LUMO levels on proceeding from the fused biphenylene rings of fluorene and dibenzosilole to the fused bithiophene ring of dithienosilole.⁸⁵

Table 2.2. Electrochemical properties of polymers **5-12**.

Polymer	$E_{\text{ox}}^{\text{onset}}$ (V) ^a	E_{ox}^{f} (V) ^b	HOMO ^{ox} (eV) ^c	$E_{g,op}$ (eV) ^c	LUMO ^{ox} (eV) ^c
TS6 (5)	1.2	1.5	-5.6	1.8	-3.8
TS6T1 (6)	0.9	1.3	-5.3	1.8	-3.5
TS6T2 (7)	0.8	1.1	-5.2	1.9	-3.3
BS8 (8)	1.6	1.8	-6.0	2.9	-3.1
BS8T1 (9)	1.4	1.8	-5.8	2.5	-3.3
BS8T2 (10)	1.2	1.7	-5.6	2.3	-3.3
F8T1 (11)	1.3	1.6	-5.7	2.5	-3.2
F8T2 (12)	1.0	1.4	-5.4	2.4	-3.0

^a Onset voltage for oxidation vs. SCE. ^b Formal oxidation potential. ^c HOMO^{ox} \equiv -IP^{ox} and LUMO^{ox} \equiv HOMO + $E_{g,op}$.

2.3.5 Thin-Film X-ray Diffraction (XRD) Analysis.

Microstructural order in the present homo- and copolymer thin films was assayed by θ - 2θ x-ray diffraction (XRD) scans (Figures 2.8 and 2.9). The measurements were taken on drop-cast films prepared from 0.5 wt % solutions in THF or 1,2,4-trichlorobenzene and annealed at 250°C under nitrogen for 30 min. The thickness of the films was determined to be 250 nm – 300 nm by profilometry.

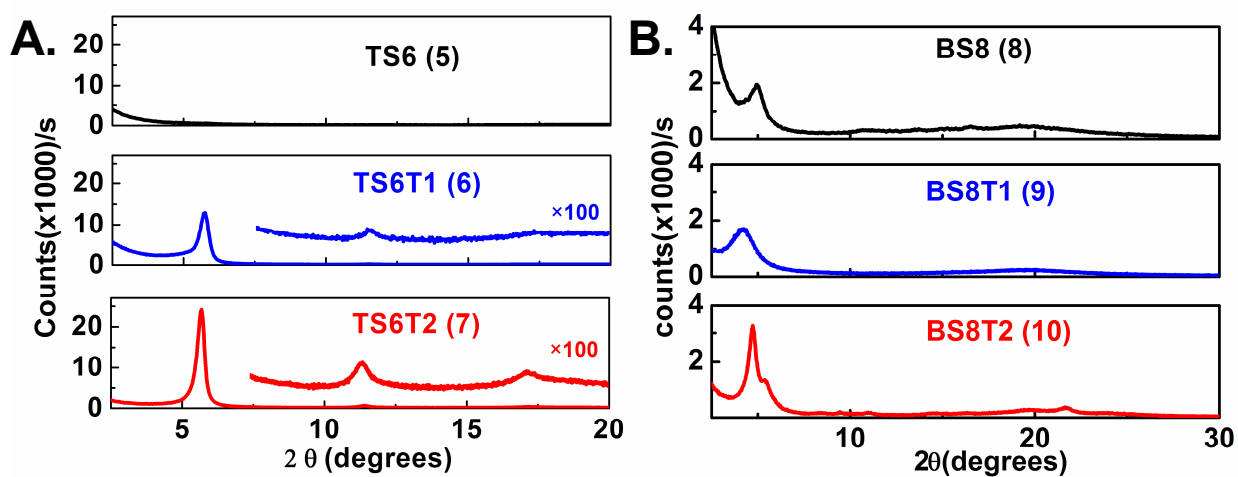


Figure 2.8. θ - 2θ X-ray diffraction (XRD) scans of drop-cast films of polymers **5-10** on silicon substrates.

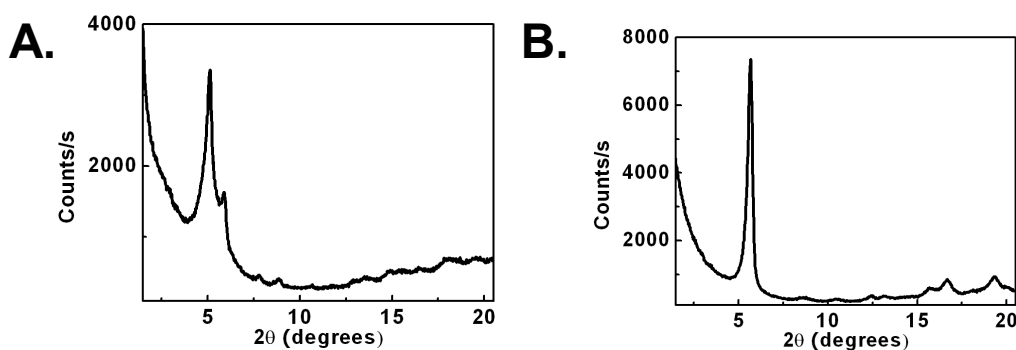


Figure 2.9. θ - 2θ X-ray diffraction (XRD) scans of drop-cast films of polymers **11** (A) and **12** (B) on silicon substrates.

As shown in Figure 2.8, each polymer thin film, with the exception of dithienosilole homopolymer **5**, is crystalline. Polymers **6** and **7** exhibit highly crystalline patterns with diffraction peaks up to third order, indicating a high degree of solid state ordering. Distinct primary diffraction features are observed at $2\theta = 5.68^\circ$ and 5.74° , corresponding to d-spacings of 15.54 and 15.38 Å for polymers **6** and **7**, respectively. Dibenzosilole-based polymers **8-10** exhibit substantially broader or weaker diffraction features compared to **6** and **7**. Homopolymer **8** has a single major reflection at $2\theta = 4.97^\circ$, corresponding a d-spacing of 17.76 Å. Polymers **9** and **10** have single major reflections at $2\theta = 4.22^\circ$ and 4.72° , corresponding to inter-chain d-spacings of 20.91 Å and 18.70 Å, respectively. Fluorene-thiophene polymers **11** and **12** exhibit multiple diffraction features, with major features at $2\theta = 5.14^\circ$ and 5.68° , corresponding to d-spacings of 17.17 Å and 15.54 Å, respectively, consistent with literature values assigned to inter-chain spacings (Figure 2.9).⁸⁶⁻⁹⁰ In dithienosilole-based copolymers **6** and **7**, the absence of π - π stacking diffraction features suggests that the polymer chains preferentially adopt layered structures with an “edge-on” orientation relative to the substrate, in analogy with the orientation

of the π - π stacks observed for regioregular P3HT, PQT-12, and PBTTT (Figure 2.2).^{25, 26, 28} The dibenzosilole-based polymers exhibit broad peaks at ca. $2\theta = 20^\circ$ for polymers **8** and **9**, and at 21.95° for **10**, corresponding to π - π stacking distances of 4.0 Å – 4.4 Å, reminiscent of the distances measured previously for fluorene-based polymeric and oligomeric semiconductors.^{89,}
90

2.3.6 Transistor Fabrication and Optimization.

OTFT devices were fabricated on low resistivity n-type silicon wafers, using thermally grown SiO₂ (300 nm) or hexamethyldisilazane (HMDS) passivated SiO₂ as the dielectric, in top-contact geometries. All device fabrication procedures were carried out in air. The active semiconducting layer was applied by spin-coating 5 mg/mL solutions in various solvents for 1 min. For top contact devices, gold contacts were patterned on top of the films using shadow masks that gave channel lengths ranging from 25 μm – 100 μm and widths from 500 μm – 2000 μm . Devices fabricated with polymers **5** and **8** exhibit no FET activity. Devices fabricated with the remaining polymers were evaluated in ambient atmosphere as p-channel OTFTs in the accumulation regime. The output and transfer characteristics of devices fabricated with active polymers **6**, **7**, and **9** – **12** are presented in Figures 2.10 – 2.12.

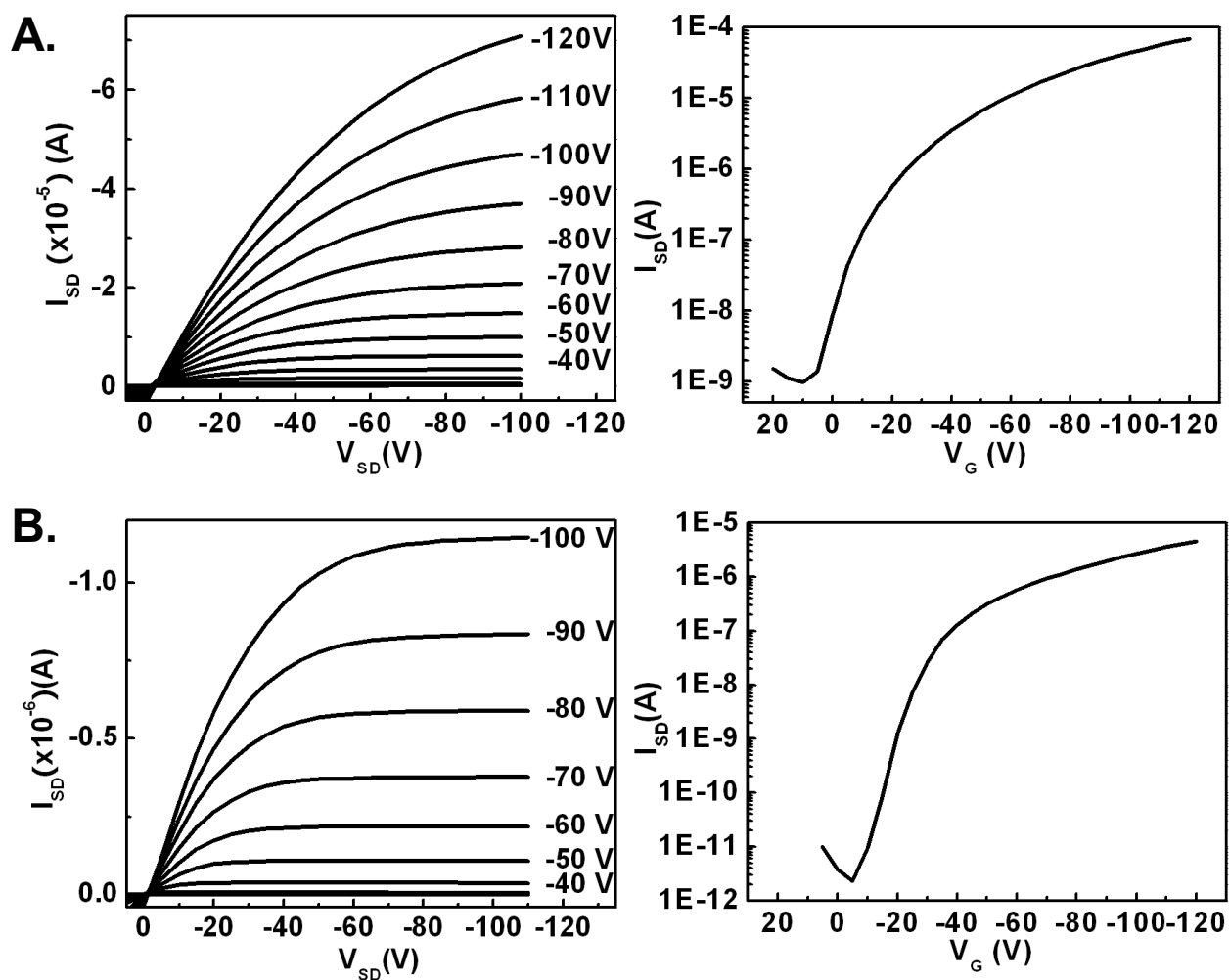


Figure 2.10. OTFT response plots of devices fabricated with polymers 7 and 10. A. Transfer plot of polymer 7 at $V_{SD} = -100$ V, and output plot of polymer 7, B. Transfer plot of polymer 10 at $V_{SD} = -100$ V, and output plot of polymer 10.

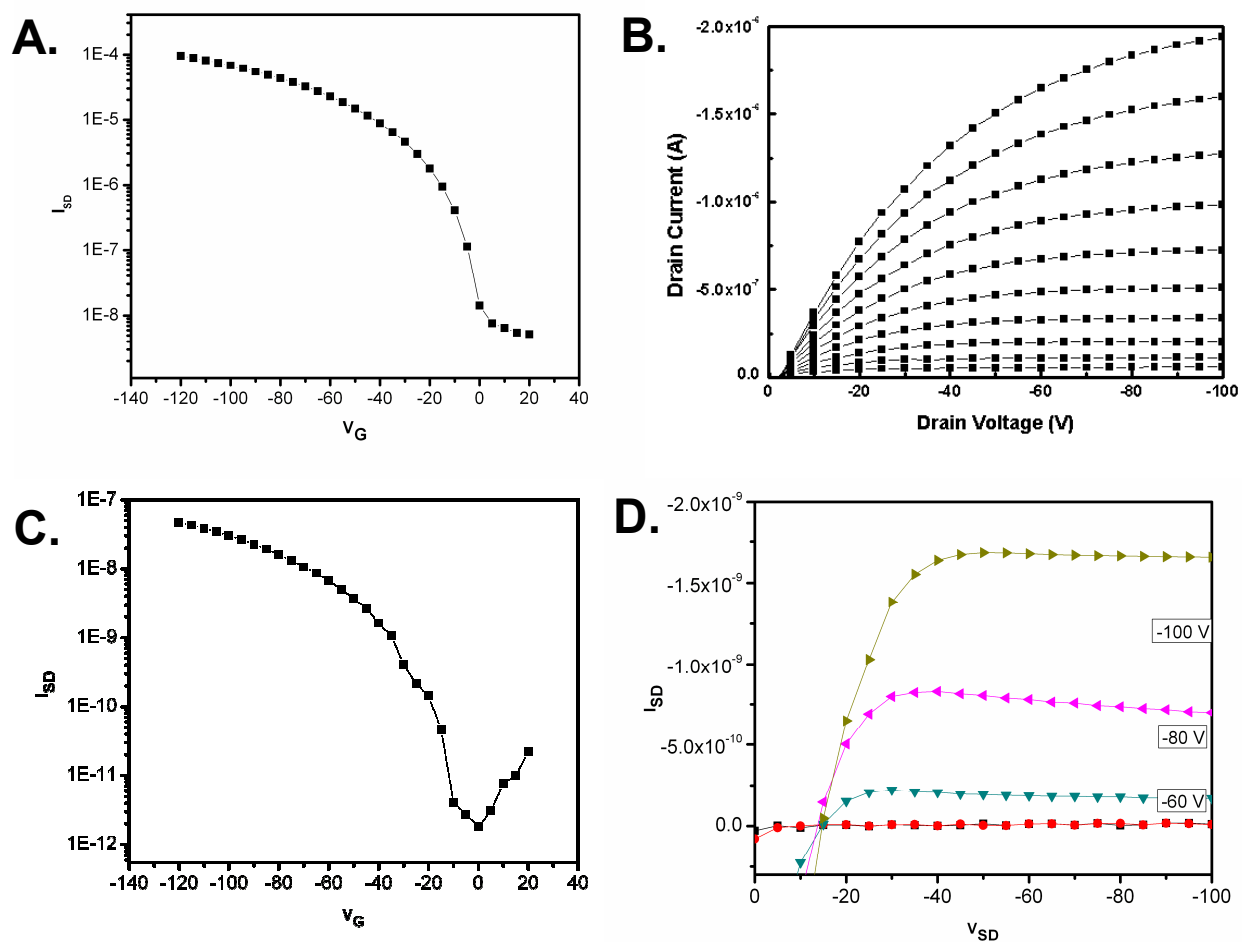


Figure 2.11. Transfer characteristics of OTFT devices fabricated with polymers **6** (A), **9** (C) at $V_{SD} = -100V$. Output characteristics of OTFT devices fabricated with polymers **6** (B), **9** (D) for various gate voltages.

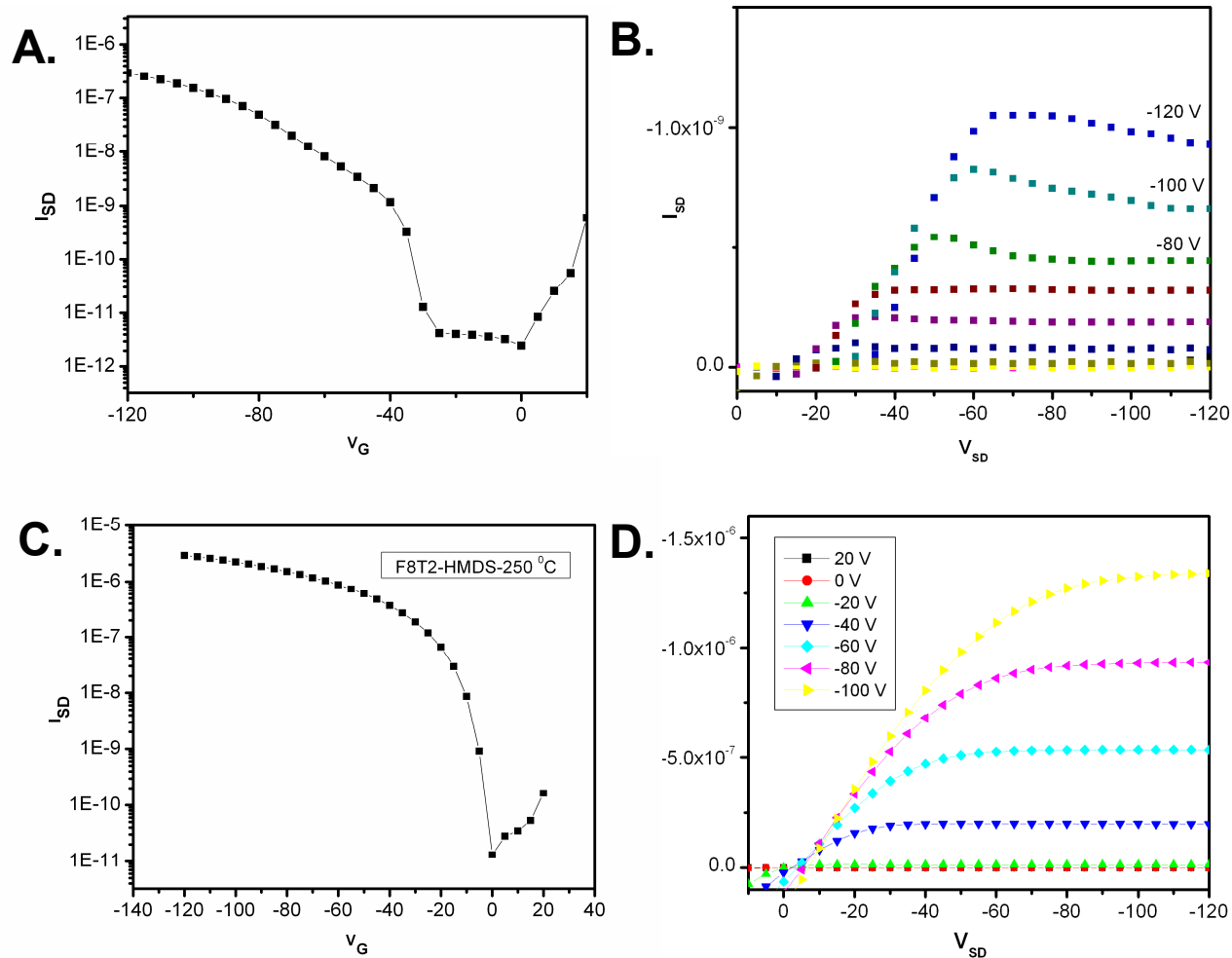


Figure 2.12. Transfer characteristics of OTFT devices fabricated with polymers **11** (A), and **12** (C) at $V_{SD} = -100$ V. Output characteristics of OTFT devices fabricated with polymers **11** (B), and **12** (D) for various gate voltages.

To select the optimum solvent for thin-film growth, solutions of **6** and **7** in 1,2,4-trichlorobenzene (TCB, b.p. 214 °C), 1,4-dichlorobenzene (DCB, b.p. 180-181 °C), chlorobenzene (CB, b.p. 131 °C), *p*-xylene (b.p. 138 °C), and *o*-xylene (b.p. 143-145 °C) were spin-coated on silicon substrates with SiO₂ as the gate dielectric. Film thicknesses were between 25 nm – 30 nm, as determined by profilometry. The solutions were heated to 80 °C to prevent gelation prior to spin coating. The resulting devices were annealed at 130 °C under nitrogen for 30 min before TFT measurements. It was found that 5 mg/mL solutions of **6** and **7** in the aforementioned solvents fail to form continuous thin films on HMDS-treated SiO₂/Si substrates. However, THF solutions of **6** and **7** form smooth thin films on the HMDS-treated SiO₂/Si substrates. In general, the TFT device performance of both polymers **6** and **7** on SiO₂/Si as the dielectric is poor in air. Additionally, the FET performance in general shows negligible dependence on solvent boiling point. Devices of **6** spin-coated from 1,2-dichlorobenzene exhibit the highest saturated hole mobility of 0.002 cm²/V·s and I_{on}/I_{off} ~10²-10³ for a channel length of 100 μm, while hole mobilities are comparable for devices having films spin-coated from the other solvents. Thin films of polymer **7** spin-coated from all solvents exhibit very similar saturated hole mobilities of ~10⁻⁴ cm²/V·s. However, *p*-xylene and *o*-xylene are found to increase the I_{on}/I_{off} ratios for these devices by one order of magnitude for **7**. Devices fabricated from polymers **9** and **10** on untreated SiO₂ substrates show hole mobilities one-to-two orders of magnitude lower than devices fabricated with polymers **6** and **7**. Polymer **9** exhibits the lowest mobility of 5×10⁻⁶ cm²/V·s with I_{on}/I_{off} = 1×10⁴ for thin films spin-coated from TCB solution. Films of **10** provide the best overall performance for devices spin-coated from TCB solution, with a mobility of 1×10⁻⁴ cm²/V·s and I_{on}/I_{off} = 1×10⁵.

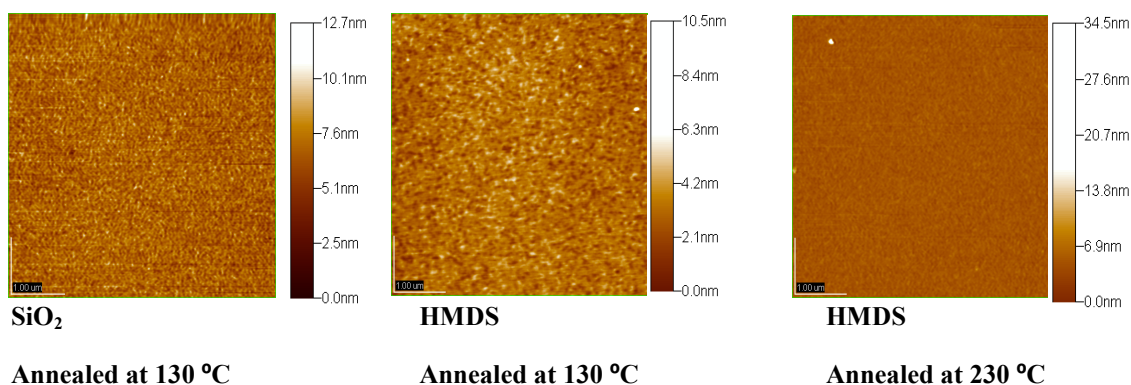


Figure 2.13. AFM Images of the spin-coated thin-films (25-30 nm) of polymer **10**. Scale bars denote 0.5 μm .

Devices fabricated with polymers **6**, **7**, **9**, and **10** spin-coated on HMDS-passivated SiO_2/Si substrates exhibit greatly enhanced TFT response. For polymers **6** and **7**, high-quality thin films can be obtained from hot THF solutions. This may be due to the low boiling point of THF compared to higher boiling solvents (1,2,4-trichlorobenzene, 1,4-dichlorobenzene, chlorobenzene, *p*-xylene), which facilitates smooth film growth on the highly hydrophobic HMDS surface before being spread during the spin-coating process. Film thicknesses were determined to be 25 nm – 30 nm by profilometry, with an RMS roughness of 0.2 nm – 0.3 nm indicated by tapping mode AFM (for representative images, see Figure 2.13). After annealing at 150 °C under nitrogen, respective mobilities of 0.01 $\text{cm}^2/\text{V}\cdot\text{s}$ and 0.007 $\text{cm}^2/\text{V}\cdot\text{s}$ are obtained for **6** and **7**, with $I_{\text{on}}/I_{\text{off}} = 1 \times 10^4$ for both. The TFT performance of devices with polymers **9** and **10** is also enhanced by this processing methodology, yielding mobilities of 5×10^{-5} $\text{cm}^2/\text{V}\cdot\text{s}$ and 0.001 $\text{cm}^2/\text{V}\cdot\text{s}$ with $I_{\text{on}}/I_{\text{off}}$ ratios of 3×10^4 and 4×10^5 , respectively.

Thermal annealing is found to greatly improve the TFT device performance for devices fabricated with polymers **6** and **7** (from THF) and **9** and **10** (from TCB), in terms of both

mobility and $I_{\text{on}}/I_{\text{off}}$ ratio. The devices were annealed under a nitrogen atmosphere at 100 °C, 150 °C, 200 °C, 250 °C, and 300 °C for 30 min, followed by cooling to room temperature by either quenching in air or by slow cooling under nitrogen. In all cases, quenched devices have mobilities superior to those of slow-cooled devices. The evolution of mobility and $I_{\text{on}}/I_{\text{off}}$ ratio for the present polymer devices is summarized in Figure 2.14. The performance maximizes at an annealing temperature of 250°C (polymer **5** was annealed at 200 °C due to the lower decomposition temperature). For devices annealed at 250°C, the highest mobilities of **6** and **7** are found to be 0.05 cm²/V·s and 0.08 cm²/V·s, with $I_{\text{on}}/I_{\text{off}}$ ratios of 1×10^5 and 5×10^4 , respectively. For polymers **9** and **10**, the maximum mobilities are 6×10^{-5} cm²/V·s and 0.006 cm²/V·s with $I_{\text{on}}/I_{\text{off}}$ ratios of 3×10^4 and 4×10^6 , respectively. OTFT devices fabricated with fluorene-based copolymers exhibit hole mobilities of 9×10^{-5} cm²/V·s with $I_{\text{on}}/I_{\text{off}}$ ratios of 2×10^5 for **11** and 0.006 cm²/V·s with $I_{\text{on}}/I_{\text{off}}$ ratios of 2×10^5 for **12**. OTFT devices fabricated with polymers **6**, **7**, **10**, and **12** switch on crisply at around 0.0 V. For polymers **9** and **11**, the turn-on voltages are slightly greater (-10 V – -30 V), probably because of the mismatch between the work function of the gold electrode (-5.1 V) and the polymer HOMO levels (*vide infra*). Higher annealing temperatures are found to have detrimental effects on all of the present polymers, even though the T_{ms} of **7** and **10** are ~300 °C. This may reflect the formation of segregated rods consisting of π - π -stacked polymer lamella that plausibly inhibit efficient charge transfer.⁹¹

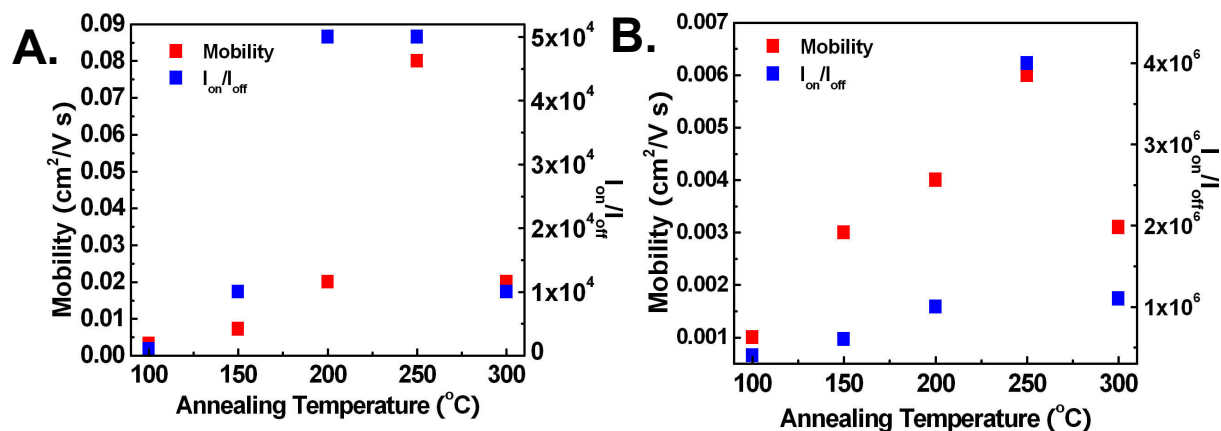


Figure 2.14. Evolution of field effect mobility and I_{on}/I_{off} ratio with annealing temperature in OTFTs of polymer 7 (A) and 10 (B).

Printed OFETs were fabricated with polymer thin films deposited by gravure printing from a highly viscous solution of **10** (0.5 wt % in TCB) on a PET-Al-CPB substrate (CPB = crosslinked polymer blend⁹² in which the dielectric layer is also printed (~ 20 wt % in AcOEt). After printing and before Au source/drain contact deposition, the printed films were annealed at ~100 °C for 30 min under vacuum. The printed devices exhibit a saturated hole mobility of 10^{-4} - 10^{-5} $\text{cm}^2/\text{V}\cdot\text{s}$ and $I_{on}/I_{off} \sim 100$ when measured in air (Figure 2.15). Although the mobility values for these gravure printed devices are lower than those for spin-coated films, all of the devices function reproducibly as p-channel transistors, which is remarkable considering the simplicity of the gravure printing technique and low annealing temperature. We believe that FET performance can be further improved by optimizing printing conditions.

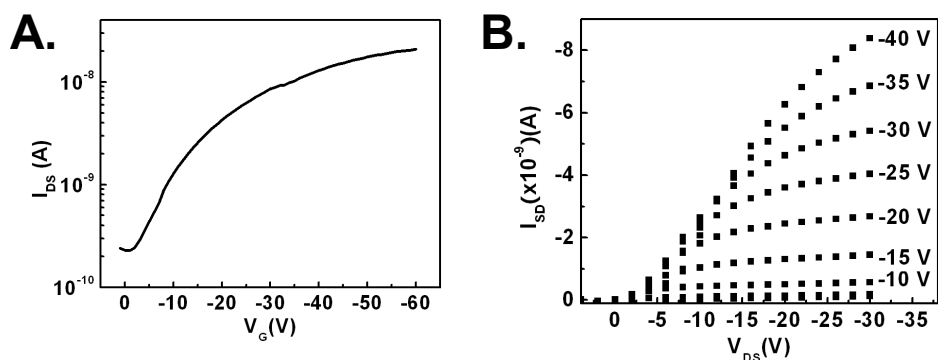


Figure 2.15. OTFT transfer (A) (at $V_{SD} = -40$ V) and output (B) plots of a gravure printed device fabricated with polymer **10** and a printed dielectric.

2.3.7 Device Air Stability.

OFETs fabricated using materials **6**, **7**, **9**, and **10** operate well in air, exhibiting very good ambient storage stability and electrical stability. The stability of the polymer devices stored in air without exclusion of light and humidity was evaluated over a period of time. As shown in Figure 2.16, the off currents of devices fabricated with **7** and exposed to air for three weeks increase by less than one order of magnitude, while the on current remains unchanged. The I_{on}/I_{off} ratios of **10**-based TFTs decline by less than one order of magnitude after 60 days. In both cases, nearly identical threshold voltages, mobilities, and I_{on}/I_{off} ratios are obtained, demonstrating excellent air stability for devices made from polymers **7** and **10**. After one year storage under ambient conditions, including laboratory exposure to light, the I_{on}/I_{off} ratios are found to be in the range $\sim 1 \times 10^3$ - 5×10^3 . The positive shift in threshold voltage after a few weeks can be attributed to slight p-doping by O_2 .⁴² Negative shifts in threshold voltage observed after prolonged ambient storage have previously been attributed to many effects, including charge trapping at the semiconductor-dielectric interface and bipolaron formation within the semiconductor.⁴² For comparison, OTFTs

of the well-known polymer P3HT were fabricated under the same conditions as **7** and **10**. The FET performance of P3HT was found to be very sensitive to air. When measured in vacuum, the devices exhibit an average initial $I_{\text{on}}/I_{\text{off}}$ ratio of $\sim 10^4$ which drops to less than 10^2 when the devices are exposed to air (Figure 2.16E), consistent with previous reports.⁹⁰ OTFT electrical stability was also tested by repeatedly switching the device on and off in air at various gate biases. For both **7** and **10**, the OTFT performance shows little indication of degradation, with $I_{\text{on}}/I_{\text{off}}$ ratios at a fixed gate voltage remaining essentially constant (Figures 2.16B and 2.16D).

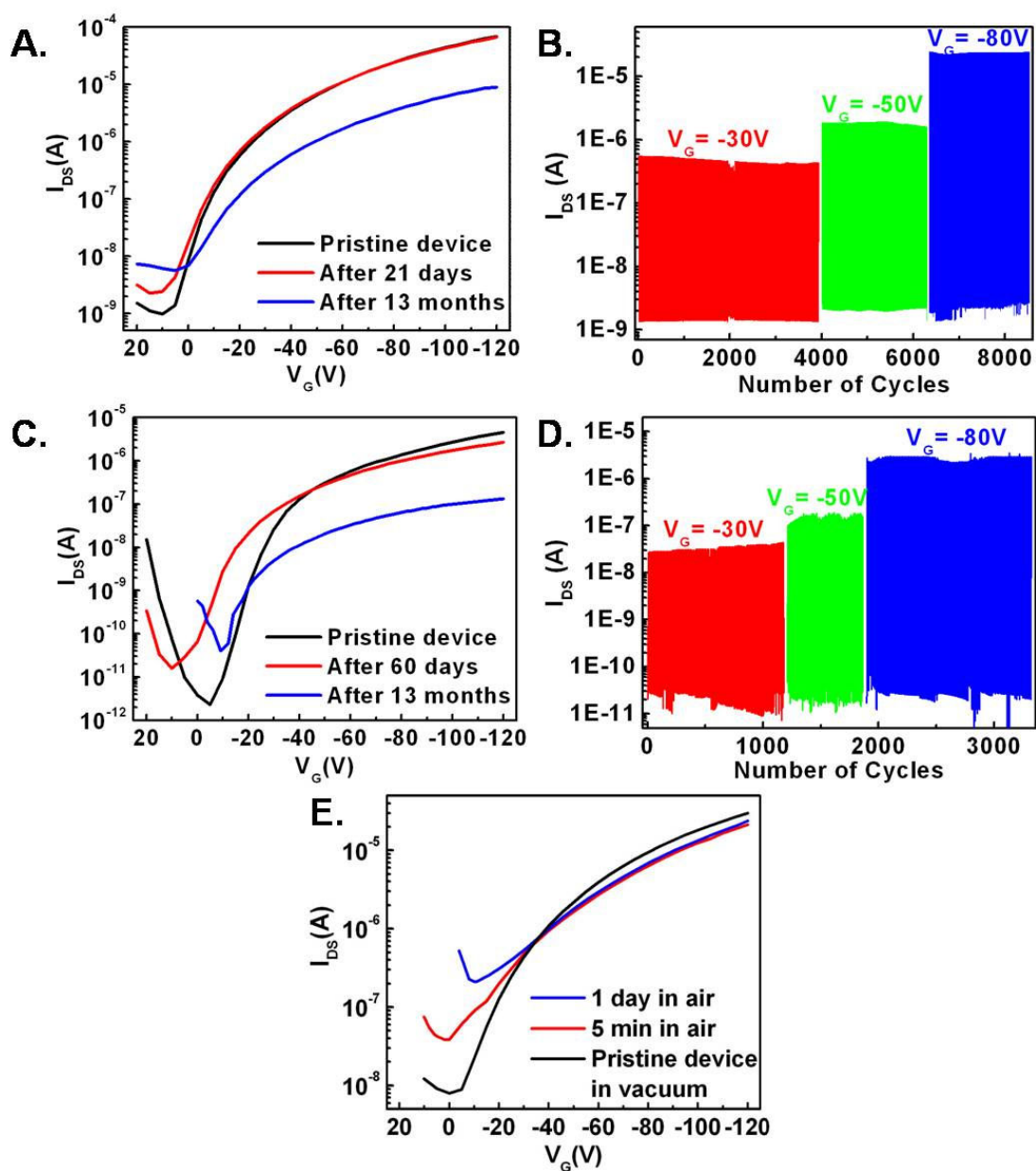


Figure 2.16. Transfer characteristics of OTFT devices fabricated with polymers **7** (A), **10** (C), and **P3HT** (E) as a function of storage time in the air. The on-off cycles (0.03 Hz) under ambient conditions for the annealed devices of polymers **7** (B) and **10** (D) at $V_{SD} = -50$ V were measured for the different gate biases indicated.

2.4 Discussion

2.4.1 Polymer Architecture vs. FET Performance.

In general, dithienosilole copolymers **6** and **7** exhibit larger hole mobilities than the corresponding dibenzosilole copolymers **9** and **10**, while bithiophene copolymers **7** and **10** have greater hole mobilities than thiophene copolymers **6** and **9**. Those factors affecting semiconducting polymer film mobilities reflect a complex interplay of electronic structure, injection, trapping, charge transfer parameters, polymer molecular weight,^{91, 93} side-chain regioregularity,²⁵ as well as macromolecular crystallinity and morphology.^{94, 95} Optimization of the molecular weights of the present polymers was attempted by using different polymerization protocols (*vide supra*). Additionally, side-chain regioregularity is not relevant here because the silole cores are symmetrical. Thus, the performance of devices fabricated with polymers **5-12** in this contribution appears to be primarily dependent on polymer crystallinity, morphology, and injection barriers.

Dithienosilole homopolymer **5** exhibits no diffraction features, even after annealing, revealing poor or no crystallinity, and is found to be FET-inactive. In contrast, polymers **6**, **7**, and **10** exhibit high FET saturated hole carrier mobilities when measured in air, most likely a consequence of the high level of molecular organization, namely crystallinity, of these polymers in the solid state as evidenced by the XRD data (Figure 2.8). Without annealing, thin films of polymers **6** and **7** are amorphous and have poor hole mobilities. However, they exhibit high-crystallinity diffraction patterns after annealing at 250 °C, each pattern having three equally spaced reflections assignable to members of the same Bragg family. Importantly, the mobility of these two polymers increases as the annealing temperature is increased, and maximizes at ~250

°C (Figure 2.14). Similar results are obtained for polymers **9** and **10**. These results argue that the degree of crystallinity is, not unexpectedly, a major factor determining the measured carrier mobility in these polymers. Judging from the number of reflections, FWHM values, and diffraction peak intensities, polymer **7** is the most crystalline of the three dithienosilole polymers. The crystallinity decrease on proceeding from **7** to **6** to **5**, apparent in the XRD spectra, correlates with the trend in carrier mobilities. In addition to the high degree of crystallinity, the preferential “edge-on” orientation of polymers **6** and **7** relative to the substrate may lead to layered structure formation with the π - π stacking direction parallel to the substrate plane, which is known to favor in-plane source-to-drain (S \rightarrow D) charge transport.²⁵ By the same token, among polymers **8**, **9** and **10**, polymer **10** appears to have the greatest crystallinity, correlating with enhanced mobility.

The trend in the melting points of the present polymers (see Table 2.1) is in accord with the observed increase in carrier mobility from the monothiophene to bithiophene copolymers. For polymers **6** and **7**, the melting point increases by ~ 40 °C, while for polymers **9** and **10**, the increase is even more substantial (~ 90 °C). The higher melting points of the bithiophene polymers, given the architectural similarity of the polymers, suggest that the macromolecules may be more densely packed in the solid state. For polymers **6** and **7**, the inter-chain lamellar d-spacings (15.54 and 15.38 Å, respectively) are somewhat smaller than twice the distance from the end of the *n*-hexyl group to the sulfur atoms of the silole core obtained in the DFT calculations (9.1 Å; Figure 2.17A), suggesting that the polymer chains likely assume an interdigitated packing motif similar to that in P3HT thin films²⁵ (Figure 2.2), although the precise orientation of the alkyl chains cannot be determined with the present XRD data alone. The interchain distances are somewhat shorter than that of P3HT (16.8 Å),²⁵ but much longer than

that of PQT-12 (12 Å; Figure 2.2).²⁸ Polymers **9** and **10** exhibit larger spacings (20.91 and 18.70 Å, respectively), which are *ca.* 3 Å longer than the previously reported layer periodicities of ~15 Å - 17 Å observed for alkyl-substituted fluorene and carbazole-based polymers and related small molecules.^{89, 90, 96}

These distances are also slightly smaller than twice the distance from the end of the *n*-octyl groups to the edge-carbon atoms of the silole core obtained from the DFT calculation (10.6 Å; Figure 2.17A). The d-spacing values of copolymers **6**, **7**, **9**, and **10** suggest that the *n*-hexyl and *n*-octyl side chains may interdigitate. Two possible packing motifs are depicted in Figures 2.17. Figure 2.17B shows a model in which the alkyl side chains do not interdigitate. In the horizontal plane, the polymer backbones are roughly perpendicular to the substrate with a tilt angle θ , and the electron-deficient silole cores overlap with bithiophene moieties. The alkyl side chains of each unit in the polymer are perpendicular to the substrate, consistent with the edge-on polymer orientation evidenced by the diffraction data. In the second model (Figure 2.17C), the polymer alkyl side chains interdigitate to some extent in the vertical plane. These models illustrate two extreme cases of the polymer thin-film microstructure, with the tilt angle highly dependent on the extent of side chain interdigitation for a given d-spacing.

Optical spectroscopy also provides polymer structural information in both solution and in the solid state. In general across the series, the addition of thiophene rings to the polymer backbone induces a red-shift in the solution optical absorption (a result in agreement with DFT calculations, *vide infra*). The one anomaly in the series is homopolymer **5** which exhibits a red-shifted absorption maximum vs. mono-thiophene-substituted **6** in THF. This result for **5** may reflect aggregation in solution, as evidenced by the strong shoulder around 400 nm;^{97, 98} in the

solid state, the shoulder disappears after vacuum annealing, indicating the elimination of this aggregation pattern in the solid state. The optical absorption maximum of polymer **6** red-shifts about 50 nm on going from solution to thin films, suggesting that in the solid state, polymer **6** achieves a higher degree of molecular organization than in solution. For polymers **7**, **9-12**, the absorption spectra of the thin films are generally similar in vibronic pattern and shape to those in dilute solutions, indicating comparable ground-state electronic structures and similar backbone conformations in the solution and solid states.

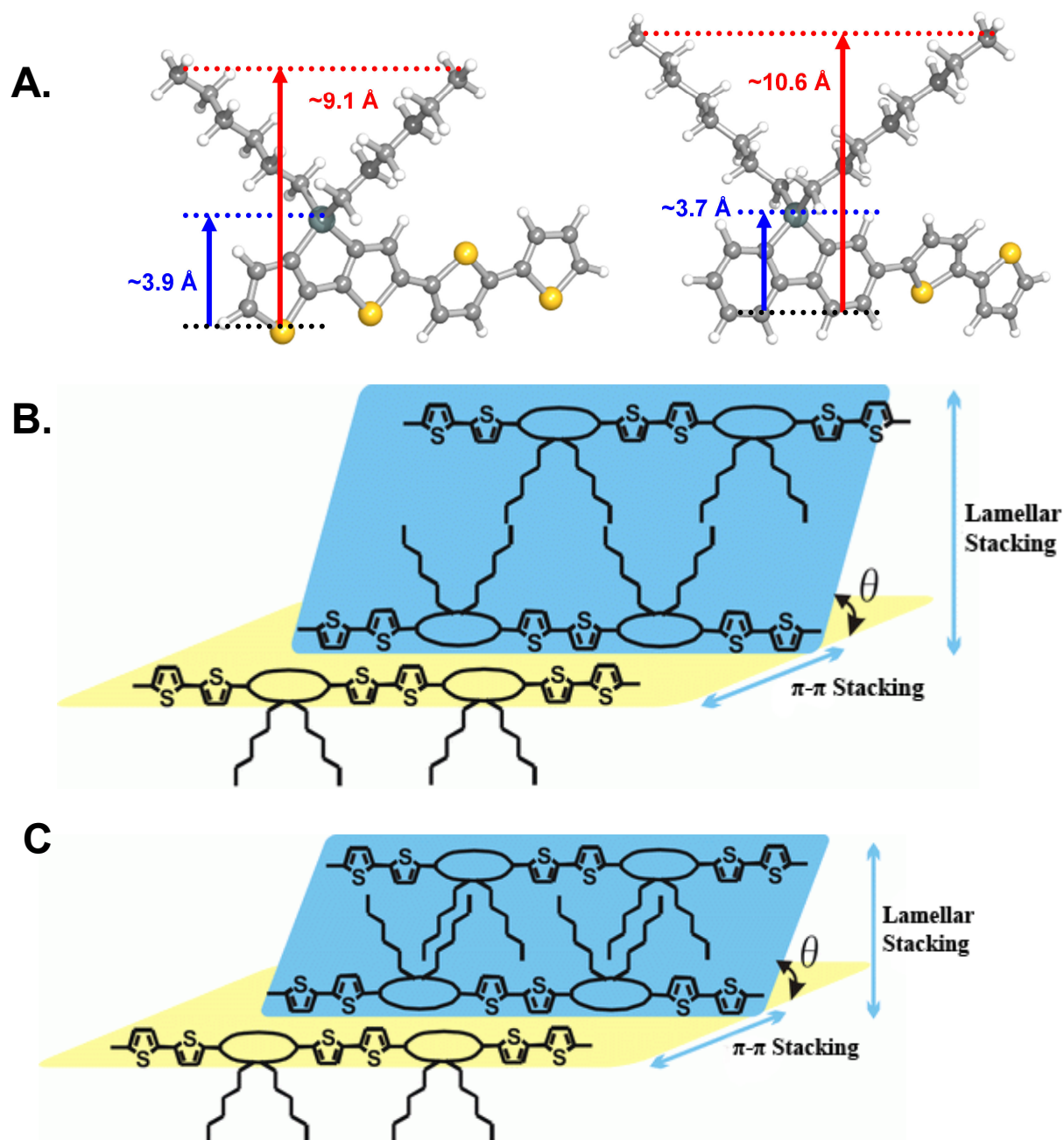


Figure 2.17. Schematic models of layered and π - π stacked silole copolymer structures **7** and **10**: DFT-calculated molecular dimensions (A), no side chain interdigitation model (B), and minimal free volume model (C).

2.4.2 Electrochemical and Optical Properties as a Function of Electronic Structure.

The solution and solid-state optical absorption data, along with the electrochemical oxidation potentials, reveal an important role for the heteroatom substitutions in the arylene backbones of the present polymer chains. To understand better the evolution of electronic states and ionization energies with substitution, electronic structure calculations at the density functional theory (DFT) level were carried out to model the polymer building blocks (Figure 2.18); note here that the 1,1'-substituents on each of the model fragments are methyl groups to simulate the influence of alkyl chains on the geometric and electronic structure properties of each arylene. Selected molecular orbital energies, low-lying singlet state energies, and the corresponding excited-state configurations are compiled in Table 2.3, while Figure 2.19 provides contour representations of selected valence MOs for the model fragments. For the three pairs of aromatic cores compared (cyclopentadiene/silole, F8/BS8, and CPDT/TS6), introduction of Si into the molecular structures energetically stabilizes both the HOMO and LUMO, with the LUMO undergoing more significant stabilization – in accord with previous theoretical analyses of related, non-semiconductor systems.^{85, 99} With no significant π -orbital character for either the central C or Si of the aromatic cores, the minimal stabilization of the HOMO in the Si-containing species is a result of the larger Si atom size, which leads to increased bond lengths to the nearest neighbor atoms by ~ 0.36 Å vs. the C analogue, and in turn decreases antibonding interactions within the *cis*-butadiene-like HOMO. In contrast, the more significant LUMO stabilization reflects the extended conjugation from the overlap between the two exocyclic Si-C bond σ^* -orbitals and the butadiene moiety π^* -orbital; in contrast, the $2p_z$ -orbitals of the C-analogs are too energetically

destabilized to effectively participate in such bonding.⁹⁹ This interaction is often invoked to explain the large electron affinities of siloles vs. their cyclopentadiene analogs.^{99, 100}

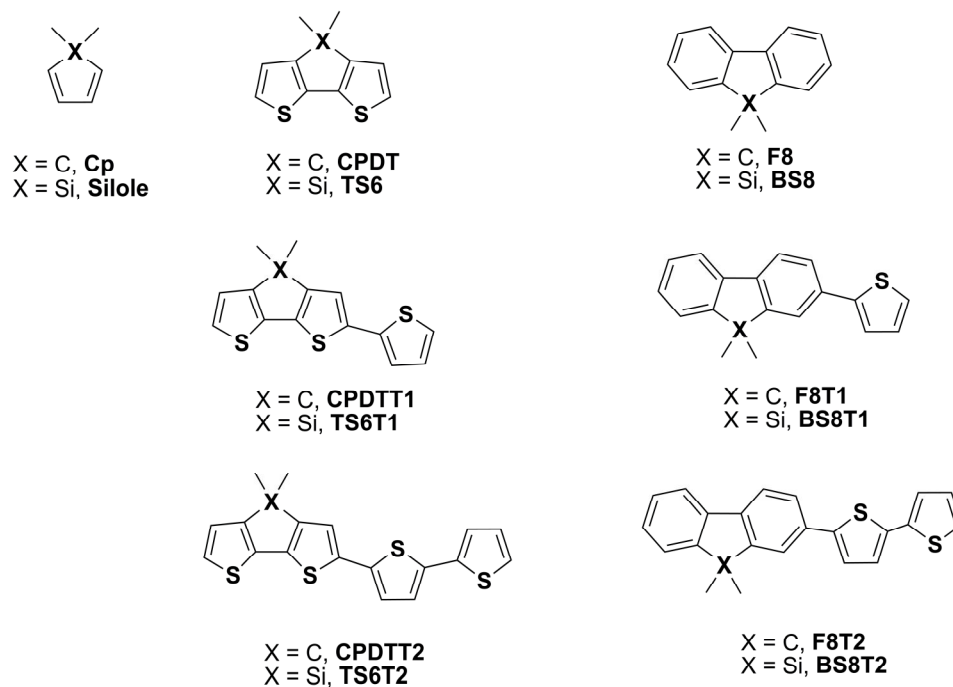


Figure 2.18. Chemical structures of model polymer building blocks for electronic structure calculations.

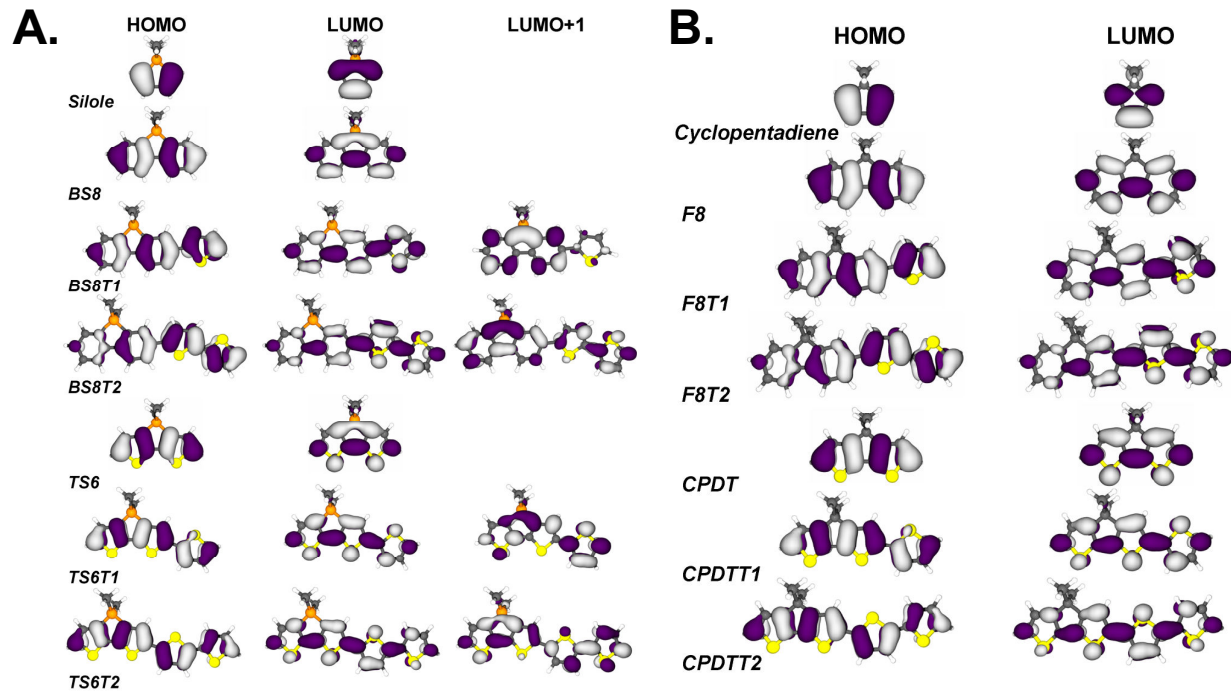


Figure 2.19. Pictorial representations of B3LYP/6-31G**⁻-derived selected valence molecular orbitals for the present silole-based polymer building blocks (A), and carbon-based polymer building blocks (B).

Subsequent introduction of thiophene rings to represent more accurately the mono- and bithiophene units of the complete polymers (Figure 2.18) leads to energetic destabilization of the HOMO and stabilization of the LUMO with each new thiophene unit; the HOMO and LUMO wavefunction densities for these monomeric systems are delocalized across the molecular structures.¹⁰¹ Note that the comparative HOMO and LUMO energies for dithieno- and dibenzo-C- and Si-substituted structures are nearly identical – a result not expected *a priori* considering the aforementioned core unit trends. Inspection of the HOMO densities for these systems shows that the wave functions are delocalized in the same manner across the structures and are linear combinations of the core HOMO with the thiophene HOMO. Using Koopmans' theorem, the DFT-derived HOMO energetic trends (Table 2.3) track the electrochemically-obtained oxidation potentials well (Table 2.2). As a complement to the ionization energies obtained from the electrochemical (adiabatic) measurements, direct adiabatic ionization potential and electron affinity calculations for the model building blocks were also performed (Table 2.3). These results reveal that Si atom inclusion in the arylene backbone makes negligible contribution to the fragment oxidation energies, in agreement with the computed frontier orbitals. Increasing the number of (closed shell) thiophene units in the monomer decreases the ionization energy, thus providing an additional mechanism for stabilizing of the oxidation products. As with the HOMO energies, the adiabatic ionization potentials track the estimated IP^{ox} values well (see Figure 2.20A); the difference in absolute values between the calculated and experimentally-estimated values is not surprising in that: i) the calculations are performed for small model monomers while the experimental data are for full polymer chains, and ii) there exist inherent limitations

(e.g., solvent polarity effects) in using eq. 1 to estimate gas-phase ionization potentials for polymers.

In a fashion analogous to the thiophene-containing monomer HOMOs, the C- and Si-substituted monomer LUMO π^* -densities are similar (Figures 2.19). For the Si-containing systems, there is no significant electron density found on the Si atom in the LUMO for any of the thiophene-substituted systems; this is in direct contrast to what was observed for the smaller aryl cores (*vide supra*) and other previously investigated silole-like systems.^{48, 49, 102} Incorporation of the thiophene units into the present structures increases the conjugation length of the carbon backbone, leading to energetic stabilization of the carbon-backbone-based π^* -orbital, thereby reducing the σ^* - π^* interaction typically observed in silole structure LUMOs.^{48, 49, 102} These σ^* - π^* interactions are not observed until the LUMO+1 levels, which lie appreciably higher in energy (on the order of 0.7 eV - 1.2 eV) above the LUMOs in these molecules; inspection of the Si atomic orbital coefficients in the LUMO and LUMO+1 levels reveals a much larger contribution to LUMO+1. These results therefore suggest that reduction of these species may be energetically more demanding, compared to their carbon analogs, than typical siloles due to the loss of the extended LUMO conjugation. Indeed, the computed LUMO energies are virtually identical for the Si- and C-containing species, thus suggesting that the reductive properties of these materials should be similar (more so than for the core aryl structures, *vide supra*). Directly calculated adiabatic electron affinities for the dithienosilole/cyclopentadiene and dibenzosilole/cyclopentadiene pairs (Table 2.3) confirm this assessment. While there is substantial correspondence between the LUMO energies and the electrochemically-derived EA^{ox} values, the agreement between the theoretical and experimental data is not as close as that for the

ionization potentials. Overall, the frontier orbital energies and calculated ionization energies are consistent with the observed polymer electrochemical characterization, where no clear reductive properties are observed although reversible and irreversible oxidative features are detected.

Using the electronic structures of the model building blocks and the time-dependent DFT (TDDFT) formalism, the lowest-lying excited state energies are found to track the computed HOMO-LUMO gaps closely (see Table 2.3). The principal transition for each model fragment is characterized as being predominantly HOMO \rightarrow LUMO in character, with minor transitions involving other nearby valence MOs. The calculated excited state energies for the model fragments exhibit optical absorption maxima red-shifts with increasing thiophene substitution, and also on going from dibenzosilole- to dithienosilole-based polymers. These trends agree well with both the experimental solution and thin-film absorption properties for the polymers (Table 2.1).

Table 2.3. Computed adiabatic ionization potentials and electron affinities (eV), selected valence molecular orbital energies (eV), HOMO-LUMO gaps (eV), and low-lying excited-state energies (eV and nm, in parentheses), oscillator strengths, and excited-state configurations as determined at the B3LYP/6-31G** level. ^(a) Computed using Δ SCF methods).

Compound	AIP ^a	AEA ^a	HOMO	LUMO	E _g	λ	Osc. Str.	Configuration
Cyclopentadiene	7.76	1.55	-5.70	-0.34	5.36	5.01 (247)	0.05	HOMO \rightarrow LUMO (99%)
Silole	7.87	0.64	-5.96	-1.09	4.87	4.39 (283)	0.05	HOMO \rightarrow LUMO (99%)
F8	7.28	0.72	-5.74	-0.76	4.98	4.62 (269)	0.27	HOMO-2 \rightarrow LUMO (11%); HOMO \rightarrow LUMO (71%); HOMO \rightarrow LUMO+1 (13%)
F8T1 (11)	6.66	-0.03	-5.40	-1.24	4.16	4.77 (260)	0.09	HOMO-2 \rightarrow LUMO (15%); HOMO \rightarrow LUMO (23%); HOMO \rightarrow LUMO+1 (61%)
F8T2 (12)	6.24	-0.52	-5.15	-1.56	3.59	3.87 (321)	0.84	HOMO \rightarrow LUMO (99%)
B88 (8)	7.27	0.45	-5.79	-0.93	4.85	3.30 (376)	1.21	HOMO \rightarrow LUMO (99%)
B88T1 (9)	6.65	-0.13	-5.42	-1.32	4.10	4.30 (288)	0.08	HOMO \rightarrow LUMO (74%); HOMO \rightarrow LUMO+1 (20%); HOMO-1 \rightarrow LUMO (30%); HOMO \rightarrow LUMO (21%); HOMO \rightarrow LUMO+1 (47%)
B88T2 (10)	6.23	-0.58	-5.15	-1.60	3.55	4.60 (270)	0.13	HOMO \rightarrow LUMO (97%)
CPDT	6.73	0.49	-5.19	-1.02	4.17	3.76 (330)	0.62	HOMO-2 \rightarrow LUMO (8%); HOMO \rightarrow LUMO+1 (80%)
CPDTT1	6.20	-0.26	-4.90	-1.54	3.36	4.14 (300)	0.14	HOMO \rightarrow LUMO (99%)
CPDTT2	5.91	-0.69	-4.80	-1.79	3.01	3.26 (381)	1.16	HOMO-1 \rightarrow LUMO (6%); HOMO \rightarrow LUMO+1 (79%); HOMO \rightarrow LUMO+2 (8%)
TS6 (5)	6.77	0.13	-5.30	-1.29	4.00	3.86 (322)	0.04	HOMO \rightarrow LUMO (99%)
TS6T1 (6)	6.23	-0.42	-4.98	-1.66	3.32	3.93 (316)	0.31	HOMO \rightarrow LUMO (99%)
TS6T2 (7)	5.94	-0.78	-4.86	-1.85	3.01	3.18 (389)	0.75	HOMO \rightarrow LUMO (100%)
						2.82 (440)	1.16	HOMO \rightarrow LUMO (100%)
						3.96 (313)	0.02	HOMO-1 \rightarrow LUMO (67%); HOMO \rightarrow LUMO+2 (31%)
						3.63 (341)	0.23	HOMO \rightarrow LUMO (99%)
						3.07 (404)	0.60	HOMO \rightarrow LUMO (99%)
						3.95 (314)	0.06	HOMO-1 \rightarrow LUMO (16%); HOMO \rightarrow LUMO+1 (80%)
						2.78 (447)	1.05	HOMO \rightarrow LUMO (99%)
						3.39 (365)	0.04	HOMO-1 \rightarrow LUMO (17%); HOMO \rightarrow LUMO+1 (80%)
						3.82 (325)	0.03	HOMO-1 \rightarrow LUMO (80%); HOMO \rightarrow LUMO+1 (16%)

2.4.3 Role of the Hole Injection Barrier.

In addition to microstructural and morphological differences among the present polymers in the solid state, there are also expected differences in the hole injection barriers from the gold electrodes to the polymer HOMO (see Figure 2.20) that likely affect OFET performance by altering contact resistance and turn-on voltage.¹⁰³⁻¹⁰⁵ According to a simple Schottky-type charge injection barrier model, the relative hole injection rates for a series of related materials should have an exponential dependence on the hole injection barrier, Φ_B , assumed to be the difference between the metal electrode Fermi level (E_F) and the polymer ionization potential (eq. 2).^{16, 106, 107}

$$\Phi_B = E_F - IP \quad (2)$$

(note that for the estimates that follow, we use the electrochemical estimate of the ionization potential, IP^{ox}). Assuming a gold Fermi level energy of 5.1 eV,⁸¹ Φ_B is expected to be small (~ 0.2 eV) for the dithienosilole-based copolymers **6** and **7**. OTFTs fabricated with polymers **6** and **7** switch on crisply at ~ 0 V, indicative of a small Φ_B . For electron-deficient dibenzosilole-based copolymers **9** and **10**, the estimated injection barriers are significantly greater at 0.7 eV and 0.5 eV, respectively. Note that these polymers exhibit significantly higher turn-on voltages of -10 V to -20 V, probably reflecting, amongst many factors, these differences in injection barriers. Fluorene-based copolymers **11** and **12** exhibit similar trends in that a high energy level offset for **11** (0.6 eV) results in higher OTFT turn-on voltages of -20 V – -30 V, whereas devices fabricated with **12** have low turn-on voltages of 0 V – -5 V, in agreement with the smaller energy level mismatch of ~ 0.3 eV. Some detectable contact resistance due to the high injection barriers

is also evident for polymers **9** and **11** as slight curvatures in the source-drain current plot at low source-drain voltages in the output curves (Figures 2.11 and 2.12).

We note interestingly that, without exception across the present polymer series, a direct correlation exists between the hole injection barrier Φ_B and FET hole mobility μ_h (Figure 2.20B): polymers **6**, **7**, **10**, and **12** are shown to have small injection barriers and large measured mobilities, while polymers **5** and **8** (inactive as semiconductors),^{103, 108} **9**, and **11** have larger injection barriers and small measured mobilities. These results suggest that injection barriers not only play a critical role in turn-on voltage and contact resistance for these polymers, but also affect the measured TFT hole transport characteristics, a result that we also observed recently for a series of carbonyl-functionalized quarterthiophene (n-type, μ_e) organic semiconductors.¹⁰⁹ Charge transport models that consider charge injection via a thermally-activated injection process (as we have done throughout) into a disordered medium – whether one considers the current to be solely injection-limited (ILC)¹¹⁰ or that there exists an interplay between ILC and space charge-limited current (SCLC)¹¹¹⁻¹¹⁴ – suggest that indeed the size of Φ_B can have a profound impact on the measured current, and hence measured μ_h in organic semiconducting systems. For these polymers, further temperature- and field-dependent studies will be required to discern further details of the limiting charge transport mechanism.

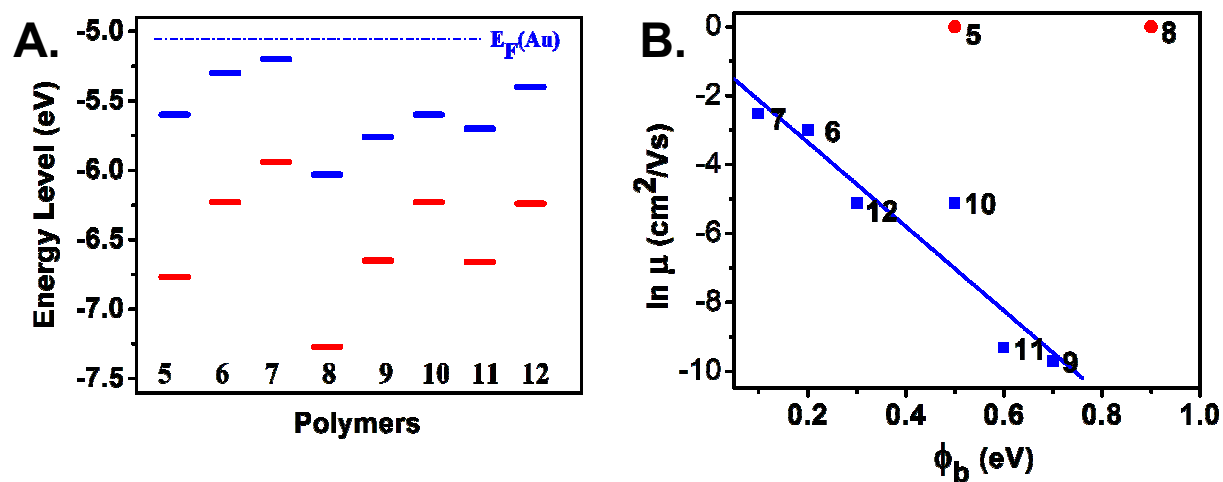


Figure 2.20. A. Comparison of theoretical (AIP, —) and experimentally-estimated (IP^{ox}, —) ionization potentials using eq. 1; differences in the ionization potentials for each species arise from a comparison of a model monomer (theoretical) versus the full polymer (experimental) measurements and neglect solvent dielectric effects in the gas-phase calculations. B. Experimental mobility as a function of hole injection barrier. Note that for polymers **5** and **8** negligible mobilities were measured.

2.5 Conclusions

We have synthesized and characterized a new family of silole-containing polymers, **5-10**. For comparison, fluorene-thiophene copolymers **11** (investigated for the first time here in an OTFT) and **12** were also synthesized. Polymers **5-12** have excellent thermal and environmental stability. Polymers **5** and **8** are found to be FET-inactive, probably because of poor film-forming tendencies and substantial hole injection barriers. Monothiophene-containing copolymers **6**, **9**, and **11** are p-type materials, with **9** and **11** exhibiting moderate hole mobilities of $\sim 10^{-4}$ cm²/V·s. Polymer **6** exhibits a substantial hole mobility of 0.05 cm²/V·s in air, with an $I_{\text{on}}/I_{\text{off}}$ ratio of 1×10^5 . Bithiophene-containing copolymers **7**, **10**, and **12** are also found to be p-type materials with excellent OTFT performance. For polymer **7**, hole mobilities up to 0.08 cm²/V·s with an $I_{\text{on}}/I_{\text{off}}$ ratio $> 5 \times 10^4$ are achieved under ambient conditions with near-zero turn-on voltage. For polymer **10**, a hole mobility of 6.0×10^{-3} cm²/V·s is obtained with a maximum current on/off ratio of 4×10^6 . OTFTs fabricated using polymers **7** and **10** are very stable upon exposure to ambient air and light. DFT calculations indicate that silicon substitution stabilizes both the HOMO and LUMO levels of the dithienosilole and dibenzosilole cores, rendering the silole copolymers less susceptible to O₂ doping. The theoretical and optical characterization data suggest high degrees of π -delocalization in the silole-based polymers with increased ionization potentials and electron affinities vs. the carbon counterparts. We also observe and discuss a direct correlation between hole injection barriers and both the OTFT measured turn-on voltages and hole mobilities. These results, in total, affirm the possibility of achieving low-cost microelectronic devices through organic materials that enable simple solution fabrication processes under ambient conditions.

Chapter Three

Design, Synthesis, and Characterization of Ladder-Type Molecules and Polymers. Air-Stable, Solution-Processable *n*-Channel Semiconductors for Thin-Film Transistors via Experiment and Theory.

3.1 Introduction

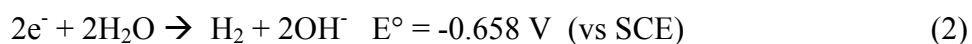
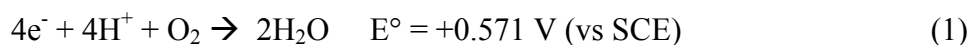
Over the past two decades, many classes of π -conjugated organic molecules and polymers have been synthesized and characterized as semiconductors for organic field-effect transistors (OFETs), mainly focusing on oligoacene and oligothiophene derivatives.^{1,2} Due to the relatively air-stable hole-transporting characteristics of these cores and HOMO energies of $\sim -4.9 - -5.5$ eV, which aligns with the work function of air-stable electrodes (Au, 5.1 eV; Pt, 5.6 eV), most of these initial semiconductor examples were *p*-channel materials.³ After the first report of *n*-channel OFETs based on metallophthalocyanines in 1990,⁴ intensive research on the rational design and synthesis of new materials with high electron affinities has afforded several series of *n*-channel semiconductors in which electron-deficient substituents/units such as perfluoralkyl ($-\text{C}_n\text{F}_{2n+1}$), $-\text{CN}$, $-\text{F}$, perfluorophenyl (C_6F_5-), carbonyl ($-\text{C}=\text{O}$), and imide [$-\text{C}(\text{O})\text{NHC}(\text{O})-$] are incorporated into thiophene-, phenylene-, and arylene-based π -conjugated cores.^{1,5} For these semiconductors, electron mobilities as high as $0.1 - 2.0 \text{ cm}^2/\text{V}\cdot\text{s}$ are obtained under vacuum/nitrogen.¹ However, only a few of the current *n*-channel semiconductors exhibit air-stable FET device operation, and this is generally achieved via fluoroalkyl-based kinetic barriers and/or stabilization-imparting MO energetics,⁶ with the exact mechanism of ambient stability not fully established.⁷ Furthermore, while single-component ambipolar semiconductors were first reported in 2003,⁸ only recently was an ambipolar coordination compound reported to operate in air with modest FET performance ($\mu_{e,h} = 10^{-4} \text{ cm}^2/\text{V}\cdot\text{s}$).⁹ Thus, while today there are a number of *n*-channel materials and a few ambipolar materials having field-effect mobilities $\geq 0.1 \text{ cm}^2/\text{V}\cdot\text{s}$, two major challenges remain: i) stabilizing the electrons during FET operation in ambient without device encapsulation, ii) solution-processibility to eliminate costly vacuum/inert

atmosphere-based deposition processes. To truly realize *n*-channel and ambipolar semiconductors in *p-n* junctions, bipolar transistors, and organic complementary circuitry (CMOS), additional device encapsulation should be avoided by enhancing ambient stability, and solubility should be increased to enable straightforward, solution-based deposition techniques such as spin-coating, drop-casting, and printing. Furthermore, the science governing device environmental stability and performance-processing relationships should be understood in greater depth.

To a first approximation, the ambient stability of *n*-channel semiconductors is controlled by the ionization potential of the injected/induced electrons, formed when the FET is in the accumulation regime – or in Koopmans' theorem¹⁰ metrics, by the LUMO energy of the neutral semiconductor.¹¹ In general, lowering organic semiconductor LUMO energies enhances FET device stability by energetically stabilizing the induced electrons during charge transport, which occurs primarily by hopping through low-lying LUMOs.⁶ The issue of ambient stability was initially addressed by de Leeuw et al. in 1997, focusing mainly on *n*-doped organic polymers which are rare compared to their *p*-doped counterparts.¹¹ Degradation of such materials in ambient is mainly due to reaction of the charge-carrying electrons with O₂ and H₂O, and is not related to intrinsic chemical instability. This process is also known as *trapping* and reduces the current flow through the FET conduction channel. Although the same trapping can be achieved by hydroxyl groups at the dielectric-semiconductor interface, the number of these trapping sites can be substantially reduced by hexamethyldisilazane (HMDS) or octadecyltrichlorosilane (OTS) surface treatments, and is not relevant to the present discussion.

In one approach to realizing air-stable n -channel device operation, Katz et al. employed molecular semiconductors with perfluoroalkyl ($-C_nF_{2n+1}$) side chains (NDIF, Figure 1) which pack in a sufficiently dense thin-film motif to form a kinetic barrier against ambient species penetration.¹² A similar effect was also observed with perfluorinated copper phthalocyanine ($CuF_{16}Pc$) and fluorocarbon-substituted oligothiophenes (DFCO-4TCO).^{13,14} Although these semiconductors exhibit initial ambient operational stability, depending on the O_2 partial pressure and film growth methodology, OFET performance degrades over periods of hours to days.⁷ Hence, semiconductors exhibiting intrinsically (i.e., thermodynamically) air-stable electron transport not affected by environmental conditions and film microstructure would be highly desirable.

As an initial approach, using solution-phase standard electrochemical potentials (eqs. 1 and 2) and assuming $pH = 7.0$ and an overpotential of 0.0 V , the limits of the semiconductor reduction potentials for stability are estimated as $\geq -0.658\text{ V}$ (vs SCE) with respect to H_2O oxidation, and $\geq +0.571\text{ V}$ (vs SCE) with respect to O_2 oxidation.¹¹



Although there are a number of π -conjugated organic materials having a first reduction potential greater than -0.658 V , electron-deficient molecules with reduction potentials surpassing $+0.571\text{ V}$ are very rare. Thus, the realization of non-fluorinated air-stable semiconductors PDI-8CN2, ADI-8CN2, and NDI-8CN2 (Figure 3.1) showed that the materials with first reduction potentials $\geq -0.4\text{ V}$ can operate in air without severe device performance degradation, suggesting the presence of an overpotential (i.e., free energy of activation) of $\sim 0.5 - 1.0\text{ V}$.¹⁵⁻¹⁷ Similar

overpotential values were also estimated by de Leeuw et al.¹¹ The present study offers further insight into such overpotential values based on a new class of ladder-type semiconductors, providing key information for the rational design of new *n*-channel materials with air-stable electron transport.

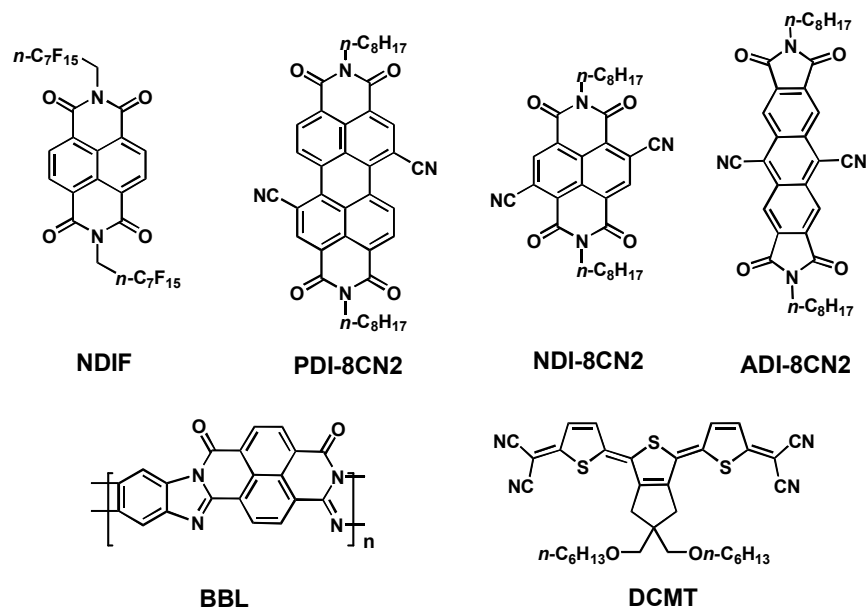


Figure 3.1. Structures of air-stable *n*-type semiconductors.

Exceptionally electron-deficient cyano-functionalized arylenediimides (PDI-8CN2, ADI-8CN2, and NDI-8CN2) represent first-generation examples of thermodynamically air-stable, *n*-channel semiconductors having high electron mobilities of 0.01 – 0.64 cm²/V·s and I_{on}/I_{off} ratios of 10⁴ – 10⁷.^{18,19} However, when these materials are processed from solution, they exhibit appreciably lower FET performance ($\mu_e \sim 10^{-3}$ cm²/V·s) reflecting measurable microstructural irregularities in the solution-processed films.²⁰ Recently, somewhat higher solution-derived PDI-8CN2 film mobilities of 0.02 – 0.1 cm²/V·s were achieved by device structure and deposition process optimization.^{21,22} Additionally, a solution-processable dicyanomethylene-substituted

terthienoquinoid derivative (DCMT, Figure 3.1) was reported to exhibit $\mu_e \sim 0.16 \text{ cm}^2/\text{V}\cdot\text{s}$ in air, however it suffers from a low $I_{\text{on}}/I_{\text{off}}$ ratio ($\sim 10^3 - 10^4$) and μ_e drops to $\sim 0.01 \text{ cm}^2/\text{V}\cdot\text{s}$ over time in ambient.²³ In contrast to these molecular results, the only reported *n*-channel polymer with air-stability is the ladder-type polymer, BBL (Figure 3.1; $\mu_e \sim 0.03 \text{ cm}^2/\text{V}\cdot\text{s}$ and $I_{\text{on/off}} = 10^5$).²⁴ The low solubility of this material requires aggressive Lewis acid solutions (GaCl_3 , methanesulfonic acid) for dissolution, which is unattractive for large-scale applications. Previously, well-known *p*-channel polymeric semiconductors were shown to exhibit *n*-channel behavior after dielectric surface treatment to remove hydroxyl (-OH) groups, however the resulting TFTs only operate under vacuum and become inactive in the presence of O_2 and moisture.²⁵ Therefore, the paucity of air-stable *n*-channel polymers which can be processed from conventional organic solvents has hindered utilizing the superior rheological properties of polymers in printing processes. This largely reflects the synthetic challenges in optimizing the delicate balance between solubility and efficient solid-state packing. Additionally, the development of air-stable *n*-channel polymers is of importance in the fundamental understanding of OFET charge transport.²⁶ Achieving high performance air-stable *n*-channel polymers requires the design of monomeric building blocks possessing several key characteristics: i) structural planarity for efficient charge delocalization/solid-state packing, ii) solubility for processibility, iii) electron-deficiency for electron injection/conduction in ambient, and iv) terminal reactive functionalities for efficient polymerization processes. To date, the incorporation of the aforementioned air-stable monomers into polymeric backbones has not yielded macromolecule-based *n*-channel OFETs which operate in air, largely because potential polymerization sites are occupied by either electron-withdrawing functionalities (-CN) or substituents with poor polymerization reactivities (-F).

A critical goal for organic CMOS is to realize solution-processable molecular/polymeric semiconductors possessing high *n*-channel mobility ($\geq 0.1 \text{ cm}^2/\text{V}\cdot\text{s}$) and air stability along with good OFET current modulation ($\geq 10^5$) characteristics. Semiconductors exhibiting these characteristics would be excellent candidates for practical OTFT applications, reflecting the intrinsic technological attractions of solution-processable materials, such as facile film formation, compatibility with low-cost manufacturing, and direct-write printing techniques on flexible plastic substrates. These considerations prompted us to seek new electron-deficient (low-lying LUMO) molecular building blocks and their corresponding polymers based on ladder-type (bis)indenofluorene architectures. Here we present a full account of the synthesis and characterization of a new family of ladder-type molecules and polymers (**1-12** and **P1-P13**, Figures 3.2 and 3.3) in which highly electron-deficient carbonyl and dicyanovinylene groups are introduced into planar indenofluorene and bisindenofluorene structures along with solubilizing alkyl chains. The design rationale explored here and embodied in constituents **1-12** is: (i) highly π -conjugated planar cores to facilitate efficient π -electron delocalization and to favor good intermolecular π - π stacking,²⁷ (ii) electron-withdrawing carbonyl and dicyanovinylene functionalities to depress LUMO energies, which is crucial for achieving electron transport and air-stability,²⁸ (iii) alkyl side chains (*n*-C₁₂H₂₅) to increase core solubility without disrupting backbone π -conjugation,²⁹ (iv) aryl bromide functionalities at the molecular termini to access the corresponding polymers via efficient Stille and Yamamoto polymerization protocols.

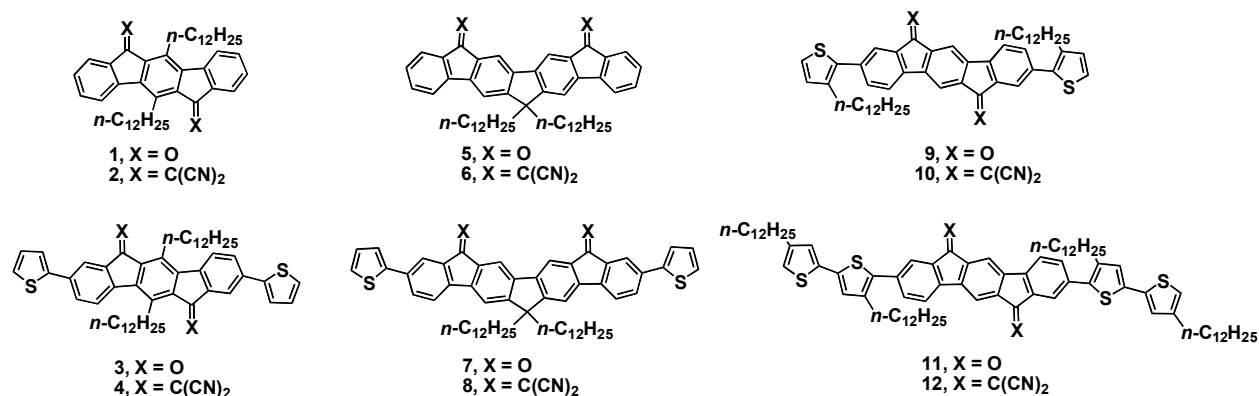


Figure 3.2. Structures of ladder-type (bis)indenofluorene-based compounds **1-12**.

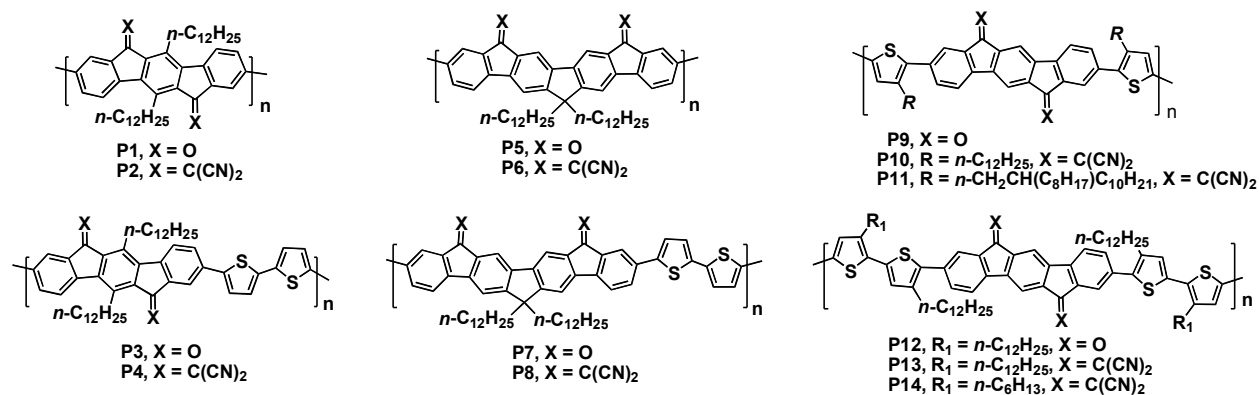


Figure 3.3. Structures of ladder-type (bis)indenofluorene-based homo- and copolymers **P1-P14**.

In order to investigate the application of each building block to the polymeric semiconductors, polymerization reactions are performed on dibromo-functionalized monomers (**M1-M6**), and nine new solution-processable polymers (**P2, P3, P4, P6, P7, P8, P12, P13, and P14**, Figure 3.3) are prepared through conventional/microwave-assisted Stille and Yamamoto polymerization protocols. All of the new compounds and polymers are characterized by optical spectroscopy, photoluminescence, cyclic voltammetry, differential scanning calorimetry (including the

elucidation of the liquid crystalline phases), and thermogravimetric analysis. Corresponding thin-films are studied by X-ray diffraction, AFM, and FET measurements. For this new family of ladder-type molecules and polymers, through modifications of core structures and functionalities, HOMO/LUMO energetics can be finely tuned ($\Delta = 0.1$ eV) over 1.0 eV, allowing determination of the MO energetic windows governing carrier polarity and environmental stability. In the present series of thin films having different crystallinities, orientations, and morphologies, it is shown that OFET air stability is principally governed by LUMO energetics with minimal contribution from the film microstructure. The onset LUMO energy level for electron stabilization during charge transport is estimated as $-4.1 - -4.0$ eV, which indicates that an overpotential of $0.9 - 1.0$ eV is operative for reaction of the organic π -anions with O_2/H_2O . Depending on the relative HOMO and LUMO energy positions versus source and drain electrode work functions, *p*-channel (μ_h up to 0.01 $cm^2/V\cdot s$), ambipolar (μ_e up to 0.01 $cm^2/V\cdot s$, μ_h up to 0.006 $cm^2/V\cdot s$), or *n*-channel behavior (μ_e up to 0.02 $cm^2/V\cdot s$) is observed under vacuum and/or ambient. For semiconductors with sufficiently low LUMO energies, air-stable *n*-channel behavior with mobilities up to 0.16 $cm^2/V\cdot s$ is realized with very high on/off ratios of $10^7 - 10^8$, representing some of the most favorable FET performance metrics achieved to date for *n*-channel, solution-processed semiconductors in ambient. Furthermore, construction of donor-acceptor structures affords low band gap materials (1.36 eV $- 1.40$ eV) with charge-injection accessible HOMO and LUMO energies, resulting in solution-processed film electron and hole mobilities of 10^{-3} $cm^2/V\cdot s - 10^{-4}$ $cm^2/V\cdot s$ and I_{on}/I_{off} ratios of $\sim 10^4$, including the first examples of molecular and polymeric ambipolar semiconductors operating in air. Correlated density functional theory calculations focus on the effects of carbonyl and dicyanovinylene substituents,

π -conjugated core dimensions, and thiophene annelation on molecular/device electronics, and provide detailed insight into intrinsic charge transport and carrier polarity characteristics.

3.2 Experimental

3.2.1 Materials and Methods.

All reagents were purchased from commercial sources and used without further purification unless otherwise noted. Anhydrous THF was distilled from Na/benzophenone. Conventional Schlenk techniques were used, and reactions were carried out under N₂ unless otherwise noted. Optical spectra were recorded on a Cary Model 1 UV-Vis spectrophotometer. Fluorescence measurements were recorded on a Photon Technology International model QM-2 fluorimeter. NMR spectra were recorded on a Varian Unity Plus 500 spectrometer (¹H, 500 MHz; ¹³C, 125 MHz). GPC analyses of polymer samples were performed on a Waters Alliance GPCV 2000 (3 columns, Waters Styragel HT 6E, HT 4, HT 2; operation temperature, 150 °C; mobile phase, 1,2,4-trichlorobenzene or THF at room temperature; flow rate, 1 mL/min) and are reported relative to polystyrene standards purchased from Aldrich. Electrospray mass spectrometry was performed with a Thermo Finnegan model LCQ Advantage mass spectrometer. Electrochemistry was performed on a C3 Cell Stand electrochemical station equipped with BAS Epsilon software (Bioanalytical Systems, Inc., Lafayette, IN).

3.2.2 Synthesis and Characterization.

Synthesis of 1,4-Di-*n*-dodecylbenzene (13). The reagent *n*-dodecylmagnesium bromide (235 mL, 235.0 mmol, 1.0 M in diethyl ether) was added dropwise, over 15 min, to a solution of 1,4-dichlorobenzene (15.00 g, 102.0 mmol) and (dppp)Cl₂Ni (70 mg) in dry ether (70 mL) at 0

°C. The cooling bath was then removed and the reaction mixture allowed to warm to room temperature (~30 min). The mixture was then refluxed for 1 day, cooled to 0 °C, and carefully quenched with water (10 mL), followed by 2 M HCl (70 mL). The aqueous layer was extracted with ether (2×50 mL), the combined organic layer was then washed with water (30 mL), dried over MgSO₄, and filtered. The solvent was then removed from the filtrate *in vacuo*, and the crude product was dried at 100 °C under high vacuum (~20 mTorr) for 10 h to remove *n*-octane and *n*-octylbromide. The product was obtained as a white solid (35.00 g, 83 % yield). ¹H NMR (CDCl₃): δ 0.88 (t, 6H), 1.30 (m, 36H), 1.61 (m, 4H), 2.59 (t, 4H), 7.10 (s, 4H) ppm.

Synthesis of 2,5-Dibromo-1,4-di-*n*-dodecylbenzene (14). Bromine (2.5 mL, 44.2 mmol) was added rapidly to a stirring solution of **5** (5.00 g, 12.1 mmol) and iodine (15 mg) in dichloromethane (15 mL) at 0 °C and stirred under rigorous exclusion of light for 2 days at room temperature. Next, 20 % aq. KOH solution (20 mL) was added until the dark color of the solution disappeared. The dichloromethane was then removed under reduced pressure and the precipitate was washed with ethanol. The crude material was purified by recrystallization from ethanol to afford the pure product as a white solid (5.20 g, 75 % yield). ¹H NMR (CDCl₃): δ 0.88 (t, 6H), 1.33 (m, 36H), 1.59 (m, 4H), 2.67 (t, 4H), 7.37 (s, 2H) ppm.

Synthesis of 2,2''-Ethoxycarbonyl-2',5'-didodecyl-[1,1';4',1'']terphenyl (15). The reagent 2,5-dibromo-1,4-di-*n*-dodecylbenzene, (0.7 g, 1.22 mmol), 2-(ethoxycarbonyl)phenylboronic acid pinacol ester (1.01 g, 3.66 mmol) and Pd(PPh₃)₄ (150 mg) was dissolved in dry toluene (25 mL) under nitrogen. Deaerated K₂CO₃ solution (2.2 g dissolved in 2.5 mL of water and 5.0 mL of ethanol) and 0.4 mL of Aliquat 336 solution was added under nitrogen and the reaction mixture was refluxed for 1 day. The organic phase was filtered through

a plug of Celite and evaporated to dryness to give a semi-solid crude product. The crude product was purified by column chromatography (silica gel, chloroform:hexane (7:3) as eluent), to give the pure product as a colorless oil (0.70 g, 45 % yield). ^1H NMR (CDCl_3): δ 0.88 (t, 6H), 0.97 (t, 6H), 1.13-1.45 (m, 40H), 2.37 (m, 4H), 4.08 (q, 4H), 6.95 (d, 2H), 7.30 (t, 2H), 7.42 (q, 2H), 7.53 (q, 2H), 7.97(d, 2H) ppm. ^{13}C NMR (CDCl_3): δ 13.8, 14.3, 14.4, 22.9, 29.5, 29.6, 29.6, 29.7, 29.8, 30.9, 30.9, 31.8, 32.2, 32.9, 32.9, 60.8 (d), 127.1 (d), 129.3 (d), 130.2 (d), 131.0 (d), 131.5, 131.6 (d), 136.8 (d), 140.4 (d), 142.8 (d), 168.4 (d) ppm.; Anal. calcd. for ($\text{C}_{48}\text{H}_{70}\text{O}_4$): C, 81.08; H, 9.92, O, 9.00. Found: C, 81.39; H, 9.64, O, 9.30.

Synthesis of 5,11-didodecylindeno[1,2-b]fluorene-6,12-dione (1). The diester **15** (1.0 g, 1.39 mmol) was added to 61 mL of 80 % H_2SO_4 (prepared from 6.1 mL of H_2O and 54.9 mL of concentrated H_2SO_4), and the mixture was heated with stirring at 120 °C for 2 h, during which time the colorless oil turned dark red. The reaction mixture was next poured into ice and filtered to collect pale orange crystals. The crude product was suspended in a stirring sodium hydrogen carbonate solution, then in water, filtered again, and dried at 70 °C under vacuum overnight to give the diketone product as a pale orange solid (0.80 g, 93 % yield). ^1H NMR (CDCl_3): δ 0.89 (t, 6H), 1.27-1.69 (m, 40H), 3.43 (broad s, 4H), 7.32 (t, 2H), 7.53 (t, 2H), 7.67 (t, 4H). ^{13}C NMR (CDCl_3): δ 14.4, 22.9, 27.2, 29.6, 29.8, 29.9, 30.0, 30.1, 30.3, 32.2, 123.6, 124.2, 128.8, 134.9, 135.2, 135.9, 138.4, 143.2, 145.1, 194.6 ppm.; m.p: 123-124 °C; MS(EI) m/z (M^+): calcd for $\text{C}_{44}\text{H}_{58}\text{O}_2$, 618.9; found, 618.4. Anal. calcd. for ($\text{C}_{44}\text{H}_{58}\text{O}_2$): C, 85.38; H, 9.45. Found: C, 85.23; H, 9.46.

Synthesis of 2,2'-(5,11-didodecylindeno[1,2-b]fluorene-6,12-diyldiene) dimalononitrile (2). Indenofluorenedione **1** (0.100 g, 0.16 mmol) and malononitrile (0.106 g, 1.60 mmol) were

dissolved in dry chlorobenzene (20 mL) under nitrogen, and 0.26 mL of pyridine and 0.17 mL of TiCl_4 were added. The resulting mixture was refluxed overnight under nitrogen during which time the color of the solution became dark green. Upon cooling, 20 mL of water was added and the product extracted with chloroform. The organic phase was washed with water, dried over MgSO_4 , filtered, and evaporated to dryness. The crude product was purified by column chromatography on silica with chloroform as the eluent, affording the dimalononitrile product as a dark green solid (0.063 g, 55 %). ^1H NMR (CDCl_3): δ 0.87 (t, 6H), 1.27-1.59 (m, 40H), 3.20 (broad s, 2H), 3.60 (broad s, 2H), 7.54 (d, 2H, $J = 8.5$ Hz), 7.60 (m, 4H), 7.70 (d, 2H, $J = 8.5$ Hz), 8.41 (s, 2H) ppm. ^{13}C NMR (CDCl_3): δ 14.3, 22.9, 23.9, 29.6, 29.9, 30.3, 31.8, 32.1, 40.7, 119.9, 121.2, 123.0, 127.3, 132.6, 132.8, 132.9, 134.2, 134.3, 135.9, 139.4, 140.3, 141.4, 142.5, 150.2, 168.4 ppm; m.p: 134-135 °C; MS(EI) m/z (M^+): calcd for $\text{C}_{57}\text{H}_{58}\text{N}_4$, 715.0; found, 714.6. Anal. calcd. for ($\text{C}_{57}\text{H}_{58}\text{N}_4$): C, 83.99; H, 8.18; N, 7.84. Found: C, 83.69; H, 8.10; N, 7.65; IR (KBr): $\nu = 2220$ cm^{-1} ($\text{C}\equiv\text{N}$). No carbonyl vibrational feature is observed.

Synthesis of 2,8-dibromo-5,11-didodecylindeno[1,2-b]fluorene-6,12-dione (M1).

Indenofluorenedione **1** (0.50 g, 0.80 mmol) was dissolved in 45 mL of CHCl_3 . Next, 20.0 mL of bromine and 0.5 g of FeCl_3 as a catalyst was added. The reaction mixture was stirred at room temperature for 1 day under rigorous exclusion of light. Next, 20 % aq. KOH solution (20 mL) was added until the dark color of the solution disappeared. Chloroform was then removed under reduced pressure, and the resulting precipitate was collected by filtration and washed with water. The crude material was purified by column chromatography (silica gel, chloroform:hexane (7:3) as the eluent) giving the pure product as an orange solid (0.53 g, 85 % yield). ^1H NMR (CDCl_3): δ 0.89 (t, 6H), 1.27-1.59 (m, 40H), 3.29 (broad s, 4H), 7.43 (d, 2H), 7.61 (d, 2H), 7.69 (s, 2H).

^{13}C NMR (CDCl_3): δ 14.4, 22.9, 27.2, 29.6, 29.7, 29.8, 29.9, 29.9, 30.2, 32.0, 32.2, 123.1, 124.9, 127.5, 135.7, 136.3, 137.7, 138.6, 141.5, 144.7, 192.9 ppm.; m.p: 122-123 °C; MS(ESI) m/z (M^+): calcd for $\text{C}_{44}\text{H}_{56}\text{Br}_2\text{O}_2$, 776.7; found, 775.9. Anal. calcd. for ($\text{C}_{44}\text{H}_{56}\text{Br}_2\text{O}_2$): C, 68.04; H, 7.27. Found: C, 67.74; H, 6.92.

Synthesis of 2,2'-(2,8-dibromo-5,11-didodecylindeno[1,2-b]fluorene-6,12-diylidene) dimalononitrile (M2). Dibromotetraphenylenedione, **M1** (0.100 g, 0.128 mmol) and malononitrile (0.085 g, 1.28 mmol) were dissolved in dry chlorobenzene (20 mL) under nitrogen, and 0.21 mL of pyridine and 0.14 mL of TiCl_4 were added. The resulting mixture was refluxed overnight under nitrogen during which time the color of the solution became dark green. Upon cooling, 20 mL of water was added and the product extracted with chloroform. The organic phase was washed with water, dried over MgSO_4 , filtered, and evaporated to dryness. The crude product was purified by column chromatography on silica with chloroform as the eluent, affording the dimalononitrile product as a dark green solid (0.060 g, 50 %). ^1H NMR (CDCl_3): δ 0.87 (t, 6H), 1.27-1.59 (m, 40H), 3.20 (broad s, 2H), 3.60 (broad s, 2H), 7.57 (d, 2H, $J = 8.5$ Hz), 7.72 (d, 2H, $J = 8.5$ Hz), 8.43 (s, 2H) ppm. ^{13}C NMR (CDCl_3): δ 14.3, 22.9, 23.9, 29.6, 29.9, 30.3, 31.8, 32.1, 40.7, 119.9, 121.2, 123.0, 127.3, 132.6, 132.8, 132.9, 134.2, 134.3, 135.9, 139.4, 140.4, 141.9, 142.9, 151.2, 168.4 ppm; m.p: 136-137 °C; MS(EI) m/z (M^+): calcd for $\text{C}_{50}\text{H}_{56}\text{Br}_2\text{N}_4$, 872.8; found, 873.0. Anal. calcd. for ($\text{C}_{57}\text{H}_{60}\text{Br}_2\text{N}_4$): C, 68.80; H, 6.47; N, 6.42. Found: C, 68.67; H, 6.48; N, 6.27; IR (KBr): $\nu = 2220$ cm^{-1} ($\text{C}\equiv\text{N}$). No carbonyl vibrational feature is observed.

Synthesis of 2,8-bisthiophene-5,11-didodecylindeno[1,2-b]fluorene-6,12-dione (3). The reagent indenofluorenedione (**M1**) (0.200 g, 0.257 mmol), 2-tributylstannylthiophene (0.231 g,

0.618 mmol), and Pd(PPh₃)₄ (20 mg) in anhydrous toluene (8.0 mL) were heated at 110 °C under nitrogen overnight. The reaction mixture was cooled down to RT and evaporated to dryness. The crude product was purified by column chromatography on silica gel with CHCl₃/hexanes (7:3) as the eluent to give final product as a purple solid (121 mg, 60.0 % yield). ¹H NMR (CDCl₃): δ 0.88-1.66 (m, 46H), 3.41 (b s, 4H), 7.11(t, 2H), 7.39 (d, 2H, J = 3.0 Hz), 7.62(d, 2H, J = 7.5 Hz), 7.74 (d, 2H, J = 7.5 Hz), 7.88 (s, 2H) ppm. m.p: 205-206 °C; MS(MALDI-TOF) m/z (M⁺): calcd. for C₅₂H₆₂O₂S₂, 783.2; found, 783.0. Anal. calcd. for C₅₂H₆₂O₂S₂: C, 79.75; H, 7.98. Found: C, 79.60; H, 7.82.

Synthesis of 2,2'-(2,8- bithiophene -5,11-didodecylindeno[1,2-b]fluorene-6,12-diyldene) dimalononitrile (4). The reagent indenofluorenedione (**M2**) (0.224 g, 0.257 mmol), 2-tributylstannylthiophene (0.231 g, 0.618 mmol), and Pd(PPh₃)₄ (20 mg) in anhydrous toluene (8.0 mL) were heated at 110 °C under nitrogen overnight. The reaction mixture was cooled down to RT and evaporated to dryness. The crude product was purified by column chromatography on silica gel with CHCl₃/hexanes (7:3) as the eluent to give final product as a purple solid (136 mg, 60.0 % yield). ¹H NMR (CDCl₃): δ 0.88-1.66 (m, 46H), 3.40 (b s, 4H), 7.10(t, 2H), 7.29 (d, 2H, J = 3.0 Hz), 7.33 (d, 2H, J = 3.0 Hz), 7.62(d, 2H, J = 7.5 Hz), 7.74 (d, 2H, J = 7.5 Hz), 7.80 (s, 2H), 7.85 (s, 2H) ppm. m.p: 225-226 °C; MS(MALDI-TOF) m/z (M⁺): calcd. for C₅₈H₆₂N₄S₂, 879.3; found, 879.0. Anal. calcd. for C₅₈H₆₂N₄S₂: C, 79.23; H, 7.11. Found: C, 79.10; H, 7.20.

Synthesis of 2,7-bis(4,4,5,5-tetramethyl-1,3,2-dioxaborolane)-9,9-didodecylfluorene (16). *t*-BuLi (43.9 ml, 74.7 mmol, 1.7 M in pentane) was added over 30 min. to a stirring solution of 2,7-dibromo-9,9-didodecylfluorene (12.02 g, 18.2 mmol) in dry THF (90.0 mL) under nitrogen at -78 °C. The reaction mixture was stirred for another 30 min. at -78 °C, and 2-isopropoxy-

4,4,5,5-tetramethyl-1,3,2-dioxaborolane (22.2 mL, 108.6 mmol) was added dropwise to the resulting mixture and stirred overnight at room temperature. The solution was then quenched with water, the THF was evaporated, and the product was extracted with 200 mL ether. The organic phase was washed with water, dried over MgSO₄, filtered, and the filtrate evaporated to dryness to give the title compound as a white solid (12.36 g, 90 % yield). ¹H NMR (CDCl₃): δ 0.55 (t, 4H), 0.88 (m, 6H), 1.01 (m, 6H), 1.15-1.28 (m, 14H), 1.4 (s, 24 H), 2.01(t, 4H), 7.72 (2H, d, *J*=7.5 Hz), 7.75 (2H, s), 7.82 (2H, d, *J*=7.5 Hz) ppm.

Synthesis of Dimethyl 6,6'-(9,9-didodecylfluorene-2,7-diyl)bis(3-bromobenzoate) (17). A mixture of **16** (3.120 g, 4.14 mmol), methyl 2-iodo-benzoate (2.547 g, 9.52 mmol), and Aliquat 336 (0.800 g) was degassed 3 times with N₂ before 30.0 mL of dry toluene was added. Tetrakis(triphenylphosphine)palladium (0.50 g) and 1M aqueous sodium carbonate solution (1.80 g in 17 mL of water) which was already deaerated for 2 h was added under N₂. The mixture was stirred vigorously and heated at reflux for 3 days. The mixture was then allowed to cool to room temperature, and the organic phase was passed through a plug of Celite to remove palladium black, and the filtrates concentrated to dryness *in vacuo*. The product was purified by column chromatography (silica gel) with ethyl acetate: hexane (1:9) as the eluent, affording the pure product as a colorless oil (3.13 g, 96 % yield). ¹H NMR (CDCl₃): δ 0.83 (t, 6H), 1.10 (s, 24H), 1.95 (m, 4H), 3.61 (s, 6H), 7.22 (s, 2H), 7.28 (d, 2H, *J* = 7.5 Hz), 7.33 (d, 2H, *J* = 7.5 Hz), 7.67 (d, 2H, *J* = 7.5 Hz), 7.74 (m, 4H, *J* = 7.5 Hz), 7.97 (d, 2H, *J* = 7.5 Hz) ppm.

Synthesis of 6,6'-didodecylbisindenofluorene-12,15-dione (5). Diester **17** (0.288 g, 0.367 mmol) was added to 13 mL of 80 % H₂SO₄ (prepared from 1.3 mL of H₂O and 11.7 mL of concentrated H₂SO₄) and the mixture was heated with stirring at 165 °C for 3 h, during which

time the white solid turned dark red. The reaction mixture was next poured into ice and filtered to collect dark colored crystals. The collected product was then extracted into dichloromethane and was washed with sodium hydrogen carbonate solution and dried over MgSO_4 . After filtration and solvent evaporation, the crude product was purified by column chromatography on silica with chloroform: hexane (7:3) as the eluent, affording the product diketone as a yellow solid (0.181 g, 70 % yield). ^1H NMR (CDCl_3): δ 0.66 (br s, 6H), 0.85-1.24 (m, 40H), 2.08 (t, 4H), 7.45 (s, 2H), 7.47 (d, 2H, $J = 8.0$ Hz), 7.64 (d, 2H, $J = 8.0$ Hz), 7.74 (m, 4H, $J = 7.5$ Hz), 7.80 (s, 2H) ppm. ^{13}C NMR (CDCl_3): δ 14.3, 22.8, 24.1, 29.4, 30.2, 31.9, 40.5, 56.6, 115.2, 116.6, 121.9, 123.1, 127.8, 134.0, 136.8, 137.3, 141.7, 143.4, 144.0, 159.0, 191.9 ppm; m.p: 138-139 °C; MS(EI) m/z (M^+): calcd for $\text{C}_{51}\text{H}_{60}\text{O}_2\text{Br}_2$, 864.8; found, 864.3. Anal. calcd. for ($\text{C}_{51}\text{H}_{60}\text{O}_2\text{Br}_2$): C, 70.83; H, 6.99. Found: C, 70.44; H, 7.18. IR (KBr): $\nu = 1722\text{cm}^{-1}$ (C=O).

Synthesis of 2,2'-(6,6'-didodecylbisindenofluorene-12,15-diyldene) dimalononitrile (6).

Tetraphenylenedione, **5** (0.424 g, 0.60 mmol) and malononitrile (0.570 g, 8.66 mmol) were dissolved in dry DMSO (14 mL) and 0.5 mL of piperidine was added. The resulting mixture was stirred at 110 °C for 5 h during which time the color of the solution became dark red. Upon cooling, the product precipitated from the solution as brown solid which was collected by filtration, washed with isopropanol, and dried in vacuo. The crude product was purified by column chromatography on silica with chloroform as the eluent, affording the dimalononitrile product as a purple solid (0.337 g, 70 % yield). ^1H NMR (CDCl_3): δ 0.64 (br s, 6H), 0.85-1.27 (m, 40H), 2.12 (t, 4H), 7.46 (s, 2H), 7.50 (d, 2H, $J = 8.0$ Hz), 7.67 (t, 2H, $J = 8.0$ Hz), 7.87 (t, 2H, $J = 8.0$ Hz), 8.52 (d, 2H, $J = 8.0$ Hz), 8.83 (s, 2H) ppm. ^{13}C NMR (CDCl_3): δ 14.2, 22.4,

24.1, 29.6, 30.1, 30.2, 31.7, 40.3, 56.7, 113.2, 112.2, 115.5, 117.9, 122.1, 123.2, 130.0, 133.9, 136.7, 137.5, 140.2, 141.0, 141.9, 157.9, 159.7 ppm; MS(EI) m/z (M^+): calcd for $C_{57}H_{62}N_4$, 803.1; found, 803.3; m.p: 251-252 °C; Anal. calcd. for ($C_{57}H_{62}N_4$): C, 85.24; H, 7.78; N, 6.98. Found: C, 85.49; H, 7.80; N, 6.88. IR (KBr): $\nu = 2220\text{ cm}^{-1}$ ($C\equiv N$). No carbonyl vibrational feature is observed.

Synthesis of 2,10-dibromo-6,6'-didodecylbisindenofluorene-12,15-dione (M3). To a solution of **5** (0.271 g, 0.383 mmol) in $CHCl_3/HOAc$ (5:1) ($V_t = 24.0\text{ mL}$) was added bromine (Br_2 ; 123.0 mg, 0.766 mmol) in one portion. The mixture was stirred at room temperature for 10 h and water (50 mL) was then added. The mixture was next extracted with chloroform (3×50 mL). The combined organic phase was washed with water (50 mL), KOH solution, and dried over $MgSO_4$. After filtration, the chloroform was removed, and the product was purified by silica gel column chromatography using chloroform as the eluent to give an orange solid (0.265 g, 80 % yield). 1H NMR ($CDCl_3$): δ 0.65 (br s, 6H), 0.85-1.25 (m, 40H), 2.09 (t, 4H), 7.45 (s, 2H), 7.51 (d, 2H, $J = 8.0\text{ Hz}$), 7.67 (d, 2H, $J = 8.0\text{ Hz}$), 7.73 (s, 2H) ppm, 7.83 (s, 2H) ppm. ^{13}C NMR ($CDCl_3$): δ 14.3, 22.8, 24.1, 29.4, 30.2, 31.9, 40.5, 56.6, 115.2, 116.6, 121.9, 123.1, 127.8, 134.0, 136.8, 137.3, 142.7, 142.4, 144.0, 161.0, 190.9 ppm; m.p: 136-137 °C; MS(ESI) m/z (M^+): calcd for $C_{51}H_{60}Br_2O_2$, 864.8; found, 864.6. Anal. calcd. for ($C_{51}H_{60}Br_2O_2$): C, 70.83; H, 6.99. Found: C, 70.74; H, 6.92.

Synthesis of 2,2'-(2,10-Dibromo-6,6'-didodecylbisindenofluorene-12,15-diyldene) dimalononitrile (M4). Dibromotetraphenylenedione, **M3** (0.520 g, 0.60 mmol) and malononitrile (0.570 g, 8.66 mmol) were dissolved in dry DMSO (14 mL) and 0.5 mL of piperidine was added. The resulting mixture was stirred at 110 °C for 5 h during which time the

color of the solution became dark red. Upon cooling, the product precipitated from the solution as brown solid which was collected by filtration, washed with isopropanol, and dried in vacuo. The crude product was purified by column chromatography on silica with chloroform as the eluent, affording the dimalononitrile product as a purple solid (0.37 g, 65 % yield). ^1H NMR (CDCl_3): δ 0.67 (br s, 6H), 0.85-1.27 (m, 40H), 2.08 (t, 4H), 7.50 (s, 2H), 7.51 (d, 2H, $J = 8.0$ Hz), 7.67 (d, 2H, $J = 8.0$ Hz), 8.52 (s, 2H), 8.83 (s, 2H) ppm. ^{13}C NMR (CDCl_3): δ 14.2, 22.4, 24.1, 29.6, 30.1, 30.2, 31.7, 40.3, 56.7, 113.2, 113.2, 115.5, 118.9, 122.1, 123.2, 130.0, 133.9, 136.7, 137.5, 141.2, 141.4, 141.9, 158.9, 159.7 ppm; MS(EI) m/z (M^+): calcd for $\text{C}_{57}\text{H}_{60}\text{Br}_2\text{N}_4$, 960.9; found, 960.3; m.p: 252-253 $^\circ\text{C}$; Anal. calcd. for ($\text{C}_{57}\text{H}_{60}\text{Br}_2\text{N}_4$): C, 71.25; H, 6.29; N, 5.83. Found: C, 71.49; H, 6.42; N, 5.59. IR (KBr): $\nu = 2222\text{ cm}^{-1}$ ($\text{C}\equiv\text{N}$). No carbonyl vibrational feature is observed.

Synthesis of 2,10-dithiophene-6,6'-didodecylbisindenofluorene-12,15-dione (7). The reagent Dibromotetraphenylenedione **M3** (0.464g, 0.531 mmol), 2-tributylstannylthiophene (0.476 g, 1.275 mmol), and $\text{Pd}(\text{PPh}_3)_4$ (50 mg) in anhydrous toluene (20.0 mL) were heated at 110 $^\circ\text{C}$ under nitrogen overnight. The reaction mixture was cooled down to RT and evaporated to dryness. The crude product was purified by column chromatography on silica gel with CHCl_3 /hexanes (7:3) as the eluent to give final product as a yellow solid (0.302 g, 65% yield). ^1H NMR (CDCl_3): δ 0.88-1.66 (m, 46H), 2.13 (t, 4H), 7.15 (t, 2H), 7.36 (d, 2H, $J = 4.5$ Hz), 7.44 (d, 2H, $J = 3.0$ Hz), 7.50 (s, 2H), 7.61 (d, 2H, $J = 7.5$ Hz), 7.78(d, 2H, $J = 7.5$ Hz), 7.97 (s, 2H), 8.03 (s, 2H) ppm. m.p: 180-181 $^\circ\text{C}$; MS(MALDI-TOF) m/z (M^+): calcd. for $\text{C}_{52}\text{H}_{62}\text{O}_2\text{S}_2$, 871.3; found, 871.9. Anal. calcd. for $\text{C}_{52}\text{H}_{62}\text{O}_2\text{S}_2$: C, 81.33; H, 7.64. Found: C, 81.15; H, 7.76.

Synthesis of 2,2'-(2,10-Dithiophene-6,6'-didodecylbisindenofluorene-12,15-diylidene)dimalononitrile (8). The reagent dibromotetraphenylenedimalononitrile **M4** (180 mg, 0.187 mmol), 2-tributylstannylthiophene (168 mg, 0.449 mmol), and Pd(PPh₃)₄ (15 mg) in anhydrous toluene (8.0 mL) were heated at 110 °C under nitrogen overnight. The reaction mixture was cooled down to RT and evaporated to dryness. The crude product was purified by column chromatography on silica gel with CHCl₃/hexanes (7:3) as the eluent to give final product as a yellow solid (0.114 g, 70 % yield). ¹H NMR (CDCl₃): δ 0.88-1.66 (m, 46H), 2.10 (t, 4H), 7.13 (t, 2H) 7.35 (d, 2H, J = 4.5 Hz), 7.44 (d, 2H, J = 3.5 Hz), 7.51 (s, 2H), 7.75(d, 2H, J = 8.0 Hz), 8.69 (s, 2H), 8.78 (s, 2H) ppm. m.p: 280-281 °C; MS(MALDI-TOF) m/z (M⁺): calcd. for C₅₂H₆₂O₂S₂, 871.3; found, 870.8. Anal. calcd. for C₅₂H₆₂O₂S₂: C, 81.33; H, 7.64. Found: C, 79.80; H, 7.74.

Synthesis of 4,4''-dibromo-2,2''-Methoxycarbonyl-[1,1';4',1'']terphenyl (18). A mixture of 1,4-benzenediboronic acid bis(pinacol) ester (4.40 g, 13.33 mmol), methyl 2-iodo-5-bromobenzoate (9.95 g, 29.18 mmol), and Aliquat 336 (1.60 mL) was degassed 3 times with N₂ before 90.0 mL of dry toluene was added. Tetrakis(triphenylphosphine)palladium (1.50 g, 1.30 mmol) and 1M aqueous sodium carbonate solution (5.73 g in 54.0 mL of water) which was already deaerated for 2 h were then added under N₂. The mixture was stirred vigorously and heated at reflux for 2 days. The mixture was then allowed to cool to room temperature, the organic phase was passed through a plug of Celite to remove palladium black, and the filtrate was concentrated to dryness *in vacuo*. The product was purified by column chromatography (silica gel) with chloroform as the eluent, affording the pure product as a white solid (6.00 g,

89% yield). $^1\text{H NMR}$ (CDCl_3): δ 3.72 (s, 6H), 7.32(d, 2H, $J = 8.0$ Hz), 7.33 (s, 4H), 7.69(d, 2H, $J = 8.0$ Hz), 8.01 (s, 2H) ppm.

Synthesis of 2,8-dibromo-indeno[1,2-b]fluorene-6,12-dione (19). The diester **1** (0.50 g, 0.99 mmol) was added to 50.0 mL of 80 % H_2SO_4 (prepared from 10.0 mL of H_2O and 40.0 mL of concentrated (99.99 %) H_2SO_4), and the mixture was heated with stirring at 120 °C for 10 h, during which time the white solid turned dark red. The reaction mixture was next poured into ice and filtered to collect the red crystals. The collected product was then washed with sodium hydrogen carbonate solution and water. The product was collected by filtration (0.40 g, 92%). The crude product was used for the next step without any further purification. m.p: > 300 °C. MS(MALDI-TOF) m/z (M^+): calcd for $\text{C}_{20}\text{H}_8\text{O}_2\text{Br}_2$, 440.1; found, 440.7. Anal. calcd. for $\text{C}_{20}\text{H}_8\text{O}_2\text{Br}_2$: C, 54.58; H, 1.83 Found: C, 54.12; H, 1.72.

Synthesis of 2,8-di-3-dodecylthiophene-indeno[1,2-b]fluorene-6,12-dione (9). The reagent 2-tributylstannyl-3-dodecylthiophene (**22**) (0.320 g, 0.591 mmol), **19** (0.120 g, 0.273 mmol), and $\text{Pd}(\text{PPh}_3)_2\text{Cl}_2$ (30.0 mg, 0.043 mmol) in anhydrous DMF (12.0 mL) were heated at 125 °C under nitrogen overnight. The reaction mixture was cooled down to RT and evaporated to dryness. The crude product was purified by column chromatography on silica gel with CHCl_3 /hexanes (7:3) as the eluent to give final product as a purple solid (70.0 mg, 35% yield). $^1\text{H NMR}$ (CDCl_3): δ 0.88-1.66 (m, 46H), 2.70 (t, 4H), 7.02 (d, 2H, $J = 4.5$ Hz), 7.29 (d, 2H, $J = 4.5$ Hz), 7.59 (d, 2H, $J = 7.5$ Hz), 7.61(d, 2H, $J = 7.5$ Hz), 7.74 (s, 2H), 7.81 (s, 2H) ppm. $^{13}\text{C NMR}$ (CDCl_3): δ 14.4, 22.96, 29.0, 29.6, 29.7, 29.8, 29.9, 30.0, 31.2, 32.2, 116.3, 121.0, 124.7, 125.5, 130.1, 134.6, 136.1, 136.4, 136.8, 139.8, 140.0, 142.3, 145.9, 192.8 ppm.; m.p: 152-153 °C; MS(MALDI-

TOF) m/z (M^+): calcd. for $C_{52}H_{62}O_2S_2$, 783.2; found, 783.0. Anal. calcd. for $C_{52}H_{62}O_2S_2$: C, 79.75; H, 7.98. Found: C, 79.50; H, 7.89.

Synthesis of 2,8-di-3-dodecylthiophene-indeno[1,2-b]fluorene-6,12-dimalononitrile (10).

A mixture of **9** (50.0 mg, 0.064 mmol) and malononitrile (60.0 mg, 0.91 mmol) was dissolved in dry chlorobenzene (5.0 mL) under nitrogen, and pyridine (0.100 mL, 1.24 mmol) and $TiCl_4$ (0.070 mL, 0.64 mmol) were added. The resulting mixture was stirred at 110 °C for 5 h under nitrogen during which time the color of the solution became dark green. Upon cooling, 20.0 mL of water was added and the product extracted with chloroform. The organic phase was washed with water, dried over $MgSO_4$, filtered, and evaporated to dryness. The crude product was then purified by column chromatography on silica gel with chloroform as the eluent, affording the dimalononitrile product as a dark green solid (22.5 mg, 40%). 1H NMR ($CDCl_3$): δ 0.88-1.67 (m, 46H), 2.74 (t, 4H), 7.05 (d, 2H, $J = 4.0$ Hz), 7.33 (d, 2H, $J = 4.0$ Hz), 7.66 (d, 2H, $J = 7.5$ Hz), 7.71 (d, 2H, $J = 7.5$ Hz), 8.52 (s, 2H), 8.60 (s, 2H) ppm. ^{13}C NMR ($CDCl_3$): δ 14.4, 22.9, 29.2, 29.6, 29.7, 29.8, 29.9, 31.1, 32.2, 112.9, 113.3, 118.4, 121.5, 125.1, 127.8, 130.3, 134.7, 134.7, 135.8, 136.1, 137.3, 139.6, 139.7, 140.5, 143.4, 159.8 ppm.; m.p: 232-233 °C; MS(EI) m/z (M^+): calcd for $C_{58}H_{62}S_2N_4$, 879.3; found, 879.5. Anal. calcd. for $C_{58}H_{62}S_2N_4$: C, 79.23; H, 7.11; N, 6.37. Found: C, 79.07; H, 7.15; N, 6.35; IR (KBr): $\nu = 2225$ cm^{-1} ($C\equiv N$). No carbonyl peak is observed.

Synthesis of 2,8-di-5-bromo-3-dodecylthiophene-indeno[1,2-b]fluorene-6,12-dione (M5).

To a solution of **9** (0.30 g, 0.383 mmol) in $CHCl_3/HOAc$ (5:1) ($V_t = 24.0$ mL) was added bromine (Br_2 ; 123.0 mg, 0.766 mmol) in one portion. The mixture was stirred at room temperature for 10 h and water (50 mL) was then added. The mixture was next extracted with

chloroform (3×50 mL). The combined organic phase was washed with water (50 mL), KOH solution, and dried over MgSO₄. After filtration, the chloroform was removed, and the product was purified by silica gel column chromatography using chloroform as the eluent to give a dark green solid (0.340 g, 95% yield). ¹H NMR (CDCl₃): δ 0.87-1.61 (m, 46H), 2.70 (t, 4H), 6.96 (s, 2H), 7.56 (d, 2H, J = 7.5 Hz), 7.61(d, 2H, J = 7.5 Hz), 7.69 (s, 2H), 7.84 (s, 2H) ppm. MS(EI) m/z (M⁺): calcd for C₅₂H₆₀Br₂O₂S₂, 941.0; found, 941.1. Anal. calcd. for (C₅₂H₆₀Br₂O₂S₂): C, 66.37; H, 6.43. Found: C, 66.34; H, 6.43.

Synthesis of 2, 8-di-5-bromo-3-dodecylthiophene-indeno[1,2-b]fluorene-6,12-dimalononitrile (M6). A mixture of **M5** (230.0 mg, 0.245 mmol) and malononitrile (230.0 mg, 3.48 mmol) was dissolved in dry chlorobenzene (20.0 mL) under nitrogen, and pyridine (0.40 mL, 4.94 mmol) and TiCl₄ (0.30 mL, 2.73 mmol) were added. The resulting mixture was stirred at 110 °C for 5 h under nitrogen during which time the color of the solution became dark green. Upon cooling, 20.0 mL of water was added and the product was extracted with chloroform. The organic phase was washed with water, dried over MgSO₄, filtered, and evaporated to dryness. The crude product was purified by column chromatography on silicagel with chloroform as the eluent, affording the product as a dark green solid (120.0 mg, 48% yield). ¹H NMR (CDCl₃): δ 0.89-1.62 (m, 46H), 2.66 (t, 4H), 7.00 (s, 2H), 7.59 (d, 2H, J = 7.5 Hz), 7.71 (d, 2H, J = 7.5 Hz), 8.47 (s, 2H), 8.62 (s, 2H) ppm. MS(EI) m/z (M⁺): calcd for C₅₈H₆₀Br₂S₂N₄, 1037.1; found, 1037.4. Anal. calcd. for C₅₈H₆₀Br₂S₂N₄: C, 67.17; H, 5.83; N, 5.40. Found: C, 66.76; H, 5.82; N, 5.18; IR (KBr): ν = 2225 cm⁻¹ (C≡N). No carbonyl peak is observed.

Synthesis of 2-bromo-3-dodecylthiophene (21). To a solution of 3-dodecylthiophene (5.00 g, 19.8 mmol) in CHCl₃/HOAc (1:1) (V_t = 20.0 mL) at 0 °C was added NBS (3.52 g, 19.8 mmol)

in portions over a period of 45 min. The reaction mixture was stirred for 1 h at 0 °C, and overnight at room temperature. The reaction mixture was then poured into water (50.0 mL) and extracted with chloroform (3×50.0 mL). The combined organic phase was washed with water (50.0 mL), NaOH solution, and dried over MgSO₄. After filtration through Celite, the chloroform was removed *in vacuo*, and the product was obtained as a colorless oil (6.05 g, 93% yield). ¹H NMR (CDCl₃): δ 0.84-1.54 (m, 23H), 2.53 (t, 2H), 6.76 (d, 1H, J = 4.5 Hz), 7.15 (d, 1H, J = 4.5 Hz).

Synthesis of 2-tributylstannyl-3-dodecylthiophene (22). To magnesium turnings (0.160 g, 6.6 mmol) in anhydrous THF (8.0 mL), heated to maintain a mild reflux, was added dropwise 2-bromo-3-dodecylthiophene (**21**; 2.00 g, 6.0 mmol). The reaction mixture was refluxed for 2 h before being transferred to a solution of tributyltin chloride (1.80 mL, 6.41 mmol) in 10.0 mL of anhydrous THF at -78 °C. The mixture was allowed to warm to room temperature and stirred overnight before being poured into water. The aqueous layer was extracted with hexanes, and the combined organic phase was washed with brine and dried over magnesium sulfate. After filtration, the solvent was removed *in vacuo* to yield the product as a yellow liquid (3.10 g, 95% yield). ¹H NMR (CDCl₃): δ 0.90-1.63 (m, 50H), 2.62 (t, 2H), 7.12 (d, 1H, J = 4.5 Hz), 7.55 (d, 1H, J = 4.5 Hz).

Synthesis of 4,4'-didodecyl-2,2'-bithiophene (24). *n*-BuLi (7.04 mL, 2.5 M in hexanes) was added dropwise to a stirring solution of 3-dodecylthiophene (4.000 g, 15.8 mmol) and N,N,N',N'-tetramethylethylenediamine (2.75 mL, 17.6 mmol) in 80.0 mL of dry ether at -78 °C. The solution was then warmed to room temperature and refluxed for 1 h. After cooling down to -78 °C, CuCl₂ (2.640 g, 19.6 mmol) was added in one portion. The reaction mixture was stirred

overnight, during which time the temperature rose to room temperature. The reaction mixture was quenched with water and extracted with chloroform, washed with water, dried over MgSO_4 , filtered, and the filtrate was evaporated to dryness. The crude product was purified by column chromatography on silica gel with hexanes as the eluent to yield a mixture of 4,4'- and 3,3'-didodecylthiophene (~15 % of the mixture by ^1H NMR). Recrystallization from an acetone:ethanol (1:1) mixture gave the pure product as a white solid (2.200 g, 55% yield). ^1H NMR (CDCl_3): δ 0.91 (t, 6H), 1.33 (m, 36H), 1.66 (q, 4H), 2.60 (t, 4H), 6.80 (s, 2H), 7.01 (s, 2H) ppm.

Synthesis of 4,4'-didocecyl-5,5'-trimethylstannyl-2,2'-bithiophene (26). To a solution of **24** (1.00 g, 2.0 mmol) in 30.0 mL of THF was added dropwise a 2.5 M solution of *n*-butyllithium in hexane (2.0 mL, 5.0 mmol) at -78 °C. The solution was stirred at -78 °C for 30 min and at room temperature for another 1 h. The solution was then cooled to -78 °C, and a 1.0 M solution of trimethyltin chloride in THF (6.0 mL, 6.0 mmol) was added in one portion. The solution was warmed to room temperature and 30.0 mL of water and 30.0 mL of ethyl acetate were added. The organic layer was washed twice with 30 mL of water and dried over magnesium sulfate. After filtration, the solvent was removed from the filtrate *in vacuo* to yield the product as a yellow oil (0.60 g, 72% yield). ^1H NMR (CDCl_3 , d): 0.40 (s, 18H), 0.95 (t, 6H), 1.33 (br, 36H), 1.60 (q, 4H), 2.61 (t, 4H), 7.18 (s, 2H).

Synthesis of 4,4'-didocecyl-5-bromo-2,2'-bithiophene (27). To a solution of 4,4'-didodecyl-2,2'-bithiophene (**24**) (0.100 g, 0.199 mmol) in $\text{CHCl}_3/\text{HOAc}$ (1:1) ($V_t = 2.0$ mL) at 0 °C was added NBS (35.7 mg, 0.199 mmol) in portions over a period of 45 min. The reaction mixture was stirred for 1 h at 0 °C, and overnight at room temperature. The reaction mixture was

then poured into water (50.0 mL) and extracted with chloroform (3×50.0 mL). The combined organic phase was washed with water (50.0 mL), NaOH solution, and dried over MgSO₄. After filtration through Celite, the chloroform was removed *in vacuo*, and the product was obtained as a colorless oil after column chromatography using hexanes as the eluent (98.0 mg, 85% yield). ¹H NMR (CDCl₃): δ 0.84-1.54 (m, 46H), 2.57 (m, 4H), 6.81 (s, 1H), 6.84 (s, 1H), 6.94 (s, 1H).

Synthesis of 4,4'-didocecyl-5-trimethylstannyl-2,2'-bithiophene (28). To a solution of **27** (100 mg, 0.172 mmol) in 4.0 mL of THF was added dropwise a 2.5 M solution of *n*-butyllithium in hexane (0.076 mL, 0.189 mmol) at -78 °C. The solution was stirred at -78 °C for 1 h. 1.0 M solution of trimethyltin chloride in THF (0.20 mL, 0.20 mmol) was then added in one portion. The solution was warmed to room temperature and 10.0 mL of water and 10.0 mL of diethylether were added. The organic layer was washed twice with 20 mL of water and dried over magnesium sulfate. After filtration, the solvent was removed from the filtrate *in vacuo* to yield the product as a yellow oil (0.103 g, 90% yield). ¹H NMR (CDCl₃): δ 0.84-1.64 (m, 46H), 2.58 (m, 4H), 6.77 (s, 1H), 6.99 (s, 1H), 7.13 (s, 1H).

Synthesis of 2,8-di-4,4'-didodecyl-2,2'-bithiophene-indeno[1,2-b]fluorene-6,12-dione (11). The reagent 5-trimethylstannyl-4,4'-didodecyl-2,2'-bithiophene (**28**) (0.457 g, 0.686 mmol), **19** (0.140 g, 0.312 mmol), and Pd(PPh₃)₂Cl₂ (45.0 mg, 0.064 mmol) in anhydrous DMF (25.0 mL) were heated at 125 °C under nitrogen overnight. The reaction mixture was cooled down to RT and evaporated to dryness. The crude product was purified by column chromatography on silica gel with CHCl₃/hexanes (4:6) as the eluent to give final product as a green solid (100.0 mg, 25% yield). ¹H NMR (CDCl₃): δ 0.88-1.66 (m, 92H), 2.60 (t, 4H), 2.67(t, 4H), 6.83 (s, 2H), 7.03 (s, 2H), 7.05 (d, 2H), 7.61(q, 4H), 7.77 (s, 2H), 7.83 (s, 2H) ppm. m.p:

96-97 °C; MS(MALDI-TOF) m/z (M^+): calcd. for $C_{52}H_{62}O_2S_2$, 1284.1; found, 1284.0. Anal. calcd. for $C_{52}H_{62}O_2S_2$: C, 78.57; H, 8.95. Found: C, 78.20; H, 8.60.

Synthesis of 2,8-di-4,4'-didodecyl-2,2'-bithiophene-indeno[1,2-b]fluorene-6,12-dimalononitrile (12). A mixture of **11** (40.0 mg, 0.031 mmol) and malononitrile (35.0 mg, 0.53 mmol) was dissolved in dry chlorobenzene (3.0 mL) under nitrogen, and pyridine (0.06 mL) and $TiCl_4$ (0.04 mL, 0.64 mmol) were added. The resulting mixture was stirred at 110 °C for 5 h under nitrogen during which time the color of the solution became dark green. Upon cooling, 20.0 mL of water was added and the product extracted with chloroform. The organic phase was washed with water, dried over $MgSO_4$, filtered, and evaporated to dryness. The crude product was then purified by column chromatography on silica gel with chloroform as the eluent, affording the dimalononitrile product as a dark green solid (25 mg, 58%). 1H NMR ($CDCl_3$): δ 0.88-1.66 (m, 92H), 2.58 (t, 4H), 2.71(t, 4H), 6.83 (s, 2H), 7.05 (s, 2H), 7.06 (d, 2H), 7.63 (d, 2H, $J = 8.0$ Hz), 7.68(d, 2H, $J = 8.0$ Hz), 8.51 (s, 2H), 8.56 (s, 2H) ppm. m.p: 96-97 °C; MS(MALDI-TOF) m/z (M^+): calcd. for $C_{52}H_{62}O_2S_2$, 1380.1; found, 1380.0. Anal. calcd. for $C_{52}H_{62}O_2S_2$: C, 78.32; H, 8.33. Found: C, 78.55; H, 8.49.

Synthesis indenofluorenedionebithiophene copolymer (P3). 2,5-Bis(tributylstannyl)thiophene (0.095 g, 0.128mmol), 2,8-Dibromo-5,11-didodecylindeno[1,2-b]fluorene-6,12-dione **M1** (0.100 g, 0.128 mmol) and $Pd(PPh_3)_4$ (10 mg) in anhydrous toluene (5 mL) were heated at 110 °C with stirring under nitrogen for two days. The reaction mixture was allowed to cool to room temperature, and was poured into methanol (300 mL). The resulting solids were subjected to Soxhlet extraction for two days in acetone, then dissolved in chlorobenzene by Soxhlet extraction, precipitated in methanol (2 times), and filtered to give the

tetraphenylenedimalononitrile copolymer as a black solid (78.0 mg, 40 %). $^1\text{H NMR}$ (CDCl_3): δ 0.78-1.67 (m, 46H), 3.40(b, 4H), 7.39 (br m, 4H), 7.45 (br s, 2H), 7.63 (br s, 2H), 7.88 (br s, 2H) ppm. Anal. calcd. for $\text{C}_{52}\text{H}_{60}\text{O}_2\text{S}_2$: C, 79.95; H, 7.74; Found: C, 79.65; H, 7.50. GPC (HT in TCB): $M_n = 9400 \text{ g mol}^{-1}$, $M_w = 11,200 \text{ g mol}^{-1}$, and $D = 1.20$ (against PS standard).

Synthesis of tetraphenylenedionebithiophene copolymer (P7). 2,5-Bis(tributylstannyl)bithiophene (0.143 g, 0.193 mmol), dibromotetraphenylenedione **M3** (0.145 g, 0.193 mmol), and $\text{Pd}(\text{PPh}_3)_4$ (25 mg) in anhydrous toluene (10 mL) were heated at 110°C with stirring under nitrogen for two days. The reaction mixture was allowed to cool to room temperature, and was poured into methanol (300 mL). The resulting solids were subjected to Soxhlet extraction for two days in acetone, then dissolved in chlorobenzene by Soxhlet extraction,, precipitated in methanol (2 times), and filtered to give the tetraphenylenedimalononitrile copolymer as a black solid (100 mg, 35 %). $^1\text{H NMR}$ (CDCl_3): δ 0.70-1.65 (br m, 46H), 2.67 (br, 4H), 7.00 (br, 4H), 7.45 (br, 2H), 7.65 (br, 4H), 7.82 (br, 4H) ppm. Anal. calcd. for $\text{C}_{59}\text{H}_{64}\text{S}_2\text{O}_2$: C, 81.51; H, 7.43; Found: C, 81.20; H, 7.10. GPC (HT in TCB): $M_n = 6200 \text{ g mol}^{-1}$, $M_w = 9,400 \text{ g mol}^{-1}$, and $D = 1.52$ (against PS standard).

Synthesis of 2,8-di-4,3'-didodecyl-2,2'-bithiophene-indeno[1,2-b]fluorene-6,12-dimalononitrile copolymer (P13). A 20 mL microwave glass vial was charged with a stirrer bar, 2,8-di-5-bromo-3-dodecylthiophene-indeno[1,2-b]fluorene-6,12-dimalononitrile (**22**) (100.0 mg, 0.096 mmol), 4,4'-didocecy-5,5'-trimethylstannyl-2,2'-bithiophene (**26**; 80.0 mg, 0.096 mmol), tris(dibenzylideneacetone)dipalladium(0) (2.0 mg, 0.002 mmol), tri-(*o*-tolylphosphine) (2.5 mg, 0.008 mmol) and chlorobenzene (2.0 mL). The glass vial was purged with nitrogen, securely sealed, and heated in a microwave reactor. A temperature ramp was used such that the

vial was heated with stirring at 140 °C for 120 seconds, then at 160 °C for 120 sec, and finally at 180 °C for 900 seconds. The power was 300 W during the reaction. After cooling to 50 °C, the crude product was precipitated with methanol. The precipitate was collected by filtration, dissolved in THF, filtered through a 0.45 µm filter, and precipitated with methanol again. This dissolution/precipitation procedure was repeated three more times. The final collected polymer was subjected to Soxhlet extraction (with acetone and methanol) and dried overnight at 100 °C to give 79.6 mg product as a dark-colored solid (60% yield). ¹H NMR (CDCl₃): δ 0.88-1.62 (br m, 92H), 2.57 (br, 4H), 2.74 (br, 4H), 7.00 (br, 2H), 7.42 (br, 2H), 7.65 (br, 4H), 8.55 (br, 4H) ppm. Anal. calcd. for C₈₀H₁₁₂S₄N₄: C, 78.43; H, 8.20; N, 4.06. Found: C, 78.87; H, 8.42; N, 3.65. GPC (HT in TCB) M_w = 23273 g/mol, M_n = 6685 g/mol, PDI = 3.48 (against PS standard).

Synthesis of tetraphenylenedimalononitrile homopolymer (P6). Ni(COD)₂ (211 mg, 0.746 mmol), 2,2'-bipyridyl (116.5 mg, 0.746 mmol), and 1,5-cyclooctadiene (COD, 0.091 mL, 0.746 mmol) were mixed in dry DMF (5 mL) and dry toluene (1.6 mL) in a glove box. The purple solution was heated to 80°C for 30 minutes. Dibromotetraphenylenedimalononitrile 10 (300 mg, 0.311 mmol) in 6 mL of dry toluene was added. The solution was stirred under argon for 1 day, and bromobenzene (1.0 mL) was added. The reaction mixture was poured in methanol and filtered. The resulting solids were subjected to Soxhlet extraction for 2 days in acetone, dissolved in THF, precipitated in methanol (3 times), and filtered to give the tetraphenylenedimalononitrile homopolymer as a yellow solid (125 mg, 50 %). ¹H NMR (CDCl₃): δ 0.75-1.24 (br m, 46H), 2.12 (br s, 4H), 7.50 (br m, 4H), 7.67 (br s, 2H), 8.55 (br s, 2H), 8.79 (br s, 2H) ppm. Anal. calcd. for C₅₇H₆₀N₄: C, 85.45; H, 7.55; N, 7.00. Found: C, 83.85;

H, 7.63; N, 6.77. GPC (HT in TCB): $M_n = 8037 \text{ g mol}^{-1}$, $M_w = 12,455 \text{ g mol}^{-1}$, and $D = 1.55$ (against PS standard).

Synthesis of tetraphenylenedimalononitrilebithiophene copolymer (P8). 2,5-Bis(tributylstannyl)bithiophene (0.45 mmol, 0.30 g), dibromotetraphenylenedimalononitrile (0.45 mmol, 0.43 g), and $\text{Pd}(\text{PPh}_3)_2\text{Cl}_2$ (40 mg) in anhydrous toluene (10 mL) were heated at 80 °C with stirring under nitrogen for two days. The reaction mixture was allowed to cool to room temperature, and was poured into methanol (300 mL). The resulting solids were subjected to Soxhlet extraction for two days in acetone, then dissolved in chloroform, precipitated in methanol (3 times), and filtered to give the tetraphenylenedimalononitrile copolymer as a black solid (210 mg, 50 %). $^1\text{H NMR}$ (CDCl_3): δ 0.74-1.23 (br m, 46H), 2.12 (br s, 4H), 7.15 (br, 4H), 7.48 (br m, 4H), 7.67 (br s, 2H), 8.51 (br s, 2H), 8.72 (br s, 2H) ppm. Anal. calcd. for $\text{C}_{65}\text{H}_{64}\text{S}_2\text{N}_4$: C, 80.87; H, 6.69; N, 5.80. Found: C, 81.35; H, 6.70; N, 5.60. GPC (HT in TCB): $M_n = 8100 \text{ g mol}^{-1}$, $M_w = 10,500 \text{ g mol}^{-1}$, and $D = 1.30$ (against PS standard).

3.2.3. Single-Crystal Structure Determination.

Single crystals of 7, M2, and M4 were grown by slow evaporation of chloroform solution and slow diffusion of methanol into chloroform solution, respectively. X-ray single crystal diffraction measurements were performed on a Bruker CCD area detector instrument with graphite-monochromated $\text{MoK}\alpha$ (0.71073 Å) radiation. The data were collected at 153(2)K, and the structures were solved by direct methods and expanded using Fourier techniques.

3.2.4 Device Fabrication and Thin Film Characterization.

Prime grade n-doped silicon wafers (100) having a 300 nm thermally grown oxide layer (Process Specialties Inc.) were used as device substrates. These were rinsed with water,

methanol, and acetone before film deposition. Trimethylsilyl functionalization of the Si/SiO₂ surface was carried out by exposing the silicon wafers to hexamethyldisilazane (HMDS) vapor at room temperature in a closed container under nitrogen overnight. Polymer films were spin-coated from 5 mg/mL solutions in THF or 1,2,4-trichlorobenzene and then annealed under nitrogen at various temperatures from 100 °C to 300 °C for 30 min. Spin-coated films were 25-30 nm-thick as assessed by profilometry. For FET device fabrication, top-contact electrodes (500 Å) were deposited by evaporating gold (pressure < 10⁻⁵ Torr); channel dimensions were 25/50/100 μm (L) by 0.2/1.0/2.5/5.0 mm (W). The capacitance of the insulator is 1 x 10⁻⁸ F/cm² for 300 nm SiO₂. TFT device measurements were carried out in a customized vacuum probe station (8 x 10⁻⁵ Torr) or in air. Coaxial and/or triaxial shielding was incorporated into Signaton probes to minimize the noise level. TFT characterization was performed with a Keithley 6430 subfemtoammeter and a Keithley 2400 source meter, operated by a locally written Labview program and GPIB communication. Thin films were analyzed by wide-angle X-ray film diffractometry (WAXRD) on a Rigaku ATX-G instrument with Cu Kα radiation and a monochromator using standard θ -2 θ techniques. All θ -2 θ scans were calibrated in situ with the reflection of the Si (100) substrates.

3.2.5 Electrochemistry.

Cyclic voltammetry was performed in an electrolyte solution of 0.1 M tetrabutylammonium hexafluorophosphate (Bu₄N⁺PF₆⁻) in dry acetonitrile. Platinum wire electrodes were used as both working and counter electrodes, and Ag wire was used as the pseudo-reference electrode. A ferrocene/ferrocenium redox couple was used as an internal standard and potentials obtained in reference to a silver electrode were converted to the saturated calomel electrode (SCE) scale.

Thin films of the polymers were coated onto the Pt working electrode by drop casting from 0.5 wt % – 1.0 wt % THF solutions and dried under vacuum at 80 °C for 2 h.

3.2.6 Computational Methodology.

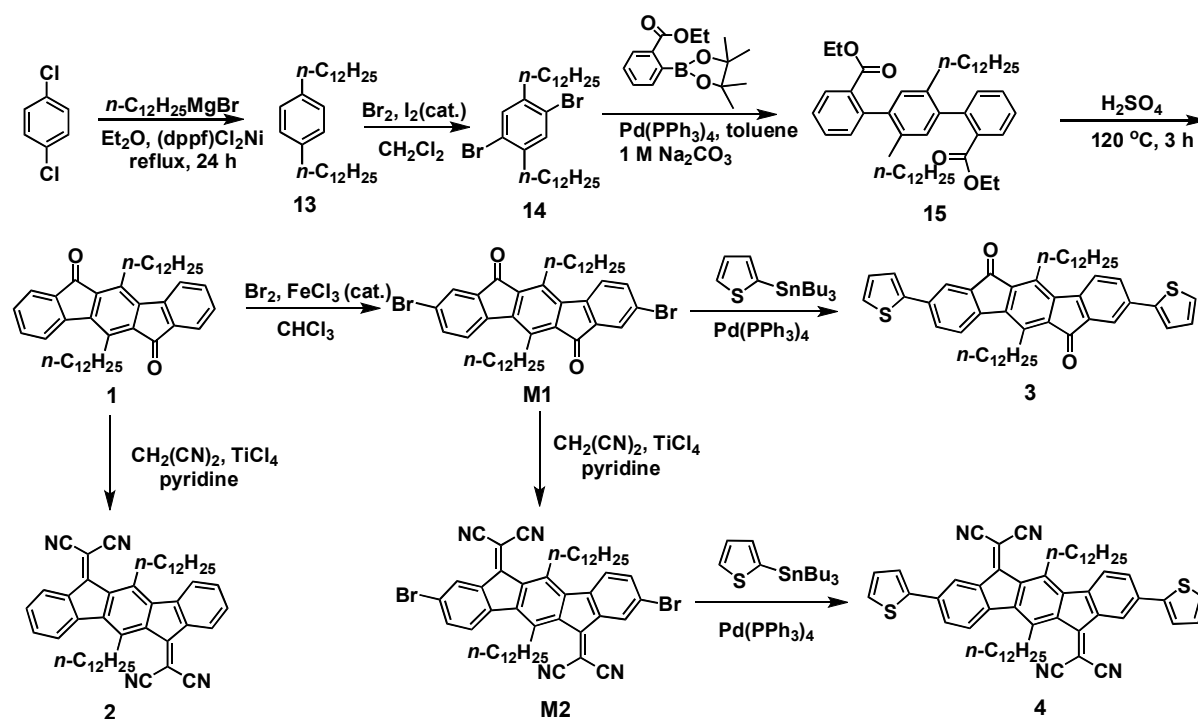
Geometry optimizations for the gas-phase neutral, radical-anion, and radical-cation states of **1** - **12** were carried out at the density functional theory level using the B3LYP functionals¹⁻³ and a 6-31G** split valence plus double polarization basis set. To ease the computational cost, all alkyl chains in the molecular structures were substituted by methyl groups. Excitation energies of the low-lying excited states have been calculated at the time-dependent DFT (TDDFT) level. All calculations were carried out with QChem (version 3.1).

3.3 Results

3.3.1 Synthesis.

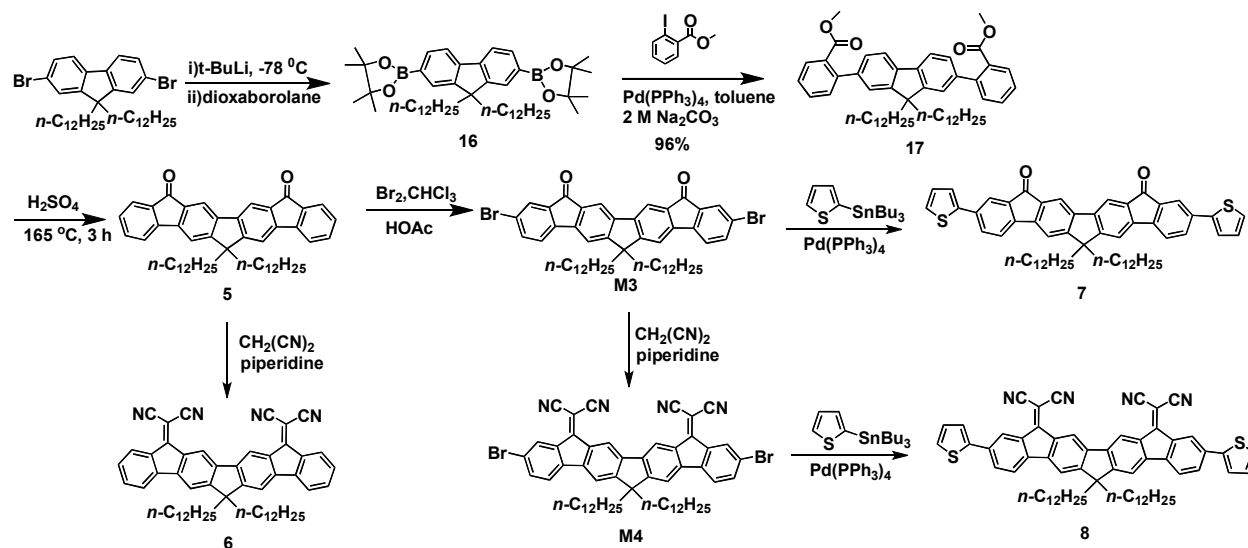
The syntheses of (bis)indenofluorene-based compounds **1** – **12** and monomers **M1** – **M6** are shown in Schemes 3.1 – 3.3 in which acid-catalyzed intramolecular Friedel-Crafts acylations are key steps in forming the ladder-type structures with electron-deficient carbonyl functionalities. As shown in Scheme 3.1, Kumada coupling of *n*-dodecylmagnesium bromide with 1,4-dichlorobenzene affords 1,4-di-*n*-dodecylbenzene (**13**) in 83% yield, which is then selectively brominated in CH₂Cl₂ under rigorous exclusion of light to afford 2,5-dibromo-1,4-di-*n*-dodecylbenzene (**14**) in 75% yield. Suzuki coupling of **14** with 2-(ethoxycarbonyl)phenylboronic acid pinacol ester gives compound **15** as a colorless oil in 45% yield. The moderate yield obtained for this Suzuki coupling is due to the presence of an electron-withdrawing group (ethyl ester) in the boronic ester reagent, which is known to decrease Suzuki coupling yields.³² Double

intramolecular Friedel-Crafts acylation is next achieved by treatment of diester **15** with concentrated sulfuric acid at 120 °C for 3 h. Indenofluorenedione product **1** is isolated as an orange solid in 93% yield. Compound **1** is then regioselectively brominated at positions 2 and 8 using FeCl₃/Br₂ with rigorous exclusion of light to afford monomer **M1** in 85% yield. Subsequent Knoevenagel condensation of **M1** and **1** to form dimalononitrile compounds **2** and **M2**, respectively, is achieved in 45-50% yield using excess malononitrile along with pyridine and TiCl₄. Compounds **3** and **4** are obtained via Stille coupling of **M1** and **M2** with 2-tributylstannylthiophene in 50% yield and 60% yield, respectively using Pd(PPh₃)₄ as the catalyst.



Scheme 3.1. Synthesis of indenofluorene-based compounds **1-4** and monomers **M1** and **M2**.

The syntheses of the bisindenofluorene-based compounds **5-8**, **M3**, and **M4** are depicted in Scheme 3.2. Fluorene boronic ester **16** is synthesized in 90% yield starting from 2,7-dibromo-9,9-didodecylfluorene which is double-lithiated with *t*-butyllithium and subsequently reacted with 2-isopropoxy-4,4,5,5-tetramethyl[1,3,2]dioxaborolane. Compound **17** is prepared by Suzuki coupling of **16** with methyl 2-iodo-benzoate in high yield (96%). The high yield obtained for this Suzuki coupling reaction is attributed to the fact that the arylhalide is in an *ortho* position relative to an electron-withdrawing group (methyl ester), which increases the yield through more favorable oxidative-addition processes during the reaction.³³ Treatment of **17** with concentrated sulfuric acid at 165 °C for 3 h induces double intramolecular Friedel-Crafts acylation, yielding bisindenofluorene diketone **5**. The yield obtained for this ring closure is 70%, with high selectivity at each reaction site (84%). Compound **5** is then brominated using FeCl₃/Br₂ with rigorous exclusion of light to afford monomer **M3** in 80% yield. Knoevenagel condensation of **5** and **M3** with malononitrile and piperidine as the base then affords **6** and **M4** in 65-70% yield as purple solids. Subsequent Stille coupling of **M3** and **M4** with 2-tributylstannylthiophene using Pd(PPh₃)₄ as the catalyst yields compounds **7** (65% yield) and **8** (70% yield), respectively.

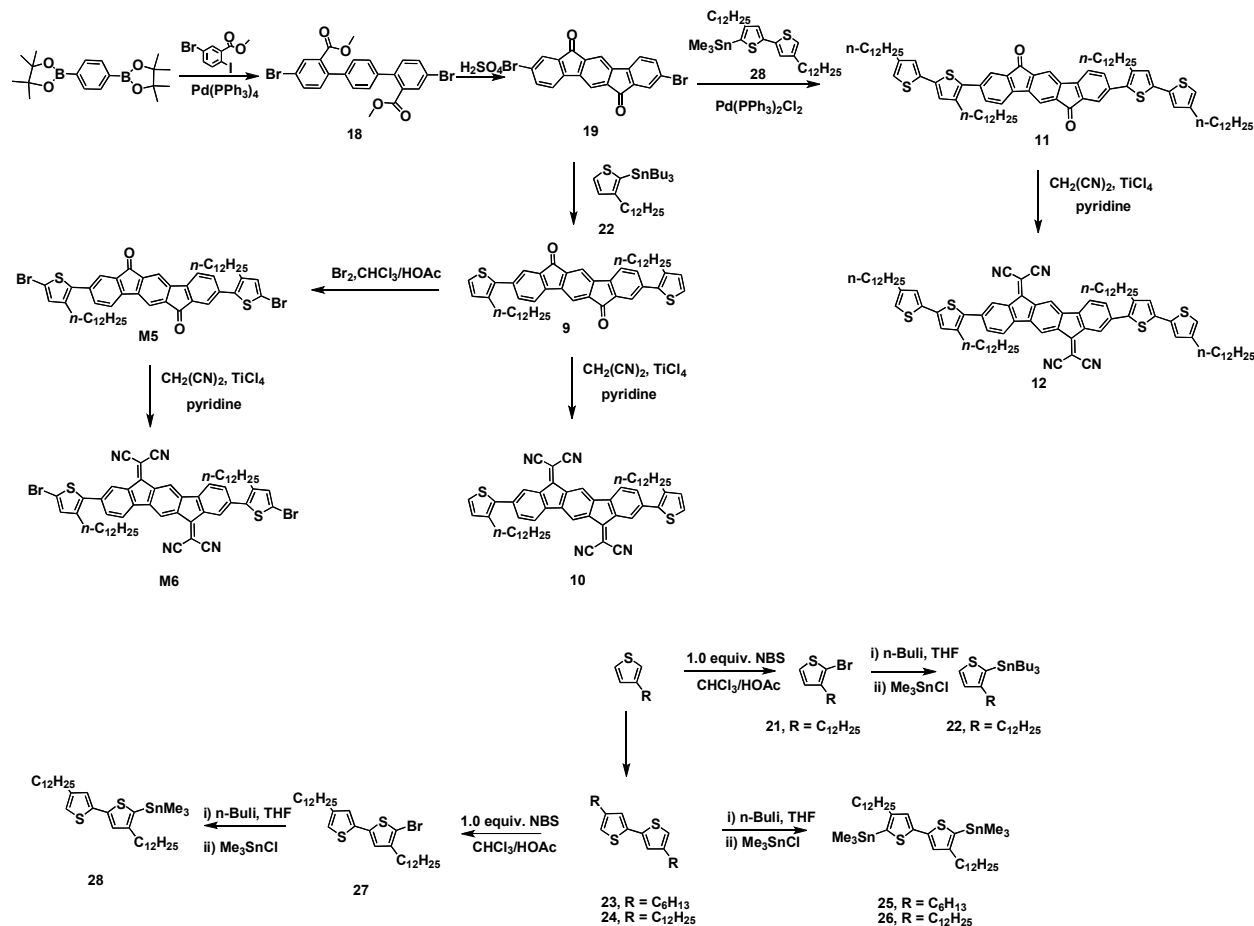


Scheme 3.2. Synthesis of bisindenofluorene-based compounds **5-8** and monomers **M3** and **M4**.

As shown in Scheme 3.3, Suzuki coupling of 1,4-benzenediboronic acid dipinacol ester with methyl 5-bromo-2-iodobenzoate yields compound **18** (89% yield). Intramolecular Friedel-Crafts acylation of **18** is achieved by H_2SO_4 treatment at 120 °C to give compound **19** (91% yield). $\text{Pd}(\text{PPh}_3)_2\text{Cl}_2$ -catalyzed Stille coupling of **19** and 2-tributylstannyl-3-dodecylthiophene (**22**) in DMF then yields compound **9** (35% yield), which undergoes reaction with excess malononitrile in the presence pyridine and TiCl_4 to afford **10** in 40% yield. Polymer building block **M5** is prepared in 95% yield by bromination of compound **9**, and subsequent Knoevenagel condensation with malononitrile yields **M6** in 45% yield. Compound **11** is obtained by the Stille coupling of **19** with 5-tributylstannyl-4,4'-didodecyl-2,2'-bithiophene (**28**) in 45% yield. Knoevenagel condensation of **11** then yields **12** in 50% yield. The syntheses of the thiophene-based compounds **21 – 28** are achieved through selective bromination and stannylation reactions. Oxidative coupling of the mono-lithiated derivatives of 3-hexylthiophene and 3-

dodecylthiophene in the presence of CuCl_2 affords **23** and **24**, respectively. Mono-bromination of **23** followed by mono-stannylation affords compound **28** in 90% yield. Selective bromination of 3-dodecylthiophene at position 2 and subsequent lithiation/stannyl chloride addition then affords **22** in 90% yield. Compounds **25** and **26**, which are used as comonomers in the polymerization reactions, are obtained from **23** and **24**, respectively, via double lithiation with *n*-BuLi, followed by the addition of Me_3SnCl in 80% and 85% yields, respectively.

Compounds **1-12** and monomers **M1-M6** are freely soluble in common organic solvents (CHCl_3 , CH_2Cl_2 , THF, toluene) which allows convenient purification by flash column chromatography. This is a significant advantage over many reported semiconductors which have poor solubilities and require high temperature vacuum sublimation techniques for purification. All of the present compounds were characterized by ^1H and ^{13}C NMR, elemental analysis, IR, and mass spectroscopy (EI/ESI/MALDI-TOF).



Scheme 3.3. Synthesis of indenofluorene-based compounds **9-12** and monomers **M5** and **M6**.

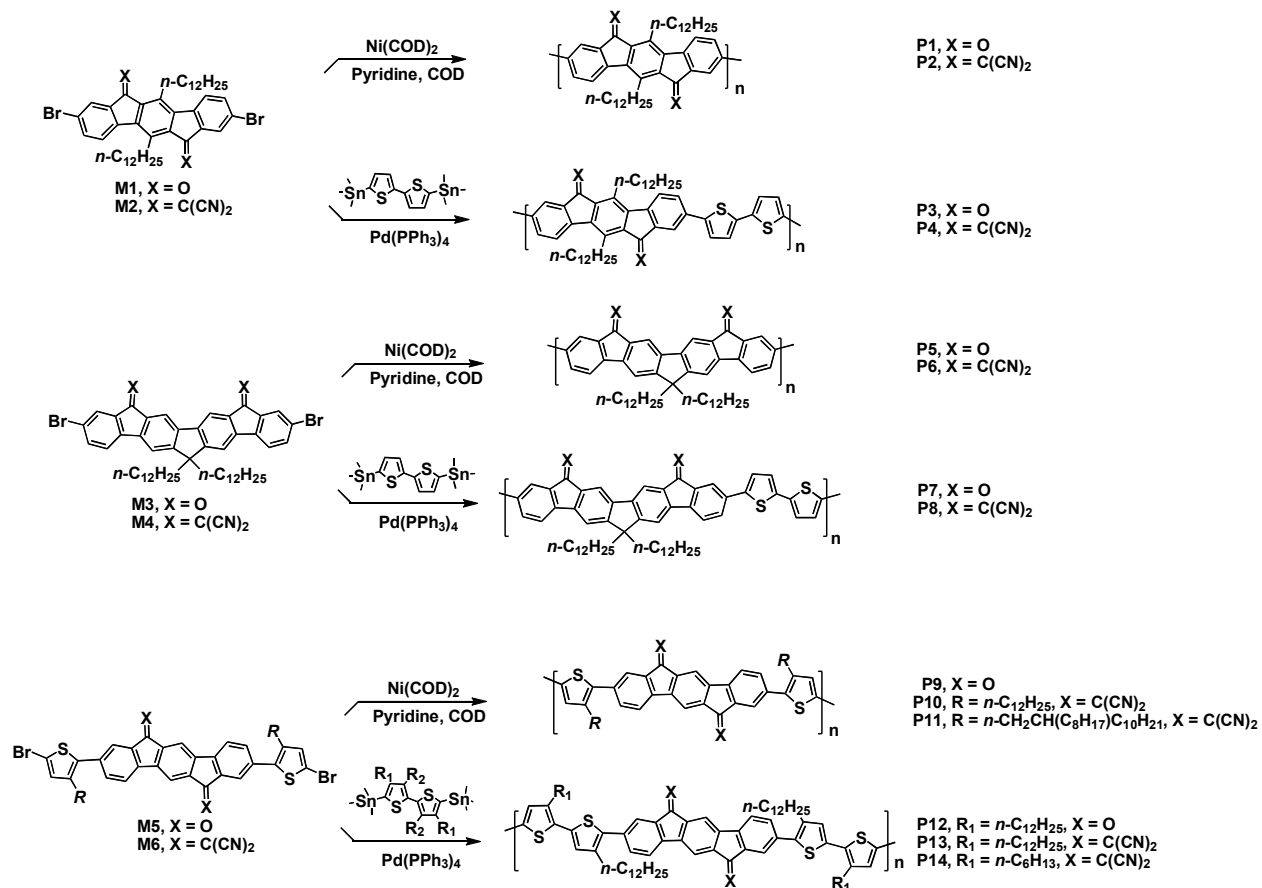
During the synthesis of **6** from **5** via Knoevenagel condensation, excess malononitrile with a piperidine base in DMF is used and the product is isolated in 65% yield. In contrast, a similar condensation for compound **1** proceeds sluggishly under the same reaction conditions, and requires a Lewis acid such as TiCl₄ for reasonable yields. This requirement was at first thought to result from increased steric repulsion at each reaction site of **1**, however the same difficulty for sterically less hindered **9** suggests that the highly electron-deficient nature of the indenofluorene core formed in this reaction ($E_{1/2}^{\text{red-1}} = -0.14 \text{ V vs SCE}$, *vide infra*) impedes the second condensation step, reflecting the significant demands of forming of such unusually electron-

deficient cores.³⁴ In order to synthesize the bithiophene-terminated ladder-type structures, dibromo-functionalized compounds **M1-M6** were first coupled with 5-tributylstannyl-2,2'-bithiophene, resulting in products with poor solubilities which prevented their further purification and characterization. The poor solubilities of these compounds are attributed to the absence of solubilizing groups on the outer thiophene units, which would otherwise compensate for the diminished solubility arising from molecular core extension. In contrast, mono-thiophene-terminated compounds **3**, **4**, **7**, and **8** are freely soluble in conventional organic solvents as a result of optimum π -conjugated core extension (i.e., a single thiophene unit at either end) while maintaining high solubility. For the sterically encumbered Stille couplings of **19** with compounds **22** and **28**, the Pd(PPh₃)₄/toluene catalyst system does not yield any significant coupling product, however Pd(PPh₃)₂Cl₂ in DMF is found to be more effective and the desired products are obtained in reasonable yields (35-40%), likely attributable to the higher turnover frequencies of more coordinatively unsaturated Pd(PPh₃)₂X₂ species.^{33,35} For this particular Stille coupling, similar yields (~ 35%) are obtained for thiophenes with “swallow tail” (2-octyldodecyl) and linear (*n*-dodecyl) alkyl substituents, indicating that the reaction is not particularly sensitive to alkyl substituent encumbrance on the thiophene reagent.

To optimize the delicate balance between solubility and thin film microstructural order, alkyl chain substituents on indenofluorene-based compound **9** and bisindenofluorene-based compound **6** were iteratively adjusted. Thus, *n*-hexyl- and *n*-octyl-substituted derivatives of compounds **5** and **6** were synthesized to examine the effect of alkyl chain on thin-film microstructure and FET performance. A “swallow tail” (C₈C₁₂) substituted derivative of **10** was also synthesized and

found to be significantly more soluble than its linear alkyl ($-n\text{-C}_{12}\text{H}_{25}$) counterpart. In addition, the copolymerization of monomer **M6** with bistannylated derivatives of 4,4'-didodecyl-2,2'-bithiophene and 4,4'-dihexyl-2,2'-bithiophene was also examined to improve polymer solubility.

Polymers **P1-P14** are synthesized according to Scheme 3.4. In general, homopolymers **P1**, **P2**, **P5**, **P6**, **P9**, **P10**, **P11** are synthesized via Yamamoto polycondensations using $\text{Ni}(\text{COD})_2$ as the catalyst and pyridine + COD as cocatalysts. Copolymers are synthesized via conventional or microwave-assisted Stille polycondensations between the dibromo-functionalized reagents **M1-M6** and bistannylbithiophene compounds. Physicochemical properties of the present polymers are summarized in Table 3.2. Carbonyl-functionalized bis(indenofluorene)-based homopolymers **P1**, **P4** and **P9** have limited solubilities which prevents further purification and characterization. Halting the polymerization process at early stages of the reaction does not yield soluble polymeric products. However, dicyanovinylene-functionalized homopolymers **P2** and **P6** are freely soluble in common organic solvents which may reflect the large local dipole moments (vide infra) of the monomeric units which enhance solvation. Interestingly, we find that bithiophene copolymers **P3**, **P4**, **P7**, and **P8** are more soluble (up to 40% by mass) than corresponding homopolymers **P1**, **P2**, **P3**, and **P4**, as a result of an increase in the degrees of rotational freedom which reduces backbone rigidity and increases solubility.³⁶



Scheme 3.4. Synthesis of (bis)indenofluorene-based homo- and copolymers **P1-P14**.

3.3.2 Thermal properties.

The thermal properties of the present compounds **1-12** and polymers **P1-P14** were investigated by thermogravimetric analysis (TGA), differential scanning calorimetry (DSC), and conventional melting point determinations. Figure 3.4 shows the thermal scans, and data are collected in Tables 3.1 and 3.3. For TGA, a 5% mass loss is defined as the thermolysis threshold. Thermolysis onset temperatures for all compounds **1-12** and polymers **P1-P15** are above 350 °C, indicative of good thermal stabilities, which allow thin film crystallinity and microstructure

analysis over a broad range of annealing temperatures, 50 – 300 °C. The observed melting points for compounds **1-12** are within ~ 0 – 5 °C of the values obtained by DSC scans. We find that molecular and macromolecular structural details have considerable influence on thermal phase transitions via the qualitative interplay of two intermolecular forces, π - π stacking interactions and alkyl chain interdigitations. Dicyanovinylene-functionalized compounds **6**, **8**, **10**, and **12** exhibit much higher melting temperatures than the corresponding carbonyl-functionalized structures **5**, **7**, **9**, and **11**. The increase of ~ 80 – 114 °C doubtless reflects substantial differences in cohesive energetics of the solid state intermolecular interactions. For each pair of compounds (**5/6**, **7/8**, **9/10**, and **11/12**), considering the similar core sizes and small increases in molecular weight (~96 amu), the melting point increases are likely a combined result of larger local/molecular dipole moments in the dicyanovinylene-functionalized compounds versus their carbonyl-functionalized counterparts, and enhanced molecular donor-acceptor characteristics which should enhance intermolecular cohesion through dipole-dipole and π - π interactions, resulting in more effective solid-state packing.¹³ The relative orientation of the dicyanovinylene groups, hence the local dipoles, at each methylene bridge appears to have little effect on the solid-state packing since similar melting point increases are observed for the indenofluorene (dicyanovinylenes *syn*) and bisindenofluorene (dicyanovinylenes *trans*) compounds.

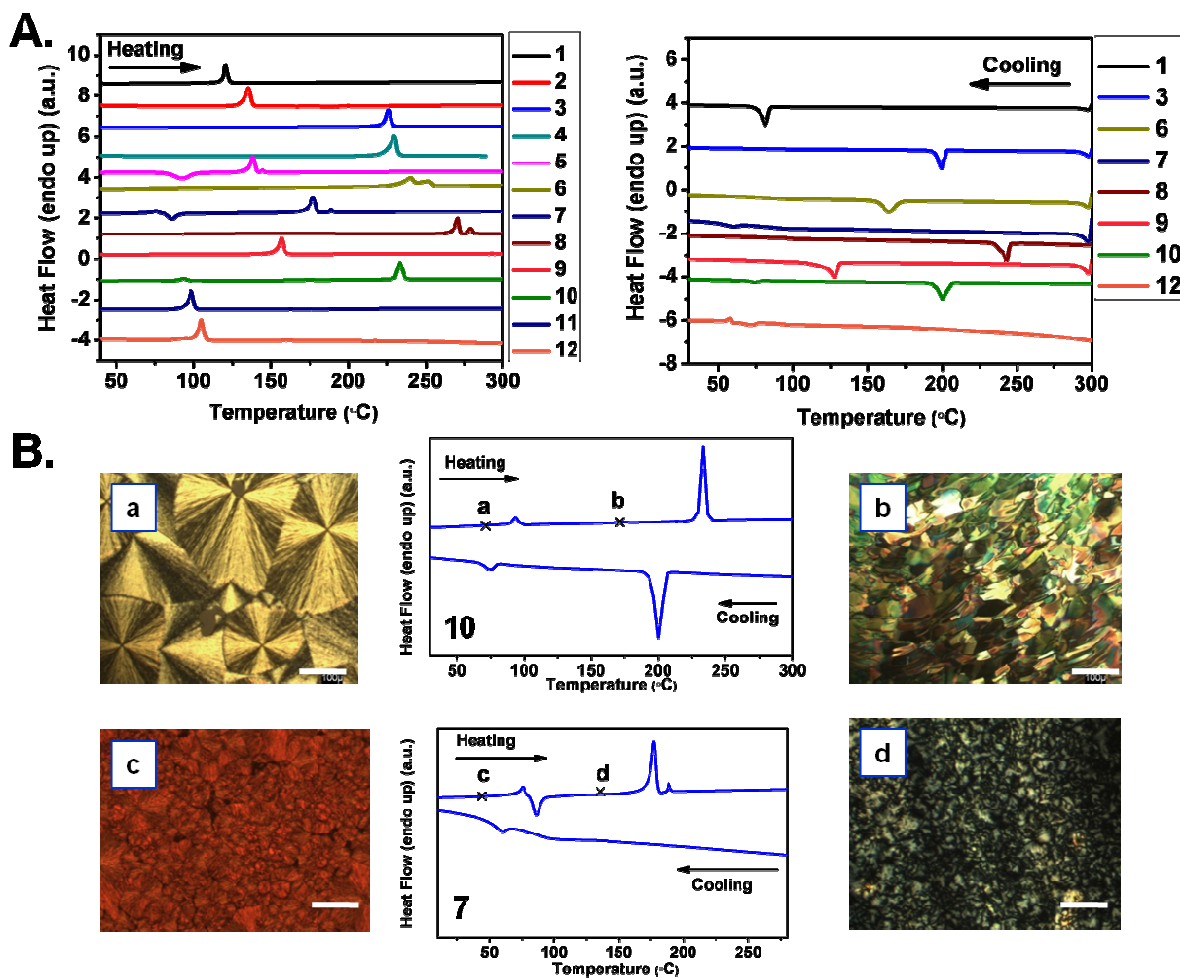


Figure 3.4. A. Differential scanning calorimetry (DSC) of the compounds **1-12** at a temperature ramp of 5 °C/min under N₂. B. Optical images of compounds **7** and **10**, taken under 90° cross-polarization conditions as a function of temperature. Scale bars denote 100 μm.

For compounds **5 – 8**, DFT calculations show that dicyanovinylene functionalization induces a relatively large dipole moment of 13 D compared to carbonyl compounds (7 D), consistent with the experimental results (see more below). On the other hand, because of the C₂-symmetric placement of the dipoles, the total molecular dipole moments are near zero for compounds **1 – 4**

and **9** – **12**. Upon conversions **1** \rightarrow **3** and **2** \rightarrow **4**, the melting points increase only by 5 – 10 °C. This small change in melting-point upon dicyanovinylene functionalization is probably due to the increased steric repulsions at the methylene bridges which cause significant deviations from core planarity, resulting in poor solid state packing. This suggestion is further confirmed by single-crystal structures and DFT calculations which show that while indenofluorene cores in compounds **1** and **9** have highly planar cores with small twist angles of $\sim 0^\circ$, upon dicyanovinylene functionalization, the core in compound **2** twists significantly from planarity ($\Delta = \sim 21^\circ$), while core planarity is preserved in compound **10** (Figures 3.5 and 3.9; see more below).

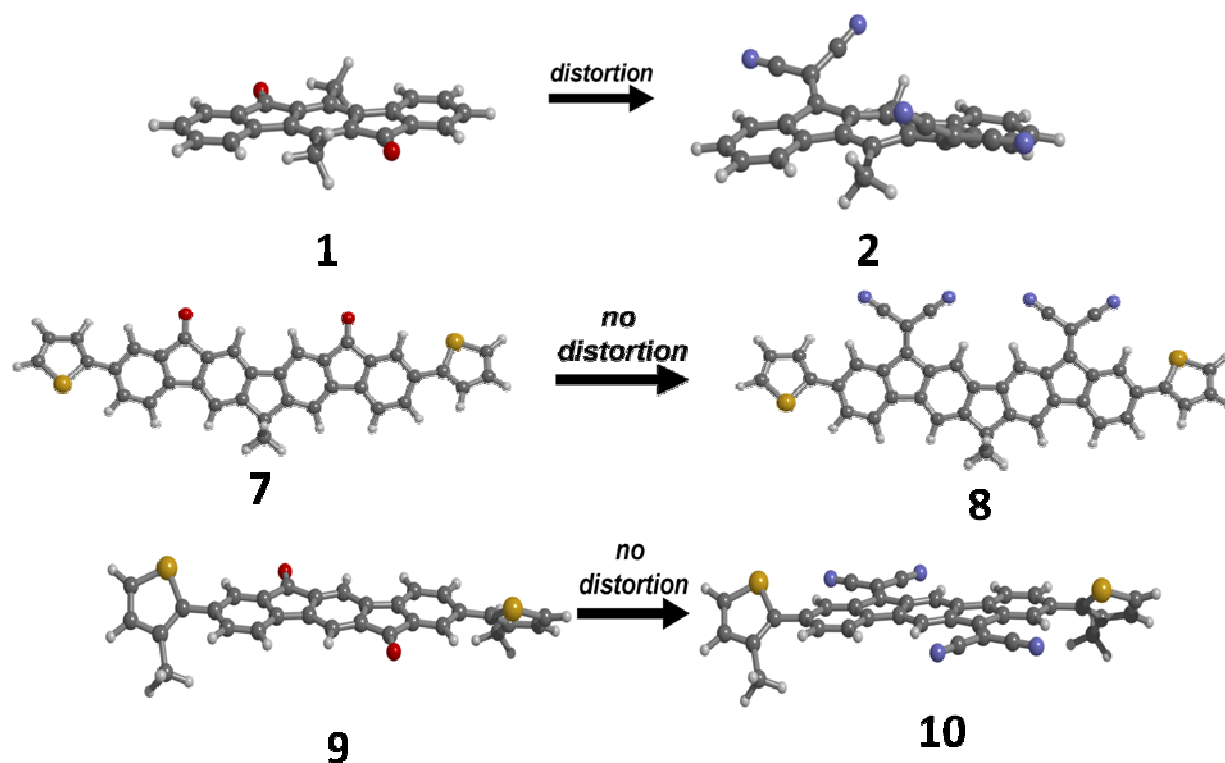


Figure 3.5. DFT-calculated molecular structures of **1**, **2**, and **7-10**.

Compounds **3**, **4**, **7**, and **8**, having additional thiophene units at the molecular termini, have higher melting temperatures ($\Delta T_{mp} \sim 40 - 100$ °C) than their indenofluorene/bisindenofluorene counterparts (**1**, **2**, **5**, and **6**), reflecting the collective effect of increased molecular weight, extended effective π -conjugation, and enhanced donor-acceptor interactions as a result of introducing thiophene donors into electron-deficient indenofluorene/bisindenofluorene acceptor cores. The only exceptions here are thiophene-terminated compounds **11** and **12** in which melting points decrease versus **9** and **10**, respectively. This depression in melting points argues that the contribution of additional alkyl chains ($C_{12}H_{25}$) on the outer thiophene rings to the overall intermolecular cohesive forces via alkyl chain interactions is weaker than the π - π stacking interactions between the cores.

To further investigate thermal phase transitions, DSC scans were performed at heating and cooling rates of 5 °C/min under N_2 , and collected in the second cycle. All of the present compounds exhibit reversible thermal features in all scans, in accord with the aforementioned excellent thermal stabilities. In the heating cycles of **5** and **7**, both exothermic features (93 °C for **5**; 85 °C for **7**) and endothermic peaks (138 °C/144 °C for **5**; 177 °C/188 °C for **7**) are observed, which was previously attributed to LC characteristics in qualitatively similar fluorene-based compounds.³⁷ In contrast, compounds **6**, **8**, and **10** exhibit multiple DSC thermal transitions with endotherms located at 240 °C/251 °C for **6**, 271 °C/279 °C for **8**, and 93 °C/234 °C for **10**, and exotherms located at 164 °C for **6**, 243 °C for **8**, and 200 °C/74 °C for **10**. As shown in Figure 3.4, polarized optical micrographs acquired during the slow cooling process (0.1 °C/min) of compounds **7** and **10** reveal the separation of anisotropic nematic and mosaic-like smectic liquid

crystal phases, respectively at $T < 180 - 225$ °C, and spherulite-like crystalline phases exhibiting birefringences at lower temperatures ($T < 80 - 90$ °C). This thermal feature at 93 °C is attributed to a crystal-to-crystal phase transition which is also observed in the corresponding thin films upon annealing (*vide infra*). The aforementioned intermolecular forces not only yield high melting points for dicyanovinylene functionalized compounds, but also enforce long-range order, which is reflected here by the presence of an LC phase. Considering the importance of molecular/macromolecular order and π - π interactions in determining charge carrier mobility, this kind of long-range ordering is crucial to realizing maximum OFET performance through alignment of the semiconducting molecules via thermally optimized processing.

The thermal properties of the present polymers were also investigated by DSC. Copolymers **P3**, **P7**, **P8**, **P12**, **P13**, and **P14** exhibit endotherms at 260 °C, 280 °C, 310 °C, 322 °C, 330 °C, and 335 °C on the heating cycle. Corresponding exotherms are observed at 290 °C and 280 °C for **P8** and **P12**, respectively. Polymer **P6** exhibits a glass transition at 120 °C with an endothermic peak at 260 °C and an exothermic peak at 243 °C. The higher endothermic transition temperature observed for **P8** versus **P6** can be attributed to the presence of the bithiophene comonomer in the former which is known to increase thermal transition temperatures in semiconducting polymers.^{1,2}

3.3.3 Optical properties.

Solution/thin-film optical and fluorescence spectra of compounds **1-12** and polymers **P1-P5** are shown in Figure 3.6, and optical data are collected in Tables 3.1 and 3.2. Due to the presence of multiple absorption transitions and large Stokes shifts, solution and solid state optical band gaps (E_g) were estimated from the low-energy band edges of the optical spectra.³⁸ The solution-based

absorption and emission measurements were carried out at very low concentrations ($< 10^{-5}$ M) in a solvent of intermediate dielectric constant (THF, $\epsilon = 7.6$) to minimize the influence of molecular aggregation and differences in molecular dipole moments (solvents with large dielectric constants can preferentially stabilize polar conformations), revealing the “intrinsic” molecular structural features such as planarity, optical HOMO – LUMO gap, and extent of π -conjugation.³⁹

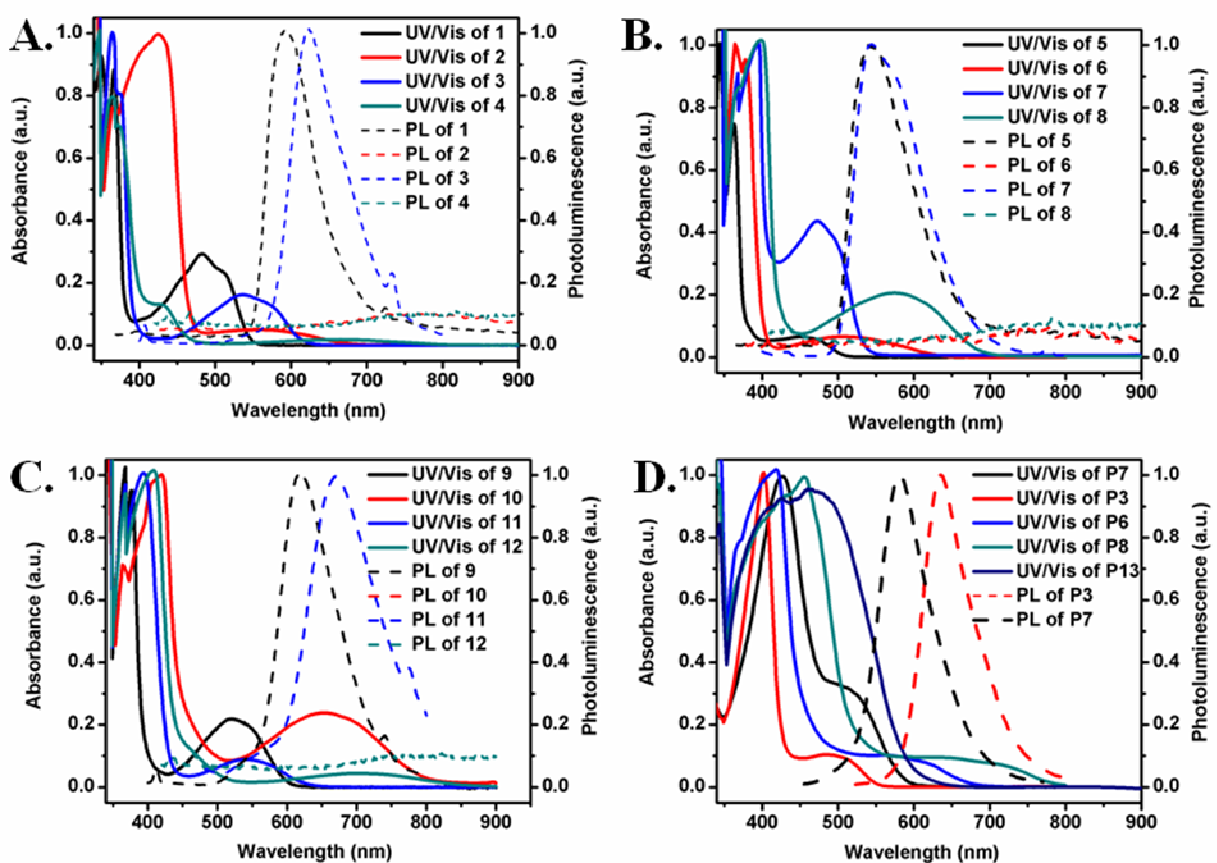


Figure 3.6. Optical absorption (solid lines) and photoluminescence (dashed lines) spectra of molecules 1-12 and polymers **P2-P4**, **P6-P8**, and **P12-P14** as THF solutions.

In THF, the absorption spectra of carbonyl-functionalized compounds **1**, **3**, **5**, **7**, **9**, and **11** exhibit three maxima, two located below 400 nm, and the third at 455 – 540 nm. The higher energy maxima – 368 nm (**1**), 374 nm (**3**), 365 nm (**5**), 394 nm (**7**), 377 nm (**9**) and 394 nm (**11**) – correspond to π - π^* transitions of the indenofluorene and bisindenofluorene backbones, whereas the weaker absorptions at lower energies – 484 nm (**1**), 537 nm (**3**), 455 nm (**5**), 472 nm (**7**), 525 nm (**9**) and 540 nm (**11**) – can be assigned to the symmetry-forbidden n - π^* transitions involving the carbonyl groups.⁴⁰ The absolute absorption maxima of all of the bis(indenofluorene)-based compounds are shifted to longer wavelengths by \sim 110-140 nm versus that of fluorenone (258 nm in THF).⁴¹ This significant bathochromic shift is consistent with enhanced π -conjugation of the molecular backbone and is attributable to the planar, ladder-type structure of these cores embedding two electron-withdrawing carbonyl groups. When the carbonyl functionalities are replaced with dicyanovinylene groups, the high energy absorption maxima shift to 426 nm for **2**, 430 nm for **4**, 378 nm for **6**, 400 nm for **8**, 418 nm for **10**, and 410 nm for **12**, and long-wavelength absorptions are now observed at 579 nm, 661 nm, 513 nm, 576 nm, 653 nm, and 711 nm for **2**, **4**, **6**, **8**, **10**, and **12**, respectively. The bathochromic shift upon dicyanovinylene functionalization is \sim 41 – 58 nm for the indenofluorene and \sim 6 – 13 nm for the bisindenofluorene core and is consistent with the reported shifts in similar ladder-type π -conjugated structures.^{42,43} Dicyanovinylene functionalization for all of the present compounds results in larger red-shifts in the low-energy absorption maxima (\sim 60 – 171 nm) than those of the π - π^* transitions (\sim 6 – 58 nm) suggesting that the optical transitions of the low-energy absorption maxima have significant contributions from the frontier MOs that are primarily localized on the methylene bridges, making them more susceptible to functionalization at these positions. This is

consistent with the previous assignment of these transitions as $n-\pi^*$ in character. Although the short-wavelength absorption maxima show negligible solvachromatism, the long-wavelength absorptions exhibit red-shifts (Figure 3.7, $\Delta\lambda = 5 - 20$ nm) with increased solvent polarity (cyclohexane \rightarrow THF \rightarrow ethanol), indicating positive solvachromatism. Since blue-shifts are typically expected for $n-\pi^*$ absorptions upon increasing the solvent polarity, the presence of a red-shift suggest that the Franck-Condon excited state ($S_{1(n-\pi^*)}$) has significant polar character. The red-shifts observed upon dicyanovinylene functionalization are attributed to LUMO energetic stabilization arising from the stronger electron-withdrawing nature of the dicyanovinylene versus carbonyl substituent, resulting in band gap contractions from 2.28 to 1.83 eV (**1** \rightarrow **2**), from 2.02 to 1.54 eV (**3** \rightarrow **4**), from 2.44 to 1.95 eV (**5** \rightarrow **6**), from 2.31 to 1.80 eV (**7** \rightarrow **8**), from 2.05 to 1.52 eV (**9** \rightarrow **10**), and from 1.94 to 1.44 eV (**11** \rightarrow **12**).⁴⁴ These gaps are considerably smaller ($\Delta E_g = 1.75 - 2.26$ eV) than those of typical non-functionalized indenofluorene cores (~ 3.70 eV), indicative of HOMO and LUMO stabilization with a greater magnitude in the latter – a crucial step towards the development of new air-stable n -channel and ambipolar semiconductors.⁴⁵

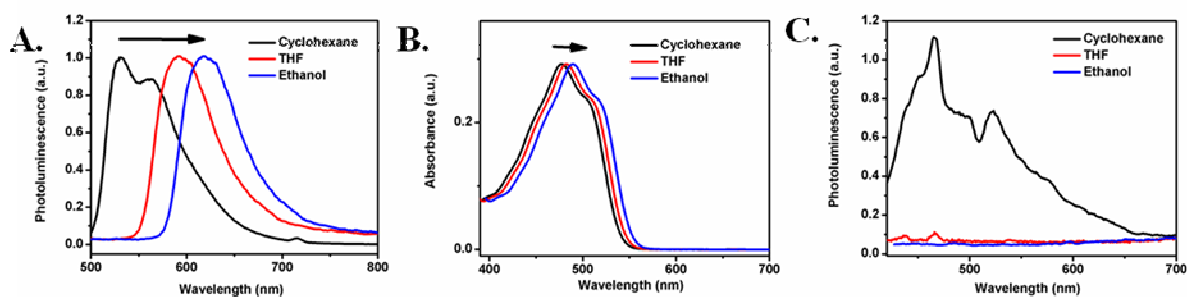


Figure 3.7. Optical absorption and photoluminescence spectra of molecules **1** (A, B) and **6** (C) in cyclohexane, THF, and ethanol solutions.

The optical absorption spectra of thiophene-terminated compounds **3**, **4**, **7**, **8**, **11**, and **12** exhibit absorption maxima that are red-shifted ($\Delta\lambda_{\text{max}} = 6 - 41$ nm) versus those of (bis)indenofluorene core structures **1**, **2**, **5**, **6**, **9**, and **10**, reflecting the effects of extended core dimensions, enhanced π -electron delocalization, and formation of donor-acceptor type structures upon appending electron-rich thiophenes to the electron-deficient cores. In addition, smaller band gaps ($\Delta E_{\text{g}} = 0.1 - 0.3$ eV) are observed for thiophene-functionalized molecules (2.02 eV (**3**), 1.54 eV (**4**), 2.31 eV (**7**), 1.80 eV (**8**), 1.94 eV (**11**), and 1.44 eV (**12**)) versus the (bis)indenofluorene core structures. These band gap contractions are further confirmed by nonsymmetric increases in the HOMO and LUMO energies with the former being larger (see electrochemical data, *vide infra*). A similar trend was previously reported for a series of thiophene-phenylene oligomers.⁴⁶

Thin film optical spectra of the present compounds were recorded on spin-coated films on glass substrates, and data are summarized in Table 3.1. Although the solution phase absorption spectra are devoid of significant fine structure, thin-film absorption spectra exhibit vibronic features with peak intervals of 0.15 – 0.20 eV, corresponding to the typical energies of aromatic C=C bond stretches.⁴⁷ This vibronic coupling may reflect molecular planarization in the thin-film phase versus the solution phase in which molecules have greater degrees of structural freedom. The film high energy absorption maxima are at 363 – 410 nm which are, except for **9** – **12**, red-shifted by $\sim 10 - 15$ nm versus the corresponding solution absorption maxima. The blue shifts observed for compounds **9** – **12** suggest significant H-type aggregate coupling between transition dipoles as in the aforementioned thiophene-phenylene series.^{46,48} The thin-film absorption maxima follow the same general trends as the solution-phase absorption maxima, indicating

similar molecular structure effects on optical features in solution and thin-films. In addition, shoulders at higher wavelengths (490 – 759 nm) appear in the thin-film phase with significant red-shifts of $\sim 27 - 169$ nm, indicating higher degrees of molecular order in the thin film microstructures compared to the solution phase. This conclusion is further confirmed by thin-film XRD and AFM data (*vide infra*).^{23,49} In general, the thin film optical band gaps follow trends similar to the solution-phase data, and they are 0.1 – 0.2 eV smaller than the corresponding solution values, indicating a greater average π -conjugation and microstructural ordering. A similar trend is observed in oligothiophenes.⁵⁰

For compound **10**, the thin-film optical absorption spectrum changes significantly on annealing. Solution-cast films exhibit two absorption maxima at 313 and 387 nm, and upon annealing at 120 °C, the absorption maxima red-shift to 340 nm and 412 nm ($\Delta\lambda_{\text{max}} \sim 25$ nm), respectively, and two new features at higher wavelengths (688 nm and 759 nm) appear. The intensity of the two new peaks and the absorption maximum at 412 nm increases upon annealing at 150 °C, suggesting a high degree of macromolecular organization in the thin film phase and enhancement of the molecular packing which is further confirmed by thin-film XRD and AFM analyses (*vide infra*).

The solution PL emission spectra of compounds **1-12** are shown in Figure 3.4 and data are collected in Table 3.1. Since 0-0 transitions are rarely observed in room temperature solution spectra, it is an accepted procedure to use $\Delta = \lambda_{\text{em}} - \lambda_{\text{abs}}$ as an estimation of the magnitude of the Stokes shift.⁵¹ When carbonyl functionalized compounds **1**, **3**, **5**, **7**, **9**, and **11** are excited at short-wavelength absorption maxima, emissions are observed at 540 – 675 nm, indicating large Stokes shifts of $\sim 150 - 390$ nm. These large Stokes shifts, which are surprising considering the planar

backbones of the present ladder-type cores, have also been observed in the literature for carbonyl-functionalized pentaphenylene compounds.⁵² Such large Stokes shifts are attributed to the fact that when two chromophore units are in conjugation (i.e., bis(indenofluorene) and carbonyl/dicyanovinylene) intramolecular energy transfer between the excited states of two chromophore units ($T_{\pi-\pi^*}/S_{\pi-\pi^*}$ and $T_{n-\pi^*}/S_{n-\pi^*}$) occur until the lowest excited state is reached, resulting in large Stokes shifts.⁵² Interestingly, excitation of the present compounds at their long-wavelength absorption maxima yields emissions identical to those of short-wavelength absorption maxima. This suggests similarities of the emission pathways and final relaxed excited states of these molecules upon either $\pi-\pi^*$ or $n-\pi^*$ excitation. This similarity in emission characteristics further confirms the presence of highly efficient intramolecular energy transfer between chromophore units ($S_{1(\pi-\pi^*)} \rightarrow S_{1(n-\pi^*)}$). As shown in Figure 3.7, the fluorescence spectra of the carbonyl compounds exhibit positive solvachromatisms, ($\Delta\lambda = 40$ nm for cyclohexane (nonpolar) \rightarrow THF (polar)), even larger than that observed in the long-wavelength absorption maxima, indicating that the dipole moment is larger in the excited state than in the ground state and the final relaxed excited state has some charge transfer (CT) characteristics. When the electron-deficiency of the core increases with dicyanovinylene functionalization, the Stokes shift increases and only very weak, broad peaks are observed at 760 – 785 nm for dicyanovinylene-functionalized compounds **2**, **4**, **6**, **8**, **10**, and **12**. This is consistent with the general observation that increased Stokes shift amplitudes generally correlate with longer excited state lifetimes, resulting in an increase in the relative probability of nonradiative decay and lower PL quantum efficiencies.⁵³ This suggests that the core electron-deficiency operates via intramolecular energy-/charge-transfers which result in large Stokes shifts and eventual quenching.⁵⁴ To investigate the

importance of charge-transfer excited states in these dicyanovinylene compounds, fluorescence spectra were recorded in cyclohexane, and broad, significantly blue-shifted fluorescence peaks at 460 – 500 nm were observed which are absent in THF (Figure 3.7). This indicates the formation of a charge-transfer excited state in relatively polar THF, resulting in fluorescence quenching. The formation of charge-transfer states for these dicyanovinylene-based compounds may be especially favorable due to arene and cyano group resonance stabilization of the corresponding cations and anions. The dicyanovinylene-functionalized compounds exhibit significant bathochromic shifts of $\sim 115 - 240$ nm in the emission maxima versus those of the carbonyl-functionalized analogues, and furthermore, upon introduction of thiophene units, emission red-shifts of $\sim 5 - 50$ nm are observed for **3**, **4**, **7**, **8**, **11**, and **12**, consistent with the optical absorption. Thin-film fluorescence spectra were obtained by excitation at $\lambda_{\text{abs}}^{\text{thin-film}}$ and data are summarized in Table 3.1. In general, the trends from solution are preserved in the thin films. The spectral shapes and maxima are similar to the solution spectra with additional peaks for compounds **1** and **3**. Thin films of the dicyanovinylene-functionalized compounds exhibit very broad, weak peaks, consistent with the solution phase results.

In THF, polymers **P2**, **P3**, **P4**, **P6**, **P7**, **P8**, **P12**, **P13**, and **P14** exhibit absorption maxima at 460, 401, 465, 418, 426, 456, 420, 461, and 460 nm, respectively, with shoulders on the red side of the bands at 600, 497, 680, 577, 514, 661, 560, 810, and 808 nm, respectively. All of these polymers show bathochromic shifts of $\sim 20 - 60$ nm compared to their monomeric counterparts (**2**, **3**, **4**, **6**, **7**, **8**, **9**, and **10**) as expected due to the extended π -conjugation. The thin-film absorption maxima are observed at 455, 393, 457, 405, 421, 435, and 471 nm for **P2**, **P3**, **P4**, **P6**, **P7**, **P8**, **P12**, **P13**, and **P14**, respectively, with shoulders at 620, 485, 705, 587, 512, 709, 605,

847, and 845 nm respectively. Band gaps are estimated to be: 1.55 eV for **P2**, 1.70 eV for **P3**, 1.45 eV for **P4**, 1.99 eV for **P6**, 2.06 eV **P7**, 1.57 eV for **P8**, 1.90 eV for **P12**, 1.38 eV for **P13**, and 1.37 eV for **P14** from the low energy absorption edges. In general, introduction of thiophene units into the polymer backbone results in red-shifts of the absorption maxima and contraction of the band gaps, reflecting the combined effects of π -electron-donating S atoms vs. the C=C linkages, the presence of donor/acceptor backbones, and the more planar conformation of five-five vs. five-six inter-ring linkages.⁵⁵

3.3.4. Electrochemical Characterization.

The electrochemical properties of the present compounds **1-12** and polymers **P1-P13** were characterized by cyclic voltammetry in solution and as thin films. Cyclic voltammograms are shown in Figure 3.8, and electrochemical data are summarized in Tables 3.1 and 3.2. The ferrocene/ferrocenium couple was used as an internal standard, and all potentials are reported vs SCE.

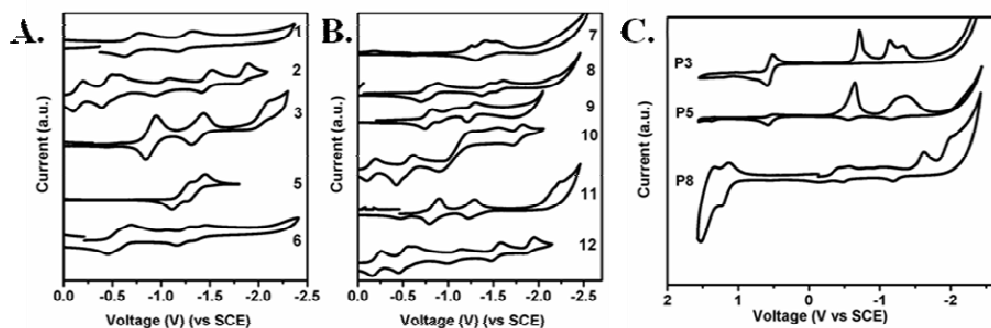


Figure 3.8. Cyclic voltammograms of molecules **1-12** as solutions in THF (A and B) and representative polymers **P3**, **P5**, and **P8** as thin films in acetonitrile (C) in 0.1 M $\text{Bu}_4\text{N}^+\text{PF}_6^-$ at scan rates of 100 mV/s.

In THF, all ladder-type compounds exhibit multiple reversible reductions with the first half-wave potentials ranging from -1.20 V to -0.12 V. The completely reversible reductions at low potential magnitudes reveal the marked electron-deficiency of these new core structures and their potential electron-transporting nature with stable doping/de-doping characteristics. Indenofluorene compounds **1**, **2**, **3**, and **4** exhibit multiple reversible reductions with first half-wave potentials of -0.77, -0.14, -0.90, and -0.24 V, respectively (vs SCE). The first half-wave reduction potentials for bisindenofluorene-based compounds **5**, **6**, **7**, and **8** are -1.20, -0.53, -1.25, and -0.72 V, respectively (vs SCE), which are $\sim 0.4 - 0.5$ V lower than those of the indenofluorene compounds having similar electron-withdrawing functionalities, suggesting lower electron affinities due to relatively large core-sizes. Indenofluorene-based compounds **9**, **10**, **11**, and **12** having thiophenes at the molecular termini also exhibit multiple reduction events with the first half-wave potentials at -0.74, -0.12, -0.85, and -0.20 V, respectively. Ladder-type diketone cores **1** and **5** can be reduced far more easily than the corresponding non-ladder terphenylene and quaterphenylene compounds which show reversible reductions at -2.40 V and -2.28 V (vs SCE), respectively.⁵⁶ Clearly, reduction potentials are shifted to more positive values with increasing degree of planarity and core electron deficiency, consistent with the initial design considerations (*vide supra*).

From the first half-wave reduction potentials, LUMO energies ($EA^{\text{red}} \approx -LUMO^{\text{red}}$ assuming that Koopmans' theorem holds) for the present compounds can be estimated by taking the SCE energy level to be -4.44 eV below the vacuum level and using the relation of eq. 1.^{11,57} Results are summarized in Table 1. Using this relationship, solution phase $LUMO^{\text{red}}$ values are estimated to lie at -3.67, -4.30, -3.54, -4.20, -3.70, -4.32, -3.59, and -4.20 eV for indenofluorene-based

compounds **1**, **2**, **3**, **4**, **9**, **10**, **11**, and **12**, respectively. The LUMO^{red} energies for bisindenofluorene-based compounds **5**, **6**, **7**, and **8** are estimated to be -3.24, -3.91, -3.19, and -3.72 eV, respectively. The low LUMO energies (≤ -3.2 eV) for all of the present ladder-type compounds suggest that these materials have high electron affinities and are good candidates for *n*-channel semiconductors. The LUMOs for **2**, **4**, **10**, and **12** are therefore within the range of those of the aforementioned air-stable arylenediimide semiconductors PDI-8CN2, ADI-8CN2, and NDI-8CN2 with LUMO^{red} < -4.0 eV.^{15,16,18}

$$\text{LUMO}^{\text{red}} = -E_{\text{red-1/2}} - 4.44 \quad (1)$$

For (bis)indenofluorene compounds **1**, **2**, **5**, **6**, and **9**, dicyanovinylene functionalization anodically displaces the first half-wave potentials by ~ 0.6 V suggesting that the highly electron-withdrawing dicyanovinylene substituents dramatically affect the LUMO energies, and in similar ways for all compounds. In marked contrast, the corresponding displacements in HOMO energies are much smaller ($\Delta \approx +0.20$ eV), suggesting that the LUMOs are primarily localized on the bridge methylenes, which renders them more susceptible to functionalization, whereas the HOMOs are more delocalized over the entire molecule, consistent with the DFT results (*vide infra*). Dicyanovinylene functionalization in both indenofluorene and bisindenofluorene cores reduces the voltage spacing between the first two reductions by 0.1 – 0.2 V and increases the number of observed reductions, reflecting the more electron-accepting nature of these derivatives and the greater number of possible reduction sites. This similarity in the first two potentials suggests that the greater facility of the second reduction is due to the enhanced electron-deficiency of the core, and that these reductions are largely malononitrile-centered, as previously observed for tricyanovinyl-capped oligothiophenes.^{58,59}

Relative core size effects on the stabilization of subsequent reductions is observed for (bis)indenofluorene compounds **1-8**. For compound pairs **1** and **5**, **2** and **6**, **3** and **7**, **4** and **8**, having similar functionalities, the potential difference between successive reduction events [$\Delta E_{1/2} = E_{1/2-2} - E_{1/2-1}$] are, without exception, found to be smaller for the bisindenofluorene cores by ~ 0.3 V versus the indenofluorene cores. This trend is attributed to more effective radical anion delocalization and decreased Coulombic repulsions within the larger bisindenofluorene π -system.^{51,60} A similar trend is observed in the α -nT and phenylene (p-nP) semiconductor series.⁶¹

Addition of thiophene substituents to the electron-deficient bis(indenofluorene) compounds **1**, **2**, **5**, **6**, **9**, and **10** results in an increase in HOMO energies by $\sim 0.2 - 0.4$ eV, reflecting the π -electron-rich thiophene nature versus the electron-deficient cores. Due to the increased effective π -conjugation lengths of the molecules, the LUMO energies exhibit smaller displacements of $\sim 0.1 - 0.2$ eV, and eventually the band gaps contract ($\Delta E_g = 0.1 - 0.3$ eV), consistent with the optical data discussed above. The DFT-derived orbital contours also show that the thiophene units make greater contributions to the HOMOs than the LUMOs, which explains the observed energy shifts upon thiophene addition. It will be seen below that the large observed positive HOMO shifts along with the smaller LUMO changes provide three new molecules **3**, **9**, and **12**, which are ambipolar semiconductors having both electron and hole injection accessible MOs.

Thin-film electrochemical data for the present compounds follow the general trends of the solution phase data, indicating similar molecular structure effects on the solution and solid-state electrochemical properties. Similar reduction values ($\Delta E_{1/2-1} < 0.1 - 0.2$ V) are observed along with more evident oxidation peaks ($E_{\text{onset-1}} = +1.10 - +1.40$ V). Electrochemical band gaps estimated from reduction and oxidation potentials ($E_g^{\text{CV}} = 1.50$ eV $-$ 2.36 eV) exhibit parallel

trends to those observed in solution/thin-film optical band gaps, supporting the accuracy of the two different techniques used to analyze electronic structure.

Cyclic voltammetric data for the present polymers were measured as thin films on Pt working electrodes in acetonitrile. Voltammograms are shown in Figure 5, and data are summarized in Table 3.2. The onset of reduction and oxidation potentials are -0.12 and 1.37 V, -0.80 and 0.98 V, -0.29 and 1.12 V, -0.37 and 1.31 V, -0.90 and 0.90 V, -0.60 and 1.12 V, -0.82 and 0.98 V, -0.29 and 1.07 V, and -0.27 and 1.10 V for polymers **P2**, **P3**, **P4**, **P6**, **P7**, **P8**, **P12**, **P13**, and **P14**, respectively. Using eq. 1, the LUMO/HOMO energies are calculated as -4.32/-5.81 eV for **P2**, -3.64/-5.42 eV for **P3**, -4.15/-5.56 eV for **P4**, -4.07/-5.75 eV for **P6**, -3.54/-5.34 eV for **P7**, -3.84/-5.56 eV for **P8**, -3.62/-5.42 eV for **P12**, -4.15/-5.51 eV for **P13**, and -4.17/-5.54 eV for **P14**. Without exception, thiophene addition to the electron-deficient core structures increases both the HOMO and LUMO energies with a larger increase in the former, and resulting in band gap contractions. The polymer electrochemical features strongly reflect the nature of the individual building blocks, indicating that polymer electronic properties are determined principally by the backbone chemical structure with negligible contributions from molecular weight differences. For **P13** and **P14**, the exceptionally low LUMO energies (-4.15 – -4.17 eV) with low band gaps (1.36 – 1.37 eV) render these polymers attractive as potential ambipolar semiconductors capable of exhibiting air-stable electron and hole transport, a phenomena yet to be observed.

3.3.5 Single-Crystal Structures.

Single-crystals of the new compounds **7**, **M2**, and **M4** were grown by slow diffusion of methanol into chloroform solution and slow evaporation of chloroform solution, respectively, and the crystal structures determined by X-ray diffraction are shown in Figure 3.9. The

conjugated backbone of thiophene-terminated bisindenofluorenedione compound **7** adopts a substantially planar molecular configuration with very small plane-to-plane twist angles of 1.3° and 1.2° between the outer phenyl rings 1 and 2, and 3 and 4, respectively. The twist angle is 2.6° between innermost two phenyl rings, 2 and 3. One of the outer thiophene rings is perfectly in the plane of the ladder core with small twist angle of 1.6° , whereas the other thiophene unit exhibits larger twist angle of 7.3° which is comparable to those observed in planar oligothiophene derivatives ($\sim 5 - 6^\circ$).^{46,48} The thiophene rings at the molecular termini display a typical trans conformation. In addition, carbonyl groups are effectively in conjugation with the conjugated backbone since they are within 2° of the molecular plane. In spite of the highly planar backbone of **7**, no evidence of π - π stacking interaction is observed, and it is seen that packing is mainly governed by van der Waals interactions between linear alkyl-chains (n -C₁₂H₂₅) forming alternating layers of insulating alkyl chains and conductive π -conjugated backbones. The conjugated backbones of **7** orient perfectly in a face-to-face manner, and the alkyl chains exhibit substantial interdigitation with greater than ~ 10 methylene (-CH₂-) units directing the self-assembly process. The minimum distance between the closest phenyl rings is measured as ~ 10.1 Å. The molecular length is measured as 24.4 Å along the conjugated backbone. To the best of our knowledge, the tetraphenylenediketone core is one of the longest ladder-type *p*-phenylene oligomer to date that has been characterized by X-ray diffraction.

In contrast to the planar backbone of **7**, the central phenyl ring of compound **M2** exhibits a torsion angle up to 9.1° resulting in a “wavey” structure. The outer phenyl rings are twisted ca. 21.5° out of the plane of the central arene ring, which approaches the $\sim 30^\circ$ maximum value beyond which there is insufficient intramolecular π -overlap to support a significant conduction

band structure.⁴⁸ As shown in Figure 3.9, the dicyanovinylene functionalities are ca. 35.8° out of the plane of the cyclopentadienyl unit between the arene rings, indicating significantly reduced conjugation between these electron-deficient functionalities and the π -conjugated core. The observed highly twisted **M2** backbone is largely a result of the steric hindrance between the alkyl chains at positions 5 and 11, and the dicyanovinylene groups at positions 6 and 12. Similar to the packing motif in **7**, van der Waals interactions between alkyl chains (over 10 methylene units (-CH₂-)) direct the crystal packing, resulting in segregated layers of alkyl chains and π -conjugated backbones. The minimum distance between the closest arene rings is measured as $\sim 8.5 \text{ \AA}$.

Dicyanovinylene functionalized bisindenofluorene compound **M4** adopts a highly planar molecular backbone with small plane-to-plane twist angles of $2.2^\circ/2.4^\circ$ and 0.8° between the outer phenyl rings and innermost two phenyl rings, respectively. In contrast to **M2**, dicyanovinylene functionalities are perfectly in the plane of cyclopentadienyl unit between the arene rings, indicative of high degree of conjugations between these functionalities and the π -conjugated core. The molecules are π -stacked in a slipped cofacial orientation along the long axis of the molecule at an interplanar π - π stacking distance of 3.54 \AA . The existence of the π - π stacking interactions in **M4** explain the observed relatively high melting points in the solid state compared to those of **7** and **M2** which do not exhibit any π - π stacking. The molecular length is measured as 18.9 \AA , and the molecular backbones of adjacent molecules exhibit π - π stacking interactions over lengths of $8.7 - 8.8 \text{ \AA}$ along the molecular axis.

The observed alkyl chain interaction-dominated crystal structures of **7** and **M2** explain the observed, relatively low melting points ($T_m < 170 \text{ }^\circ\text{C}$) compared to previously reported

oligothiophenes and other dicyanovinylene-functionalized compounds of the present new family (**6**, **8**, and **10**), which exhibit much stronger π - π interactions. Despite the lack of π - π interactions in the single crystal structures, the molecules exhibit highly ordered π - π stacked lamella structures in the thin-film phase (*vide infra*).

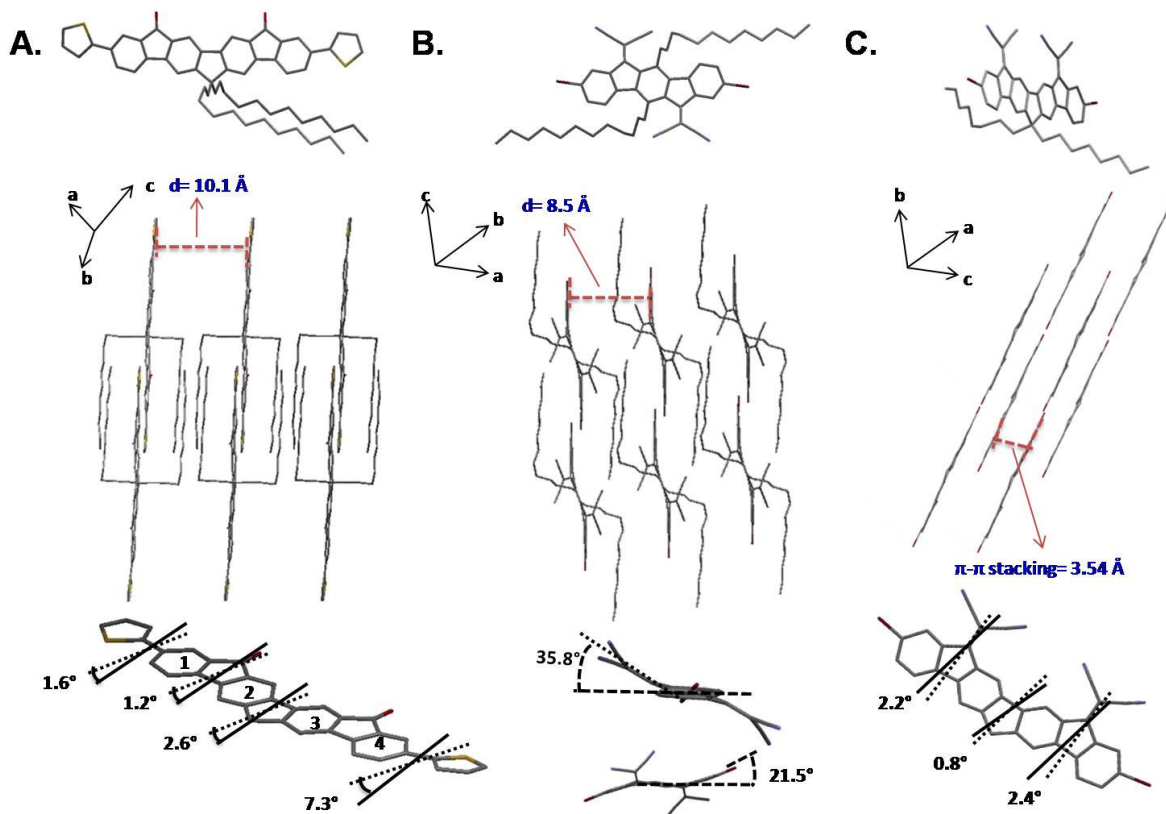


Figure 3.9. Single crystal X-ray structures of A. bisindenofluorenediketone compound **7**, B. indenofluorenedicyanovinylene monomer **M2**, and C. bisindenofluorenedicyanovinylene compound **M4**.

3.3.6. Thin Film Morphology.

Thin film microstructures, morphologies, and molecular orientations for the present new class of materials were studied by θ -2 θ x-ray diffraction (XRD), grazing incidence X-ray diffraction

(GIXRD), and AFM. Additionally, XRD rocking curves were recorded to evaluate out-of-plane film texturing. Since direct in situ characterization of microstructure at the buried dielectric-semiconductor interface, the active region for charge transport,⁶² is not possible with conventional techniques, we studied the morphology of the semiconductor surface and crystallinity across the entire film, with the reasonable assumption that they resemble the basic microstructure at the interface. This approach has been previously successful in elucidating thin film feature-device performance relationships for a variety of thiophene-, arylene-, and acene-based semiconductors.^{13, 19,55} Measurements were carried out on vacuum-deposited and spin-coated thin-films grown on OTS-treated Si/SiO₂ substrates. The thicknesses of all films were 50 – 60 nm by profilometry. The XRD scans reveal that films of compounds **1**, **3**, **4-12**, prepared by vacuum deposition or solution-casting, are highly textured. Representative XRD scans and AFM images of solution-cast films are shown in Figures 3.10 and 3.11, respectively, and data are collected in Table 3.4.

Out-of-plane $\theta - 2\theta$ XRD scans exhibit several sharp low angle reflections with high intensities up to fourth order, revealing that vacuum-deposited films are highly ordered. However, in general, the solution-deposited films show lower degrees of crystallinity order compared to the vacuum-deposited films, which can be explained by the relatively high rate of the film growth using this method ($T_D < 1$ min) for solution-cast films, resulting in relatively less-ordered microstructures versus the vacuum-deposited films ($T_D > 1$ h).²¹ The only exception is the thin films of **10** which exhibit very high degrees of crystallinity from solution, similar to the vacuum-deposited devices, and indicating very favorable molecular ordering for this particular donor-acceptor compound from solution. For all films, a single family of diffraction

peaks are observed without the presence of an obvious π - π stacking feature, and d-spacing values are estimated from the (100) diffraction peaks as 17.1 – 32.7 Å, implicating a crystalline polymorph where the majority of the molecules have an edge-on orientation on the substrate with the π - π stacking direction parallel to the substrate, thereby favoring in-plane charge transport from source to drain. From the GIXRD measurements, π - π stacking distances are estimated as 3.1 – 3.7 Å which is in the range of distances measured for many oligo-/poly-thiophene and fluorene-based semiconductors.^{1,55,63} Note that exceptionally short stacking distances of 3.1 Å are observed for thin-films of **10**, **P13**, and **P14**, indicating geometrically favorable π - π interactions between molecular backbones. Rocking curves of the first-order reflections (100) for all samples indicate a high degree of texturing (fwhm = 0.03 – 0.04°, corresponding to the resolution of the instrument), demonstrating that the film microstructure layers are uniformly oriented relative to the substrate plane. Due to the presence of alkyl-chain interdigitation, the estimation of molecular tilt angles from d-spacings and estimated molecular lengths is not straightforward as it was in oligothiophene- and acene-based semiconductors.¹³ For indenofluorene-based compounds **1-4** and **9-12**, in which the *n*-dodecyl chains protrude directly from the thiophene or arene units, the molecular backbone tilt-angles relative to the substrate are highly dependent on the degree of alkyl-chain interdigitation. For bisindenofluorene-based compounds **5-8**, in which alkyl chains protrude from the bridge methylene, molecular orientation was studied by changing alkyl substituent length. Thin-films of **6** were fabricated from *n*-hexyl (C₆H₁₃), *n*-octyl (C₈H₁₇), and *n*-dodecyl (C₁₂H₂₅) substituted derivatives under exactly the same conditions to compare out-of plane crystallinity. Although the crystallinities are qualitatively similar judging from XRD intensities, FWHM, and numbers of visible reflections, the d-spacing

value gradually decreases when the substituents are changed from *n*-dodecyl to *n*-octyl, to *n*-hexyl chains (18.2 Å → 15.6 Å → 14.1 Å), corresponding to a change of 0.65 Å per carbon atom. This difference corresponds to the difference in the distance from the end of the alkyl groups to the edge carbon atoms of the central fluorene core obtained by DFT calculations (~ 0.7 Å per atom), suggesting that the alkyl chains are oriented along the substrate surface normal with tilt angles of ~ 20°, and molecular backbone is nearly perpendicular to the substrate.

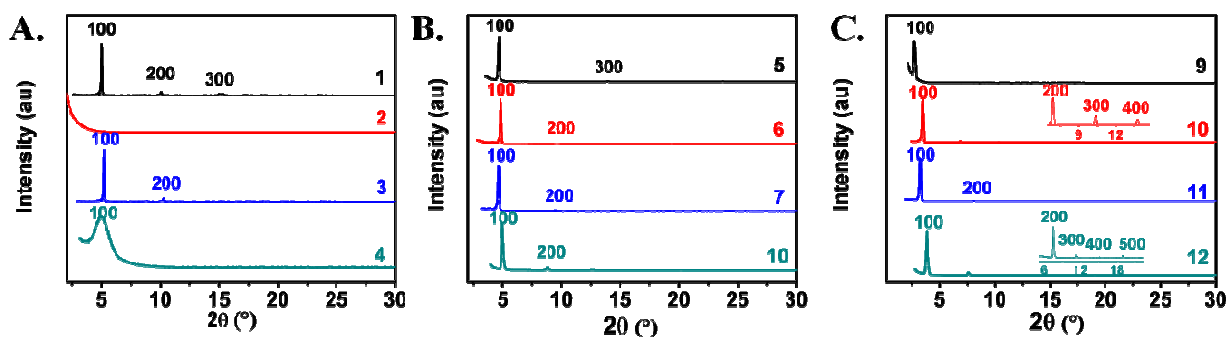


Figure 3.10. θ - 2θ X-ray diffraction (XRD) scans of spin-cast films of compounds **1-12** on silicon substrates.

The degrees of crystallinity of solution-cast films of **10** are highly dependent on annealing temperature. As shown in Figure 3.11, a change in the preferential crystalline phase/orientation is observed upon annealing with the d-spacing decreasing from 32.7 Å to 25.7 Å and with a significant increase in the 100 peak intensity (5000 count/s → 65,000 count/s), and higher order reflections (200, 300, and 400) evident, indicative of higher degree of molecular ordering, enhanced alkyl-chain interdigitation ($\Delta > 7$ methylene (-CH₂-) units), and/or molecular tilting from the substrate normal. The crystalline phase transition occurs at 80 – 100 °C, corresponding to the thermal transition observed at 93 °C by DSC (*vide supra*). AFM analysis shows that upon

annealing, the morphology changes from ball-like grains with sizes of $< 0.1 \mu\text{m}$ to very large $\sim 3 - 5 \mu\text{m}$ plate-like grains of terraced islands with step heights of $\sim 2.8 \text{ nm}$, corresponding to the observed lamellar XRD d-spacing. The large polycrystalline grains of **10** are unlike any film reported for a solution-cast *n*-channel semiconductor to date, and are significantly larger than the length scale of lithographically accessible channel lengths ($\sim 100 \text{ nm}$), offering the possibility of fabrication of grain boundary-free, single-crystal like transistors from straightforwardly solution-processed thin films. The same crystalline phase transformation is observed for the polymers **P13** and **P14**, however it is not associated with an increase in the grain size, indicating that molecular ordering occurs only within the grain without facilitating connection and ordering between grains. Importantly, we observe that these two different types of crystallinity increases for **P13/P14** versus **10** have totally different impacts on the final OTFT device performances (*vide infra*). Based on the aforementioned GIXRD, out-of-plane XRD, and AFM results at different film annealing temperatures, the molecular plane of **10** is estimated to be nearly perpendicular to the substrate ($\theta \approx 90^\circ$) and the alkyl chains are interdigitated over > 7 methylene ($-\text{CH}_2-$) units, consistent with the single-crystal structural features. A schematic figure showing the layered and π - π stacked thin-film microstructure of **10** is shown in Figure 3.12.

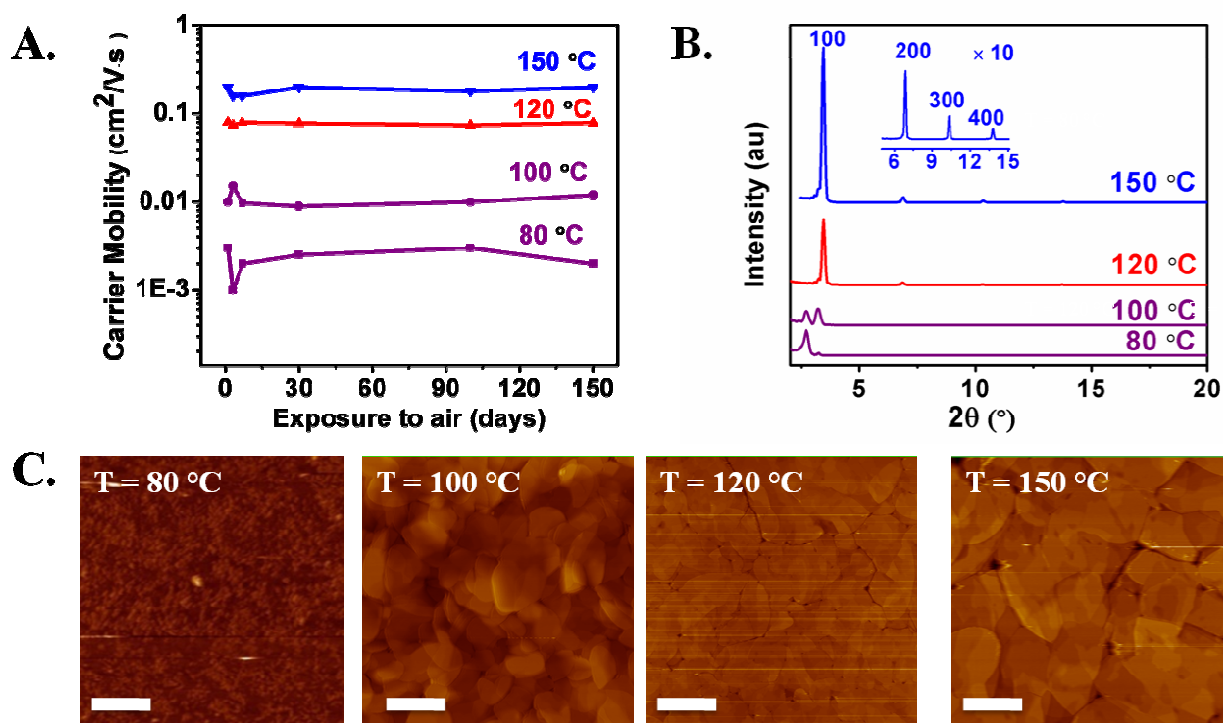


Figure 3.11. A. Electron mobilities measured in ambient for TFTs fabricated with spin-coated **10** and annealed at the indicated temperatures (80 °C – 150 °C) vs storage time of the devices in air without excluding light or ambient humidity (25% – 40 %). B. $\theta - 2\theta$ X-ray diffraction (XRD) scans of spin-coated **10** thin films at different annealing temperatures (Note that peak intensities are not normalized for comparison purposes). C. Tapping mode AFM images of **10** thin films at different annealing temperatures. Scale bars denote 1 μm .

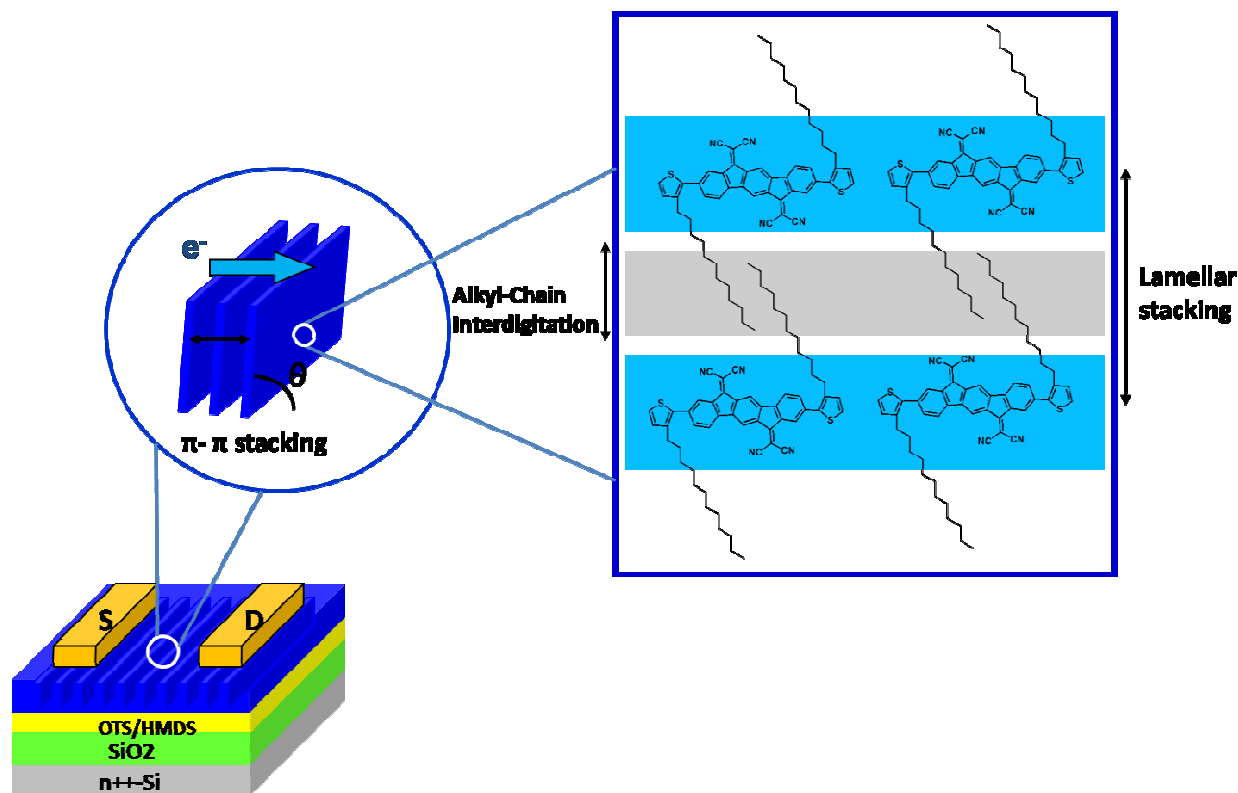


Figure 3.12. Schematic model of the layered and π - π stacked thin-film microstructure of **10**. The gray region shows the interdigitated alkyl chains forming an insulating barrier between conducting π -conjugated backbones (blue region). Note that the tilt angle (θ) strongly depends on the extent of alkyl-chain interdigitation for a given d-spacing.

3.3.7 Thin Film Transistor Device Characterization.

OTFTs with top-contact/bottom gate device structures were fabricated by either vacuum deposition or spin-coating on OTS-treated $\text{SiO}_2/\text{p}^+\text{-Si}$ substrates. All spin-coating processes were carried out in ambient, and devices were then annealed at 80 – 150 °C for 30 min under nitrogen. Vapor phase depositions were carried out under high vacuum (1×10^{-6} Torr) with the substrates maintained at temperatures (T_D) of 70 °C or 110 °C. Finally, gold contacts were patterned by

thermal evaporation using shadow masks by thermal evaporation to give channel lengths of 25 – 100 μm and widths of 500 – 2000 μm . FET properties were evaluated under positive or negative gate bias in ambient/vacuum to explore the majority charge carrier type, device performance, and environmental stability. FET data are summarized in Tables 3.2 and 3.3, and representative transfer and output plots are shown in Figure 3.13.

Devices fabricated with compounds **1**, **2**, and **5** are found to exhibit no FET activity, whereas compounds **3**, **4**, and **6** – **12** exhibit FET activity as *p*-channel, *n*-channel, or *ambipolar* semiconductors. It is found that compounds **7** and **11** are *p*-channel semiconductors with air-stable hole mobilities up to 0.001 $\text{cm}^2/\text{V}\cdot\text{s}$ and 1×10^{-4} $\text{cm}^2/\text{V}\cdot\text{s}$, respectively. Compounds **3**, **9**, and **12** exhibit ambipolar behavior with appreciable electron mobilities up to 0.01 $\text{cm}^2/\text{V}\cdot\text{s}$ and hole mobilities up to 0.006 $\text{cm}^2/\text{V}\cdot\text{s}$. Although compounds **3** and **9** operate only under vacuum, similar to most reported ambipolar semiconductors in the literature,⁶⁴ FETs fabricated with **12** are found to operate in ambient. To the best of our knowledge, this is the first example of a thiophene-based molecular semiconductor showing air-stable charge transport of both holes and electrons.^{1, 64} Additionally, FETs based on **9** exhibit highly balanced electron and hole mobilities of 0.006 $\text{cm}^2/\text{V}\cdot\text{s}$ ($\mu_e/\mu_h \sim 1.0$) for the vacuum-deposited films ($T_D = 110$ °C) which indicates that the solid-state microstructure and MO energetics facilitate both hole and electron transport with similar efficiency.¹³

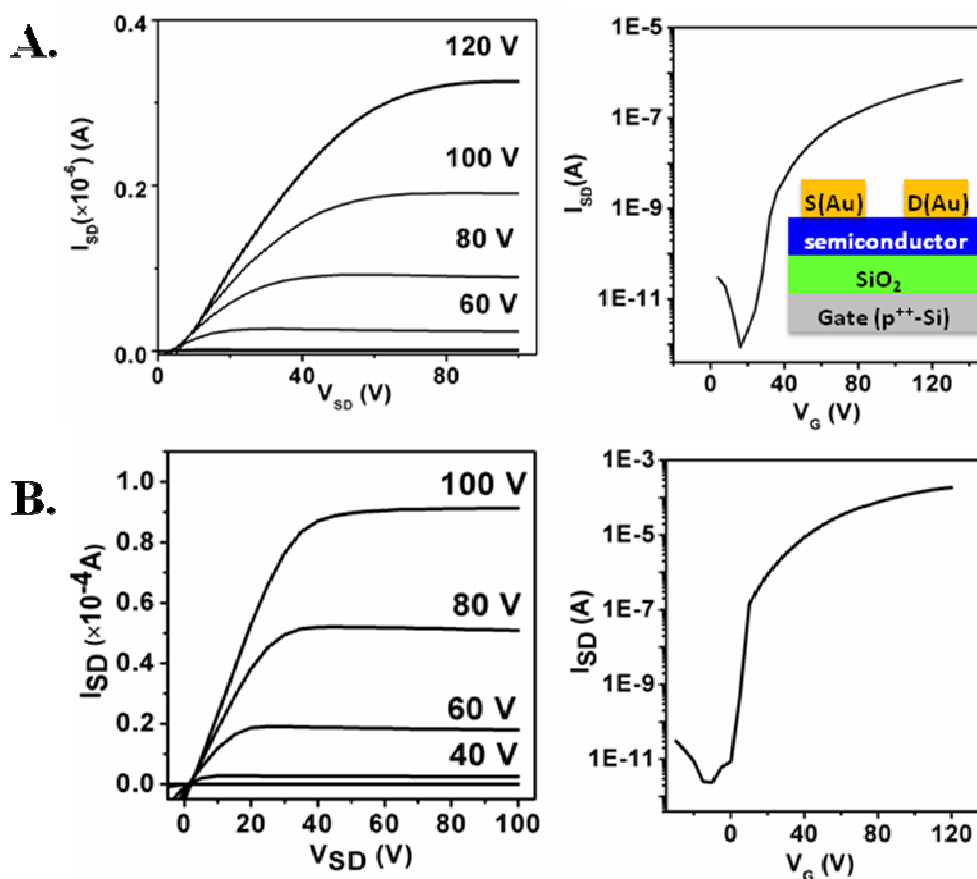


Figure 3.13. OTFT data for devices fabricated with compounds **6** and **10**. A. Output and transfer ($V_{SD} = 100$ V) plots for films of **6**, B. Output and transfer ($V_{SD} = 100$ V) plots for films of **10**. The general structure of an OTFT device is given in the inset.

OTFTs fabricated with dicyanovinylene-functionalized compounds **4**, **6**, **8**, and **10** exhibit n -channel behavior with electron mobilities and I_{on}/I_{off} ratios of $0.001 \text{ cm}^2/\text{V}\cdot\text{s}$ and 10^5 (**4**), $0.006 \text{ cm}^2/\text{V}\cdot\text{s}$ and 10^6 (**6**), $0.02 \text{ cm}^2/\text{V}\cdot\text{s}$ and 10^6 (**8**), and $0.16 \text{ cm}^2/\text{V}\cdot\text{s}$ and 10^7 (**10**). Devices of **6** and **8** are adversely affected by ambient conditions and operate only under vacuum (Figure 3.14). However, highly electron-deficient (low energy LUMO) compounds **4** and **10** exhibit stable n -channel activities in air, a significant advance over many reported n -channel semiconducting

materials.⁶ Devices stored under ambient without excluding light or humidity exhibit very stable device performance over time, and similar electron mobilities and $I_{\text{on}}/I_{\text{off}}$ ratios are measured after 5 months storage in air (Figure 3.14).

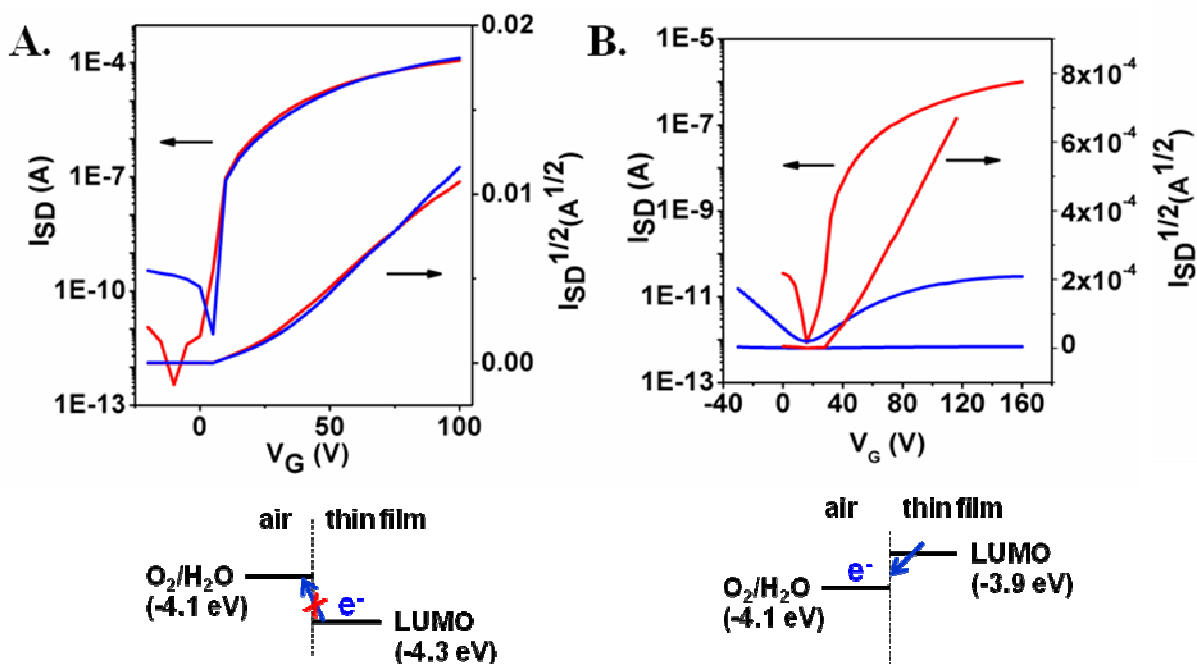


Figure 3.14. Transfer curves of compounds **10** (A) and **6** (B) under vacuum (red curves) and in ambient (blue curves). Note that the transfer curve for **10** was recorded after 5 months of storage in ambient. Below: the band lineups of LUMO energies of **10** and **6** with respect to the $\text{O}_2/\text{H}_2\text{O}$ electrochemical redox couple at air-thin film interface.

Solution-cast thin-films (50 – 65 nm) were fabricated by spin-coating 5 mg/mL solutions of the semiconductors in air, and devices were then annealed at 80 – 150 °C under N_2 for 30 min. Although the polymeric semiconductors are found to form smooth thin films from any solvent, molecular semiconductors tend to form continuous thin films only from low-boiling point solvents (e.g., CHCl_3 , THF). This may be due to the high volatility of the solvent which

facilitates rapid, smooth film growth on the highly hydrophobic OTS surface (advancing aqueous contact angle = 110 – 120°) before being spread during the spin-coating process.⁵⁵ Charge carrier transport type and ambient stability trends follow those of the vacuum-deposited films, although in general one to two orders of magnitude lower mobilities (1×10^{-4} cm²/V·s – 0.16 cm²/V·s) are measured for the solution-cast devices. This depressed performance principally reflects the low degree of microstructural order achieved in solution-cast films as evidenced by the XRD and AFM data. Surprisingly, although vacuum-deposited devices of **3** exhibit ambipolar behavior, solution-cast devices exhibit only *p*-channel activity ($\mu_h = 0.001$ cm²/V·s, $I_{on}/I_{off} = 10^5$), suggesting that differences in microstructural ordering obtained via different deposition techniques may lead to changes in overall charge transport characteristics. This phenomena has been previously observed for (tri)dicyanovinylene-capped oligothiophenes.^{65, 66} Among all of the present solution-cast devices, compound **10** is found to exhibit the highest mobility ($\mu_e = 0.16$ cm²/V·s) with an exceptionally high I_{on}/I_{off} ratio ($10^7 - 10^8$) and low threshold voltages (0.0 V – 5.0 V) after annealing at 150 °C, indicating that microstructures favorable for efficient charge transport can be achieved by solution casting, likely due to strong long-range intermolecular interactions. Note that this high electron mobility is one of the largest in the literature for a solution-cast *n*-channel semiconductor film operating in air.⁶ Furthermore, air-stability and an exceptionally high I_{on}/I_{off} ratio makes **10** a very attractive candidate as the *n*-channel semiconductor in the fabrication of CMOS-like printed organic circuitry. For **10**, the annealing temperature is found to have a significant impact on FET device performance, and a two orders of magnitude enhancement in mobility is realized by increasing the annealing temperature from 80 °C to 150 °C.

Following the similar trends as their molecular building blocks, polymers **P3**, **P6**, **P7**, **P8**, **P12**, **P13**, and **P14** are found to exhibit *p*-channel (**P3**, **P7**, **P12**), *ambipolar* (**P8**, **P13**, **P14**), and *n*-channel (**P6**) activity in spin-coated OTFTs. Carbonyl-functionalized bithiophene copolymers **P3**, **P7**, and **P12** exhibit air-stable hole mobilities of $0.001 \text{ cm}^2/\text{V}\cdot\text{s}$, $3 \times 10^{-4} \text{ cm}^2/\text{V}\cdot\text{s}$ and $0.01 \text{ cm}^2/\text{V}\cdot\text{s}$ with $I_{\text{on}}/I_{\text{off}}$ ratios of $1 \times 10^4 - 1 \times 10^5$, respectively. Dicyanovinylene-functionalized bithiophene copolymers **P8**, **P13**, and **P14** exhibit highly balanced electron and hole mobilities of $0.5 \times 10^{-4} \text{ cm}^2/\text{V}\cdot\text{s}$, $2 \times 10^{-4} \text{ cm}^2/\text{V}\cdot\text{s}$ and $2 \times 10^{-4} \text{ cm}^2/\text{V}\cdot\text{s}$, respectively with $I_{\text{on}}/I_{\text{off}}$ ratios of 10^4 . Polymer **P8** exhibits ambipolar behavior only under vacuum, whereas polymers **P13** and **P14** are found to operate stably under ambient. To the best of our knowledge, **P13** and **P14** are the first examples of polymeric semiconductors exhibiting both electron and hole mobility under ambient. Dicyanovinylene-functionalized bisindenofluorene homopolymer **P6** exhibits an electron mobility of $0.5 \times 10^{-4} \text{ cm}^2/\text{V}\cdot\text{s}$ with an $I_{\text{on}}/I_{\text{off}}$ ratio of 10^4 under vacuum.

3.4 Discussion

3.4.1 Electrochemical and Optical Properties as a Function of Electronic Structure.

To better understand the ionization energetic and mobility properties, the neutral, radical-anion, and radical-cation states of **1** - **12** were evaluated at the B3LYP/6-31G** level of theory. For compounds **2** and **7**, good agreement is found between the calculated *gas-phase* and X-ray crystallographic geometries, although the DFT geometries tend to evidence slightly less bond-length alternation (i.e., more delocalization) within the fused carbon-carbon backbones. Calculated electron affinities, ionization potentials, and intermolecular reorganization energies are detailed in Table 3.5. Across the series, dicyanovinylene functionalization significantly increases the electron affinity. While the magnitude of the impact is lower, dicyanovinylene

substitution also renders oxidation more difficult. Thiophene introduction in molecules **3**, **4**, and **7 - 12** has minimal impact on the electron affinity, but (as expected *a priori*) decreases the ionization potential thus making oxidation easier. These results, including the relative impact on the ionization energies, are in excellent agreement with the electrochemical reduction and oxidation potentials (Tables 3.1 and 3.3).

The impact of dicyanovinylene functionalization on the calculated electronic structures of **1 - 12** is similar (Table 3.6). For the dicyanovinylene systems, the stronger electron-withdrawing ability of dicyanovinylene versus carbonyl induces considerable energetic stabilization of the LUMO. Contour representations of selected valence molecular orbitals for the model fragments are shown in Figure 3.15. For both the dicyanovinylene and carbonyl structures, a significant portion of the respective LUMO electronic densities is localized on the respective electron acceptor units and at the center of the fused aromatic backbone. Thiophene substitution in **3**, **4**, and **7 - 12** minimally impacts both the LUMO energetics and electron density distribution. The HOMO is also energetically stabilized by dicyanovinylene substitution, although the influence is not as large. The densities of the respective HOMO wave functions are distributed across the fused aromatic backbones with little or no density on the electron-accepting substituents. Unlike the LUMO, both the energetics and wave function distribution are influenced by the thiophene substitution in **3**, **4**, and **7 - 12**: the HOMO electronic density is fully delocalized across the aromatic core and onto the thiophene units, and the energies are destabilized. The substantial influence of the dicyanovinylene substituents on the LUMO leads to far smaller HOMO-LUMO gaps ($\Delta_{\text{HL}} > 0.4$ eV) across the series versus the carbonyl-substituted structures. This is particularly noteworthy for the thiophene-substituted structures, where the additional influence

of the thiophenes leads to a substantial decrease in Δ_{HL} . These MO energetic results across the series are in agreement with the experimental estimates of provided by the optical and electrochemical studies (Tables 3.1 and 3.3).

Using the electronic structures of the model compounds, time-dependent DFT (TDDFT) calculations of the lowest-lying excited state energies are found to track the calculated and experimental Δ_{HL} data closely (detailed information pertaining to low-lying excited state energies, oscillator strengths, and electronic configurations can be found in Tables 3.7 – 3.18). The initial transition for each model fragment is characterized as being predominantly HOMO \rightarrow LUMO in character, with some minor transitions involving other nearby valence MOs. Thus, experimental optical band gaps estimated from the low energy band edges of the long-wavelength absorption bands should give an accurate estimation of HOMO-LUMO gap. Additionally, the calculated excited state energies for the model fragments exhibit red-shifts in the optical absorption maxima with increasing thiophene substitution, as observed experimentally.

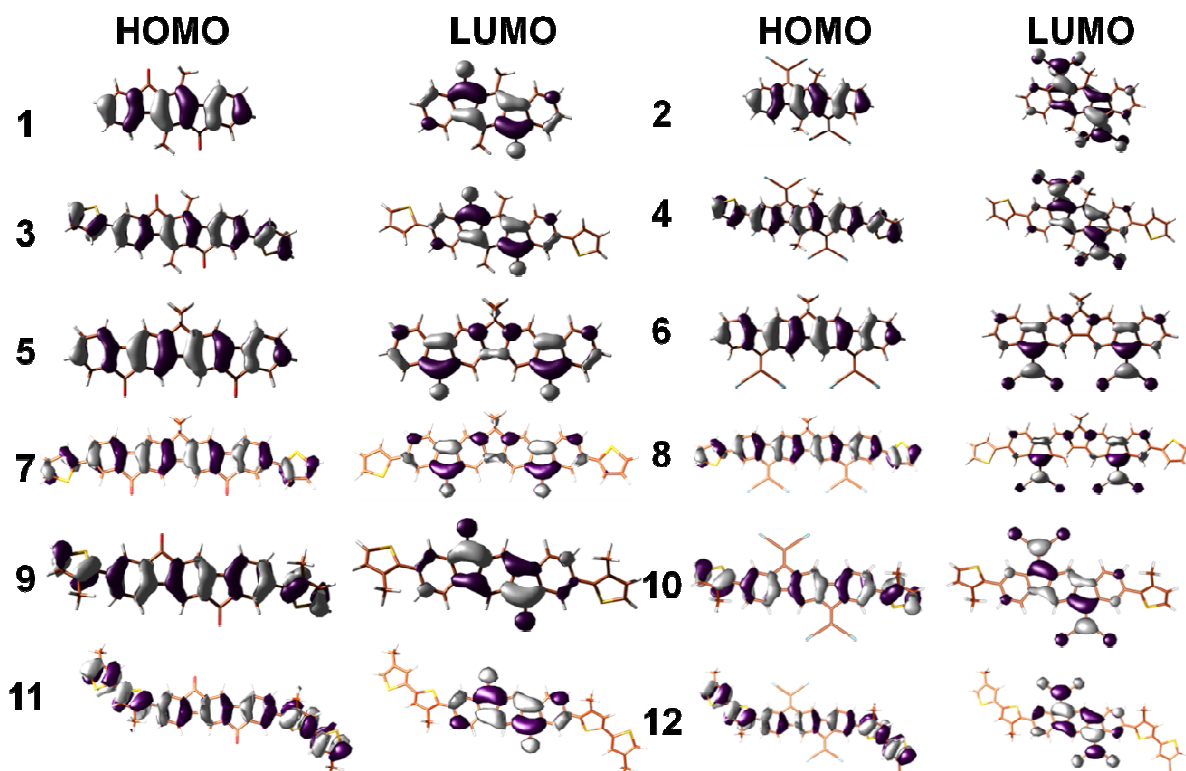


Figure 3.15. HOMO and LUMO pictorial representation for the present carbonyl- (1, 3, 5, 7, 9, and 11) and dicyanovinylene-substituted (2, 4, 6, 8, 10, and 12) semiconductors.

3.4.2 Molecular Architecture and HOMO/LUMO Energetics vs. FET Performance and Air Stability.

The present carbonyl- and dicyanovinylene-functionalized ladder-type molecules and polymers comprise a unique family of semiconductors exhibiting *n*-channel and/or *p*-channel charge transport under both vacuum and ambient. Through functional group and core modifications, the intrinsic molecular properties governing majority carrier sign, device performance, and air-stability can be deduced. Analyses of the molecular physicochemical properties, thin film

microstructures, and FET device performance/air-stability reveal strong correlations between these parameters.

The relative positions of the HOMO/LUMO energies versus the work function of the source/drain electrodes (Au: 5.1 eV)²⁵ are crucial in determining the major charge-carrier type in FETs.⁶⁷ According to a simple Schottky-type charge injection barrier model, the relative electron and hole injection rates have an exponential dependence on the electron (Φ_e) and hole injection barriers (Φ_h), defined as the difference between the metal electrode Fermi level (E_F) and the semiconductor LUMO and HOMO energies, respectively.⁶⁸ Furthermore, the relative positions of these orbitals with respect to H_2O - and O_2 -oxidation/reduction reactions determine the ambient stabilities of the electrons/holes during the charge transport process.¹¹ As shown in Figure 15, the optically/electrochemically estimated HOMO and LUMO energy levels of the present compounds and polymers span a wide range of energies up to 1.0 eV (-3.19 eV \rightarrow -4.32 eV for LUMOs, and -5.34 eV \rightarrow -6.16 eV for HOMOs) providing important information on molecular orbital energetic-majority charge carrier type-ambient stability relationships. In general, decreasing the LUMO energy is found to facilitate electron injection/transport, whereas hole injection/transport is found to be enhanced by increasing the HOMO energy. Thiophene-terminated carbonyl-functionalized compound **7** is a *p*-channel semiconductor and does not exhibit significant *n*-channel behavior as a result of a high electron-injection barrier ($\Phi_e = 0.8$ eV). Upon increasing the electron-deficiency of the system (**7** \rightarrow **3** and **9**), LUMO energies fall and *n*-channel activities are observed along with *p*-channel activities as a result of similar electron and hole injection barriers ($\Phi_{e/h} = 0.5$ eV – 0.6 eV). Especially, for compound **9**, highly balanced electron and hole mobilities ($\mu_e/\mu_h \sim 1.0$) most likely reflect balanced electron and hole

injection barriers. Upon dicyanovinylene functionalization, both HOMO and LUMO energies are lowered even further which results in an increased hole injection barrier and a decreased relative electron injection barrier, thus facilitating electron transport. Experimentally, dicyanovinylene-based compounds **4**, **6**, **8**, and **10** are *n*-channel semiconductors with negligible *p*-channel activity, reflecting high hole injection barriers ($\Phi_h = 0.7 - 0.9$ eV). Similar correlations are also observed for polymeric semiconductors: highly electron-deficient homopolymer **P6** exhibits unipolar *n*-channel behavior and bithiophene copolymers **P3**, **P7**, and **P12** are found to be *p*-channel semiconductors. In contrast, donor-acceptor copolymers **P8**, **P13**, and **P14**, having the highly electron-deficient dicyanovinylene (bis)indenofluorene unit as an acceptor and bithiophene as a donor, exhibit ambipolar behavior as a result of the low band gaps (1.3 – 1.6 eV), resulting in balanced hole/electron injection barriers.

Interestingly, diketone-functionalized compounds **1** and **5** exhibit no FET response for vapor-deposited/solution-cast films, in contrast to their highly reversible electrochemical reduction properties, low LUMO levels (≤ -3.2 eV), and high crystallinities. Such inactivity may be due to minimal orbital overlap in the thin film phase which would reduce the transfer integral for charge transport between molecules in the conduction channel.^{26, 69} However, the addition of thiophenes to the molecular termini of the core structures (**1** and **5**) facilitates charge transport, yielding ambipolar (**3**) and *p*-channel (**7**) FET behavior, which indicates the beneficial effects of increased effective π -conjugation length and core size on charge transport.

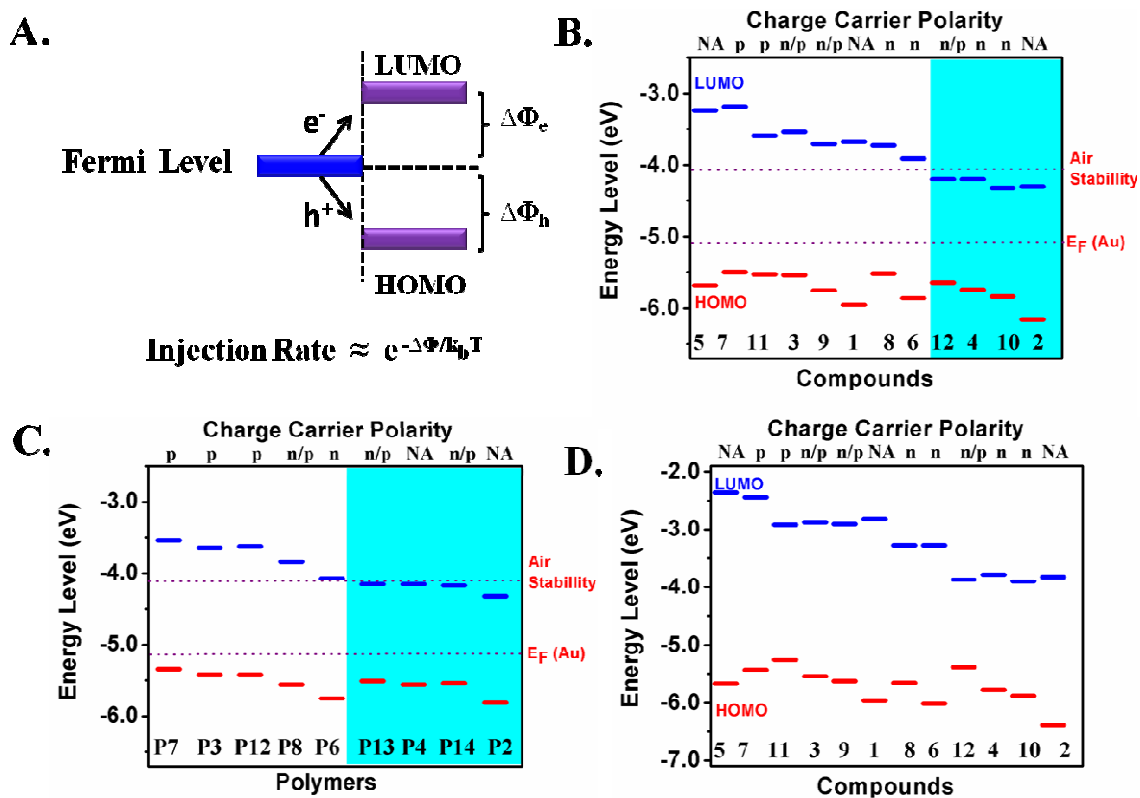


Figure 3.16. (A) Schematic of a Schottky-type injection barrier between a metal electrode and an organic semiconductor, showing electron/hole injection barriers. The energy diagram for compounds 1-12, and polymers P2, P3, P6, P7, P8, and P12-P14 showing experimentally estimated (B and C) and theoretical (D) HOMO/LUMO energy levels, and charge carrier polarity. Blue region indicates TFT devices with ambient stability. The dashed lines indicate the Fermi level of the gold electrode and the air-stability limit. The dashed lines indicate the Fermi level of the gold electrode and the air-stability limit.

In general, for the solution-processed OFETs, thin-film crystallinity and grain size are found to be the key parameters in performance, regardless of the intrinsic HOMO/LUMO energetics. Semiconductors forming highly crystalline thin-films (judged by FWHM, XRD peak intensities,

the presence of higher order of reflections, and rocking curves) generally have superior FET performance versus films having lower degrees of crystallinity. As an example, although compound **10** forms highly crystalline films with large grains (3 – 5 μm) due to the favorable orientation of the alkyl chain substituents (β, β') which do not interfere with the molecular planarity and promote self-assembly, thin-films of **4** have poor crystallinity with small grains ($< 0.1 \mu\text{m}$) as a result of non-favorable alkyl chain orientations, disrupting molecular planarity and eventually, intermolecular interactions. Considering the identical molecular backbone structures, the differences in thin-film microstructure and device performance ($\mu_e = 0.0001 \text{ cm}^2/\text{V}\cdot\text{s}$ for **4**, and $\mu_e = 0.16 \text{ cm}^2/\text{V}\cdot\text{s}$ for **10**) reflect the differences in the DSC- and single-crystal-identified solid-state cohesive forces (*vide supra*). In addition to the degree of crystallinity, grain size determined by AFM is found to be crucial for efficient charge transport. For **10** and **P13**, although the degree of crystallinity increases significantly on annealing (Figure 10), charge carrier mobility increases only for **10** ($0.001 \text{ cm}^2/\text{V}\cdot\text{s} \rightarrow 0.16 \text{ cm}^2/\text{V}\cdot\text{s}$) whereas it remains essentially constant ($0.0001 \text{ cm}^2/\text{V}\cdot\text{s}$) for **P13**. AFM analysis shows that the crystallinity increase in **10** is associated with an increase in grain size ($0.1 \mu\text{m} \rightarrow 5 \mu\text{m}$), whereas the grain size remains same ($< 0.1 \mu\text{m}$) for **P13**, suggesting that charge transport here may be largely limited by the grain boundary density since the intermolecular charge hopping across the grain boundaries is not as efficient as the within ordered domains. Here we show that increasing grain size by annealing is a promising approach to enhance the charge carrier mobility, similar to previously reported solution-processed FETs of oligo-/poly-thiophenes.⁷⁰ Generally, we do not observe correlations between device performance and injection barrier, however the threshold voltage is found to be affected by the magnitude of the injection barrier. For example, when

aluminum (work function = 4.2 eV) is used as the source and drain electrodes for thin-films of **6** and **P6**, 10 V – 20 V lower threshold voltages are measured compared to the devices with Au electrodes as a result of the lower injection barrier ($\Delta\Phi_e \sim 0.9$ eV). Compounds **4**, **10**, and **12**, having the lowest LUMO energies (< -4.20 eV) among all compounds examined, exhibit very low threshold voltages of ~ 0 V – 5 V, whereas other *n*-channel compounds (LUMO > -4.0 eV) exhibit higher threshold voltages of ~ 20 V – 30 V, probably reflecting, among many factors, the differences in injection barriers which are also evident in the slight curvatures in the source-drain current plots at low source-drain voltages in the output curves of **6** and **8** (Figure 3.13).

Although the present realization of thermodynamically air-stable *n*-channel semiconductors shows that low LUMO energies are necessary for efficient charge transport in ambient, the exact parameters governing the air-stability still remain unresolved.⁷ Therefore, it is still important to further understand the structural and electronic criteria leading to the ambient stability in *n*-channel organic semiconductors. To investigate the effects of molecular energetics on device ambient stability, HOMO/LUMO energies were finely tuned ($\Delta \sim 0.1$ eV) over 1.0 eV for a series of semiconductors, and their impact on the ambient stability explored (Figure 3.16). FETs fabricated with **4**, **10**, **12**, **P13**, and **P14** operate stably in air, without any device performance degradation, whereas the other *n*-channel semiconductors **3**, **6**, **8**, **9**, **P6**, and **P8** only operate satisfactorily under vacuum. Assuming similar thin film microstructures and morphologies for the present molecules/polymers, and assuming that Marcus reorganization energies, intermolecular orbital overlap, interface dipoles, and charge traps are essentially constant due to molecular structure/device similarities, the differences in air-stability must mainly be a function of LUMO energy.¹³ The low LUMO energies of the former semiconductors can stabilize the

injected charge carriers against the reactions with ambient species (O_2/H_2O). Detailed analysis of the molecular/polymeric orbital energetics indicates that an onset LUMO energy of $-4.1 - -4.0$ eV is essential to stabilize electrons during charge transport, and an overpotential of $0.9 - 1.0$ eV is operative in the reactions of negatively charged organic π -anions with O_2/H_2O . This overpotential must reflect the energetic barriers to the penetration of ambient species into the active conduction channel,^{1, 5, 62} which is in proximity to the gate dielectric and $\sim 40 - 50$ nm underneath the semiconductor/air interface.⁷¹ The density of grain boundaries, through which ambient species most likely penetrate the film doubtless affects the magnitude of the overpotential. We suggest that the differences between the actual energies of the film electrons during the charge transport on OTS-treated Si/SiO₂ substrates and the LUMOs estimated from solution/thin-film cyclic voltammetries also contribute to the exact overpotential value.

Although the thin film microstructure is crucial to FET device performance, its impact on ambient stability is still unresolved. If the semiconductor film microstructure (morphology and crystallinity) plays a role in ambient stability, one would expect a thin film with a high degree of crystallinity, large grains, and a low density of grain boundaries to be less susceptible to the diffusion of environmental traps into the thin-film, and therefore to be more stable in air compared to a film with a high density of grain boundaries and a low degree of crystallinity. We investigated the air stability trends in solution-cast thin films of compound **10**. The unique thermal response of the TFT devices based on **10** allows us to prepare thin films with a wide range of grain sizes ($0.1 \mu\text{m} - 5 \mu\text{m}$) with morphologies changing from small ball-like grains to large plate-like grains, and having a wide range of crystallinities, including different crystalline phases, XRD intensities (200 counts/s – 60,000 counts/s), and FWHMs ($0.2 - 0.4^\circ$). As shown in

Figure 8, regardless of these microstructural variations, all **10** thin films exhibit similar stability trends in air with little to no degradation. In marked contrast, for the films of semiconductors with LUMOs outside the ambient stability window (> -4.0 eV – -4.1 eV), regardless of film microstructure, devices always exhibit severe degradation in air. These observations argue that although film microstructure is important for the device performance, its contribution to the air-stability is minimal, and ambient stability is mainly governed by LUMO energetics, consistent with other recent work on core-cyanated perylenes.⁷ These results are critical to the development of new air-stable *n*-channel semiconductors.

3.5 Conclusions

A new family of carbonyl-/dicyanovinylene-functionalized bis(indenofluorene) compounds **1-12** and their corresponding homo- and copolymers **P1-P14** has been synthesized and characterized by DSC, TGA, melting point, solution/thin-film UV-vis, PL, and cyclic voltammetry measurements. Optical and electrochemical data demonstrate that HOMO/LUMO energetics can be finely tuned in steps of ~ 0.1 eV over a window of 1.0 eV via core and functional group modifications. Vapor-deposited and solution-cast thin films are characterized by XRD and AFM, indicating the presence of well-organized lamellar microstructures with the common preferential molecular/chain “edge-on” orientation relative to the substrate. Strong correlations are seen between molecular physicochemical properties, thin film microstructures, and FET device performance/air-stability. We observe that the relative positions of HOMO and LUMO energies versus the source and drain electrode work functions affect the charge injection barriers, which eventually determine the charge carrier characteristics. For the semiconductors with high electron injection barriers and low hole injection barriers (**7**, **11**, **P3**, **P7**, and **P12**), *p*-

channel (μ_h up to $0.01 \text{ cm}^2/\text{V}\cdot\text{s}$) behavior is observed. For the semiconductors with balanced electron and hole injection barriers (**3**, **9**, **12**, **P8**, **P13**, and **P14**), ambipolar (μ_e up to $0.01 \text{ cm}^2/\text{V}\cdot\text{s}$ and μ_h up to $0.006 \text{ cm}^2/\text{V}\cdot\text{s}$) behavior is observed, including the first examples of molecular and polymeric ambipolar semiconductors operating in air, achieved via the synthesis of low band gap ($1.36 \text{ eV} - 1.40 \text{ eV}$) donor-acceptor structures. Furthermore, *n*-channel behavior (μ_e up to $0.02 \text{ cm}^2/\text{V}\cdot\text{s}$) is observed for semiconductors **4**, **6**, **8**, **10**, and **P6** with low electron injection barriers. For semiconductors with sufficiently low LUMO energies ($< -4.1 \text{ eV}$), air-stable *n*-channel behavior with mobilities up to $0.16 \text{ cm}^2/\text{V}\cdot\text{s}$ are realized with exceptionally high on/off ratios of $10^7 - 10^8$, exhibiting some of the best solution-based FET performance reported to date for an *n*-channel semiconductor in ambient. Analysis of the air-stability of a series of thin semiconductor films with different crystallinities, orientations, and morphologies reveals that air-stability for the present semiconductors is principally governed by the LUMO energy with negligible contribution from film microstructure. We estimate the onset LUMO energy for electron stabilization during charge transport to be $-4.0 - -4.1 \text{ eV}$, indicating an overpotential of $0.9 - 1.0 \text{ eV}$ to the reaction of the *n*-type charge carriers with $\text{O}_2/\text{H}_2\text{O}$. Density functional theory (DFT) calculations fully explain the observed electronic structure trends associated with core structure and functional group alterations. The findings presented here demonstrate that through rational molecular/macromolecular design guided by computational modeling, a new family of highly electron-deficient ladder-type semiconductors is realized with desired molecular/OFET properties. Furthermore, the present results provide key information related to the structural and electronic criteria controlling the air-stability of *n*-channel materials.

Table 3.1. Summary of Thermal, Optical Absorption/Emission, and Electrochemical Properties of Compounds **1-12**, and Corresponding Estimated Frontier Molecular Orbital Energies.

Comp	mp (°C)	T _{DSC} (°C) ^d heating (cooling)	T _{TGA} ^b (°C)	E _{sol.} ^{red-1/2} (V) ^c	E _{film} ^{red-1} (V) ^d	E _{LUMO} (eV) ^e	E _{HOMO} (eV) ^f	λ _{abs} ^{solution} (nm)	λ _{em} ^{sol} (nm) ^h	λ _{abs} ^{thin-film} (nm)	λ _{em} ^{thin-film} (nm)	(E _g (eV)) ^k (nm)
1	122	121 (82)	380	-0.77	-0.73	-3.67	-5.95	368, 484 (2.28)	590	375, 533 (2.16)	561, 587	
2	136	135 (N.A.)	400	-0.14	-0.15	-4.30	-6.16	426, 579 (1.83)	762 ⁱ	423, 576 (1.80)	755 ⁱ	
3	220	225 (200)	395	-0.90	-0.73	-3.54	-5.54	374, 537 (2.02)	623	364, 620 (1.80)	530, 570	
4	225	229 (N.A.)	360	-0.24	-0.20	-4.20	-5.74	430, 661 (1.54)	770 ⁱ	440, 690 (1.50)	750 ⁱ	
5	138	138, 144 (N.A.)	375	-1.20	-1.10	-3.24	-5.68	365, 455 (2.44)	540	372, 490 (2.34)	551	
6	252	240, 251 (164)	385	-0.53	-0.54	-3.91	-5.86	378, 513 (1.95)	768 ⁱ	385, 610 (1.86)	760 ⁱ	
7	180	177, 188 (60)	405	-1.25	-1.25	-3.19	-5.50	394, 472 (2.31)	545	406, 531 (2.16)	569	
8	280	271, 279 (243)	410	-0.72	-0.70	-3.72	-5.52	400, 576 (1.80)	785 ⁱ	410, 652 (1.72)	720 ⁱ	
9	152	155 (128)	420	-0.74	-0.72	-3.70	-5.75	377, 525 (2.05)	619	365, 594 (1.89)	640	
10	232	93, 234 (200, 74)	403	-0.12	-0.20	-4.32	-5.84	418, 653 (1.52)	780 ⁱ	412, 759 (1.50)	730 ⁱ	
11	96	98 (N.A.)	382	-0.85	-0.80	-3.59	-5.53	394, 540 (1.94)	670	380, 611 (1.86)	670	
12	103	105 (73)	370	-0.20	-0.30	-4.20	-5.64	410, 711 (1.44)	785 ⁱ	378, 738 (1.40)	740 ⁱ	

^a From DSC scans under nitrogen at a scan rate of 5 °C/min. ^b Onset decomposition temperature measured by thermogravimetric analysis under nitrogen. ^c 0.1 M Bu₄N⁺PF₆⁻ in THF (vs SCE) at a scan rate of 100 mV/s. ^d As thin-film with 0.1 M Bu₄N⁺PF₆⁻ in Acetonitrile (vs SCE). ^e Estimated from the equation: E_{LUMO} = -4.44 eV - E_{sol.}^{red-1/2}. ^f E_{HOMO} is calculated from: E_g = E_{LUMO} - E_{HOMO}. ^g From optical absorption in THF, optical band gap is estimated from the low energy band edge of the UV-Vis spectrum. ^h From optical emission in THF. ⁱ Broad, weak emission peak. ^k From optical absorption as spin-coated thin-film on glass, optical band gap is estimated from the low energy band edge of the UV-Vis spectrum.

Table 3.2. Majority charge carrier types, field-effect mobilities (μ), threshold voltages (V_T), and current I_{on}/I_{off} ratios for thin-films of compounds **1-12** fabricated by spin-coating/vacuum-deposition on OTS-treated Si/p⁺-SiO₂ substrates.^a The mobility values, threshold voltages, and I_{on}/I_{off} ratios given are the average values for 10 devices with the standard deviations less than 5%.

Comp.	Polarity	Vapor deposition ($T_D = 70^\circ\text{C}$)			Vapor deposition ($T_D = 110^\circ\text{C}$)			Solution-processed		
		μ (cm ² /V s)	I_{on}/I_{off}	V_T (V)	μ (cm ² /V s)	I_{on}/I_{off}	V_T (V)	μ (cm ² /V s)	I_{on}/I_{off}	V_T (V)
3	N, P	0.002 (e ⁻)	10 ³	+45 V (e ⁻)	0.01 (e ⁻)	10 ⁶	+60 V (e ⁻)	0.001 (h ⁺)	10 ⁴	-42 V (h ⁺)
		2×10 ⁻⁴ (h ⁺)		-50 V (h ⁺)	6×10 ⁻⁴ (h ⁺)	10 ⁷	-40 V (h ⁺)			
4^b	N (Air-Stable)	4×10 ⁻⁴	10 ⁴	+10V	0.001	10 ⁵	+3V	0.0001	10 ⁴	+7 V
6	N	0.002	10 ⁵	+25 V	0.006	10 ⁶	+30 V	0.0004	10 ⁵	+32 V
7	P	0.6×10 ⁻³	10 ⁵	-25 V	0.001	10 ⁵	-18V	0.0001	10 ⁵	-27 V
8	N	0.004	10 ⁵	+20 V	0.02	10 ⁶	+20 V	0.0003	10 ⁴	+25 V
9	N, P	0.002 (e ⁻ , h ⁺)	10 ⁴	+50 V (e ⁻)	0.006 (e ⁻ , h ⁺)	10 ⁴	+50 V (e ⁻)	0.0002 (e ⁻ , h ⁺)	10 ⁴	+60 V (e ⁻)
				-32 V (h ⁺)			-30 V (h ⁺)			-35 V (h ⁺)
10^b	N (Air-Stable)	0.03	10 ⁶	+2V	0.16	10 ⁷	+5V	0.16	10 ⁸	+5V
11	P	- ^c	- ^c	- ^c	- ^c	- ^c	- ^c	0.0001	10 ⁴	-30 V (h ⁺)
12^b	N, P (Air-Stable)	- ^c	- ^c	- ^c	- ^c	- ^c	- ^c	0.001 (e ⁻)	10 ⁵	+20 V (e ⁻)
								1×10 ⁻⁴ (h ⁺)		-25 V (h ⁺)

Table 3.7. Low-lying excited-state energies (eV and nm), oscillator strengths, and excited-state configurations for **1** as determined at the B3LYP/6-31G** level.

λ/eV	λ/nm	Osc. Str.	Configuration
2.47	502	0.02	HOMO \rightarrow LUMO (99%)
3.46	358	0.02	HOMO \rightarrow LUMO+1 (56%); HOMO-2 \rightarrow LUMO (28%); HOMO-4 \rightarrow LUMO (7%)
3.51	354	0.05	HOMO-2 \rightarrow LUMO (54%); HOMO \rightarrow LUMO+1 (25%); HOMO \rightarrow LUMO+2 (11%)
4.00	310	0.03	HOMO-5 \rightarrow LUMO (79%); HOMO-6 \rightarrow LUMO (10%)
4.36	284	1.16	HOMO \rightarrow LUMO+2 (81%); HOMO-2 \rightarrow LUMO (12%)
4.58	271	0.01	HOMO-2 \rightarrow LUMO+1 (91%)

Table 3.8. Low-lying excited-state energies (eV and nm), oscillator strengths, and excited-state configurations for **2** as determined at the B3LYP/6-31G** level.

λ/eV	λ/nm	Osc. Str.	Configuration
1.93	643	0.99	HOMO \rightarrow LUMO (99%)
2.94	422	0.38	HOMO-1 \rightarrow LUMO (83%); HOMO-3 \rightarrow LUMO (12%)
3.04	408	0.01	HOMO-2 \rightarrow LUMO (84%); HOMO \rightarrow LUMO+1 (7%); HOMO-1 \rightarrow LUMO+1 (5%)
3.15	394	0.10	HOMO-3 \rightarrow LUMO (82%); HOMO-1 \rightarrow LUMO (13%)
3.71	334	0.05	HOMO-1 \rightarrow LUMO+1 (86%); HOMO-2 \rightarrow LUMO (6%); HOMO-6 \rightarrow LUMO (5%)
3.86	321	0.17	HOMO-2 \rightarrow LUMO+1 (71%); HOMO \rightarrow LUMO+2 (14%); HOMO-5 \rightarrow LUMO (10%)
4.08	304	0.40	HOMO-5 \rightarrow LUMO (61%); HOMO-4 \rightarrow LUMO+1 (14%); HOMO \rightarrow LUMO+2 (9%); HOMO-1 \rightarrow LUMO+2 (8%)
4.12	301	0.16	HOMO-4 \rightarrow LUMO+1 (68%); HOMO \rightarrow LUMO+2 (14%); HOMO-5 \rightarrow LUMO (10%)
4.32	287	0.80	HOMO \rightarrow LUMO+2 (53%); HOMO-2 \rightarrow LUMO +1(18%); HOMO-5 \rightarrow LUMO (12%); HOMO-4 \rightarrow LUMO+1 (10%)
4.41	281	0.05	HOMO-6 \rightarrow LUMO (85%); HOMO-1 \rightarrow LUMO (6%)
4.52	274	0.01	HOMO-1 \rightarrow LUMO+2 (76%); HOMO \rightarrow LUMO+3 (14%)

Table 3.9. Low-lying excited-state energies (eV and nm), oscillator strengths, and excited-state configurations for **3** as determined at the B3LYP/6-31G** level.

λ/eV	λ/nm	Osc. Str.	Configuration
2.11	589	0.11	HOMO \rightarrow LUMO (98%)
3.38	367	0.32	HOMO \rightarrow LUMO+2 (60%); HOMO-6 \rightarrow LUMO (15%); HOMO-4 \rightarrow LUMO (10%); HOMO-7 \rightarrow LUMO (7%)
3.43	362	0.02	HOMO-2 \rightarrow LUMO (89%); HOMO-7 \rightarrow LUMO (7%)
3.69	336	1.38	HOMO-4 \rightarrow LUMO (53%); HOMO \rightarrow LUMO+2 (30%); HOMO-6 \rightarrow LUMO (9%)
3.72	333	0.33	HOMO-6 \rightarrow LUMO (37%); HOMO-4 \rightarrow LUMO (34%); HOMO-7 \rightarrow LUMO (19%); HOMO \rightarrow LUMO+2 (6%)
3.79	327	0.11	HOMO-1 \rightarrow LUMO+1 (92%)
4.04	307	0.07	HOMO-9 \rightarrow LUMO (85%)

Table 3.10 Low-lying excited-state energies (eV and nm), oscillator strengths, and excited-state configurations for **4** as determined at the B3LYP/6-31G** level.

λ/eV	λ/nm	Osc. Str.	Configuration
1.48	840	0.04	HOMO \rightarrow LUMO (98%)
2.78	447	0.01	HOMO-3 \rightarrow LUMO (73%); HOMO \rightarrow LUMO (15%); HOMO-5 \rightarrow LUMO (7%)
2.92	424	0.16	HOMO-2 \rightarrow LUMO (44%); HOMO-1 \rightarrow LUMO+1 (23%); HOMO-3 \rightarrow LUMO (13%); HOMO-7 \rightarrow LUMO (10%); HOMO \rightarrow LUMO+2 (6%)
2.98	416	0.06	HOMO-1 \rightarrow LUMO+1 (69%); HOMO-2 \rightarrow LUMO (13%); HOMO-7 \rightarrow LUMO (10%); HOMO-3 \rightarrow LUMO+2 (5%)
3.16	393	0.43	HOMO-7 \rightarrow LUMO (40%); HOMO \rightarrow LUMO+2 (24%); HOMO-2 \rightarrow LUMO (20%); HOMO-3 \rightarrow LUMO (7%)
3.36	369	1.67	HOMO \rightarrow LUMO+2 (61%); HOMO-7 \rightarrow LUMO (35%)
3.84	323	0.06	HOMO-4 \rightarrow LUMO+1 (97%)
3.99	311	0.29	HOMO-6 \rightarrow LUMO+1 (80%); HOMO-9 \rightarrow LUMO (10%)
4.18	297	0.17	HOMO-2 \rightarrow LUMO+2 (40%); HOMO-9 \rightarrow LUMO (34%); HOMO-6 \rightarrow LUMO+1 (10%); HOMO-3 \rightarrow LUMO+2 (5%)
4.27	290	0.03	HOMO-9 \rightarrow LUMO (48%); HOMO-2 \rightarrow LUMO+2 (33%); HOMO \rightarrow LUMO+4 (12%)
4.46	278	0.20	HOMO-3 \rightarrow LUMO+2 (70%); HOMO \rightarrow LUMO+5 (17%)
4.51	275	0.11	HOMO-1 \rightarrow LUMO+3 (33%); HOMO \rightarrow LUMO+4 (27%); HOMO-5 \rightarrow LUMO+2 (22%); HOMO-2 \rightarrow LUMO+2 (9%)
4.54	273	0.13	HOMO-5 \rightarrow LUMO+2 (63%); HOMO \rightarrow LUMO+4 (9%); HOMO-1 \rightarrow LUMO+3 (7%); HOMO \rightarrow LUMO+5 (5%)
4.58	271	0.02	HOMO-1 \rightarrow LUMO+3 (27%); HOMO \rightarrow LUMO+4 (25%); HOMO \rightarrow LUMO+5 (21%); HOMO-8 \rightarrow LUMO+1 (19%)

Table 3.11. Low-lying excited-state energies (eV and nm), oscillator strengths, and excited-state configurations for **5** as determined at the B3LYP/6-31G** level.

λ/eV	λ/nm	Osc. Str.	Configuration
2.72	455	0.08	HOMO \rightarrow LUMO (95%)
3.64	340	0.59	HOMO \rightarrow LUMO+2 (83%); HOMO-5 \rightarrow LUMO (9%)
3.87	320	0.07	HOMO-1 \rightarrow LUMO+1 (93%)
4.24	292	1.32	HOMO-5 \rightarrow LUMO (65%); HOMO-4 \rightarrow LUMO+1 (15%); HOMO \rightarrow LUMO+2 (14%)
4.36	285	0.03	HOMO-6 \rightarrow LUMO (35%); HOMO-5 \rightarrow LUMO+1 (29%); HOMO-4 \rightarrow LUMO (24%)
4.46	278	0.11	HOMO-4 \rightarrow LUMO+1 (38%); HOMO-7 \rightarrow LUMO (26%); HOMO \rightarrow LUMO+4 (12%); HOMO-6 \rightarrow LUMO+1 (9%); HOMO-5 \rightarrow LUMO (6%)
4.49	276	0.02	HOMO-6 \rightarrow LUMO (37%); HOMO-5 \rightarrow LUMO+1 (29%); HOMO-7 \rightarrow LUMO+1 (12%); HOMO-4 \rightarrow LUMO (6%); HOMO \rightarrow LUMO+5 (5%)

Table 3.12. Low-lying excited-state energies (eV and nm), oscillator strengths, and excited-state configurations for **6** as determined at the B3LYP/6-31G** level.

λ/eV	λ/nm	Osc. Str.	Configuration
2.16	575	0.01	HOMO \rightarrow LUMO (96%)
3.23	384	0.02	HOMO-3 \rightarrow LUMO+1 (90%)
3.31	374	0.02	HOMO-1 \rightarrow LUMO (58%); HOMO-2 \rightarrow LUMO+1 (33%)
3.47	357	0.24	HOMO \rightarrow LUMO+2 (39%); HOMO-1 \rightarrow LUMO+1 (26%); HOMO-2 \rightarrow LUMO (15%); HOMO-5 \rightarrow LUMO (11%); HOMO-4 \rightarrow LUMO+1 (7%)
3.52	353	0.04	HOMO-1 \rightarrow LUMO+1 (29%); HOMO-5 \rightarrow LUMO (20%); HOMO-2 \rightarrow LUMO (19%); HOMO-4 \rightarrow LUMO+1 (17%); HOMO \rightarrow LUMO+2 (9%)
3.64	340	0.71	HOMO-2 \rightarrow LUMO+1 (61%); HOMO-1 \rightarrow LUMO (33%)
3.86	321	1.49	HOMO \rightarrow LUMO+2 (46%); HOMO-5 \rightarrow LUMO (37%); HOMO-4 \rightarrow LUMO+1 (6%)
3.88	320	0.08	HOMO-4 \rightarrow LUMO+1 (66%); HOMO-5 \rightarrow LUMO (29%)
4.23	293	0.08	HOMO-6 \rightarrow LUMO (80%); HOMO-2 \rightarrow LUMO+2 (11%)
4.27	291	0.08	HOMO-6 \rightarrow LUMO+1 (63%); HOMO-1 \rightarrow LUMO+2 (28%)
4.44	280	0.02	HOMO-2 \rightarrow LUMO+2 (68%); HOMO \rightarrow LUMO+4 (17%); HOMO-6 \rightarrow LUMO (12%)

Table 3.13. Low-lying excited-state energies (eV and nm), oscillator strengths, and excited-state configurations for **7** as determined at the B3LYP/6-31G** level.

λ/eV	λ/nm	Osc. Str.	Configuration
2.48	501	0.30	HOMO \rightarrow LUMO (93%)
3.22	385	0.15	HOMO-1 \rightarrow LUMO+1 (77%); HOMO \rightarrow LUMO+2 (11%); HOMO \rightarrow LUMO (5%)
3.29	376	1.33	HOMO \rightarrow LUMO+2 (82%); HOMO-1 \rightarrow LUMO+1 (13%)
3.63	342	0.02	HOMO-2 \rightarrow LUMO (91%)
4.08	304	0.38	HOMO-5 \rightarrow LUMO (43%); HOMO-5 \rightarrow LUMO+1 (19%); HOMO-6 \rightarrow LUMO (15%); HOMO-8 \rightarrow LUMO (10%)
4.10	302	0.07	HOMO-6 \rightarrow LUMO (45%); HOMO-5 \rightarrow LUMO (23%); HOMO-6 \rightarrow LUMO+1 (18%)
4.11	302	0.05	HOMO-3 \rightarrow LUMO (33%); HOMO-4 \rightarrow LUMO+1 (19%); HOMO-7 \rightarrow LUMO (18%); HOMO-3 \rightarrow LUMO+1 (11%); HOMO \rightarrow LUMO+3 (5%)
4.13	300	0.63	HOMO-8 \rightarrow LUMO (35%); HOMO-7 \rightarrow LUMO+1 (20%); HOMO \rightarrow LUMO+3 (7%); HOMO-3 \rightarrow LUMO (7%); HOMO-6 \rightarrow LUMO (6%); HOMO-4 \rightarrow LUMO+1 (6%)
4.14	299	0.10	HOMO-7 \rightarrow LUMO (40%); HOMO-4 \rightarrow LUMO+1 (13%); HOMO \rightarrow LUMO+3 (10%); HOMO-3 \rightarrow LUMO (8%); HOMO-8 \rightarrow LUMO (6%); HOMO-6 \rightarrow LUMO (6%)
4.25	292	0.04	HOMO-2 \rightarrow LUMO+2 (23%); HOMO-10 \rightarrow LUMO (19%); HOMO-7 \rightarrow LUMO+1 (17%); HOMO \rightarrow LUMO+4 (14%); HOMO \rightarrow LUMO+5 (6%); HOMO-8 \rightarrow LUMO (6%)
4.30	289	0.08	HOMO-7 \rightarrow LUMO+1 (32%); HOMO-1 \rightarrow LUMO+3 (21%); HOMO-8 \rightarrow LUMO (18%); HOMO \rightarrow LUMO+4 (10%)
4.35	285	0.26	HOMO-1 \rightarrow LUMO+3 (40%); HOMO-2 \rightarrow LUMO+2 (23%); HOMO-9 \rightarrow LUMO (7%); HOMO \rightarrow LUMO+4 (7%)
4.36	285	0.07	HOMO-9 \rightarrow LUMO (57%); HOMO-8 \rightarrow LUMO+1 (9%); HOMO \rightarrow LUMO+6 (6%); HOMO-1 \rightarrow LUMO+3 (5%)
4.41	281	0.01	HOMO-5 \rightarrow LUMO+1 (43%); HOMO-5 \rightarrow LUMO (15%); HOMO-11 \rightarrow LUMO (13%); HOMO-10 \rightarrow LUMO (8%)
4.42	281	0.01	HOMO-6 \rightarrow LUMO+1 (49%); HOMO-6 \rightarrow LUMO (15%); HOMO-10 \rightarrow LUMO (9%); HOMO \rightarrow LUMO+5 (6%); HOMO-1 \rightarrow LUMO+3 (5%)
4.43	280	0.07	HOMO-6 \rightarrow LUMO+1 (18%); HOMO-1 \rightarrow LUMO+3 (13%); HOMO \rightarrow LUMO+5 (12%); HOMO-10 \rightarrow LUMO (11%); HOMO-9 \rightarrow LUMO+1 (8%); HOMO-5 \rightarrow LUMO+1 (8%); HOMO-6 \rightarrow LUMO (7%); HOMO \rightarrow LUMO+4 (5%)
4.46	278	0.01	HOMO-4 \rightarrow LUMO+2 (64%); HOMO \rightarrow LUMO+4 (8%); HOMO-8 \rightarrow LUMO+1 (5%)
4.47	278	0.01	HOMO-8 \rightarrow LUMO+1 (43%); HOMO-11 \rightarrow LUMO (13%); HOMO-4 \rightarrow LUMO+2 (8%); HOMO-10 \rightarrow LUMO+1 (8%)
4.56	272	0.07	HOMO-9 \rightarrow LUMO+1 (29%); HOMO-2 \rightarrow LUMO+2 (19%); HOMO-11 \rightarrow LUMO+1 (16%); HOMO \rightarrow LUMO+4 (13%); HOMO \rightarrow LUMO+5 (9%)

Table 3.14. Low-lying excited-state energies (eV and nm), oscillator strengths, and excited-state configurations for **8** as determined at the B3LYP/6-31G** level.

λ/eV	λ/nm	Osc. Str.	Configuration
1.87	663	0.06	HOMO \rightarrow LUMO (92%); HOMO-1 \rightarrow LUMO+1 (5%)
2.99	415	0.02	HOMO-2 \rightarrow LUMO (92%)
3.17	391	1.29	HOMO \rightarrow LUMO+2 (89%)
3.30	376	0.02	HOMO-3 \rightarrow LUMO (50%); HOMO-4 \rightarrow LUMO (17%); HOMO-3 \rightarrow LUMO+1 (16%); HOMO-4 \rightarrow LUMO+1 (11%) HOMO-4 \rightarrow LUMO (35%); HOMO \rightarrow LUMO+1 (24%); HOMO-3 \rightarrow LUMO+1 (9%); HOMO-5 \rightarrow LUMO (9%);
3.32	374	0.02	HOMO-3 \rightarrow LUMO (9%); HOMO-5 \rightarrow LUMO+1 (9%) HOMO-6 \rightarrow LUMO (60%); HOMO-6 \rightarrow LUMO+1 (24%);
3.36	370	0.05	HOMO-3 \rightarrow LUMO+1 (5%) HOMO-3 \rightarrow LUMO+1 (41%); HOMO-4 \rightarrow LUMO (31%);
3.48	357	0.23	HOMO-7 \rightarrow LUMO+1 (8%); HOMO-8 \rightarrow LUMO (5%) HOMO-7 \rightarrow LUMO (31%); HOMO-1 \rightarrow LUMO+2 (25%); HOMO-4 \rightarrow LUMO+1 (16%); HOMO-8 \rightarrow LUMO+1 (15%);
3.50	354	0.05	HOMO \rightarrow LUMO+3 (5%)
3.60	345	0.02	HOMO-6 \rightarrow LUMO+1 (65%); HOMO-6 \rightarrow LUMO (23%) HOMO-4 \rightarrow LUMO+1 (37%); HOMO-3 \rightarrow LUMO (21%);
3.63	342	0.48	HOMO-7 \rightarrow LUMO (12%); HOMO-6 \rightarrow LUMO (10%)
3.64	341	0.06	HOMO-6 \rightarrow LUMO+1 (93%); HOMO-6 \rightarrow LUMO (93%) HOMO-7 \rightarrow LUMO+1 (45%); HOMO-8 \rightarrow LUMO (25%);
3.67	338	0.94	HOMO-3 \rightarrow LUMO+1 (8%); HOMO \rightarrow LUMO+2 (5%) HOMO-1 \rightarrow LUMO+2 (53%); HOMO-7 \rightarrow LUMO (21%);
3.69	336	0.02	HOMO \rightarrow LUMO+3 (9%); HOMO-9 \rightarrow LUMO (7%) HOMO-9 \rightarrow LUMO (47%); HOMO \rightarrow LUMO+3 (20%); HOMO-8 \rightarrow LUMO+1 (11%); HOMO-1 \rightarrow LUMO+2 (7%);
3.77	329	0.02	HOMO-7 \rightarrow LUMO (5%) HOMO-8 \rightarrow LUMO (37%); HOMO-9 \rightarrow LUMO+1 (31%);
3.80	326	0.15	HOMO-7 \rightarrow LUMO+1 (21%) HOMO-9 \rightarrow LUMO+1 (56%); HOMO-8 \rightarrow LUMO (13%); HOMO-7 \rightarrow LUMO+1 (11%); HOMO-9 \rightarrow LUMO (6%);
3.93	316	0.01	HOMO-8 \rightarrow LUMO+1 (6%) HOMO \rightarrow LUMO+3 (57%); HOMO-8 \rightarrow LUMO+1 (19%);
4.03	308	0.03	HOMO-1 \rightarrow LUMO+2 (8%); HOMO-9 \rightarrow LUMO (5%) HOMO-2 \rightarrow LUMO+2 (63%); HOMO-4 \rightarrow LUMO+2 (14%);
4.17	298	0.05	HOMO \rightarrow LUMO+4 (10%) HOMO-1 \rightarrow LUMO+3 (79%); HOMO-2 \rightarrow LUMO+2 (6%);
4.27	291	0.48	HOMO-4 \rightarrow LUMO+2 (5%)
4.29	289	0.04	HOMO-3 \rightarrow LUMO+2 (77%); HOMO \rightarrow LUMO+6 (6%)

Table 3.15. Low-lying excited-state energies (eV and nm), oscillator strengths, and excited-state configurations for **9** as determined at the B3LYP/6-31G** level.

λ/eV	λ/nm	Osc. Str.	Configuration
2.16	573	0.08	HOMO \rightarrow LUMO (97%)
3.28	378	0.02	HOMO-2 \rightarrow LUMO (76%); HOMO-4 \rightarrow LUMO (11%); HOMO-6 \rightarrow LUMO (8%)
3.42	362	0.69	HOMO \rightarrow LUMO+2 (80%); HOMO-7 \rightarrow LUMO (12%)
3.46	358	0.07	HOMO-4 \rightarrow LUMO (81%); HOMO-2 \rightarrow LUMO (13%)
3.78	328	0.18	HOMO-1 \rightarrow LUMO+1 (91%)
3.88	319	1.00	HOMO \rightarrow LUMO (72%); HOMO \rightarrow LUMO (13%)
4.18	297	0.11	HOMO-9 \rightarrow LUMO (77%); HOMO-7 \rightarrow LUMO (5%)
4.52	274	0.26	HOMO-2 \rightarrow LUMO+2 (75%); HOMO-6 \rightarrow LUMO+2 (10%)

Table 3.16. Low-lying excited-state energies (eV and nm), oscillator strengths, and excited-state configurations for **10** as determined at the B3LYP/6-31G** level.

λ/eV	λ/nm	Osc. Str.	Configuration
1.47	844	0.02	HOMO \rightarrow LUMO (98%)
2.64	470	0.01	HOMO-4 \rightarrow LUMO (74%); HOMO-2 \rightarrow LUMO (20%)
3.05	406	0.43	HOMO-5 \rightarrow LUMO (91%)
3.19	389	0.02	HOMO-7 \rightarrow LUMO (64%); HOMO \rightarrow LUMO+2 (32%)
3.48	357	1.73	HOMO \rightarrow LUMO+2 (63%); HOMO-7 \rightarrow LUMO (32%)
3.49	355	0.01	HOMO-3 \rightarrow LUMO+1 (97%)
3.97	312	0.47	HOMO-6 \rightarrow LUMO+1 (86%)
4.26	291	0.11	HOMO-9 \rightarrow LUMO (40%); HOMO-5 \rightarrow LUMO+2 (30%); HOMO-8 \rightarrow LUMO+1 (12%); HOMO-4 \rightarrow LUMO+2 (9%)
4.31	288	0.05	HOMO-2 \rightarrow LUMO+2 (94%)
4.46	278	0.06	HOMO \rightarrow LUMO+4 (35%); HOMO-5 \rightarrow LUMO+2 (16%); HOMO-9 \rightarrow LUMO (15%); HOMO-8 \rightarrow LUMO+1 (15%); HOMO-4 \rightarrow LUMO+2 (12%)
4.53	273	0.45	HOMO-4 \rightarrow LUMO+2 (56%); HOMO-5 \rightarrow LUMO+2 (18%); HOMO-8 \rightarrow LUMO+1 (11%)

Table 3.17. Low-lying excited-state energies (eV and nm), oscillator strengths, and excited-state configurations for **11** as determined at the B3LYP/6-31G** level.

λ/eV	λ/nm	Osc. Str.	Configuration
1.92	646	0.16	HOMO \rightarrow LUMO (96%)
2.76	449	0.01	HOMO-2 \rightarrow LUMO (93%)
3.03	409	1.59	HOMO \rightarrow LUMO+2 (92%)
3.20	388	0.12	HOMO-1 \rightarrow LUMO+1 (96%)
3.28	378	0.01	HOMO-1 \rightarrow LUMO+2 (97%)
3.63	342	0.03	HOMO \rightarrow LUMO+3 (90%)
3.69	336	0.66	HOMO-10 \rightarrow LUMO (50%); HOMO-1 \rightarrow LUMO+3 (14%); HOMO-12 \rightarrow LUMO (12%); HOMO \rightarrow LUMO+4 (11%); HOMO-2 \rightarrow LUMO+2 (7%)
3.80	327	0.34	HOMO-1 \rightarrow LUMO+3 (63%); HOMO-2 \rightarrow LUMO+2 (23%)
3.85	322	0.03	HOMO \rightarrow LUMO+4 (64%); HOMO-1 \rightarrow LUMO+3 (15%); HOMO-2 \rightarrow LUMO+2 (14%)
4.03	308	0.01	HOMO-12 \rightarrow LUMO (42%); HOMO-10 \rightarrow LUMO (34%); HOMO-13 \rightarrow LUMO (11%)
4.07	305	0.01	HOMO-1 \rightarrow LUMO+4 (76%); HOMO-11 \rightarrow LUMO (14%)
4.16	298	0.10	HOMO-12 \rightarrow LUMO (38%); HOMO-13 \rightarrow LUMO (36%); HOMO-2 \rightarrow LUMO+2 (10%); HOMO \rightarrow LUMO+4 (5%)
4.28	290	0.34	HOMO-2 \rightarrow LUMO+2 (38%); HOMO-13 \rightarrow LUMO (27%); HOMO \rightarrow LUMO+4 (7%); HOMO \rightarrow LUMO+6 (6%); HOMO- 10 \rightarrow LUMO (5%)
4.47	278	0.01	HOMO-4 \rightarrow LUMO+2 (42%); HOMO-3 \rightarrow LUMO+1 (37%); HOMO-6 \rightarrow LUMO+2 (7%)

Table 3.18. Low-lying excited-state energies (eV and nm), oscillator strengths, and excited-state configurations for **12** as determined at the B3LYP/6-31G** level.

λ/eV	λ/nm	Osc. Str.	Configuration
1.11	1113	0.06	HOMO \rightarrow LUMO (98%)
2.25	551	0.02	HOMO-1 \rightarrow LUMO+1 (99%)
2.83	438	1.41	HOMO \rightarrow LUMO+2 (95%)
3.04	407	0.49	HOMO-7 \rightarrow LUMO (52%); HOMO-8 \rightarrow LUMO (42%)
3.17	391	0.40	HOMO-10 \rightarrow LUMO (75%); HOMO-11 \rightarrow LUMO (16%)
3.28	378	0.40	HOMO-11 \rightarrow LUMO (73%); HOMO-10 \rightarrow LUMO (19%)
3.51	353	0.02	HOMO \rightarrow LUMO+3 (92%)
3.67	338	0.57	HOMO-1 \rightarrow LUMO+3 (84%); HOMO-2 \rightarrow LUMO+2 (8%)
3.76	330	0.01	HOMO-8 \rightarrow LUMO+1 (51%); HOMO-7 \rightarrow LUMO+1 (40%)
3.84	323	0.24	HOMO \rightarrow LUMO+4 (66%); HOMO-1 \rightarrow LUMO+3 (22%); HOMO-2 \rightarrow LUMO+2 (6%)
3.89	319	0.14	HOMO-9 \rightarrow LUMO+1 (60%); HOMO-2 \rightarrow LUMO+2 (25%)
4.14	299	0.21	HOMO-2 \rightarrow LUMO+2 (31%); HOMO \rightarrow LUMO+4 (18%); HOMO-9 \rightarrow LUMO+1 (17%); HOMO-13 \rightarrow LUMO (9%); HOMO-4 \rightarrow LUMO+2 (9%)
4.20	295	0.04	HOMO-4 \rightarrow LUMO+2 (52%); HOMO \rightarrow LUMO+6 (16%); HOMO-7 \rightarrow LUMO+2 (7%); HOMO-6 \rightarrow LUMO+2 (6%)
4.25	292	0.12	HOMO \rightarrow LUMO+6 (37%); HOMO-4 \rightarrow LUMO+2 (18%); HOMO-9 \rightarrow LUMO+1 (8%); HOMO-6 \rightarrow LUMO+2 (8%); HOMO-7 \rightarrow LUMO+2 (7%); HOMO-8 \rightarrow LUMO+2 (6%); HOMO-1 \rightarrow LUMO+5 (5%)
4.31	287	0.01	HOMO-13 \rightarrow LUMO (35%); HOMO \rightarrow LUMO+6 (17%); HOMO-6 \rightarrow LUMO+2 (13%); HOMO-7 \rightarrow LUMO+2 (11%); HOMO-8 \rightarrow LUMO+2 (8%)
4.37	284	0.10	HOMO-6 \rightarrow LUMO+2 (51%); HOMO-4 \rightarrow LUMO+2 (11%); HOMO-1 \rightarrow LUMO+5 (7%); HOMO-7 \rightarrow LUMO+2 (6%); HOMO-8 \rightarrow LUMO+2 (5%)

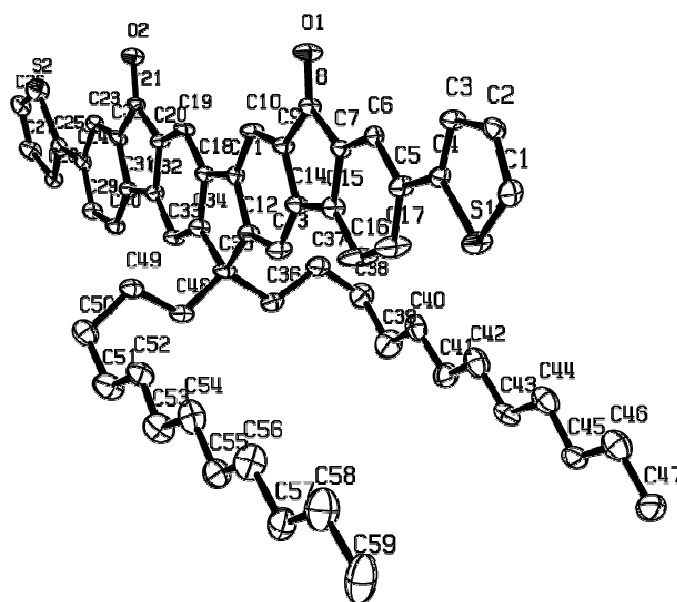


Figure 3.17. ORTEP drawing of compound **7** (30% thermal ellipsoids; hydrogen atoms are omitted for clarity).

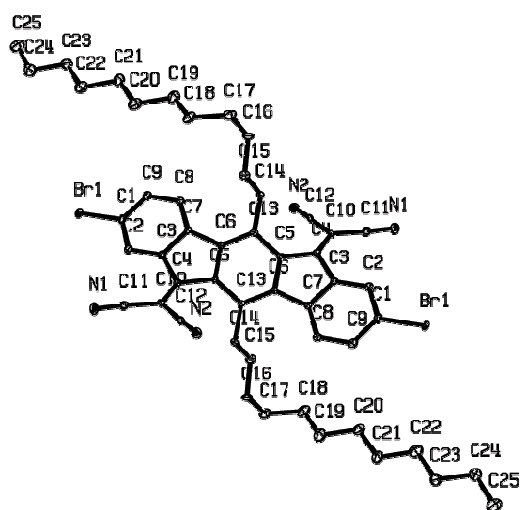


Figure 3.18. ORTEP drawing of compound **M2**. (30% thermal ellipsoids; hydrogen atoms are omitted for clarity).

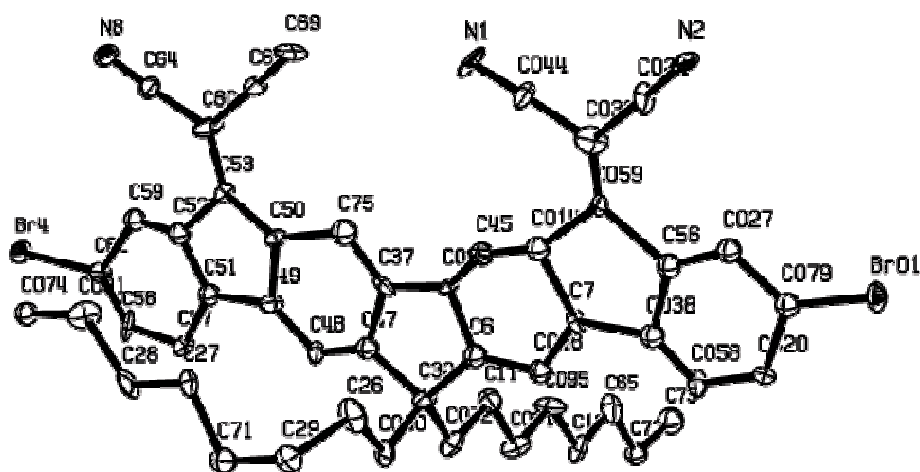


Figure 3.19. ORTEP drawing of compound **M4**. (30% thermal ellipsoids; hydrogen atoms are omitted for clarity).

Data Collection of 7.

A orange plate crystal of C₅₉ H₆₆ O₂ S₂ having approximate dimensions of 0.258 x 0.227 x 0.023 mm was mounted using oil (Infineum V8512) on a glass fiber. All measurements were made on a CCD area detector with graphite monochromated MoK α radiation.

Cell constants and an orientation matrix for data collection corresponded to a Triclinic cell with dimensions:

$$\begin{aligned}
 a &= 12.1895(5) \text{ \AA} & \alpha &= 112.494(2)^\circ \\
 b &= 13.8723(5) \text{ \AA} & \beta &= 110.943(2)^\circ \\
 c &= 16.2994(6) \text{ \AA} & \gamma &= 90.675(3)^\circ \\
 V &= 2342.75(15) \text{ \AA}^3
 \end{aligned}$$

For $Z = 2$ and F.W. = 871.24, the calculated density is 1.235 g/cm³. Based on a statistical analysis of intensity distribution, and the successful solution and refinement of the structure, the space group was determined to be:

P-1

The data were collected at a temperature of 100(2)K with a theta range for data collection of 1.47 to 30.47°. Data were collected in 0.5° oscillations with 20

second exposures. The crystal-to-detector distance was 60.00 mm.

Data Reduction

Of the 26891 reflections which were collected, 12893 were unique ($R_{int} = 0.1919$). Data were collected using APEX2 V2.1-4 (Bruker, 2007) detector and processed using SAINTPLUS from Bruker.

The linear absorption coefficient, μ , for MoK α radiation is 0.158 mm⁻¹. A numerical absorption correction was applied. Minimum and maximum transmission factors were: 0.9603 and 0.9963, respectively. The data were corrected for Lorentz and polarization effects. No crystals examined diffracted beyond 1.1 Å resolution.

Structure Solution and Refinement

The structure was solved by direct methods and expanded using Fourier techniques³. The non-hydrogen atoms were refined anisotropically. Hydrogen atoms were included in idealized positions, but not refined. The final cycle of full-matrix least-squares refinement⁴ on F² was based on 12893 reflections and 569 variable parameters and converged (largest parameter shift was 0.000 times its esd) with unweighted and weighted agreement factors of:

$$R_1 = \sum |F_o| - |F_c| / \sum |F_o| = 0.0869$$

$$wR^2 = \{ \sum [w(F_o^2 - F_c^2)^2] / \sum [w(F_o^2)^2] \}^{1/2} = 0.2066$$

The weighting scheme was calc.

$$\text{calc } w = 1 / [\sigma^2(F_o^2) + (0.1438P)^2 + 0.0000P] \text{ where } P = (F_o^2 + 2F_c^2) / 3$$

The standard deviation of an observation of unit weight⁵ was 0.830.

The weighting scheme was based on counting statistics and included a factor to downweight the intense reflections. Plots of $\sum w (|F_o| - |F_c|)^2$ versus $|F_o|$, reflection order in data collection, $\sin \theta / \lambda$ and various classes of indices showed no unusual trends. The maximum and minimum peaks on the final difference Fourier map corresponded to 0.829 and -0.401 e-/Å³, respectively.

Neutral atom scattering factors were taken from Cromer and Waber⁶. Anomalous dispersion effects were included in Fcalc⁷; the values for Df' and Df'' were those of Creagh and McAuley⁸. The values for the mass attenuation coefficients are those of Creagh and Hubbell⁹. All calculations were performed using the Bruker SHELXTL3 crystallographic software package.

References

- (1) APEX2 V2.1-4 Bruker Analytical X-ray Instruments, Inc.: Madison, WI, 2007
- (2) APEX2 V2.1-4 Bruker Analytical X-ray Instruments, Inc.: Madison, WI, 2007
- (3) Sheldrick, G.M. SHELXTL Version 6.14; Bruker Analytical X-ray Instruments, Inc.: Madison, WI, 2003

- (4) Full-Matrix Least-Squares refinement on F^2 :

$$wR^2 = \{\Sigma[w(F_o^2 - F_c^2)^2] / \Sigma[w(F_o^2)^2]\}^{1/2}$$

- (5) $GooF = S = \{\Sigma[w(F_o^2 - F_c^2)^2] / (n-p)\}^{1/2}$ n = number of reflections; p = total number of reflections refined

- (6) Cromer, D. T. & Waber, J. T.; "International Tables for X-ray Crystallography Vol. IV, The Kynoch Press, Birmingham, England, Table 2.2 A (1974).

- (7) Ibers, J. A. & Hamilton, W. C.; Acta Crystallogr., 17, 781 (1964).

- (8) Creagh, D. C. & McAuley, W.J. ; "International Tables for Crystallography", Vol C, (A.J.C. Wilson, ed.), Kluwer Academic Publishers, Boston, Table 4.2.6.8, pages 219-222 (1992).

- (9) Creagh, D. C. & Hubbell, J.H.; "International Tables for Crystallography", Vol C, (A.J.C. Wilson, ed.), Kluwer Academic Publishers, Boston, Table 4.2.4.3, pages 200-206 (1992).

Table 3.19. Crystal data and structure refinement for compound 7.

Identification code	compound 7
Empirical formula	C ₅₉ H ₆₆ O ₂ S ₂
Formula weight	871.24
Temperature	100(2) K
Wavelength	0.71073 Å
Crystal system, space group	Triclinic, P-1
Unit cell dimensions	a = 12.1895(5) Å α = 112.494(2) ° b = 13.8723(5) Å β = 110.943(2) ° c = 16.2994(6) Å γ = 90.675(3) °
Volume	2342.75(15) Å ³
Z, Calculated density	2, 1.235 Mg/m ³
Absorption coefficient	0.158 mm ⁻¹
F(000)	936
Crystal size	0.258 x 0.227 x 0.023 mm
Theta range for data collection	1.47 to 30.47 °
Limiting indices	-8 ≤ h ≤ 17, -19 ≤ k ≤ 18, -23 ≤ l ≤ 22
Reflections collected / unique	26891 / 12893 [R(int) = 0.1919]
Completeness to theta = 25.00	94.3 %
Absorption correction	Numerical
Max. and min. transmission	0.9963 and 0.9603

Refinement method	Full-matrix least-squares on F ²
Data / restraints / parameters	12893 / 0 / 569
Goodness-of-fit on F ²	0.830
Final R indices [I>2sigma(I)]	R1 = 0.0869, wR2 = 0.2066
R indices (all data)	R1 = 0.3368, wR2 = 0.3307
Largest diff. peak and hole	0.829 and -0.401 e-/Å ⁻³

Table 3.20. Atomic coordinates and equivalent isotropic displacement parameters ($\text{\AA}^2 \times 10^3$) for compound 7. $U(\text{eq})$ is defined as one third of the trace of the orthogonalized U_{ij} tensor.

	x	y	z	$U(\text{eq})$
S(1)	0.20889(16)	0.53596(14)	0.33999(11)	47(1)
S(2)	1.28260(18)	1.22738(15)	1.74660(12)	54(1)
O(1)	0.3945(4)	0.9090(3)	0.8365(3)	43(1)
O(2)	0.9012(3)	1.1260(3)	1.3949(3)	37(1)
C(1)	0.0818(5)	0.5653(5)	0.2727(4)	39(2)
C(2)	0.0478(5)	0.6479(5)	0.3253(4)	34(2)
C(3)	0.1260(5)	0.6917(5)	0.4254(4)	34(2)
C(4)	0.2178(5)	0.6395(4)	0.4444(4)	29(1)
C(5)	0.3179(5)	0.6614(5)	0.5368(4)	34(2)
C(6)	0.3255(5)	0.7438(4)	0.6232(4)	26(1)
C(7)	0.4219(5)	0.7614(4)	0.7078(4)	27(1)
C(8)	0.4523(5)	0.8434(5)	0.8089(4)	31(2)
C(9)	0.5680(5)	0.8249(4)	0.8695(4)	31(2)
C(10)	0.6353(5)	0.8784(4)	0.9672(4)	30(2)
C(11)	0.7394(5)	0.8423(4)	1.0022(4)	28(1)
C(12)	0.7755(5)	0.7547(4)	0.9428(4)	31(2)
C(13)	0.7080(6)	0.7028(5)	0.8451(4)	39(2)
C(14)	0.6030(5)	0.7385(5)	0.8090(4)	33(2)
C(15)	0.5115(5)	0.6999(5)	0.7090(4)	37(2)
C(16)	0.5058(7)	0.6179(6)	0.6256(5)	76(3)
C(17)	0.4073(6)	0.5999(6)	0.5412(4)	64(2)
C(18)	0.8301(5)	0.8791(4)	1.1021(4)	28(1)
C(19)	0.8342(5)	0.9616(4)	1.1862(4)	28(1)
C(20)	0.9306(5)	0.9773(4)	1.2696(4)	27(1)
C(21)	0.9589(5)	1.0578(5)	1.3692(4)	30(1)
C(22)	1.0714(5)	1.0389(5)	1.4312(4)	30(1)
C(23)	1.1358(5)	1.0915(5)	1.5297(4)	32(2)
C(24)	1.2391(5)	1.0564(5)	1.5710(4)	30(1)
C(25)	1.3102(5)	1.1115(5)	1.6774(4)	34(2)
C(26)	1.3931(6)	1.2335(6)	1.8481(4)	47(2)
C(27)	1.4501(6)	1.1518(6)	1.8340(4)	48(2)
C(28)	1.4086(5)	1.0725(4)	1.7336(3)	25(1)
C(29)	1.2761(5)	0.9733(5)	1.5132(4)	33(2)
C(30)	1.2116(5)	0.9213(5)	1.4149(4)	32(2)
C(31)	1.1087(5)	0.9534(4)	1.3733(4)	28(1)

C(32)	1.0204(5)	0.9153(4)	1.2722(4)	30(2)
C(33)	1.0169(5)	0.8329(4)	1.1875(4)	28(1)
C(34)	0.9197(5)	0.8163(5)	1.1029(4)	32(2)
C(35)	0.8948(5)	0.7325(5)	1.0012(4)	33(2)
C(36)	0.8788(5)	0.6187(4)	0.9955(4)	37(2)
C(37)	0.7809(6)	0.5916(5)	1.0240(4)	45(2)
C(38)	0.7682(7)	0.4829(5)	1.0230(5)	55(2)
C(39)	0.7517(8)	0.3924(6)	0.9225(5)	73(3)
C(40)	0.6453(6)	0.3917(6)	0.8361(5)	55(2)
C(41)	0.6298(7)	0.3030(6)	0.7468(5)	55(2)
C(42)	0.5266(7)	0.2983(6)	0.6595(6)	63(2)
C(43)	0.5134(6)	0.2095(6)	0.5678(5)	52(2)
C(44)	0.4022(7)	0.1988(6)	0.4801(5)	58(2)
C(45)	0.3954(7)	0.1125(6)	0.3863(5)	55(2)
C(46)	0.2854(7)	0.1003(6)	0.2988(5)	65(2)
C(47)	0.2759(8)	0.0086(6)	0.2006(6)	76(3)
C(48)	0.9921(5)	0.7457(5)	0.9651(4)	36(2)
C(49)	1.0114(6)	0.8524(5)	0.9599(4)	40(2)
C(50)	1.1184(7)	0.8658(6)	0.9358(5)	56(2)
C(51)	1.1057(7)	0.7767(7)	0.8354(5)	68(2)
C(52)	0.9913(6)	0.7597(6)	0.7447(5)	51(2)
C(53)	0.9883(7)	0.6803(7)	0.6538(5)	67(2)
C(54)	0.8779(7)	0.6646(6)	0.5667(5)	61(2)
C(55)	0.8687(8)	0.5801(6)	0.4733(6)	64(2)
C(56)	0.7605(8)	0.5670(6)	0.3883(5)	70(2)
C(57)	0.7464(7)	0.4752(6)	0.2910(6)	68(2)
C(58)	0.6309(9)	0.4619(7)	0.2069(6)	87(3)
C(59)	0.6187(9)	0.3588(7)	0.1129(6)	105(4)

Table 3.21. Bond lengths [Å] and angles [deg] for compound 7.

S(1)-C(1)	1.706(6)
S(1)-C(4)	1.722(5)
S(2)-C(26)	1.691(6)
S(2)-C(25)	1.693(6)
O(1)-C(8)	1.206(7)
O(2)-C(21)	1.220(6)
C(1)-C(2)	1.316(8)
C(2)-C(3)	1.433(7)
C(3)-C(4)	1.349(8)
C(4)-C(5)	1.475(7)
C(5)-C(17)	1.391(9)
C(5)-C(6)	1.404(8)
C(6)-C(7)	1.385(7)
C(7)-C(15)	1.393(8)
C(7)-C(8)	1.506(7)
C(8)-C(9)	1.496(7)
C(9)-C(10)	1.381(7)
C(9)-C(14)	1.413(8)
C(10)-C(11)	1.380(7)
C(11)-C(12)	1.423(8)
C(11)-C(18)	1.483(7)
C(12)-C(13)	1.380(7)
C(12)-C(35)	1.536(7)
C(13)-C(14)	1.389(8)
C(14)-C(15)	1.485(7)
C(15)-C(16)	1.376(8)
C(16)-C(17)	1.395(8)
C(18)-C(19)	1.393(7)
C(18)-C(34)	1.404(8)
C(19)-C(20)	1.379(7)
C(20)-C(32)	1.399(8)
C(20)-C(21)	1.485(7)
C(21)-C(22)	1.481(8)
C(22)-C(23)	1.384(7)
C(22)-C(31)	1.402(8)
C(23)-C(24)	1.390(8)
C(24)-C(29)	1.380(8)
C(24)-C(25)	1.497(7)
C(25)-C(28)	1.477(8)

C(26)-C(27)	1.323(9)
C(27)-C(28)	1.470(8)
C(29)-C(30)	1.380(7)
C(30)-C(31)	1.367(7)
C(31)-C(32)	1.485(7)
C(32)-C(33)	1.401(7)
C(33)-C(34)	1.394(7)
C(34)-C(35)	1.532(8)
C(35)-C(48)	1.537(9)
C(35)-C(36)	1.551(8)
C(36)-C(37)	1.517(9)
C(37)-C(38)	1.507(9)
C(38)-C(39)	1.576(10)
C(39)-C(40)	1.533(10)
C(40)-C(41)	1.448(9)
C(41)-C(42)	1.503(9)
C(42)-C(43)	1.481(10)
C(43)-C(44)	1.533(9)
C(44)-C(45)	1.512(10)
C(45)-C(46)	1.518(10)
C(46)-C(47)	1.581(10)
C(48)-C(49)	1.535(8)
C(49)-C(50)	1.519(9)
C(50)-C(51)	1.580(10)
C(51)-C(52)	1.562(9)
C(52)-C(53)	1.457(10)
C(53)-C(54)	1.504(10)
C(54)-C(55)	1.488(10)
C(55)-C(56)	1.479(10)
C(56)-C(57)	1.556(10)
C(57)-C(58)	1.522(11)
C(58)-C(59)	1.604(12)
C(1)-S(1)-C(4)	92.0(3)
C(26)-S(2)-C(25)	92.5(3)
C(2)-C(1)-S(1)	112.3(4)
C(1)-C(2)-C(3)	112.6(6)
C(4)-C(3)-C(2)	113.0(5)
C(3)-C(4)-C(5)	129.4(5)
C(3)-C(4)-S(1)	110.1(4)
C(5)-C(4)-S(1)	120.4(4)
C(17)-C(5)-C(6)	117.8(5)
C(17)-C(5)-C(4)	120.8(5)

C(6)-C(5)-C(4)	121.4(5)
C(7)-C(6)-C(5)	118.9(5)
C(6)-C(7)-C(15)	121.7(5)
C(6)-C(7)-C(8)	129.9(5)
C(15)-C(7)-C(8)	108.3(5)
O(1)-C(8)-C(9)	126.7(5)
O(1)-C(8)-C(7)	127.5(5)
C(9)-C(8)-C(7)	105.7(5)
C(10)-C(9)-C(14)	122.4(5)
C(10)-C(9)-C(8)	129.4(5)
C(14)-C(9)-C(8)	108.2(5)
C(11)-C(10)-C(9)	115.6(5)
C(10)-C(11)-C(12)	122.8(5)
C(10)-C(11)-C(18)	129.9(5)
C(12)-C(11)-C(18)	107.2(5)
C(13)-C(12)-C(11)	120.8(5)
C(13)-C(12)-C(35)	127.8(5)
C(11)-C(12)-C(35)	111.3(4)
C(12)-C(13)-C(14)	116.8(5)
C(13)-C(14)-C(9)	121.5(5)
C(13)-C(14)-C(15)	130.1(5)
C(9)-C(14)-C(15)	108.5(5)
C(16)-C(15)-C(7)	120.6(5)
C(16)-C(15)-C(14)	130.1(6)
C(7)-C(15)-C(14)	109.3(5)
C(15)-C(16)-C(17)	117.2(6)
C(5)-C(17)-C(16)	123.7(6)
C(19)-C(18)-C(34)	121.5(5)
C(19)-C(18)-C(11)	129.2(5)
C(34)-C(18)-C(11)	109.3(5)
C(20)-C(19)-C(18)	116.1(5)
C(19)-C(20)-C(32)	123.3(5)
C(19)-C(20)-C(21)	128.4(5)
C(32)-C(20)-C(21)	108.3(5)
O(2)-C(21)-C(22)	126.8(5)
O(2)-C(21)-C(20)	127.0(5)
C(22)-C(21)-C(20)	106.2(5)
C(23)-C(22)-C(31)	121.7(5)
C(23)-C(22)-C(21)	129.6(5)
C(31)-C(22)-C(21)	108.7(5)
C(22)-C(23)-C(24)	118.1(5)
C(29)-C(24)-C(23)	119.7(5)
C(29)-C(24)-C(25)	121.0(5)

C(23)-C(24)-C(25)	119.3(5)
C(28)-C(25)-C(24)	125.2(5)
C(28)-C(25)-S(2)	112.8(4)
C(24)-C(25)-S(2)	122.0(5)
C(27)-C(26)-S(2)	113.8(5)
C(26)-C(27)-C(28)	115.3(6)
C(27)-C(28)-C(25)	105.6(5)
C(24)-C(29)-C(30)	121.9(5)
C(31)-C(30)-C(29)	119.2(5)
C(30)-C(31)-C(22)	119.3(5)
C(30)-C(31)-C(32)	132.6(5)
C(22)-C(31)-C(32)	108.1(5)
C(20)-C(32)-C(33)	120.6(5)
C(20)-C(32)-C(31)	108.8(5)
C(33)-C(32)-C(31)	130.6(5)
C(34)-C(33)-C(32)	116.5(5)
C(33)-C(34)-C(18)	121.9(5)
C(33)-C(34)-C(35)	127.0(5)
C(18)-C(34)-C(35)	111.1(5)
C(34)-C(35)-C(12)	101.0(4)
C(34)-C(35)-C(48)	112.8(5)
C(12)-C(35)-C(48)	111.7(5)
C(34)-C(35)-C(36)	111.6(5)
C(12)-C(35)-C(36)	110.1(5)
C(48)-C(35)-C(36)	109.4(5)
C(37)-C(36)-C(35)	115.7(5)
C(38)-C(37)-C(36)	116.2(6)
C(37)-C(38)-C(39)	112.2(6)
C(40)-C(39)-C(38)	115.0(7)
C(41)-C(40)-C(39)	112.5(7)
C(40)-C(41)-C(42)	114.8(6)
C(43)-C(42)-C(41)	114.7(6)
C(42)-C(43)-C(44)	114.8(6)
C(45)-C(44)-C(43)	113.7(6)
C(44)-C(45)-C(46)	114.4(6)
C(45)-C(46)-C(47)	114.8(7)
C(49)-C(48)-C(35)	115.2(5)
C(50)-C(49)-C(48)	112.5(5)
C(49)-C(50)-C(51)	112.1(6)
C(52)-C(51)-C(50)	118.1(6)
C(53)-C(52)-C(51)	115.2(6)
C(52)-C(53)-C(54)	114.9(7)
C(55)-C(54)-C(53)	116.4(7)

C(56)-C(55)-C(54)	115.6(7)
C(55)-C(56)-C(57)	116.2(7)
C(58)-C(57)-C(56)	114.1(7)
C(57)-C(58)-C(59)	110.3(8)

Table 3.22. Torsion angles [deg] for compound 7.

C(4)-S(1)-C(1)-C(2)	0.0(5)
S(1)-C(1)-C(2)-C(3)	-0.2(7)
C(1)-C(2)-C(3)-C(4)	0.2(8)
C(2)-C(3)-C(4)-C(5)	178.3(6)
C(2)-C(3)-C(4)-S(1)	-0.2(7)
C(1)-S(1)-C(4)-C(3)	0.1(5)
C(1)-S(1)-C(4)-C(5)	-178.5(5)
C(3)-C(4)-C(5)-C(17)	-177.6(7)
S(1)-C(4)-C(5)-C(17)	0.8(9)
C(3)-C(4)-C(5)-C(6)	3.1(11)
S(1)-C(4)-C(5)-C(6)	-178.5(5)
C(17)-C(5)-C(6)-C(7)	1.2(10)
C(4)-C(5)-C(6)-C(7)	-179.5(6)
C(5)-C(6)-C(7)-C(15)	0.4(9)
C(5)-C(6)-C(7)-C(8)	179.7(6)
C(6)-C(7)-C(8)-O(1)	2.6(11)
C(15)-C(7)-C(8)-O(1)	-178.0(7)
C(6)-C(7)-C(8)-C(9)	-179.0(6)
C(15)-C(7)-C(8)-C(9)	0.3(7)
O(1)-C(8)-C(9)-C(10)	-2.0(11)
C(7)-C(8)-C(9)-C(10)	179.7(6)
O(1)-C(8)-C(9)-C(14)	178.1(7)
C(7)-C(8)-C(9)-C(14)	-0.3(7)
C(14)-C(9)-C(10)-C(11)	0.2(9)
C(8)-C(9)-C(10)-C(11)	-179.7(6)
C(9)-C(10)-C(11)-C(12)	-0.9(9)
C(9)-C(10)-C(11)-C(18)	-178.5(6)
C(10)-C(11)-C(12)-C(13)	1.7(10)
C(18)-C(11)-C(12)-C(13)	179.8(6)
C(10)-C(11)-C(12)-C(35)	-180.0(6)
C(18)-C(11)-C(12)-C(35)	-1.9(7)
C(11)-C(12)-C(13)-C(14)	-1.6(10)
C(35)-C(12)-C(13)-C(14)	-179.6(6)
C(12)-C(13)-C(14)-C(9)	0.9(10)
C(12)-C(13)-C(14)-C(15)	-179.6(6)
C(10)-C(9)-C(14)-C(13)	-0.2(10)
C(8)-C(9)-C(14)-C(13)	179.8(6)
C(10)-C(9)-C(14)-C(15)	-179.8(6)
C(8)-C(9)-C(14)-C(15)	0.1(7)

C(6)-C(7)-C(15)-C(16)	-1.0(11)
C(8)-C(7)-C(15)-C(16)	179.6(7)
C(6)-C(7)-C(15)-C(14)	179.2(6)
C(8)-C(7)-C(15)-C(14)	-0.2(7)
C(13)-C(14)-C(15)-C(16)	0.7(13)
C(9)-C(14)-C(15)-C(16)	-179.7(8)
C(13)-C(14)-C(15)-C(7)	-179.5(7)
C(9)-C(14)-C(15)-C(7)	0.1(8)
C(7)-C(15)-C(16)-C(17)	0.0(12)
C(14)-C(15)-C(16)-C(17)	179.8(8)
C(6)-C(5)-C(17)-C(16)	-2.3(12)
C(4)-C(5)-C(17)-C(16)	178.4(8)
C(15)-C(16)-C(17)-C(5)	1.7(14)
C(10)-C(11)-C(18)-C(19)	-1.4(11)
C(12)-C(11)-C(18)-C(19)	-179.3(6)
C(10)-C(11)-C(18)-C(34)	178.7(6)
C(12)-C(11)-C(18)-C(34)	0.8(7)
C(34)-C(18)-C(19)-C(20)	-0.3(9)
C(11)-C(18)-C(19)-C(20)	179.8(6)
C(18)-C(19)-C(20)-C(32)	-0.1(9)
C(18)-C(19)-C(20)-C(21)	-179.9(6)
C(19)-C(20)-C(21)-O(2)	-0.6(11)
C(32)-C(20)-C(21)-O(2)	179.6(6)
C(19)-C(20)-C(21)-C(22)	179.4(6)
C(32)-C(20)-C(21)-C(22)	-0.4(7)
O(2)-C(21)-C(22)-C(23)	0.4(11)
C(20)-C(21)-C(22)-C(23)	-179.7(6)
O(2)-C(21)-C(22)-C(31)	-179.8(6)
C(20)-C(21)-C(22)-C(31)	0.2(7)
C(31)-C(22)-C(23)-C(24)	-0.8(9)
C(21)-C(22)-C(23)-C(24)	179.0(6)
C(22)-C(23)-C(24)-C(29)	1.9(9)
C(22)-C(23)-C(24)-C(25)	-179.7(5)
C(29)-C(24)-C(25)-C(28)	-12.9(9)
C(23)-C(24)-C(25)-C(28)	168.7(6)
C(29)-C(24)-C(25)-S(2)	167.9(5)
C(23)-C(24)-C(25)-S(2)	-10.4(8)
C(26)-S(2)-C(25)-C(28)	0.7(5)
C(26)-S(2)-C(25)-C(24)	179.9(5)
C(25)-S(2)-C(26)-C(27)	-0.9(6)
S(2)-C(26)-C(27)-C(28)	0.9(8)
C(26)-C(27)-C(28)-C(25)	-0.4(8)
C(24)-C(25)-C(28)-C(27)	-179.5(6)

S(2)-C(25)-C(28)-C(27)	-0.3(6)
C(23)-C(24)-C(29)-C(30)	-1.8(9)
C(25)-C(24)-C(29)-C(30)	179.8(6)
C(24)-C(29)-C(30)-C(31)	0.6(10)
C(29)-C(30)-C(31)-C(22)	0.4(9)
C(29)-C(30)-C(31)-C(32)	-179.9(6)
C(23)-C(22)-C(31)-C(30)	-0.3(9)
C(21)-C(22)-C(31)-C(30)	179.8(6)
C(23)-C(22)-C(31)-C(32)	179.9(6)
C(21)-C(22)-C(31)-C(32)	0.0(7)
C(19)-C(20)-C(32)-C(33)	0.6(10)
C(21)-C(20)-C(32)-C(33)	-179.6(6)
C(19)-C(20)-C(32)-C(31)	-179.4(6)
C(21)-C(20)-C(32)-C(31)	0.4(7)
C(30)-C(31)-C(32)-C(20)	180.0(7)
C(22)-C(31)-C(32)-C(20)	-0.3(7)
C(30)-C(31)-C(32)-C(33)	0.0(12)
C(22)-C(31)-C(32)-C(33)	179.7(6)
C(20)-C(32)-C(33)-C(34)	-0.7(9)
C(31)-C(32)-C(33)-C(34)	179.3(6)
C(32)-C(33)-C(34)-C(18)	0.3(9)
C(32)-C(33)-C(34)-C(35)	179.7(6)
C(19)-C(18)-C(34)-C(33)	0.2(10)
C(11)-C(18)-C(34)-C(33)	-179.9(6)
C(19)-C(18)-C(34)-C(35)	-179.3(6)
C(11)-C(18)-C(34)-C(35)	0.6(7)
C(33)-C(34)-C(35)-C(12)	178.9(6)
C(18)-C(34)-C(35)-C(12)	-1.7(7)
C(33)-C(34)-C(35)-C(48)	-61.6(8)
C(18)-C(34)-C(35)-C(48)	117.8(6)
C(33)-C(34)-C(35)-C(36)	62.0(8)
C(18)-C(34)-C(35)-C(36)	-118.6(6)
C(13)-C(12)-C(35)-C(34)	-179.6(6)
C(11)-C(12)-C(35)-C(34)	2.2(7)
C(13)-C(12)-C(35)-C(48)	60.2(8)
C(11)-C(12)-C(35)-C(48)	-118.0(6)
C(13)-C(12)-C(35)-C(36)	-61.6(8)
C(11)-C(12)-C(35)-C(36)	120.2(6)
C(34)-C(35)-C(36)-C(37)	57.5(6)
C(12)-C(35)-C(36)-C(37)	-53.8(6)
C(48)-C(35)-C(36)-C(37)	-177.0(5)
C(35)-C(36)-C(37)-C(38)	-177.3(5)
C(36)-C(37)-C(38)-C(39)	-54.8(8)

C(37)-C(38)-C(39)-C(40)	-57.2(9)
C(38)-C(39)-C(40)-C(41)	-176.2(7)
C(39)-C(40)-C(41)-C(42)	180.0(7)
C(40)-C(41)-C(42)-C(43)	178.1(7)
C(41)-C(42)-C(43)-C(44)	175.1(7)
C(42)-C(43)-C(44)-C(45)	175.9(7)
C(43)-C(44)-C(45)-C(46)	179.6(6)
C(44)-C(45)-C(46)-C(47)	-178.7(7)
C(34)-C(35)-C(48)-C(49)	-59.4(6)
C(12)-C(35)-C(48)-C(49)	53.6(6)
C(36)-C(35)-C(48)-C(49)	175.8(4)
C(35)-C(48)-C(49)-C(50)	172.9(5)
C(48)-C(49)-C(50)-C(51)	59.5(7)
C(49)-C(50)-C(51)-C(52)	54.3(9)
C(50)-C(51)-C(52)-C(53)	176.9(7)
C(51)-C(52)-C(53)-C(54)	-179.9(7)
C(52)-C(53)-C(54)-C(55)	-176.9(7)
C(53)-C(54)-C(55)-C(56)	-179.1(7)
C(54)-C(55)-C(56)-C(57)	-177.0(7)
C(55)-C(56)-C(57)-C(58)	177.3(7)
C(56)-C(57)-C(58)-C(59)	-174.4(7)

Symmetry transformations used to generate equivalent atoms:

Data Collection of M2.

A green block crystal of C₅₀ H₅₆ Br₂ N₄ having approximate dimensions of 0.24 x 0.20 x 0.09 mm was mounted using oil (Infinitec V8512) on a glass fiber. All measurements were made on a CCD area detector with graphite monochromated CuK α radiation.

Cell constants and an orientation matrix for data collection corresponded to a Triclinic cell with dimensions:

$$\begin{aligned} a &= 8.4993(4) \text{ \AA} & \alpha &= 76.650(3)^\circ \\ b &= 10.0232(4) \text{ \AA} & \beta &= 80.592(3)^\circ \\ c &= 14.3879(6) \text{ \AA} & \gamma &= 66.240(3)^\circ \\ V &= 1088.09(9) \text{ \AA}^3 \end{aligned}$$

For $Z = 1$ and F.W. = 872.81, the calculated density is 1.332 g/cm³. Based on a statistical analysis of intensity distribution, and the successful solution and refinement of the structure, the space group was determined to be:

P-1

The data were collected at a temperature of 100(2)K with a theta range for data collection of 4.90 to 66.73°. Data were collected in 0.5° oscillations with 10 second exposures. The crystal-to-detector distance was 50.00 mm.

Data Reduction

Of the 8558 reflections which were collected, 3412 were unique ($R_{int} = 0.0327$). Data were collected using APEX2 V2.1-4 (Bruker, 2007) detector and processed using SAINTPLUS from Bruker.

The linear absorption coefficient, μ , for CuK α radiation is 2.649 mm⁻¹. A numerical absorption correction was applied, minimum and maximum transmission factors were: 0.5725 and 0.7926, respectively. The data were corrected for Lorentz and polarization effects.

Structure Solution and Refinement

The structure was solved by direct methods and expanded using Fourier techniques³. The non-hydrogen atoms were refined anisotropically.

Hydrogen atoms were included in idealized positions, but not refined. The final cycle of full-matrix least-squares refinement⁴ on F² was based on 3412 reflections and 254 variable parameters and converged (largest parameter shift was 0.003 times its esd) with unweighted and weighted agreement factors of:

$$R1 = \Sigma |F_o| - |F_c| / \Sigma |F_o| = 0.0365$$

$$wR^2 = \{ \Sigma [w(F_o^2 - F_c^2)^2] / \Sigma [w(F_o^2)^2] \}^{1/2} = 0.0928$$

The weighting scheme was calc.

$$\text{calc } w = 1 / [\sigma^2(F_o^2) + (0.0586P)^2 + 0.5517P] \text{ where } P = (F_o^2 + 2F_c^2) / 3$$

The standard deviation of an observation of unit weight⁵ was 1.053.

The weighting scheme was based on counting statistics and included a factor to downweight the intense reflections. Plots of $\Sigma w (|F_o| - |F_c|)^2$ versus $|F_o|$, reflection order in data collection, $\sin \theta / \lambda$ and various classes

of indices showed no unusual trends. The maximum and minimum peaks on the final difference Fourier map corresponded to 0.718 and -0.469 e-/Å³, respectively.

Neutral atom scattering factors were taken from Cromer and Waber⁶.

Anomalous dispersion effects were included in Fcalc⁷; the values for Df and Df' were those of Creagh and McAuley⁸. The values for the mass attenuation coefficients are those of Creagh and Hubbell⁹. All calculations were performed using the Bruker SHELXTL³ crystallographic software package.

Table 3.23. Crystal data and structure refinement for M2.

Identification code	s97y
Empirical formula	C ₅₀ H ₅₆ Br ₂ N ₄
Formula weight	872.81
Temperature	100(2) K
Wavelength	1.54178 Å
Crystal system, space group	Triclinic, P-1
Unit cell dimensions	a = 8.4993(4) Å α = 76.650(3) ° b = 10.0232(4) Å β = 80.592(3) ° c = 14.3879(6) Å γ = 66.240(3) °
Volume	1088.09(8) Å ³
Z, Calculated density	1, 1.332 Mg/m ³
Absorption coefficient	2.649 mm ⁻¹
F(000)	454
Crystal size	0.24 x 0.20 x 0.09 mm
Theta range for data collection	4.90 to 66.73 °
Limiting indices	-10 ≤ h ≤ 9, -9 ≤ k ≤ 11, -16 ≤ l ≤ 16
Reflections collected / unique	8558 / 3412 [R(int) = 0.0327]
Completeness to theta = 66.73	89.0 %
Absorption correction	Numerical
Max. and min. transmission	0.7926 and 0.5725
Refinement method	Full-matrix least-squares on F ²

Data / restraints / parameters 3412 / 0 / 254

Goodness-of-fit on F^2 1.053

Final R indices [$I > 2\sigma(I)$] $R_1 = 0.0365$, $wR_2 = 0.0928$

R indices (all data) $R_1 = 0.0422$, $wR_2 = 0.0955$

Largest diff. peak and hole 0.718 and -0.469 $e^{-}/\text{\AA}^{-3}$

Table 3.24. Atomic coordinates and equivalent isotropic displacement parameters ($\text{Å}^2 \times 10^3$) for M2. $U(\text{eq})$ is defined as one third of the trace of the orthogonalized U_{ij} tensor.

	x	y	z	$U(\text{eq})$
Br(1)	0.52690(4)	0.71022(3)	1.518937(19)	25(1)
N(1)	0.4041(3)	0.4455(3)	1.27395(18)	30(1)
N(2)	0.3146(3)	0.6476(2)	0.97640(17)	25(1)
C(1)	0.4855(4)	0.8108(3)	1.39061(19)	21(1)
C(2)	0.4989(3)	0.7299(3)	1.32148(19)	20(1)
C(3)	0.4813(3)	0.8046(3)	1.22772(19)	18(1)
C(4)	0.4844(3)	0.7556(3)	1.13814(18)	17(1)
C(5)	0.5032(3)	0.8711(3)	1.05870(19)	17(1)
C(6)	0.4570(3)	1.0008(3)	1.09753(18)	16(1)
C(7)	0.4479(3)	0.9584(3)	1.20285(19)	18(1)
C(8)	0.4294(4)	1.0368(3)	1.2749(2)	23(1)
C(9)	0.4495(4)	0.9620(3)	1.3688(2)	24(1)
C(10)	0.4332(3)	0.6456(3)	1.13073(19)	19(1)
C(11)	0.4155(3)	0.5360(3)	1.2116(2)	20(1)
C(12)	0.3724(3)	0.6440(3)	1.0436(2)	18(1)
C(13)	0.5589(3)	0.8629(3)	0.96233(19)	17(1)
C(14)	0.6565(3)	0.7191(3)	0.92664(19)	19(1)
C(15)	0.8411(3)	0.7051(3)	0.88817(19)	21(1)
C(16)	0.9400(4)	0.5671(3)	0.8440(2)	25(1)
C(17)	1.1169(4)	0.5614(4)	0.7965(2)	31(1)
C(18)	1.1111(4)	0.6776(4)	0.7058(2)	32(1)
C(19)	1.0570(4)	0.6483(4)	0.6188(2)	36(1)
C(20)	1.0336(4)	0.7742(4)	0.5331(2)	37(1)
C(21)	1.0072(4)	0.7370(4)	0.4416(2)	39(1)
C(22)	0.9776(4)	0.8635(4)	0.3564(2)	38(1)
C(23)	0.9530(4)	0.8229(4)	0.2656(2)	37(1)
C(24)	0.9204(5)	0.9462(4)	0.1791(3)	43(1)
C(25)	0.8997(4)	0.8972(4)	0.0906(3)	43(1)

Table 3.25. Bond lengths [Å] and angles [deg] for M2.

Br(1)-C(1)	1.902(3)
N(1)-C(11)	1.142(4)
N(2)-C(12)	1.141(4)
C(1)-C(2)	1.386(4)
C(1)-C(9)	1.388(4)
C(2)-C(3)	1.383(4)
C(2)-H(2)	0.9500
C(3)-C(7)	1.419(4)
C(3)-C(4)	1.474(4)
C(4)-C(10)	1.368(4)
C(4)-C(5)	1.466(4)
C(5)-C(13)	1.400(4)
C(5)-C(6)	1.417(4)
C(6)-C(13)#1	1.405(4)
C(6)-C(7)	1.474(4)
C(7)-C(8)	1.393(4)
C(8)-C(9)	1.386(4)
C(8)-H(8)	0.9500
C(9)-H(9)	0.9500
C(10)-C(12)	1.438(4)
C(10)-C(11)	1.438(4)
C(13)-C(6)#1	1.405(4)
C(13)-C(14)	1.506(4)
C(14)-C(15)	1.537(4)
C(14)-H(14A)	0.9900
C(14)-H(14B)	0.9900
C(15)-C(16)	1.523(4)
C(15)-H(15A)	0.9900
C(15)-H(15B)	0.9900
C(16)-C(17)	1.531(4)
C(16)-H(16A)	0.9900
C(16)-H(16B)	0.9900
C(17)-C(18)	1.528(5)
C(17)-H(17A)	0.9900
C(17)-H(17B)	0.9900
C(18)-C(19)	1.526(4)
C(18)-H(18A)	0.9900
C(18)-H(18B)	0.9900
C(19)-C(20)	1.520(5)
C(19)-H(19A)	0.9900

C(19)-H(19B)	0.9900
C(20)-C(21)	1.521(5)
C(20)-H(20A)	0.9900
C(20)-H(20B)	0.9900
C(21)-C(22)	1.516(5)
C(21)-H(21A)	0.9900
C(21)-H(21B)	0.9900
C(22)-C(23)	1.523(5)
C(22)-H(22A)	0.9900
C(22)-H(22B)	0.9900
C(23)-C(24)	1.510(5)
C(23)-H(23A)	0.9900
C(23)-H(23B)	0.9900
C(24)-C(25)	1.524(5)
C(24)-H(24A)	0.9900
C(24)-H(24B)	0.9900
C(25)-H(25A)	0.9800
C(25)-H(25B)	0.9800
C(25)-H(25C)	0.9800
C(2)-C(1)-C(9)	122.3(3)
C(2)-C(1)-Br(1)	119.0(2)
C(9)-C(1)-Br(1)	118.7(2)
C(3)-C(2)-C(1)	117.3(2)
C(3)-C(2)-H(2)	121.3
C(1)-C(2)-H(2)	121.3
C(2)-C(3)-C(7)	121.7(2)
C(2)-C(3)-C(4)	131.9(2)
C(7)-C(3)-C(4)	106.4(2)
C(10)-C(4)-C(5)	125.2(2)
C(10)-C(4)-C(3)	125.5(2)
C(5)-C(4)-C(3)	107.1(2)
C(13)-C(5)-C(6)	123.7(2)
C(13)-C(5)-C(4)	129.6(2)
C(6)-C(5)-C(4)	106.7(2)
C(13)#1-C(6)-C(5)	120.9(2)
C(13)#1-C(6)-C(7)	130.9(2)
C(5)-C(6)-C(7)	108.1(2)
C(8)-C(7)-C(3)	119.1(2)
C(8)-C(7)-C(6)	132.0(2)
C(3)-C(7)-C(6)	108.6(2)
C(9)-C(8)-C(7)	119.4(2)
C(9)-C(8)-H(8)	120.3

C(7)-C(8)-H(8)	120.3
C(8)-C(9)-C(1)	120.1(2)
C(8)-C(9)-H(9)	119.9
C(1)-C(9)-H(9)	119.9
C(4)-C(10)-C(12)	121.4(2)
C(4)-C(10)-C(11)	122.7(2)
C(12)-C(10)-C(11)	115.4(2)
N(1)-C(11)-C(10)	177.7(3)
N(2)-C(12)-C(10)	176.0(3)
C(5)-C(13)-C(6)#1	114.8(2)
C(5)-C(13)-C(14)	123.5(2)
C(6)#1-C(13)-C(14)	120.8(2)
C(13)-C(14)-C(15)	110.9(2)
C(13)-C(14)-H(14A)	109.5
C(15)-C(14)-H(14A)	109.5
C(13)-C(14)-H(14B)	109.5
C(15)-C(14)-H(14B)	109.5
H(14A)-C(14)-H(14B)	108.1
C(16)-C(15)-C(14)	112.6(2)
C(16)-C(15)-H(15A)	109.1
C(14)-C(15)-H(15A)	109.1
C(16)-C(15)-H(15B)	109.1
C(14)-C(15)-H(15B)	109.1
H(15A)-C(15)-H(15B)	107.8
C(15)-C(16)-C(17)	112.6(2)
C(15)-C(16)-H(16A)	109.1
C(17)-C(16)-H(16A)	109.1
C(15)-C(16)-H(16B)	109.1
C(17)-C(16)-H(16B)	109.1
H(16A)-C(16)-H(16B)	107.8
C(18)-C(17)-C(16)	114.6(3)
C(18)-C(17)-H(17A)	108.6
C(16)-C(17)-H(17A)	108.6
C(18)-C(17)-H(17B)	108.6
C(16)-C(17)-H(17B)	108.6
H(17A)-C(17)-H(17B)	107.6
C(19)-C(18)-C(17)	114.5(3)
C(19)-C(18)-H(18A)	108.6
C(17)-C(18)-H(18A)	108.6
C(19)-C(18)-H(18B)	108.6
C(17)-C(18)-H(18B)	108.6
H(18A)-C(18)-H(18B)	107.6
C(20)-C(19)-C(18)	113.0(3)

C(20)-C(19)-H(19A)	109.0
C(18)-C(19)-H(19A)	109.0
C(20)-C(19)-H(19B)	109.0
C(18)-C(19)-H(19B)	109.0
H(19A)-C(19)-H(19B)	107.8
C(19)-C(20)-C(21)	113.5(3)
C(19)-C(20)-H(20A)	108.9
C(21)-C(20)-H(20A)	108.9
C(19)-C(20)-H(20B)	108.9
C(21)-C(20)-H(20B)	108.9
H(20A)-C(20)-H(20B)	107.7
C(22)-C(21)-C(20)	114.1(3)
C(22)-C(21)-H(21A)	108.7
C(20)-C(21)-H(21A)	108.7
C(22)-C(21)-H(21B)	108.7
C(20)-C(21)-H(21B)	108.7
H(21A)-C(21)-H(21B)	107.6
C(21)-C(22)-C(23)	113.0(3)
C(21)-C(22)-H(22A)	109.0
C(23)-C(22)-H(22A)	109.0
C(21)-C(22)-H(22B)	109.0
C(23)-C(22)-H(22B)	109.0
H(22A)-C(22)-H(22B)	107.8
C(24)-C(23)-C(22)	114.9(3)
C(24)-C(23)-H(23A)	108.5
C(22)-C(23)-H(23A)	108.5
C(24)-C(23)-H(23B)	108.5
C(22)-C(23)-H(23B)	108.5
H(23A)-C(23)-H(23B)	107.5
C(23)-C(24)-C(25)	112.1(3)
C(23)-C(24)-H(24A)	109.2
C(25)-C(24)-H(24A)	109.2
C(23)-C(24)-H(24B)	109.2
C(25)-C(24)-H(24B)	109.2
H(24A)-C(24)-H(24B)	107.9
C(24)-C(25)-H(25A)	109.5
C(24)-C(25)-H(25B)	109.5
H(25A)-C(25)-H(25B)	109.5
C(24)-C(25)-H(25C)	109.5
H(25A)-C(25)-H(25C)	109.5
H(25B)-C(25)-H(25C)	109.5

Symmetry transformations used to generate equivalent atoms:

#1 -x+1,-y+2,-z+2

Table 3.26. Torsion angles [deg] for M2.

C(9)-C(1)-C(2)-C(3)	2.4(4)
Br(1)-C(1)-C(2)-C(3)	-175.04(19)
C(1)-C(2)-C(3)-C(7)	-1.1(4)
C(1)-C(2)-C(3)-C(4)	-178.6(3)
C(2)-C(3)-C(4)-C(10)	30.1(4)
C(7)-C(3)-C(4)-C(10)	-147.7(3)
C(2)-C(3)-C(4)-C(5)	-165.9(3)
C(7)-C(3)-C(4)-C(5)	16.4(3)
C(10)-C(4)-C(5)-C(13)	-35.3(4)
C(3)-C(4)-C(5)-C(13)	160.6(3)
C(10)-C(4)-C(5)-C(6)	146.2(3)
C(3)-C(4)-C(5)-C(6)	-17.9(3)
C(13)-C(5)-C(6)-C(13)#1	9.2(4)
C(4)-C(5)-C(6)-C(13)#1	-172.2(2)
C(13)-C(5)-C(6)-C(7)	-166.0(2)
C(4)-C(5)-C(6)-C(7)	12.6(3)
C(2)-C(3)-C(7)-C(8)	-1.1(4)
C(4)-C(3)-C(7)-C(8)	177.0(2)
C(2)-C(3)-C(7)-C(6)	173.3(2)
C(4)-C(3)-C(7)-C(6)	-8.7(3)
C(13)#1-C(6)-C(7)-C(8)	-3.6(5)
C(5)-C(6)-C(7)-C(8)	171.0(3)
C(13)#1-C(6)-C(7)-C(3)	-177.0(3)
C(5)-C(6)-C(7)-C(3)	-2.4(3)
C(3)-C(7)-C(8)-C(9)	2.0(4)
C(6)-C(7)-C(8)-C(9)	-170.8(3)
C(7)-C(8)-C(9)-C(1)	-0.8(4)
C(2)-C(1)-C(9)-C(8)	-1.5(4)
Br(1)-C(1)-C(9)-C(8)	175.9(2)
C(5)-C(4)-C(10)-C(12)	-7.5(4)
C(3)-C(4)-C(10)-C(12)	153.7(3)
C(5)-C(4)-C(10)-C(11)	-179.4(2)
C(3)-C(4)-C(10)-C(11)	-18.1(4)
C(4)-C(10)-C(11)-N(1)	-136(7)
C(12)-C(10)-C(11)-N(1)	51(7)

C(4)-C(10)-C(12)-N(2)	-90(4)
C(11)-C(10)-C(12)-N(2)	83(4)
C(6)-C(5)-C(13)-C(6)#1	-8.7(4)
C(4)-C(5)-C(13)-C(6)#1	173.0(3)
C(6)-C(5)-C(13)-C(14)	161.1(2)
C(4)-C(5)-C(13)-C(14)	-17.1(4)
C(5)-C(13)-C(14)-C(15)	-113.8(3)
C(6)#1-C(13)-C(14)-C(15)	55.4(3)
C(13)-C(14)-C(15)-C(16)	-175.4(2)
C(14)-C(15)-C(16)-C(17)	174.1(2)
C(15)-C(16)-C(17)-C(18)	-69.0(3)
C(16)-C(17)-C(18)-C(19)	-72.4(3)
C(17)-C(18)-C(19)-C(20)	173.7(3)
C(18)-C(19)-C(20)-C(21)	171.0(3)
C(19)-C(20)-C(21)-C(22)	178.0(3)
C(20)-C(21)-C(22)-C(23)	179.5(3)
C(21)-C(22)-C(23)-C(24)	179.2(3)
C(22)-C(23)-C(24)-C(25)	179.2(3)

Symmetry transformations used to generate equivalent atoms:

#1 -x+1,-y+2,-z+2

Data Collection of M4

A dark block crystal of C₅₀ H₄₅ Br₂ Cl₃ N₄ having approximate dimensions of 0.25 x 0.22 x 0.21 mm was mounted using oil (Infineum V8512) on a glass fiber. All measurements were made on a CCD area detector with graphite monochromated MoK α radiation.

Cell constants and an orientation matrix for data collection corresponded to a Orthorhombic cell with dimensions:

$$\begin{aligned} a &= 22.2091(6) \text{ \AA} \\ b &= 22.2174(7) \text{ \AA} \\ c &= 36.3970(10) \text{ \AA} \\ V &= 17959.3(9) \text{ \AA}^3 \end{aligned}$$

For $Z = 16$ and F.W. = 968.07, the calculated density is 1.432 g/cm³. Based on a statistical analysis of intensity distribution, and the successful solution and refinement of the structure, the space group was determined to be:

Iba2

The data were collected at a temperature of 100(2)K with a theta range for data collection of 1.07 to 30.55°. Data were collected in 0.5° oscillations with 10 second exposures. The crystal-to-detector distance was 60.00 mm.

Data Reduction

Of the 193890 reflections which were collected, 27207 were unique ($R_{int} = 0.1096$). Data were collected using APEX2 V2.1-4 (Bruker, 2007) detector and processed using SAINTPLUS from Bruker.

The linear absorption coefficient, μ , for MoK α radiation is 2.024 mm⁻¹. A numerical absorption correction was applied. Minimum and maximum transmission factors were: 0.6306 and 0.6759, respectively. The data were corrected for Lorentz and polarization effects.

Structure Solution and Refinement

The structure was solved by direct methods and expanded using Fourier techniques³. The non-hydrogen atoms were refined anisotropically.

Hydrogen atoms were included in idealized positions, but not refined. The unit cell and the consistency in the reflections looked like it was tetrahedral. No solution could be found and using Platon ADDSYM (Spek, 2006) no extra symmetry is found in the reported model. The crystal under investigation was found to be merohedrally twinned. The orientation matrix for the component was found to be $\begin{pmatrix} 0 & -1 & 0 \\ -1 & 0 & 0 \\ 0 & 0 & -1 \end{pmatrix}$. The twin fraction refined to a value of 0.3405(1). The final cycle of full-matrix least-squares refinement on F² was based on 27207 reflections and 1068 variable parameters and converged (largest parameter shift was 0.005 times its esd) with unweighted and weighted agreement factors of:

$$R1 = \sum |F_o| - |F_c| / \sum |F_o| = 0.0436$$

$$wR^2 = \{ \sum [w(F_o^2 - F_c^2)^2] / \sum [w(F_o^2)^2] \}^{1/2} = 0.0684$$

The weighting scheme was calc.

$$\text{calc } w = 1 / [\sigma^2(F_o^2) + (0.0142P)^2 + 0.0000P] \text{ where } P = (F_o^2 + 2F_c^2) / 3$$

The standard deviation of an observation of unit weight⁵ was 1.033.

The weighting scheme was based on counting statistics and included a factor to downweight the intense reflections. Plots of $\sum w (|F_o| - |F_c|)^2$ versus $|F_o|$, reflection order in data collection, $\sin \theta / \lambda$ and various classes of indices showed no unusual trends. The maximum and minimum peaks on the final difference Fourier map corresponded to 0.572 and -0.490 e-/Å³, respectively.

Neutral atom scattering factors were taken from Cromer and Waber⁶.

Anomalous dispersion effects were included in F_{calc}⁷; the values for D_f and D_f' were those of Creagh and McAuley⁸. The values for the mass attenuation coefficients are those of Creagh and Hubbell⁹. All calculations were performed using the Bruker SHELXTL3 crystallographic software package.

Table 3.27. Crystal data and structure refinement for M4.

Identification code	s02z
Empirical formula	C ₅₀ H ₄₅ Br ₂ Cl ₃ N ₄
Formula weight	968.07
Temperature	100(2) K
Wavelength	0.71073 Å
Crystal system, space group	Orthorhombic, Iba2
Unit cell dimensions	a = 22.2091(6) Å b = 22.2174(7) Å c = 36.3970(10) Å
Volume	17959.3(9) Å ³
Z, Calculated density	16, 1.432 Mg/m ³
Absorption coefficient	2.024 mm ⁻¹
F(000)	7904
Crystal size	0.25 x 0.22 x 0.21 mm
Theta range for data collection	1.07 to 30.55 °
Limiting indices	-29 ≤ h ≤ 31, -31 ≤ k ≤ 31, -51 ≤ l ≤ 52
Reflections collected / unique	193890 / 27207 [R(int) = 0.1096]
Completeness to theta = 30.55	99.8 %
Absorption correction	Numerical
Max. and min. transmission	0.6759 and 0.6306
Refinement method	Full-matrix least-squares on F ²

Data / restraints / parameters 27207 / 1 / 1068
Goodness-of-fit on F^2 1.033
Final R indices [$I > 2\sigma(I)$] $R_1 = 0.0436$, $wR_2 = 0.0684$
R indices (all data) $R_1 = 0.0837$, $wR_2 = 0.0720$
Absolute structure parameter 0.079(6)
Largest diff. peak and hole 0.572 and -0.490 $e^{-\text{\AA}^{-3}}$

Table 3.28. Atomic coordinates and equivalent isotropic displacement parameters ($\text{\AA}^2 \times 10^3$) for M4. $U(\text{eq})$ is defined as one third of the trace of the orthogonalized U_{ij} tensor.

	x	y	z	$U(\text{eq})$
Br(1)	0.07821(3)	0.67390(2)	0.296170(19)	25(1)
Br(2)	0.08604(3)	-0.17556(3)	0.314130(17)	25(1)
Br(3)	1.17431(2)	0.41086(3)	0.546154(19)	29(1)
Br(4)	0.32354(2)	0.42355(3)	0.564769(17)	18(1)
Cl(1)	0.28103(8)	0.39962(8)	0.39663(4)	55(1)
Cl(2)	0.17196(7)	0.42135(7)	0.43699(4)	37(1)
Cl(3)	0.28706(6)	0.43659(8)	0.47257(4)	46(1)
Cl(4)	0.08343(6)	0.21595(7)	0.64489(4)	43(1)
Cl(5)	0.07178(6)	0.32849(6)	0.68360(4)	33(1)
Cl(6)	0.06059(7)	0.21616(7)	0.72293(4)	44(1)
N(1)	0.0776(2)	0.5280(2)	0.18394(13)	31(1)
N(2)	0.0829(2)	0.3369(2)	0.18683(12)	28(1)
N(3)	0.0721(2)	0.1507(2)	0.19013(12)	29(1)
N(4)	0.0758(2)	-0.0412(2)	0.19530(12)	26(1)
N(5)	1.0277(2)	0.4236(2)	0.43500(13)	28(1)
N(6)	0.8368(2)	0.4265(2)	0.43772(13)	33(1)
N(7)	0.6491(2)	0.4242(2)	0.44055(12)	28(1)
N(8)	0.4575(2)	0.4260(2)	0.44565(12)	29(1)
C(1)	0.0785(2)	0.5909(2)	0.30738(16)	20(1)
C(2)	0.0787(2)	0.5501(2)	0.27800(15)	14(1)
C(3)	0.0802(2)	0.4890(2)	0.28688(15)	13(1)
C(4)	0.0802(2)	0.4352(2)	0.26295(15)	14(1)
C(5)	0.0813(2)	0.3828(2)	0.28760(14)	12(1)
C(6)	0.0808(2)	0.3209(3)	0.28034(16)	18(1)
C(7)	0.0840(2)	0.2827(2)	0.31051(14)	11(1)
C(8)	0.0826(2)	0.2162(2)	0.31148(13)	12(1)
C(9)	0.0782(2)	0.1750(2)	0.28332(14)	15(1)
C(10)	0.0780(2)	0.1143(2)	0.29263(15)	12(1)
C(11)	0.0772(2)	0.0594(2)	0.27033(15)	14(1)
C(12)	0.0783(2)	0.0074(2)	0.29606(17)	13(1)
C(13)	0.0788(2)	-0.0545(2)	0.28987(14)	14(1)
C(14)	0.0806(2)	-0.0913(2)	0.32112(15)	15(1)
C(15)	0.0810(2)	-0.0686(3)	0.35617(15)	18(1)
C(16)	0.0816(2)	-0.0076(2)	0.36174(16)	18(1)

C(17)	0.0804(2)	0.0307(2)	0.33231(15)	13(1)
C(18)	0.0822(2)	0.0966(2)	0.32996(15)	13(1)
C(19)	0.08702(19)	0.1386(2)	0.35796(14)	14(1)
C(20)	0.08860(19)	0.1981(2)	0.34856(13)	11(1)
C(21)	0.1000(2)	0.2531(2)	0.37312(12)	13(1)
C(22)	0.0891(2)	0.3039(2)	0.34637(13)	13(1)
C(23)	0.08814(19)	0.3652(2)	0.35378(13)	14(1)
C(24)	0.0833(2)	0.4044(2)	0.32393(14)	10(1)
C(25)	0.0812(2)	0.4705(2)	0.32344(15)	12(1)
C(26)	0.0803(2)	0.5110(2)	0.35175(16)	17(1)
C(27)	0.0788(2)	0.5716(3)	0.34353(16)	20(1)
C(28)	0.0802(2)	0.4339(2)	0.22526(13)	17(1)
C(29)	0.0783(2)	0.4873(3)	0.20274(15)	19(1)
C(30)	0.0813(2)	0.3791(2)	0.20403(14)	18(1)
C(31)	0.0761(2)	0.0566(2)	0.23284(13)	15(1)
C(32)	0.0761(2)	0.0010(2)	0.21266(16)	17(1)
C(33)	0.0737(2)	0.1088(3)	0.20923(14)	19(1)
C(34)	0.0611(2)	0.2548(2)	0.40808(13)	17(1)
C(35)	-0.0070(2)	0.2540(2)	0.40260(15)	17(1)
C(36)	-0.0409(2)	0.2533(2)	0.43882(14)	21(1)
C(37)	-0.1094(2)	0.2539(2)	0.43355(13)	23(1)
C(38)	-0.1443(2)	0.2535(2)	0.47012(13)	24(1)
C(39)	-0.2122(2)	0.2561(2)	0.46498(13)	24(1)
C(40)	-0.2464(2)	0.2585(3)	0.50160(16)	29(2)
C(41)	-0.3141(2)	0.2604(3)	0.49706(16)	39(2)
C(42)	0.16797(19)	0.25263(19)	0.38445(12)	14(1)
C(43)	0.2122(2)	0.2567(2)	0.35288(13)	18(1)
C(44)	0.2731(2)	0.2276(2)	0.36110(13)	21(1)
C(45)	0.2713(2)	0.1593(2)	0.36590(14)	22(1)
C(46)	0.2558(2)	0.1266(2)	0.32979(13)	20(1)
C(47)	0.2534(2)	0.0582(2)	0.33373(15)	23(1)
C(48)	0.2464(2)	0.0263(2)	0.29656(17)	23(1)
C(49)	0.2449(2)	-0.0413(3)	0.29876(19)	36(2)
C(50)	1.0907(2)	0.4167(2)	0.55733(15)	15(1)
C(51)	1.0506(2)	0.4198(2)	0.52869(15)	18(1)
C(52)	0.9891(2)	0.4215(2)	0.53728(15)	12(1)
C(53)	0.9357(2)	0.4234(2)	0.51350(14)	12(1)
C(54)	0.8828(2)	0.4224(2)	0.53843(14)	12(1)
C(55)	0.8216(2)	0.4230(2)	0.53121(14)	12(1)
C(56)	0.7831(2)	0.4186(2)	0.56126(13)	12(1)
C(57)	0.7167(2)	0.4178(2)	0.56258(14)	12(1)
C(58)	0.6749(2)	0.4213(2)	0.53401(14)	13(1)
C(59)	0.6138(2)	0.4201(2)	0.54355(15)	10(1)

C(60)	0.5590(2)	0.4216(2)	0.52101(15)	15(1)
C(61)	0.5083(2)	0.4212(2)	0.54640(17)	13(1)
C(62)	0.4451(2)	0.4227(2)	0.54040(15)	17(1)
C(63)	0.4088(2)	0.4235(2)	0.57218(15)	15(1)
C(64)	0.4303(2)	0.4231(2)	0.60691(14)	16(1)
C(65)	0.4925(2)	0.4214(2)	0.61298(15)	14(1)
C(66)	0.5301(2)	0.4202(2)	0.58307(14)	11(1)
C(67)	0.5963(2)	0.4179(2)	0.58088(16)	14(1)
C(68)	0.6379(2)	0.4133(2)	0.60909(14)	15(1)
C(69)	0.6990(2)	0.4126(2)	0.59927(13)	11(1)
C(70)	0.75208(19)	0.4019(2)	0.62412(12)	11(1)
C(71)	0.8040(2)	0.4134(2)	0.59709(13)	11(1)
C(72)	0.8658(2)	0.4136(2)	0.60457(14)	14(1)
C(73)	0.9045(2)	0.4191(2)	0.57508(14)	12(1)
C(74)	0.9710(2)	0.4195(2)	0.57407(14)	13(1)
C(75)	1.0116(2)	0.4177(2)	0.60255(16)	19(1)
C(76)	1.0731(2)	0.4165(2)	0.59374(15)	19(1)
C(77)	0.9335(2)	0.4247(2)	0.47627(13)	14(1)
C(78)	0.9876(2)	0.4242(2)	0.45365(15)	18(1)
C(79)	0.8791(3)	0.4254(2)	0.45504(14)	20(1)
C(80)	0.5561(2)	0.4227(2)	0.48365(14)	16(1)
C(81)	0.6093(2)	0.4231(2)	0.46003(15)	22(1)
C(82)	0.4998(3)	0.4242(3)	0.46298(16)	22(1)
C(83)	0.7539(2)	0.4402(2)	0.65909(12)	12(1)
C(84)	0.7537(2)	0.5076(2)	0.65355(14)	16(1)
C(85)	0.7526(2)	0.5425(2)	0.68985(14)	19(1)
C(86)	0.7515(2)	0.6099(2)	0.68441(13)	20(1)
C(87)	0.7511(2)	0.6452(2)	0.72096(13)	25(1)
C(88)	0.7493(2)	0.7133(2)	0.71541(14)	28(1)
C(89)	0.7457(3)	0.7464(3)	0.75182(17)	36(2)
C(90)	0.7459(3)	0.8156(2)	0.74722(16)	44(2)
C(91)	0.75407(19)	0.3338(2)	0.63547(12)	14(1)
C(92)	0.74651(19)	0.2894(2)	0.60393(13)	15(1)
C(93)	0.7726(2)	0.2274(2)	0.61158(13)	14(1)
C(94)	0.8430(2)	0.2275(2)	0.61532(13)	23(1)
C(95)	0.8742(2)	0.2432(2)	0.57929(13)	17(1)
C(96)	0.9428(2)	0.2438(2)	0.58236(14)	21(1)
C(97)	0.9728(2)	0.2528(2)	0.54494(18)	25(1)
C(98)	1.0417(2)	0.2536(3)	0.54633(19)	32(2)
C(99)	0.2476(2)	0.4446(3)	0.43076(15)	30(2)
C(100)	0.0477(3)	0.2539(2)	0.68106(14)	25(1)

Table 3.29. Bond lengths [Å] and angles [deg] for M4.

Br(1)-C(1)	1.889(5)
Br(2)-C(14)	1.892(5)
Br(3)-C(50)	1.905(5)
Br(4)-C(63)	1.913(5)
Cl(1)-C(99)	1.759(6)
Cl(2)-C(99)	1.772(5)
Cl(3)-C(99)	1.765(5)
Cl(4)-C(100)	1.753(5)
Cl(5)-C(100)	1.744(5)
Cl(6)-C(100)	1.762(5)
N(1)-C(29)	1.135(6)
N(2)-C(30)	1.128(6)
N(3)-C(33)	1.164(6)
N(4)-C(32)	1.130(6)
N(5)-C(78)	1.121(6)
N(6)-C(79)	1.132(6)
N(7)-C(81)	1.133(6)
N(8)-C(82)	1.132(6)
C(1)-C(27)	1.384(8)
C(1)-C(2)	1.402(7)
C(2)-C(3)	1.396(7)
C(2)-H(2)	0.9500
C(3)-C(25)	1.393(7)
C(3)-C(4)	1.479(7)
C(4)-C(28)	1.372(7)
C(4)-C(5)	1.469(7)
C(5)-C(6)	1.401(7)
C(5)-C(24)	1.407(7)
C(6)-C(7)	1.388(7)
C(6)-H(6)	0.9500
C(7)-C(22)	1.392(7)
C(7)-C(8)	1.479(7)
C(8)-C(9)	1.377(7)
C(8)-C(20)	1.415(6)
C(9)-C(10)	1.391(7)
C(9)-H(9)	0.9500
C(10)-C(18)	1.417(7)
C(10)-C(11)	1.465(7)
C(11)-C(31)	1.366(7)
C(11)-C(12)	1.488(7)

C(12)-C(13)	1.393(7)
C(12)-C(17)	1.418(7)
C(13)-C(14)	1.402(7)
C(13)-H(13)	0.9500
C(14)-C(15)	1.372(7)
C(15)-C(16)	1.370(7)
C(15)-H(15)	0.9500
C(16)-C(17)	1.368(7)
C(16)-H(16)	0.9500
C(17)-C(18)	1.467(7)
C(18)-C(19)	1.386(7)
C(19)-C(20)	1.366(7)
C(19)-H(19)	0.9500
C(20)-C(21)	1.536(6)
C(21)-C(22)	1.510(6)
C(21)-C(34)	1.538(6)
C(21)-C(42)	1.564(6)
C(22)-C(23)	1.389(7)
C(23)-C(24)	1.396(7)
C(23)-H(23)	0.9500
C(24)-C(25)	1.469(7)
C(25)-C(26)	1.369(7)
C(26)-C(27)	1.379(7)
C(26)-H(26)	0.9500
C(27)-H(27)	0.9500
C(28)-C(29)	1.442(7)
C(28)-C(30)	1.442(7)
C(31)-C(32)	1.437(7)
C(31)-C(33)	1.444(7)
C(34)-C(35)	1.527(6)
C(34)-H(34A)	0.9900
C(34)-H(34B)	0.9900
C(35)-C(36)	1.519(7)
C(35)-H(35A)	0.9900
C(35)-H(35B)	0.9900
C(36)-C(37)	1.534(7)
C(36)-H(36A)	0.9900
C(36)-H(36B)	0.9900
C(37)-C(38)	1.540(7)
C(37)-H(37A)	0.9900
C(37)-H(37B)	0.9900
C(38)-C(39)	1.520(7)
C(38)-H(38A)	0.9900

C(38)-H(38B)	0.9900
C(39)-C(40)	1.535(7)
C(39)-H(39A)	0.9900
C(39)-H(39B)	0.9900
C(40)-C(41)	1.513(7)
C(40)-H(40A)	0.9900
C(40)-H(40B)	0.9900
C(41)-H(41A)	0.9800
C(41)-H(41B)	0.9800
C(41)-H(41C)	0.9800
C(42)-C(43)	1.515(6)
C(42)-H(42A)	0.9900
C(42)-H(42B)	0.9900
C(43)-C(44)	1.529(6)
C(43)-H(43A)	0.9900
C(43)-H(43B)	0.9900
C(44)-C(45)	1.528(7)
C(44)-H(44A)	0.9900
C(44)-H(44B)	0.9900
C(45)-C(46)	1.541(6)
C(45)-H(45A)	0.9900
C(45)-H(45B)	0.9900
C(46)-C(47)	1.527(7)
C(46)-H(46A)	0.9900
C(46)-H(46B)	0.9900
C(47)-C(48)	1.535(7)
C(47)-H(47A)	0.9900
C(47)-H(47B)	0.9900
C(48)-C(49)	1.505(7)
C(48)-H(48A)	0.9900
C(48)-H(48B)	0.9900
C(49)-H(49A)	0.9800
C(49)-H(49B)	0.9800
C(49)-H(49C)	0.9800
C(50)-C(51)	1.373(7)
C(50)-C(76)	1.381(7)
C(51)-C(52)	1.402(7)
C(51)-H(51)	0.9500
C(52)-C(74)	1.399(7)
C(52)-C(53)	1.469(7)
C(53)-C(77)	1.356(6)
C(53)-C(54)	1.485(7)
C(54)-C(55)	1.384(7)

C(54)-C(73)	1.420(7)
C(55)-C(56)	1.391(7)
C(55)-H(55)	0.9500
C(56)-C(71)	1.389(6)
C(56)-C(57)	1.477(7)
C(57)-C(58)	1.396(7)
C(57)-C(69)	1.396(6)
C(58)-C(59)	1.402(7)
C(58)-H(58)	0.9500
C(59)-C(67)	1.414(7)
C(59)-C(60)	1.468(7)
C(60)-C(80)	1.361(7)
C(60)-C(61)	1.456(7)
C(61)-C(66)	1.420(7)
C(61)-C(62)	1.421(7)
C(62)-C(63)	1.410(7)
C(62)-H(62)	0.9500
C(63)-C(64)	1.351(7)
C(64)-C(65)	1.400(7)
C(64)-H(64)	0.9500
C(65)-C(66)	1.373(7)
C(65)-H(65)	0.9500
C(66)-C(67)	1.472(7)
C(67)-C(68)	1.386(7)
C(68)-C(69)	1.404(7)
C(68)-H(68)	0.9500
C(69)-C(70)	1.504(6)
C(70)-C(83)	1.531(6)
C(70)-C(71)	1.537(6)
C(70)-C(91)	1.568(6)
C(71)-C(72)	1.400(7)
C(72)-C(73)	1.380(7)
C(72)-H(72)	0.9500
C(73)-C(74)	1.478(7)
C(74)-C(75)	1.374(7)
C(75)-C(76)	1.404(7)
C(75)-H(75)	0.9500
C(76)-H(76)	0.9500
C(77)-C(79)	1.434(7)
C(77)-C(78)	1.456(7)
C(80)-C(82)	1.459(7)
C(80)-C(81)	1.462(7)
C(83)-C(84)	1.511(6)

C(83)-H(83A)	0.9900
C(83)-H(83B)	0.9900
C(84)-C(85)	1.532(7)
C(84)-H(84A)	0.9900
C(84)-H(84B)	0.9900
C(85)-C(86)	1.511(7)
C(85)-H(85A)	0.9900
C(85)-H(85B)	0.9900
C(86)-C(87)	1.544(7)
C(86)-H(86A)	0.9900
C(86)-H(86B)	0.9900
C(87)-C(88)	1.526(7)
C(87)-H(87A)	0.9900
C(87)-H(87B)	0.9900
C(88)-C(89)	1.518(7)
C(88)-H(88A)	0.9900
C(88)-H(88B)	0.9900
C(89)-C(90)	1.546(7)
C(89)-H(89A)	0.9900
C(89)-H(89B)	0.9900
C(90)-H(90A)	0.9800
C(90)-H(90B)	0.9800
C(90)-H(90C)	0.9800
C(91)-C(92)	1.523(6)
C(91)-H(91A)	0.9900
C(91)-H(91B)	0.9900
C(92)-C(93)	1.520(6)
C(92)-H(92A)	0.9900
C(92)-H(92B)	0.9900
C(93)-C(94)	1.569(6)
C(93)-H(93A)	0.9900
C(93)-H(93B)	0.9900
C(94)-C(95)	1.524(6)
C(94)-H(94A)	0.9900
C(94)-H(94B)	0.9900
C(95)-C(96)	1.526(6)
C(95)-H(95A)	0.9900
C(95)-H(95B)	0.9900
C(96)-C(97)	1.530(7)
C(96)-H(96A)	0.9900
C(96)-H(96B)	0.9900
C(97)-C(98)	1.532(7)
C(97)-H(97A)	0.9900

C(97)-H(97B)	0.9900
C(98)-H(98A)	0.9800
C(98)-H(98B)	0.9800
C(98)-H(98C)	0.9800
C(99)-H(99)	1.0000
C(100)-H(100)	1.0000
C(27)-C(1)-C(2)	121.7(5)
C(27)-C(1)-Br(1)	120.6(4)
C(2)-C(1)-Br(1)	117.8(4)
C(3)-C(2)-C(1)	116.9(5)
C(3)-C(2)-H(2)	121.6
C(1)-C(2)-H(2)	121.6
C(25)-C(3)-C(2)	120.6(5)
C(25)-C(3)-C(4)	108.9(5)
C(2)-C(3)-C(4)	130.5(5)
C(28)-C(4)-C(5)	126.5(5)
C(28)-C(4)-C(3)	127.2(5)
C(5)-C(4)-C(3)	106.3(5)
C(6)-C(5)-C(24)	120.8(5)
C(6)-C(5)-C(4)	131.5(5)
C(24)-C(5)-C(4)	107.7(5)
C(7)-C(6)-C(5)	116.7(5)
C(7)-C(6)-H(6)	121.6
C(5)-C(6)-H(6)	121.6
C(6)-C(7)-C(22)	122.6(5)
C(6)-C(7)-C(8)	128.9(5)
C(22)-C(7)-C(8)	108.5(4)
C(9)-C(8)-C(20)	121.9(5)
C(9)-C(8)-C(7)	130.3(5)
C(20)-C(8)-C(7)	107.7(4)
C(8)-C(9)-C(10)	117.6(5)
C(8)-C(9)-H(9)	121.2
C(10)-C(9)-H(9)	121.2
C(9)-C(10)-C(18)	120.2(5)
C(9)-C(10)-C(11)	132.2(5)
C(18)-C(10)-C(11)	107.5(5)
C(31)-C(11)-C(10)	126.3(5)
C(31)-C(11)-C(12)	126.4(5)
C(10)-C(11)-C(12)	107.3(5)
C(13)-C(12)-C(17)	120.7(5)
C(13)-C(12)-C(11)	131.7(5)
C(17)-C(12)-C(11)	107.6(5)

C(12)-C(13)-C(14)	116.4(5)
C(12)-C(13)-H(13)	121.8
C(14)-C(13)-H(13)	121.8
C(15)-C(14)-C(13)	122.6(5)
C(15)-C(14)-Br(2)	119.3(4)
C(13)-C(14)-Br(2)	118.0(4)
C(16)-C(15)-C(14)	120.2(5)
C(16)-C(15)-H(15)	119.9
C(14)-C(15)-H(15)	119.9
C(17)-C(16)-C(15)	119.9(5)
C(17)-C(16)-H(16)	120.0
C(15)-C(16)-H(16)	120.0
C(16)-C(17)-C(12)	120.1(5)
C(16)-C(17)-C(18)	131.7(5)
C(12)-C(17)-C(18)	108.1(5)
C(19)-C(18)-C(10)	121.5(5)
C(19)-C(18)-C(17)	129.1(5)
C(10)-C(18)-C(17)	109.3(5)
C(20)-C(19)-C(18)	118.0(5)
C(20)-C(19)-H(19)	121.0
C(18)-C(19)-H(19)	121.0
C(19)-C(20)-C(8)	120.8(5)
C(19)-C(20)-C(21)	129.0(4)
C(8)-C(20)-C(21)	110.2(4)
C(22)-C(21)-C(20)	101.1(4)
C(22)-C(21)-C(34)	115.2(4)
C(20)-C(21)-C(34)	114.0(4)
C(22)-C(21)-C(42)	109.3(4)
C(20)-C(21)-C(42)	107.9(4)
C(34)-C(21)-C(42)	108.9(4)
C(23)-C(22)-C(7)	120.8(5)
C(23)-C(22)-C(21)	127.6(4)
C(7)-C(22)-C(21)	111.4(4)
C(22)-C(23)-C(24)	117.5(5)
C(22)-C(23)-H(23)	121.3
C(24)-C(23)-H(23)	121.3
C(23)-C(24)-C(5)	121.4(5)
C(23)-C(24)-C(25)	129.4(5)
C(5)-C(24)-C(25)	109.2(5)
C(26)-C(25)-C(3)	121.6(5)
C(26)-C(25)-C(24)	130.5(5)
C(3)-C(25)-C(24)	107.9(5)
C(25)-C(26)-C(27)	118.6(5)

C(25)-C(26)-H(26)	120.7
C(27)-C(26)-H(26)	120.7
C(26)-C(27)-C(1)	120.6(5)
C(26)-C(27)-H(27)	119.7
C(1)-C(27)-H(27)	119.7
C(4)-C(28)-C(29)	123.5(5)
C(4)-C(28)-C(30)	123.6(5)
C(29)-C(28)-C(30)	112.9(4)
N(1)-C(29)-C(28)	177.4(6)
N(2)-C(30)-C(28)	178.4(6)
C(11)-C(31)-C(32)	123.4(5)
C(11)-C(31)-C(33)	124.0(5)
C(32)-C(31)-C(33)	112.7(5)
N(4)-C(32)-C(31)	176.7(6)
N(3)-C(33)-C(31)	179.6(6)
C(35)-C(34)-C(21)	116.6(4)
C(35)-C(34)-H(34A)	108.1
C(21)-C(34)-H(34A)	108.1
C(35)-C(34)-H(34B)	108.1
C(21)-C(34)-H(34B)	108.1
H(34A)-C(34)-H(34B)	107.3
C(36)-C(35)-C(34)	112.3(4)
C(36)-C(35)-H(35A)	109.2
C(34)-C(35)-H(35A)	109.2
C(36)-C(35)-H(35B)	109.2
C(34)-C(35)-H(35B)	109.2
H(35A)-C(35)-H(35B)	107.9
C(35)-C(36)-C(37)	112.6(4)
C(35)-C(36)-H(36A)	109.1
C(37)-C(36)-H(36A)	109.1
C(35)-C(36)-H(36B)	109.1
C(37)-C(36)-H(36B)	109.1
H(36A)-C(36)-H(36B)	107.8
C(36)-C(37)-C(38)	113.0(4)
C(36)-C(37)-H(37A)	109.0
C(38)-C(37)-H(37A)	109.0
C(36)-C(37)-H(37B)	109.0
C(38)-C(37)-H(37B)	109.0
H(37A)-C(37)-H(37B)	107.8
C(39)-C(38)-C(37)	113.1(4)
C(39)-C(38)-H(38A)	109.0
C(37)-C(38)-H(38A)	109.0
C(39)-C(38)-H(38B)	109.0

C(37)-C(38)-H(38B)	109.0
H(38A)-C(38)-H(38B)	107.8
C(38)-C(39)-C(40)	112.7(4)
C(38)-C(39)-H(39A)	109.1
C(40)-C(39)-H(39A)	109.1
C(38)-C(39)-H(39B)	109.1
C(40)-C(39)-H(39B)	109.1
H(39A)-C(39)-H(39B)	107.8
C(41)-C(40)-C(39)	113.4(5)
C(41)-C(40)-H(40A)	108.9
C(39)-C(40)-H(40A)	108.9
C(41)-C(40)-H(40B)	108.9
C(39)-C(40)-H(40B)	108.9
H(40A)-C(40)-H(40B)	107.7
C(40)-C(41)-H(41A)	109.5
C(40)-C(41)-H(41B)	109.5
H(41A)-C(41)-H(41B)	109.5
C(40)-C(41)-H(41C)	109.5
H(41A)-C(41)-H(41C)	109.5
H(41B)-C(41)-H(41C)	109.5
C(43)-C(42)-C(21)	115.2(4)
C(43)-C(42)-H(42A)	108.5
C(21)-C(42)-H(42A)	108.5
C(43)-C(42)-H(42B)	108.5
C(21)-C(42)-H(42B)	108.5
H(42A)-C(42)-H(42B)	107.5
C(42)-C(43)-C(44)	113.6(4)
C(42)-C(43)-H(43A)	108.9
C(44)-C(43)-H(43A)	108.9
C(42)-C(43)-H(43B)	108.9
C(44)-C(43)-H(43B)	108.9
H(43A)-C(43)-H(43B)	107.7
C(45)-C(44)-C(43)	114.8(4)
C(45)-C(44)-H(44A)	108.6
C(43)-C(44)-H(44A)	108.6
C(45)-C(44)-H(44B)	108.6
C(43)-C(44)-H(44B)	108.6
H(44A)-C(44)-H(44B)	107.5
C(44)-C(45)-C(46)	112.1(4)
C(44)-C(45)-H(45A)	109.2
C(46)-C(45)-H(45A)	109.2
C(44)-C(45)-H(45B)	109.2
C(46)-C(45)-H(45B)	109.2

H(45A)-C(45)-H(45B)	107.9
C(47)-C(46)-C(45)	113.4(4)
C(47)-C(46)-H(46A)	108.9
C(45)-C(46)-H(46A)	108.9
C(47)-C(46)-H(46B)	108.9
C(45)-C(46)-H(46B)	108.9
H(46A)-C(46)-H(46B)	107.7
C(46)-C(47)-C(48)	112.3(4)
C(46)-C(47)-H(47A)	109.1
C(48)-C(47)-H(47A)	109.1
C(46)-C(47)-H(47B)	109.1
C(48)-C(47)-H(47B)	109.1
H(47A)-C(47)-H(47B)	107.9
C(49)-C(48)-C(47)	114.6(5)
C(49)-C(48)-H(48A)	108.6
C(47)-C(48)-H(48A)	108.6
C(49)-C(48)-H(48B)	108.6
C(47)-C(48)-H(48B)	108.6
H(48A)-C(48)-H(48B)	107.6
C(48)-C(49)-H(49A)	109.5
C(48)-C(49)-H(49B)	109.5
H(49A)-C(49)-H(49B)	109.5
C(48)-C(49)-H(49C)	109.5
H(49A)-C(49)-H(49C)	109.5
H(49B)-C(49)-H(49C)	109.5
C(51)-C(50)-C(76)	123.0(5)
C(51)-C(50)-Br(3)	118.3(4)
C(76)-C(50)-Br(3)	118.7(4)
C(50)-C(51)-C(52)	117.7(5)
C(50)-C(51)-H(51)	121.2
C(52)-C(51)-H(51)	121.2
C(74)-C(52)-C(51)	119.5(5)
C(74)-C(52)-C(53)	109.4(4)
C(51)-C(52)-C(53)	131.0(5)
C(77)-C(53)-C(52)	128.1(5)
C(77)-C(53)-C(54)	125.7(5)
C(52)-C(53)-C(54)	106.2(4)
C(55)-C(54)-C(73)	120.8(5)
C(55)-C(54)-C(53)	131.3(5)
C(73)-C(54)-C(53)	107.8(4)
C(54)-C(55)-C(56)	116.9(5)
C(54)-C(55)-H(55)	121.5
C(56)-C(55)-H(55)	121.5

C(71)-C(56)-C(55)	122.7(5)
C(71)-C(56)-C(57)	107.5(4)
C(55)-C(56)-C(57)	129.8(5)
C(58)-C(57)-C(69)	122.1(5)
C(58)-C(57)-C(56)	129.7(5)
C(69)-C(57)-C(56)	108.2(4)
C(57)-C(58)-C(59)	117.3(5)
C(57)-C(58)-H(58)	121.4
C(59)-C(58)-H(58)	121.4
C(58)-C(59)-C(67)	120.3(5)
C(58)-C(59)-C(60)	131.6(5)
C(67)-C(59)-C(60)	108.0(4)
C(80)-C(60)-C(61)	126.7(5)
C(80)-C(60)-C(59)	126.7(5)
C(61)-C(60)-C(59)	106.6(5)
C(66)-C(61)-C(62)	118.8(5)
C(66)-C(61)-C(60)	109.4(5)
C(62)-C(61)-C(60)	131.7(6)
C(63)-C(62)-C(61)	116.0(5)
C(63)-C(62)-H(62)	122.0
C(61)-C(62)-H(62)	122.0
C(64)-C(63)-C(62)	124.4(5)
C(64)-C(63)-Br(4)	118.8(4)
C(62)-C(63)-Br(4)	116.8(4)
C(63)-C(64)-C(65)	119.8(5)
C(63)-C(64)-H(64)	120.1
C(65)-C(64)-H(64)	120.1
C(66)-C(65)-C(64)	118.4(5)
C(66)-C(65)-H(65)	120.8
C(64)-C(65)-H(65)	120.8
C(65)-C(66)-C(61)	122.5(5)
C(65)-C(66)-C(67)	130.6(5)
C(61)-C(66)-C(67)	106.9(5)
C(68)-C(67)-C(59)	122.1(5)
C(68)-C(67)-C(66)	128.9(5)
C(59)-C(67)-C(66)	109.0(5)
C(67)-C(68)-C(69)	117.2(5)
C(67)-C(68)-H(68)	121.4
C(69)-C(68)-H(68)	121.4
C(57)-C(69)-C(68)	120.9(4)
C(57)-C(69)-C(70)	111.6(4)
C(68)-C(69)-C(70)	127.3(4)
C(69)-C(70)-C(83)	115.6(4)

C(69)-C(70)-C(71)	100.1(4)
C(83)-C(70)-C(71)	114.9(4)
C(69)-C(70)-C(91)	109.5(4)
C(83)-C(70)-C(91)	108.4(4)
C(71)-C(70)-C(91)	107.9(4)
C(56)-C(71)-C(72)	120.6(5)
C(56)-C(71)-C(70)	111.4(4)
C(72)-C(71)-C(70)	127.7(4)
C(73)-C(72)-C(71)	117.4(5)
C(73)-C(72)-H(72)	121.3
C(71)-C(72)-H(72)	121.3
C(72)-C(73)-C(54)	121.6(5)
C(72)-C(73)-C(74)	129.9(5)
C(54)-C(73)-C(74)	108.4(4)
C(75)-C(74)-C(52)	122.3(5)
C(75)-C(74)-C(73)	129.6(5)
C(52)-C(74)-C(73)	108.1(4)
C(74)-C(75)-C(76)	117.8(5)
C(74)-C(75)-H(75)	121.1
C(76)-C(75)-H(75)	121.1
C(50)-C(76)-C(75)	119.6(5)
C(50)-C(76)-H(76)	120.2
C(75)-C(76)-H(76)	120.2
C(53)-C(77)-C(79)	124.6(5)
C(53)-C(77)-C(78)	122.4(5)
C(79)-C(77)-C(78)	113.0(4)
N(5)-C(78)-C(77)	177.1(6)
N(6)-C(79)-C(77)	178.6(6)
C(60)-C(80)-C(82)	123.8(5)
C(60)-C(80)-C(81)	123.3(5)
C(82)-C(80)-C(81)	112.9(4)
N(7)-C(81)-C(80)	177.1(6)
N(8)-C(82)-C(80)	177.1(6)
C(84)-C(83)-C(70)	116.1(4)
C(84)-C(83)-H(83A)	108.3
C(70)-C(83)-H(83A)	108.3
C(84)-C(83)-H(83B)	108.3
C(70)-C(83)-H(83B)	108.3
H(83A)-C(83)-H(83B)	107.4
C(83)-C(84)-C(85)	112.8(4)
C(83)-C(84)-H(84A)	109.0
C(85)-C(84)-H(84A)	109.0
C(83)-C(84)-H(84B)	109.0

C(85)-C(84)-H(84B)	109.0
H(84A)-C(84)-H(84B)	107.8
C(86)-C(85)-C(84)	112.9(4)
C(86)-C(85)-H(85A)	109.0
C(84)-C(85)-H(85A)	109.0
C(86)-C(85)-H(85B)	109.0
C(84)-C(85)-H(85B)	109.0
H(85A)-C(85)-H(85B)	107.8
C(85)-C(86)-C(87)	113.0(4)
C(85)-C(86)-H(86A)	109.0
C(87)-C(86)-H(86A)	109.0
C(85)-C(86)-H(86B)	109.0
C(87)-C(86)-H(86B)	109.0
H(86A)-C(86)-H(86B)	107.8
C(88)-C(87)-C(86)	112.9(4)
C(88)-C(87)-H(87A)	109.0
C(86)-C(87)-H(87A)	109.0
C(88)-C(87)-H(87B)	109.0
C(86)-C(87)-H(87B)	109.0
H(87A)-C(87)-H(87B)	107.8
C(89)-C(88)-C(87)	111.5(4)
C(89)-C(88)-H(88A)	109.3
C(87)-C(88)-H(88A)	109.3
C(89)-C(88)-H(88B)	109.3
C(87)-C(88)-H(88B)	109.3
H(88A)-C(88)-H(88B)	108.0
C(88)-C(89)-C(90)	112.8(5)
C(88)-C(89)-H(89A)	109.0
C(90)-C(89)-H(89A)	109.0
C(88)-C(89)-H(89B)	109.0
C(90)-C(89)-H(89B)	109.0
H(89A)-C(89)-H(89B)	107.8
C(89)-C(90)-H(90A)	109.5
C(89)-C(90)-H(90B)	109.5
H(90A)-C(90)-H(90B)	109.5
C(89)-C(90)-H(90C)	109.5
H(90A)-C(90)-H(90C)	109.5
H(90B)-C(90)-H(90C)	109.5
C(92)-C(91)-C(70)	115.1(4)
C(92)-C(91)-H(91A)	108.5
C(70)-C(91)-H(91A)	108.5
C(92)-C(91)-H(91B)	108.5
C(70)-C(91)-H(91B)	108.5

H(91A)-C(91)-H(91B)	107.5
C(93)-C(92)-C(91)	114.0(4)
C(93)-C(92)-H(92A)	108.7
C(91)-C(92)-H(92A)	108.7
C(93)-C(92)-H(92B)	108.7
C(91)-C(92)-H(92B)	108.7
H(92A)-C(92)-H(92B)	107.6
C(92)-C(93)-C(94)	113.3(4)
C(92)-C(93)-H(93A)	108.9
C(94)-C(93)-H(93A)	108.9
C(92)-C(93)-H(93B)	108.9
C(94)-C(93)-H(93B)	108.9
H(93A)-C(93)-H(93B)	107.7
C(95)-C(94)-C(93)	112.2(4)
C(95)-C(94)-H(94A)	109.2
C(93)-C(94)-H(94A)	109.2
C(95)-C(94)-H(94B)	109.2
C(93)-C(94)-H(94B)	109.2
H(94A)-C(94)-H(94B)	107.9
C(94)-C(95)-C(96)	113.1(4)
C(94)-C(95)-H(95A)	109.0
C(96)-C(95)-H(95A)	109.0
C(94)-C(95)-H(95B)	109.0
C(96)-C(95)-H(95B)	109.0
H(95A)-C(95)-H(95B)	107.8
C(95)-C(96)-C(97)	111.8(4)
C(95)-C(96)-H(96A)	109.3
C(97)-C(96)-H(96A)	109.3
C(95)-C(96)-H(96B)	109.3
C(97)-C(96)-H(96B)	109.3
H(96A)-C(96)-H(96B)	107.9
C(96)-C(97)-C(98)	114.1(5)
C(96)-C(97)-H(97A)	108.7
C(98)-C(97)-H(97A)	108.7
C(96)-C(97)-H(97B)	108.7
C(98)-C(97)-H(97B)	108.7
H(97A)-C(97)-H(97B)	107.6
C(97)-C(98)-H(98A)	109.5
C(97)-C(98)-H(98B)	109.5
H(98A)-C(98)-H(98B)	109.5
C(97)-C(98)-H(98C)	109.5
H(98A)-C(98)-H(98C)	109.5
H(98B)-C(98)-H(98C)	109.5

Cl(1)-C(99)-Cl(3)	110.0(3)
Cl(1)-C(99)-Cl(2)	108.9(3)
Cl(3)-C(99)-Cl(2)	109.3(3)
Cl(1)-C(99)-H(99)	109.5
Cl(3)-C(99)-H(99)	109.5
Cl(2)-C(99)-H(99)	109.5
Cl(5)-C(100)-Cl(4)	111.0(3)
Cl(5)-C(100)-Cl(6)	110.9(3)
Cl(4)-C(100)-Cl(6)	110.4(3)
Cl(5)-C(100)-H(100)	108.2
Cl(4)-C(100)-H(100)	108.2
Cl(6)-C(100)-H(100)	108.2

Symmetry transformations used to generate equivalent atoms:

Table 3.30. Torsion angles [deg] for M4.

C(27)-C(1)-C(2)-C(3)	-0.9(8)
Br(1)-C(1)-C(2)-C(3)	178.7(4)
C(1)-C(2)-C(3)-C(25)	0.1(7)
C(1)-C(2)-C(3)-C(4)	179.2(5)
C(25)-C(3)-C(4)-C(28)	-179.0(5)
C(2)-C(3)-C(4)-C(28)	1.9(9)
C(25)-C(3)-C(4)-C(5)	0.0(5)
C(2)-C(3)-C(4)-C(5)	-179.2(5)
C(28)-C(4)-C(5)-C(6)	-2.0(9)
C(3)-C(4)-C(5)-C(6)	179.0(5)
C(28)-C(4)-C(5)-C(24)	177.7(5)
C(3)-C(4)-C(5)-C(24)	-1.3(5)
C(24)-C(5)-C(6)-C(7)	-1.5(7)
C(4)-C(5)-C(6)-C(7)	178.2(5)
C(5)-C(6)-C(7)-C(22)	-1.9(7)
C(5)-C(6)-C(7)-C(8)	178.0(5)
C(6)-C(7)-C(8)-C(9)	0.3(9)
C(22)-C(7)-C(8)-C(9)	-179.8(5)
C(6)-C(7)-C(8)-C(20)	178.5(5)
C(22)-C(7)-C(8)-C(20)	-1.5(5)
C(20)-C(8)-C(9)-C(10)	1.9(7)
C(7)-C(8)-C(9)-C(10)	179.9(5)
C(8)-C(9)-C(10)-C(18)	0.0(7)
C(8)-C(9)-C(10)-C(11)	-176.3(5)
C(9)-C(10)-C(11)-C(31)	-0.3(8)
C(18)-C(10)-C(11)-C(31)	-177.0(5)

C(9)-C(10)-C(11)-C(12)	179.2(5)
C(18)-C(10)-C(11)-C(12)	2.5(5)
C(31)-C(11)-C(12)-C(13)	0.4(9)
C(10)-C(11)-C(12)-C(13)	-179.1(5)
C(31)-C(11)-C(12)-C(17)	178.9(4)
C(10)-C(11)-C(12)-C(17)	-0.6(5)
C(17)-C(12)-C(13)-C(14)	0.9(7)
C(11)-C(12)-C(13)-C(14)	179.3(5)
C(12)-C(13)-C(14)-C(15)	0.8(7)
C(12)-C(13)-C(14)-Br(2)	-176.5(4)
C(13)-C(14)-C(15)-C(16)	-2.2(8)
Br(2)-C(14)-C(15)-C(16)	175.1(4)
C(14)-C(15)-C(16)-C(17)	1.6(8)
C(15)-C(16)-C(17)-C(12)	0.1(7)
C(15)-C(16)-C(17)-C(18)	-178.2(5)
C(13)-C(12)-C(17)-C(16)	-1.4(7)
C(11)-C(12)-C(17)-C(16)	179.9(4)
C(13)-C(12)-C(17)-C(18)	177.3(4)
C(11)-C(12)-C(17)-C(18)	-1.5(5)
C(9)-C(10)-C(18)-C(19)	-0.5(7)
C(11)-C(10)-C(18)-C(19)	176.7(4)
C(9)-C(10)-C(18)-C(17)	179.4(4)
C(11)-C(10)-C(18)-C(17)	-3.5(5)
C(16)-C(17)-C(18)-C(19)	1.4(9)
C(12)-C(17)-C(18)-C(19)	-177.0(5)
C(16)-C(17)-C(18)-C(10)	-178.4(5)
C(12)-C(17)-C(18)-C(10)	3.1(6)
C(10)-C(18)-C(19)-C(20)	-1.0(7)
C(17)-C(18)-C(19)-C(20)	179.1(5)
C(18)-C(19)-C(20)-C(8)	3.0(7)
C(18)-C(19)-C(20)-C(21)	-173.2(4)
C(9)-C(8)-C(20)-C(19)	-3.6(7)
C(7)-C(8)-C(20)-C(19)	178.0(4)
C(9)-C(8)-C(20)-C(21)	173.2(4)
C(7)-C(8)-C(20)-C(21)	-5.2(5)
C(19)-C(20)-C(21)-C(22)	-174.4(5)
C(8)-C(20)-C(21)-C(22)	9.2(5)
C(19)-C(20)-C(21)-C(34)	-50.2(6)
C(8)-C(20)-C(21)-C(34)	133.4(4)
C(19)-C(20)-C(21)-C(42)	70.9(6)
C(8)-C(20)-C(21)-C(42)	-105.5(4)
C(6)-C(7)-C(22)-C(23)	3.4(7)
C(8)-C(7)-C(22)-C(23)	-176.5(4)

C(6)-C(7)-C(22)-C(21)	-172.3(4)
C(8)-C(7)-C(22)-C(21)	7.8(5)
C(20)-C(21)-C(22)-C(23)	174.4(5)
C(34)-C(21)-C(22)-C(23)	51.0(6)
C(42)-C(21)-C(22)-C(23)	-72.0(6)
C(20)-C(21)-C(22)-C(7)	-10.3(5)
C(34)-C(21)-C(22)-C(7)	-133.7(4)
C(42)-C(21)-C(22)-C(7)	103.4(4)
C(7)-C(22)-C(23)-C(24)	-1.4(7)
C(21)-C(22)-C(23)-C(24)	173.5(4)
C(22)-C(23)-C(24)-C(5)	-1.9(7)
C(22)-C(23)-C(24)-C(25)	-180.0(5)
C(6)-C(5)-C(24)-C(23)	3.4(7)
C(4)-C(5)-C(24)-C(23)	-176.3(4)
C(6)-C(5)-C(24)-C(25)	-178.2(4)
C(4)-C(5)-C(24)-C(25)	2.1(5)
C(2)-C(3)-C(25)-C(26)	0.6(7)
C(4)-C(3)-C(25)-C(26)	-178.6(5)
C(2)-C(3)-C(25)-C(24)	-179.5(4)
C(4)-C(3)-C(25)-C(24)	1.3(5)
C(23)-C(24)-C(25)-C(26)	-4.0(9)
C(5)-C(24)-C(25)-C(26)	177.8(5)
C(23)-C(24)-C(25)-C(3)	176.1(5)
C(5)-C(24)-C(25)-C(3)	-2.1(6)
C(3)-C(25)-C(26)-C(27)	-0.6(7)
C(24)-C(25)-C(26)-C(27)	179.6(5)
C(25)-C(26)-C(27)-C(1)	-0.2(8)
C(2)-C(1)-C(27)-C(26)	1.0(8)
Br(1)-C(1)-C(27)-C(26)	-178.6(4)
C(5)-C(4)-C(28)-C(29)	179.2(5)
C(3)-C(4)-C(28)-C(29)	-2.0(8)
C(5)-C(4)-C(28)-C(30)	0.0(8)
C(3)-C(4)-C(28)-C(30)	178.8(5)
C(4)-C(28)-C(29)-N(1)	162(14)
C(30)-C(28)-C(29)-N(1)	-19(14)
C(4)-C(28)-C(30)-N(2)	-147(24)
C(29)-C(28)-C(30)-N(2)	34(25)
C(10)-C(11)-C(31)-C(32)	179.2(5)
C(12)-C(11)-C(31)-C(32)	-0.2(8)
C(10)-C(11)-C(31)-C(33)	-2.0(7)
C(12)-C(11)-C(31)-C(33)	178.6(5)
C(11)-C(31)-C(32)-N(4)	175(100)
C(33)-C(31)-C(32)-N(4)	-4(10)

C(11)-C(31)-C(33)-N(3)	111(100)
C(32)-C(31)-C(33)-N(3)	-70(100)
C(22)-C(21)-C(34)-C(35)	58.2(6)
C(20)-C(21)-C(34)-C(35)	-58.1(6)
C(42)-C(21)-C(34)-C(35)	-178.7(4)
C(21)-C(34)-C(35)-C(36)	177.7(4)
C(34)-C(35)-C(36)-C(37)	178.8(4)
C(35)-C(36)-C(37)-C(38)	-179.7(4)
C(36)-C(37)-C(38)-C(39)	178.2(4)
C(37)-C(38)-C(39)-C(40)	-177.5(4)
C(38)-C(39)-C(40)-C(41)	-179.3(5)
C(22)-C(21)-C(42)-C(43)	-48.1(5)
C(20)-C(21)-C(42)-C(43)	61.0(5)
C(34)-C(21)-C(42)-C(43)	-174.7(4)
C(21)-C(42)-C(43)-C(44)	-152.8(4)
C(42)-C(43)-C(44)-C(45)	66.5(5)
C(43)-C(44)-C(45)-C(46)	67.4(5)
C(44)-C(45)-C(46)-C(47)	-179.7(4)
C(45)-C(46)-C(47)-C(48)	-172.3(4)
C(46)-C(47)-C(48)-C(49)	178.9(4)
C(76)-C(50)-C(51)-C(52)	-1.4(8)
Br(3)-C(50)-C(51)-C(52)	177.3(4)
C(50)-C(51)-C(52)-C(74)	-0.5(7)
C(50)-C(51)-C(52)-C(53)	-178.5(5)
C(74)-C(52)-C(53)-C(77)	-178.8(5)
C(51)-C(52)-C(53)-C(77)	-0.7(10)
C(74)-C(52)-C(53)-C(54)	-0.1(6)
C(51)-C(52)-C(53)-C(54)	178.1(5)
C(77)-C(53)-C(54)-C(55)	-0.7(9)
C(52)-C(53)-C(54)-C(55)	-179.5(5)
C(77)-C(53)-C(54)-C(73)	178.0(5)
C(52)-C(53)-C(54)-C(73)	-0.8(5)
C(73)-C(54)-C(55)-C(56)	-1.7(7)
C(53)-C(54)-C(55)-C(56)	176.9(5)
C(54)-C(55)-C(56)-C(71)	-0.5(7)
C(54)-C(55)-C(56)-C(57)	-179.7(4)
C(71)-C(56)-C(57)-C(58)	-179.5(5)
C(55)-C(56)-C(57)-C(58)	-0.3(9)
C(71)-C(56)-C(57)-C(69)	0.6(5)
C(55)-C(56)-C(57)-C(69)	179.9(5)
C(69)-C(57)-C(58)-C(59)	0.6(7)
C(56)-C(57)-C(58)-C(59)	-179.3(4)
C(57)-C(58)-C(59)-C(67)	2.6(7)

C(57)-C(58)-C(59)-C(60)	-178.5(5)
C(58)-C(59)-C(60)-C(80)	2.2(9)
C(67)-C(59)-C(60)-C(80)	-178.7(5)
C(58)-C(59)-C(60)-C(61)	-178.1(5)
C(67)-C(59)-C(60)-C(61)	0.9(6)
C(80)-C(60)-C(61)-C(66)	-179.8(5)
C(59)-C(60)-C(61)-C(66)	0.6(6)
C(80)-C(60)-C(61)-C(62)	-1.1(9)
C(59)-C(60)-C(61)-C(62)	179.3(5)
C(66)-C(61)-C(62)-C(63)	0.3(7)
C(60)-C(61)-C(62)-C(63)	-178.2(5)
C(61)-C(62)-C(63)-C(64)	0.3(7)
C(61)-C(62)-C(63)-Br(4)	-178.5(4)
C(62)-C(63)-C(64)-C(65)	-0.5(8)
Br(4)-C(63)-C(64)-C(65)	178.3(4)
C(63)-C(64)-C(65)-C(66)	0.0(7)
C(64)-C(65)-C(66)-C(61)	0.6(8)
C(64)-C(65)-C(66)-C(67)	-179.6(5)
C(62)-C(61)-C(66)-C(65)	-0.8(7)
C(60)-C(61)-C(66)-C(65)	178.1(5)
C(62)-C(61)-C(66)-C(67)	179.3(4)
C(60)-C(61)-C(66)-C(67)	-1.8(6)
C(58)-C(59)-C(67)-C(68)	-4.0(8)
C(60)-C(59)-C(67)-C(68)	176.9(4)
C(58)-C(59)-C(67)-C(66)	177.1(4)
C(60)-C(59)-C(67)-C(66)	-2.0(6)
C(65)-C(66)-C(67)-C(68)	3.7(9)
C(61)-C(66)-C(67)-C(68)	-176.4(5)
C(65)-C(66)-C(67)-C(59)	-177.5(5)
C(61)-C(66)-C(67)-C(59)	2.4(6)
C(59)-C(67)-C(68)-C(69)	1.9(7)
C(66)-C(67)-C(68)-C(69)	-179.4(5)
C(58)-C(57)-C(69)-C(68)	-2.7(7)
C(56)-C(57)-C(69)-C(68)	177.2(4)
C(58)-C(57)-C(69)-C(70)	172.9(4)
C(56)-C(57)-C(69)-C(70)	-7.2(5)
C(67)-C(68)-C(69)-C(57)	1.4(7)
C(67)-C(68)-C(69)-C(70)	-173.5(4)
C(57)-C(69)-C(70)-C(83)	134.0(4)
C(68)-C(69)-C(70)-C(83)	-50.7(7)
C(57)-C(69)-C(70)-C(71)	10.1(5)
C(68)-C(69)-C(70)-C(71)	-174.7(4)
C(57)-C(69)-C(70)-C(91)	-103.2(4)

C(68)-C(69)-C(70)-C(91)	72.0(6)
C(55)-C(56)-C(71)-C(72)	1.5(7)
C(57)-C(56)-C(71)-C(72)	-179.2(4)
C(55)-C(56)-C(71)-C(70)	-173.2(4)
C(57)-C(56)-C(71)-C(70)	6.1(5)
C(69)-C(70)-C(71)-C(56)	-9.7(5)
C(83)-C(70)-C(71)-C(56)	-134.2(4)
C(91)-C(70)-C(71)-C(56)	104.7(4)
C(69)-C(70)-C(71)-C(72)	176.1(5)
C(83)-C(70)-C(71)-C(72)	51.6(6)
C(91)-C(70)-C(71)-C(72)	-69.5(6)
C(56)-C(71)-C(72)-C(73)	-0.1(7)
C(70)-C(71)-C(72)-C(73)	173.6(4)
C(71)-C(72)-C(73)-C(54)	-2.1(7)
C(71)-C(72)-C(73)-C(74)	-178.5(5)
C(55)-C(54)-C(73)-C(72)	3.1(7)
C(53)-C(54)-C(73)-C(72)	-175.8(5)
C(55)-C(54)-C(73)-C(74)	-179.8(4)
C(53)-C(54)-C(73)-C(74)	1.3(5)
C(51)-C(52)-C(74)-C(75)	2.0(8)
C(53)-C(52)-C(74)-C(75)	-179.6(5)
C(51)-C(52)-C(74)-C(73)	-177.5(5)
C(53)-C(52)-C(74)-C(73)	0.9(6)
C(72)-C(73)-C(74)-C(75)	-4.1(9)
C(54)-C(73)-C(74)-C(75)	179.2(5)
C(72)-C(73)-C(74)-C(52)	175.4(5)
C(54)-C(73)-C(74)-C(52)	-1.3(6)
C(52)-C(74)-C(75)-C(76)	-1.6(8)
C(73)-C(74)-C(75)-C(76)	177.9(5)
C(51)-C(50)-C(76)-C(75)	1.8(8)
Br(3)-C(50)-C(76)-C(75)	-176.8(4)
C(74)-C(75)-C(76)-C(50)	-0.3(8)
C(52)-C(53)-C(77)-C(79)	178.8(5)
C(54)-C(53)-C(77)-C(79)	0.2(8)
C(52)-C(53)-C(77)-C(78)	0.0(9)
C(54)-C(53)-C(77)-C(78)	-178.5(5)
C(53)-C(77)-C(78)-N(5)	174(100)
C(79)-C(77)-C(78)-N(5)	-5(13)
C(53)-C(77)-C(79)-N(6)	154(27)
C(78)-C(77)-C(79)-N(6)	-27(27)
C(61)-C(60)-C(80)-C(82)	0.5(9)
C(59)-C(60)-C(80)-C(82)	-180.0(5)
C(61)-C(60)-C(80)-C(81)	179.9(5)

C(59)-C(60)-C(80)-C(81)	-0.5(8)
C(60)-C(80)-C(81)-N(7)	-164(12)
C(82)-C(80)-C(81)-N(7)	16(12)
C(60)-C(80)-C(82)-N(8)	164(13)
C(81)-C(80)-C(82)-N(8)	-15(13)
C(69)-C(70)-C(83)-C(84)	-58.0(5)
C(71)-C(70)-C(83)-C(84)	57.9(5)
C(91)-C(70)-C(83)-C(84)	178.7(4)
C(70)-C(83)-C(84)-C(85)	177.3(4)
C(83)-C(84)-C(85)-C(86)	-179.2(4)
C(84)-C(85)-C(86)-C(87)	-179.4(4)
C(85)-C(86)-C(87)-C(88)	-179.4(4)
C(86)-C(87)-C(88)-C(89)	177.1(5)
C(87)-C(88)-C(89)-C(90)	178.2(5)
C(69)-C(70)-C(91)-C(92)	47.4(5)
C(83)-C(70)-C(91)-C(92)	174.3(3)
C(71)-C(70)-C(91)-C(92)	-60.6(5)
C(70)-C(91)-C(92)-C(93)	156.7(4)
C(91)-C(92)-C(93)-C(94)	-66.4(5)
C(92)-C(93)-C(94)-C(95)	-66.3(5)
C(93)-C(94)-C(95)-C(96)	179.8(4)
C(94)-C(95)-C(96)-C(97)	173.6(4)
C(95)-C(96)-C(97)-C(98)	-179.9(4)

Symmetry transformations used to generate equivalent atoms:

References

References for Chapter One

1. Facchetti, A. *Mater. Today* **2007**, 10.
2. Dimitrakopoulos, C. D.; Malenfant, P. R. L., *Adv. Mater.* **2002**, 14, 99-117.
3. van Mullekom, H. A. M.; Vekemans, J. A. J. M.; Havinga, E. E.; Meijer, E. W. *Mater. Sci. and Eng.* **2001**, 32, 1-40.
4. Sirringhaus, H. *Adv. Mater.* **2005**, 17, 2411.
5. Murphy, A. R.; Frechet, M. J. *Chem. Rev.* **2007**, 107, 1066-1096.
6. Yoon, M. H.; DiBenedetto, S. A.; Russell, M. T.; Facchetti, A.; Marks, T. J., *Chem. Mater.* **2007**, 19, 4864-4881.
7. Coropceanu, V.; Cornil, J.; Filho, da Silva D. A.; Olivier, Y.; Silbey, R.; Brédas, J.-L. *Chem. Rev.* **2007**, 107(4), 926 – 952.
8. Hutchison, G. R.; Ratner, M. A.; Marks, T. J., *J. Am. Chem. Soc.* **2005**, 127, 16866-16881.
9. Bao, Z. *Adv. Mater.* **2000**, 12, 227-230.
10. Forrest, S. R. *Nature* **2004**, 428, 911.
11. Garnier, F.; Hajlaoui, R.; Yassar, A.; Srivastava, P. *Science* **1994**, 265, 1684.
12. Sirringhaus, H.; Kawase, T.; Friend, R. H.; Shimoda, T.; Inbasekaran, M.; Wu, W.; Woo, E. P. *Science* **2000**, 290, 2123.
13. Burroughes, J. H.; Bradley, D. D. C.; Brown, A. R.; Marks, R. N.; Mackay, K.; Friend, R. H.; Burns, P. L.; Holmes, A. B. *Nature* **1990**, 347, 539.

14. Brabec, C. J.; Sariciftci, N. S.; Hummelen, J. C. *Adv. Funct. Mater.* **2001**, *11*, 15.
15. Sze, S. M.; Ng, K. K. *Physics of Semiconductor Devices*; John Wiley & Sons, Inc., Hoboken, New Jersey, 2007.
16. Horowitz, G. *Adv. Mater.* **1998**, *10*, 365-377.
17. Katz, H. E.; Bao, Z.; Gilat S. L. *Acc. Chem. Res.* **2001**, *34*, 359-369.
18. Katz, H. E.; Bao, Z. *J. Phys. Chem. B* **2000**, *104*, 671.
19. Zaumseil, J.; Sirringhaus, H. *Chem. Rev.* **2007**, *107*, 1296-1323.
20. Facchetti, A.; Yoon, M. H.; Stern, C. L.; Hutchison, G. R.; Ratner, M. A.; Marks, T. J., *J. Am. Chem. Soc.* **2004**, *126*, 13480-13501.
21. Horowitz, G. *J. Mater. Res.* **2004**, *19*, 1946-1962.
22. Shen, Y.; Hosseini, A. R.; Wong, M. H.; Malliaras, G. G. *Chem. Phys. Chem.* **2004**, *5*, 16.
23. Facchetti, A.; Yoon, M. H.; Stern, C. L.; Hutchison, G. R.; Ratner, M. A.; Marks, T. J., *J. Am. Chem. Soc.* **2004**, *126*, 13480-13501.
24. Horowitz, G.; Hajlaoui, R.; Delannoy, P. *J. Phys. III* **1995**, *5*, 355.
25. Bredas, J. L.; Calbert, J. P.; da Silva, D. A.; Cornil, J. *Proc. Natl. Acad. Sci. U.S.A.* **2002**, *99*, 5804.
26. Horowitz, G.; Hajlaoui, M. E.; Hajlaoui, R. *J. Appl. Phys.* **2000**, *87*, 4456.
27. Tsumura, A.; Koezuka, K.; Ando, T. *Appl. Phys. Lett.* **1986**, *49*, 1210.
28. Newman, C. R.; Frisbie, C. D.; Silva Filho, D. A.; Bredas, J. L.; Ewbank, P. C.; Mann, K. R. *Chem. Mater.* **2004**, *16*, 4436.
29. Mas-Torrent, M.; Rovira, C. *Chem. Soc. Rev.* **2008**, *37*, 827-838.

30. Lu, G.; Usta, H.; Risko, C.; Wang, L.; Facchetti, A.; Ratner, M. A.; Marks, T. J. *J. Am. Chem. Soc.* **2008**, *130*, 7670-7685.
31. De Leeuw, D. M.; Simenon, M. M. J.; Brown, A. R.; Einerhand, R. E. F. *Synth. Met.* **1997**, *87*, 53-59.
32. Dosch, H.; Jansen, M.; Kern, K.; Klauk, H. *J. Am. Chem. Soc.* **2008**, *130*, 4637-4645.
33. Anthopoulos, T. D.; Setayesh, S.; Smits, E.; Coelle, M.; Cantatore, E.; Blom, P. W. M.; de Leeuw, D. M. *Adv. Mater.* **2006**, *18*, 1900-1904.

References for Chapter Two

1. Murphy, A. R.; Frechet, J. M. J., *Chem. Rev.* **2007**, 107, 1066-1096.
2. Facchetti, A., *Mater. Today* **2007**, 10.
3. Dimitrakopoulos, C. D.; Malenfant, P. R. L., *Adv. Mater.* **2002**, 14, 99-117.
4. Katz, H. E., *Chem. Mater.* **2004**, 16, 4748-4756.
5. Bernius, M.; Inbasekaran, M.; Woo, E.; Wu, W. S.; Wujkowski, L., *Thin Solid Films* **2000**, 363, 55-57.
6. Kraft, A.; Grimsdale, A. C.; Holmes, A. B., *Angew. Chem., Intl. Ed. Engl.* **1998**, 37, 402-428.
7. Brabec, C. J.; Sariciftci, N. S.; Hummelen, J. C., *Adv. Funct. Mater.* **2001**, 11, 15-26.
8. Huynh, W. U.; Dittmer, J. J.; Alivisatos, A. P., *Science* **2002**, 295, 2425-2427.
9. Yu, G.; Gao, J.; Hummelen, J. C.; Wudl, F.; Heeger, A. J., *Science* **1995**, 270, 1789-1791.
10. Berlin, A.; Zotti, G.; Zecchin, S.; Schiavon, G.; Vercelli, B.; Zanelli, A., *Chem. Mater.* **2004**, 16, 3667-3676.
11. Huitema, H. E. A.; Gelinck, G. H.; van der Putten, J. B. P. H.; Kuijk, K. E.; Hart, K. M.; Cantatore, E.; de Leeuw, D. M., *Adv. Mater.* **2002**, 14, 1201-1204.

12. Mach, P.; Rodriguez, S. J.; Nortrup, R.; Wiltzius, P.; Rogers, J. A., *Appl. Phys. Lett.* **2001**, 78, 3592-3594.
13. Fichou, D.; Horowitz, G.; Nishikitani, Y.; Garnier, F., *Chemtronics* **1988**, 3, 176-178.
14. Horowitz, G.; Fichou, D.; Peng, X. Z.; Xu, Z. G.; Garnier, F., *Solid State Commun.* **1989**, 72, 381-384.
15. Peng, X. Z.; Horowitz, G.; Fichou, D.; Garnier, F., *Appl. Phys. Lett.* **1990**, 57, 2013-2015.
16. Facchetti, A.; Mushrush, M.; Yoon, M. H.; Hutchison, G. R.; Ratner, M. A.; Marks, T. J., *J. Am. Chem. Soc.* **2004**, 126, 13859-13874.
17. Facchetti, A.; Yoon, M. H.; Stern, C. L.; Hutchison, G. R.; Ratner, M. A.; Marks, T. J., *J. Am. Chem. Soc.* **2004**, 126, 13480-13501.
18. Facchetti, A.; Yoon, M. H.; Stern, C. L.; Katz, H. E.; Marks, T. J., *Angew. Chem., Intl. Ed. Engl.* **2003**, 42, 3900-3903.
19. Katz, H. E.; Bao, Z. N.; Gilat, S. L., *Acc. Chem. Res* **2001**, 34, 359-369.
20. Garnier, F.; Hajlaoui, R.; Yassar, A.; Srivastava, P., *Science* **1994**, 265, 1684-1686.
21. Rogers, J. A.; Bao, Z.; Baldwin, K.; Dodabalapur, A.; Crone, B.; Raju, V. R.; Kuck, V.; Katz, H.; Amundson, K.; Ewing, J.; Drzaic, P., *Proc. Natl. Acad. Sci. U.S.A.* **2001**, 98, 4835-4840.
22. Sirringhaus, H.; Kawase, T.; Friend, R. H.; Shimoda, T.; Inbasekaran, M.; Wu, W.; Woo, E. P., *Science* **2000**, 290, 2123-2126.
23. Bao, Z.; Dodabalapur, A.; Lovinger, A. J., *Appl. Phys. Lett.* **1996**, 69, 4108-4110.

24. Bao, Z. N.; Lovinger, A. J., *Chem. Mater.* **1999**, 11, 2607-2612.
25. Sirringhaus, H.; Brown, P. J.; Friend, R. H.; Nielsen, M. M.; Bechgaard, K.; Langeveld-Voss, B. M. W.; Spiering, A. J. H.; Janssen, R. A. J.; Meijer, E. W.; Herwig, P.; de Leeuw, D. M., *Nature* **1999**, 401, 685-688.
26. McCulloch, I.; Heeney, M.; Bailey, C.; Genevicius, K.; Macdonald, I.; Shkunov, M.; Sparrowe, D.; Tierney, S.; Wagner, R.; Zhang, W. M.; Chabinyk, M. L.; Kline, R. J.; McGehee, M. D.; Toney, M. F., *Nat. Mater.* **2006**, 5, 328-333.
27. Heeney, M.; Bailey, C.; Genevicius, K.; Shkunov, M.; Sparrowe, D.; Tierney, S.; McCulloch, I., *J. Am. Chem. Soc.* **2005**, 127, 1078-1079.
28. Ong, B. S.; Wu, Y. L.; Liu, P.; Gardner, S., *J. Am. Chem. Soc.* **2004**, 126, 3378-3379.
29. Pan, H.; Wu, Y.; Li, Y.; Liu, P.; Ong, B. S.; S. Zhu, G. X., *Adv. Funct. Mater.* **2007**, 17, 3574 - 3579.
30. Meijer, E. J.; Detcheverry, C.; Baesjou, P. J.; van Veenendaal, E.; de Leeuw, D. M.; Klapwijk, T. M., *J. Appl. Phys.* **2003**, 93, 4831-4835.
31. Abdou, M. S. A.; Orfino, F. P.; Xie, Z. W.; Deen, M. J.; Holdcroft, S., *Adv. Mater.* **1994**, 6, 838-841.
32. Ficker, J.; Ullmann, A.; Fix, W.; Rost, H.; Clemens, W., *J. Appl. Phys.* **2003**, 94, 2638-2641.
33. de Leeuw, D. M.; Simenon, M. M. J.; Brown, A. R.; Einerhand, R. E. F., *Synth. Met.* **1997**, 87, 53-59.
34. Koopmans, T., *Physica* **1933**, 1, 104.
35. McCulloch, L.; Bailey, C.; Giles, M.; Heeney, M.; Love, I.; Shkunov, M.; Sparrowe,

- D.; Tierney, S., *Chem. Mater.* **2005**, 17, 1381-1385.
36. Sirringhaus, H.; Wilson, R. J.; Friend, R. H.; Inbasekaran, M.; Wu, W.; Woo, E. P.; Grell, M.; Bradley, D. D. C., *Appl. Phys. Lett.* **2000**, 77, 406-408.
37. Masuda, H.; Kaeriyama, K., *Makromol. Chem., Rapid Commun.* **1992**, 13, 461-465.
38. Waltman, R. J.; Diaz, A. F.; Bargon, J., *J. Electrochem. Soc.* **1984**, 131, 1452-1456.
39. Pomerantz, M.; Yang, H.; Cheng, Y., *Macromolecules* **1995**, 28, 5706-5708.
40. Pomerantz, M.; Cheng, Y.; Kasim, R. K.; Elsenbaumer, R. L., *J. Mater. Chem.* **1999**, 9, 2155-2163.
41. Amarasekara, A. S.; Pomerantz, M., *Synthesis* **2003**, 2255-2258.
42. Murphy, A. R.; Liu, J. S.; Luscombe, C.; Kavulak, D.; Frechet, J. M. J.; Kline, R. J.; McGehee, M. D., *Chem. Mater.* **2005**, 17, 4892-4899.
43. Chabynyc, M. L.; Toney, M. F.; Kline, R. J.; McCulloch, I.; Heeney, M., *J. Am. Chem. Soc.* **2007**, 129, 3226-3237.
44. Kline, R. J.; DeLongchamp, D. M.; Fischer, D. A.; Lin, E. K.; Richter, L. J.; Chabynyc, M. L.; Toney, M. F.; Heeney, M.; McCulloch, I., *Macromolecules* **2007**, 40, 7960-7965.
45. DeLongchamp, D. M.; Kline, R. J.; Lin, E. K.; Fischer, D. A.; Richter, L. J.; Lucas, L. A.; Heeney, M.; McCulloch, I.; Northrup, J. E., *Adv. Mater.* **2007**, 19, 833 - 837.
46. Wetzell, D. M.; Brauman, J. I., *J. Am. Chem. Soc.* **1988**, 110, 8333-8336.
47. Risko, C.; Kushto, G. P.; Kafati, Z. H.; Bredas, J. L., *J. Chem. Phys.* **2004**, 121, 9031-9038.
48. Yamaguchi, S.; Tamao, K., *Bull. Chem. Soc. Jpn.* **1996**, 69, 2327-2334.

49. Zhan, X. W.; Risko, C.; Amy, F.; Chan, C.; Zhao, W.; Barlow, S.; Kahn, A.; Bredas, J. L.; Marder, S. R., *J. Am. Chem. Soc.* **2005**, 127, 9021-9029.
50. Chan, K. L.; McKiernan, M. J.; Towns, C. R.; Holmes, A. B., *J. Am. Chem. Soc.* **2005**, 127, 7662-7663.
51. Chen, J. W.; Law, C. C. W.; Lam, J. W. Y.; Dong, Y. P.; Lo, S. M. F.; Williams, I. D.; Zhu, D. B.; Tang, B. Z., *Chem. Mater.* **2003**, 15, 1535-1546.
52. Liu, M. S.; Luo, J. D.; Jen, A. K. Y., *Chem. Mater.* **2003**, 15, 3496-3500.
53. Murata, H.; Kafafi, Z. H.; Uchida, M., *Appl. Phys. Lett.* **2002**, 80, 189-191.
54. Tamao, K.; Uchida, M.; Izumizawa, T.; Furukawa, K.; Yamaguchi, S., *J. Am. Chem. Soc.* **1996**, 118, 11974-11975.
55. Mi, B. X.; Dong, Y. Q.; Li, Z.; Lam, J. W. Y.; Haussler, M.; Sung, H. H. Y.; Kwok, H. S.; Dong, Y. P.; Williams, I. D.; Liu, Y. Q.; Luo, Y.; Shuai, Z. G.; Zhu, D. B.; Tang, B. Z., *Chem. Commun.* **2005**, 3583-3585.
56. Boudreault, P.-L. T.; Michaud, A.; Leclerc, M., *Macromol. Rapid Commun.* **2007**, 28, 2176-2179.
57. Wang, Y.; Hou, L. T.; Yang, K. X.; Chen, J. W.; Wang, F.; Cao, Y., *Macromol. Chem. Phys.* **2005**, 206, 2190-2198.
58. Ohshita, J.; Lee, K. H.; Hamamoto, D.; Kunugi, Y.; Ikadai, J.; Kwak, Y. W.; Kunai, A., *Chem. Lett.* **2004**, 33, 892-893.
59. Wang, F.; Luo, J.; Yang, K. X.; Chen, J. W.; Huang, F.; Cao, Y., *Macromolecules* **2005**, 38, 2253-2260.

60. Hutchison, G. R.; Ratner, M. A.; Marks, T. J., *J. Am. Chem. Soc.* **2005**, 127, 16866-16881.
61. Usta, H.; Lu, G.; Facchetti, A.; Marks, T. J., *J. Am. Chem. Soc.* **2006**, 128, 9034-9035.
62. Kong, J.; White, C. A.; Krylov, A. I.; Sherrill, D.; Adamson, R. D.; Furlani, T. R.; Lee, M. S.; Lee, A. M.; Gwaltney, S. R.; Adams, T. R.; Ochsenfeld, C.; Gilbert, A. T. B.; Kedziora, G. S.; Rassolov, V. A.; Maurice, D. R.; Nair, N.; Shao, Y. H.; Besley, N. A.; Maslen, P. E.; Dombroski, J. P.; Daschel, H.; Zhang, W. M.; Korambath, P. P.; Baker, J.; Byrd, E. F. C.; Van Voorhis, T.; Oumi, M.; Hirata, S.; Hsu, C. P.; Ishikawa, N.; Florian, J.; Warshel, A.; Johnson, B. G.; Gill, P. M. W.; Head-Gordon, M.; Pople, J. A., *J. Comput. Chem.* **2000**, 21, 1532-1548.
63. Chen, W. PhD Thesis, Iowa State University, 1997.
64. Lothrop, W. C., *J. Am. Chem. Soc.* **1941**, 63, 1187-1191.
65. Murata, M.; Oyama, T.; Watanabe, S.; Masuda, Y., *J. Org. Chem.* **2000**, 65, 164-168.
66. Ishiyama, T.; Murata, M.; Miyaura, N., *J. Org. Chem.* **1995**, 60, 7508-7510.
67. Bernius, M.; Inbasekaran, M.; Woo, E.; Wu, W. S.; Wujkowski, L., *J. Mater. Sci.: Mater. Electron.* **2000**, 11, 111-116.
68. Inbasekaran, M.; Wu, W.; Woo, E. P. Process for preparing conjugated polymers. U.S. Patent 5,777,070, 1998.
69. Jayakannan, M.; van Dongen, J. L. J.; Janssen, R. A. J., *Macromolecules* **2001**, 34, 5386-5393.
70. Forster, M.; Annan, K. O.; Scherf, U., *Macromolecules* **1999**, 32, 3159-3162.
71. Gronowitz, S.; Bobosik, V.; Lawitz, K., *Chem. Scr.* **1984**, 23, 120-122.

72. Gronowitz, S.; Lawitz, K., *Chem. Scr.* **1983**, 22, 265-266.
73. Kirschbaum, T.; Azumi, R.; Mena-Osteritz, E.; Bauerle, P., *New J. Chem.* **1999**, 23, 241-250.
74. Kirschbaum, T.; Briehn, C. A.; Bauerle, P., *J. Chem. Soc., Perkin Trans. I* **2000**, 8, 1211-1216.
75. Kaeriyama, K.; Tsukahara, Y.; Negoro, S.; Tanigaki, N.; Masuda, H., *Synth. Met.* **1997**, 84, 263-264.
76. Shin, S. H.; Park, J. S.; Park, J. W.; Kim, H. K., *Synth. Met.* **1999**, 102, 1060-1062.
77. Brennan, D. J.; Townsend, P. H.; Welsh, D. M.; Dibbs, M. G.; Shaw, J. M.; Miklovich, J. L.; Boeke, R. B., *Mat. Res. Soc. Symp. Proc.* **2003**, 771, L6.1.1-L6.1.5.
78. Chen, T. A.; Wu, X. M.; Rieke, R. D., *J. Am. Chem. Soc.* **1995**, 117, 233-244.
79. Zhu, Y.; Alam, M. M.; Jenekhe, S. A., *Macromolecules* **2002**, 35, 9844-9846.
80. Zhu, Y.; Champion, R. D.; Jenekhe, S. A., *Macromolecules* **2006**, 39, 8712-8719.
81. Chua, L. L.; Zaumseil, J.; Chang, J. F.; Ou, E. C. W.; Ho, P. K. H.; Sirringhaus, H.; Friend, R. H., *Nature* **2005**, 434, 194-199.
82. Ohshita, J.; Nodono, M.; Kai, H.; Watanabe, T.; Kunai, A.; Komaguchi, K.; Shiotani, M.; Adachi, A.; Okita, K.; Harima, Y.; Yamashita, K.; Ishikawa, M., *Organometallics* **1999**, 18, 1453-1459.
83. Ohshita, J.; Nodono, M.; Watanabe, T.; Ueno, Y.; Kunai, A.; Harima, Y.; Yamashita, K.; Ishikawa, M., *J. Organomet. Chem.* **1998**, 553, 487-491.
84. Yamaguchi, S.; Xu, C. H.; Tamao, K., *J. Am. Chem. Soc.* **2003**, 125, 13662-13663.

85. Yang, S. Y.; Kan, Y. H.; Yang, G. C.; Su, Z. M.; Zhao, L., *Chem. Phys. Lett.* **2006**, 429, 180-184.
86. Grell, M.; Bradley, D. D. C.; Ungar, G.; Hill, J.; Whitehead, K. S., *Macromolecules* **1999**, 32, 5810-5817.
87. Kawana, S.; Durrell, M.; Lu, J.; Macdonald, J. E.; Grell, M.; Bradley, D. D. C.; Jukes, P. C.; Jones, R. A. L.; Bennett, S. L., *Polymer* **2002**, 43, 1907-1913.
88. Yamamoto, T.; Kokubo, H.; Morikita, T., *J. Polym. Sci., Part B: Polym. Phys.* **2001**, 39, 1713-1718.
89. Lim, E.; Jung, B. J.; Lee, J.; Shim, H. K.; Lee, J. I.; Yang, Y. S.; Do, L. M., *Macromolecules* **2005**, 38, 4531-4535.
90. Wu, Y.; Li, Y.; Gardner, S.; Ong, B. S., *J. Am. Chem. Soc.* **2005**, 127, 614-618.
91. Kline, R. J.; McGehee, M. D.; Kadnikova, E. N.; Liu, J. S.; Frechet, J. M. J.; Toney, M. F., *Macromolecules* **2005**, 38, 3312-3319.
92. Facchetti, A.; Yoon, M. H.; Marks, T. J., *Adv. Mater.* **2005**, 17, 1705-1725.
93. Zen, A.; Saphiannikova, M.; Neher, D.; Grenzer, J.; Grigorian, S.; Pietsch, U.; Asawapirom, U.; Janietz, S.; Scherf, U.; Lieberwirth, I.; Wegner, G., *Macromolecules* **2006**, 39, 2162-2171.
94. Yang, H. C.; Shin, T. J.; Yang, L.; Cho, K.; Ryu, C. Y.; Bao, Z. N., *Adv. Funct. Mater.* **2005**, 15, 671-676.
95. Zhang, R.; Li, B.; Iovu, M. C.; Jeffries-EL, M.; Sauve, G.; Cooper, J.; Jia, S. J.; Tristram-Nagle, S.; Smilgies, D. M.; Lambeth, D. N.; McCullough, R. D.; Kowalewski, T., *J. Am. Chem. Soc.* **2006**, 128, 3480-3481.

96. Boudreault, P.-L. T.; Wakim, S.; Blouin, N.; Simard, M.; essier, C.; Tao, Y.; Leclerc, M., *J. Am. Chem. Soc.* **2007**, 129, 9125-9136.
97. Koren, A. B.; Curtis, M. D.; Kampf, J. W., *Chem. Mater.* **2000**, 12, 1519-1522.
98. Yamamoto, T.; Komarudin, D.; Arai, M.; Lee, B. L.; Suganuma, H.; Asakawa, N.; Inoue, Y.; Kubota, K.; Sasaki, S.; Fukuda, T.; Matsuda, H., *J. Am. Chem. Soc.* **1998**, 120, 2047-2058.
99. Yamaguchi, S.; Itami, Y.; Tamao, K., *Organometallics* **1998**, 17, 4910-4916.
100. Faustov, V. I.; Egorov, M. P.; Nefedov, O. M.; Molin, Y. N., *Phys. Chem. Chem. Phys.* **2000**, 2, 4293-4297.
101. Belletête, M.; Beaupré, S.; Bouchard, J.; Blondin, P.; Leclerc, M.; Durocher, G., *J. Phys. Chem. B* **2000**, 104, 9118-9125.
102. Yamaguchi, S.; Tamao, K., *J. Chem. Soc., Dalton Trans.* **1998**, 3693-3702.
103. Liao, L. S.; Fung, M. K.; Lee, C. S.; Lee, S. T.; Inbasekaran, M.; Woo, E. P.; Wu, W. W., *Appl. Phys. Lett.* **2000**, 76, 3582-3584.
104. Heeney, M.; Bailey, C.; Giles, M.; Shkunov, M.; Sparrowe, D.; Tierney, S.; Zhang, W. M.; McCulloch, I., *Macromolecules* **2004**, 37, 5250-5256.
105. Bürgi, L.; Richards, T. J.; Friend, R. H.; Siringhaus, H., *J. Appl. Phys.* **2003**, 94, 6129-6137.
106. Chwang, A. B.; Frisbie, C. D., *J. Phys. Chem. B* **2000**, 104, 12202-12209.
107. Mahapatro, A. K.; Ghosh, S., *Appl. Phys. Lett.* **2002**, 80, 4840-4842.
108. Janietz, S.; Bradley, D. D. C.; Grell, M.; Giebeler, C.; Inbasekaran, M.; Woo, E. P.,

- Appl. Phys. Lett.* **1998**, 73, 2453-2455.
109. Yoon, M. H.; DiBenedetto, S. A.; Russell, M. T.; Facchetti, A.; Marks, T. J., *Chem. Mater.* **2007**, 19, 4864-4881.
110. Burin, A. L.; Ratner, M. A., In *Computational Materials Chemistry: Methods and Applications*, Gordon, L. A. C. a. M. S., Ed. Kluwer Academic Publishers: Netherlands, 2004; pp 308-367.
111. Arkhipov, V. I.; Emelianova, E. V.; Tak, Y. H.; Bäessler, H., *J. App. Phys.* **1998**, 84.
112. Arkhipov, V. I.; Wolf, U.; Bäessler, H., *Phys. Rev. B* **1999**, 59, 7514-7520.
113. Arkhipov, V. I.; Seggern, H. v.; Emelianova, E. V., *App. Phys. Lett.* **2003**, 83, 5074-5076.
114. Zheng, Y.; Kunardi, L.; Troadec, C.; Wee, A. T. S.; Chandrasekhar, N., *App. Surf. Sci.* **2006**, 252, 4023-4025.

References for Chapter Three

1. Facchetti, A., *Mater. Today* **2007**, 10, 28-37.
2. Murphy, A. R.; Frechet, J. M. J., *Chem. Rev.* **2007**, 107, 1066-1096.
3. Fichou, D. *Handbook of Oligo- and Polythiophenes*; Wiley-VCH, New York, 1998.
4. Guillaud, G.; Sadound, M. Al; Maitrot, M. *Chem. Phys. Lett.* **1990**, 167, 503-506.
5. Dimitrakopoulos, C. D.; Malenfant, P. R. L., *Adv. Mater.* **2002**, 14, 99-117.
6. Newman, C.R.; Frisbie, C. D.; Filho, D. A. da S.; Bre´das, J.-L.; Ewbank, P. C.; Mann, K. R. *Chem. Mater.* **2004**, 16, 4436-4451.

7. Weitz, R. T.; Amsharov, K.; Zschieschang, U.; Villas, E. B.; Goswami, D. K.; Burghard, M.; Dosch, H.; Jansen, M.; Kern, K.; Klauk, H. *J. Am. Chem. Soc.* **2008**, *130*, 4637-4645.
8. Meijer, E. J.; de Leeuw, D. M.; Setayesh, S.; van Veenendaal, E.; Huisman, B. H.; Blom, P. W. M.; Hummelen, J. C.; Scherf, U.; Klapwijk, T. M. *Nat. Mater.* **2003**, *2*, 678-682.
9. Anthopoulos, T. D.; Setayesh, S.; Smits, E.; Coelle, M.; Cantatore, E.; Blom, P. W. M.; de Leeuw, D. M. *Adv. Mater.* **2006**, *18*, 1900-1904.
10. Koopmans, T., *Physica* **1933**, *1*, 104.
11. de Leeuw, D. M.; Simenon, M. M. J.; Brown, A. R.; Einerhand, R. E. F. *Synth. Met.* **1997**, *87*, 53-59.
12. Katz, H. E.; Lovinger, A. J.; Johnson, J.; Kloc, C.; Seigrist, T.; Li, W.; Lin, Y.-Y.; Dodabalapur, A. *Nature* **2000**, *404*, 478-481.
13. Yoon, M. H.; DiBenedetto, S. A.; Russell, M. T.; Facchetti, A.; Marks, T. J., *Chem. Mater.* **2007**, *19*, 4864-4881.
14. Bao, Z.; Lovinger, A. J.; Brown, J. *J. Am. Chem. Soc.* **1998**, *120*, 207-208.
15. Wang, Z.; Kim, C.; Facchetti, A.; Marks, T. J. *J. Am. Chem. Soc.* **2007**, *129*, 13362-13363.
16. Jones, B. A.; Ahrens, M. J.; Yoon, M. H.; Facchetti, A.; Marks, T. J.; Wasielewski, M. R., *Angew. Chem., Intl. Ed. Engl.* **2004**, *43*, 6363-6366.
17. Schmidt, R.; Ling, M. M.; Oh, J. H.; Winkler, M.; Könemann, M.; Bao, Z.; Würthner, F. *Adv. Mater.* **2007**, *19*, 3692-3695.

18. Jones, B. A.; Facchetti, A.; Marks, T. J.; Wasielewski, M. R. *Chem. Mater.* **2007**, *19*, 2703-2705.
19. Jones, B. A.; Facchetti, A.; Wasielewski, M. R.; Marks, T. J. *J. Am. Chem. Soc.* **2007**, *129*, 15259-15278.
20. Lee, Y.-L.; Hsu, H.-L.; Chen, S.-Y.; Yew T.-R. *J. Phys. Chem. C* **2008**, *112*, 1694-1699.
21. Yan, H.; Zheng, Y.; Blache, R.; Newman, C.; Lu, S.; Woerle, J.; Facchetti, A. *Adv. Mater.* **2008**, *9999*, 1-6.
22. Yoo, B.; Jones, B. A.; Basu, D.; Fine, D.; Jung, T.; Mohapatra, S.; Facchetti, A.; Dimmler, K.; Wasielewski, M. R.; Marks, T. J.; Dodabalapur, A. *Adv. Mater.* **2007**, *19*, 4028-4032.
23. Handa, S.; Miyazaki, E.; Takimiya, K.; Kunugi, Y. *J. Am. Chem. Soc.* **2007**, *129*, 11684-11685.
24. Babel, A.; Jenekhe, S. A. *J. Am. Chem. Soc.* **2003**, *125*, 13656-13657.
25. Chua, L. L.; Zaumseil, J.; Chang, J. F.; Ou, E. C. W.; Ho, P. K. H.; Sirringhaus, H.; Friend, R. H., *Nature* **2005**, *434*, 194-199.
26. Hutchison, G. R.; Ratner, M. A.; Marks, T. J., *J. Am. Chem. Soc.* **2005**, *127*, 16866-16881.
27. Woody, K. B.; Bullock, J. E.; Parkin, S. R.; Watson, M. D. *Macromolecules* **2007**, *40*, 4470-4473.
28. Thompson, B. C.; Kim, Y.-G.; McCarley, T. D.; Reynolds, J. R. *J. Am. Chem. Soc.* **2006**, *128*, 12714-12725.

29. Anthony, J. E. *Chem. Rev.* **2006**, *106*, 5028-5048.
30. Usta, H.; Facchetti, A.; Marks, T. J. *Org. Lett.* **2008**, *10*, 1385-1388.
31. Usta, H.; Facchetti, A.; Marks, T. J. *J. Am. Chem. Soc.* **2008**, *130*, 8580-8581.
32. Abraham, M. H., and Grellier, P. L. (1985) In *Chemistry of the Metal-Carbon Bond* (eds. Hartley, F. R., and Patai, S.). J. Wiley, New York, p. 115.
33. Suzuki A. *Proc. Jpn. Acad. Ser. B* **2004**, *80*, 359-371.
34. Frank, W.; Gompper, R. *Tetrahedron Lett.* **1987**, *28*, 3083-3086.
35. Trouillet, L.; Nicola, A. D.; Guillerez, S. *Chem. Mater.* **2000**, *12*, 1611-1621.
36. Crouch, D. J.; Skabara, P. J.; Lohr, J. E.; McDouall, J. J. W.; Heeney, M.; McCulloch, I.; Sparrowe, D.; Shkunov, M.; Coles, S. J.; Horton, P. N.; Hursthouse, M. B. *Chem. Mater.* **2005**, *17*, 6567-6578.
37. Lim, E.; Jung, B. J.; Lee, J.; Shim, H. K.; Lee, J. I.; Yang, Y. S.; Do, L. M., *Macromolecules* **2005**, *38*, 4531-4535.
38. Zhu, Y.; Alam, M. M.; Jenekhe, S. A. *Macromolecules* **2002**, *35*, 9844-9846.
39. Hernandez, V.; Lopez Navarrete, T. J. *J. Phys. Chem.* **1994**, *101*, 1369-1377.
40. Oldridge, L.; Kastler, M.; Müllen, K. *Chem. Commun.* **2006**, *8*, 885-887.
41. Jaramillo-Isaza, F.; Turner, L. M. *J. Mater. Chem.* **2006**, *16*, 83-89.
42. Berlin, A.; Zotti, G.; Zecchin, S.; Schiavon, G.; Vercelli, B.; Zanelli, A. *Chem. Mater.* **2004**, *16*, 3667-3676.
43. Lambert, T. L.; Ferraris, J. P. *J. Chem. Soc., Chem. Commun.* **1991**, 752-754.
44. Ferraris, J. P.; Lambert, T. L. *J. Chem. Soc., Chem. Commun.* **1991**, 1268-1270.

45. Merlet, S.; Birau, M.; Wang, Z. Y. *Org. Lett.* **2002**, *4*, 2157-2159.
46. Facchetti, A.; Letizia, J.; Yoon, M.-H.; Mushrush, M.; Katz, H. E.; Marks, T. J. *Chem. Mater.* **2004**, *16*, 4715-4727.
47. Yassar, A.; Horowitz, G.; Valat, P.; Wintgens, V.; Hmyene, M.; Deloffre, F.; Srivastava, P.; Lang, P.; Garnier, F. *J. Phys. Chem.* **1995**, *99*, 9155-9159.
48. Facchetti, A.; Yoon, M. H.; Stern, C. L.; Hutchison, G. R.; Ratner, M. A.; Marks, T. J., *J. Am. Chem. Soc.* **2004**, *126*, 13480-13501.
49. Pan, H.; Wu, Y.; Li, Y.; Liu, P.; Ong, B.S.; Zhu, S.; Xu, G. *Adv. Funct. Mater.* **2007**, *17*, 3574-3579.
50. Meng, H.; Zheng, J.; Lovinger, A. J.; Wang, B.-C.; Van Patten, P. G.; Bao, Z. *Chem. Mater.* **2003**, *15*, 1778-1787.
51. Pope, M.; Swenberg, C. E. *Electronic Processes in Organic Crystals*; Oxford University Press: New York, 1982.
52. Jacob, J.; Sax, S.; Piok, T.; List, E. J. W.; Grimsdale, A. C.; Müllen, K. *J. Am. Chem. Soc.* **2004**, *126*, 6987-6995.
53. Berlaman, I. B. *Fluorescence Spectra of Aromatic Molecules*; Academic Press: New York, 1971.
54. Turro, N.J. *Modern Molecular Photochemistry*; University Science Books: Sausalito, 1991.
55. Lu, G.; Usta, H.; Risko, C.; Wang, L.; Facchetti, A.; Ratner, M. A.; Marks, T. J. *J. Am. Chem. Soc.* **2008**, *130*, 7670-7685.

56. Meerholz, K.; Heinze, J. *Electrochim. Acta* **1996**, *41*, 1839-1854.
57. Zhu, Y.; Champion, R. D.; Jenekhe, S. A., *Macromolecules* **2006**, *39*, 8712-8719.
58. Bader, M. M.; Custelcean, R.; Ward, M. D. *Chem. Mater.* **2003**, *15*, 616-618.
59. Pappenfus, T. D.; Burand, M. W.; Janzen, D. E.; Mann, K. R. *Org. Lett.* **2003**, *5*, 1535-1538.
60. Yoon, M.-H.; Facchetti, A.; Stern, C. E.; Marks, T. J. *J. Am. Chem. Soc.* **2006**, *128*, 5792-5801.
61. Meerholz, K.; Heinze, J. *Electrochim. Acta* **1996**, *41*, 1839-1854.
62. Horowitz, G. *J. Mater. Res.* **2004**, *19*, 1946-1962.
63. Murphy, A. R.; Liu, J. S.; Luscombe, C.; Kavulak, D.; Frechet, J. M. J.; Kline, R. J.; McGehee, M. D., *Chem. Mater.* **2005**, *17*, 4892-4899.
64. Zaumseil, J.; Sirringhaus, H. *Chem. Rev.* **2007**, *107*, 1296-1323.
65. Chesterfield, R. J.; Newman, C. R.; Pappenfus, T. M.; Ewbank, P. C.; Haukaas, M. H.; Mann, K. R.; Miller, L. L.; Frisbie, C. D. *Adv. Mater.* **2003**, *15*, 1278-1282.
66. Cai, X.; Burand, M. W.; Newman, C. R.; da Sliva Filho, D. A.; Pappenfus, T. M.; Bader, M. M.; Bredas, J.-L.; Mann, K. R.; Frisbie, C. D. *J. Phys. Chem. B* **2006**, *110*, 14590-14597.
67. Chwang, A. B.; Frisbie, C. D. *J. Phys. Chem. B* **2000**, *104*, 12202-12209.
68. Facchetti, A.; Mushrush, M.; Yoon, M.-H.; Hutchison, G. R.; Ratner, M. A.; Marks, T. J. *J. Am. Chem. Soc.* **2004**, *126*, 13859-13874.
69. Kim, E.-G.; Coropceanu, V.; Gruhn, N. E.; Sanchez-Carrera, R. S.; Snoeberger, R.; Matzger,

- A. J.; Bredas, J.-L. *J. Am. Chem. Soc.* **2007**, *129*, 13072-13081.
- 70.** Mcculloch, I.; Heeney, M.; Bailey, C.; Genevicius, K.; Macdonald, I.; Shkunov, M.; Sparrowe, D.; Tierney, S.; Wagner, R.; Zhang, W. M.; Chabinye, M. L.; Kline, R. J.; McGehee, M. D.; Toney, M. F., *Nat. Mater.* **2006**, *5*, 328-333.
- 71.** Hamer, W.J.; Wood, R.E; Condon, in E.U.; Odishaw, in E.U. (eds.), *Handbook of Physics*, McGraw-Hill, New York, 1958.

HAKAN USTA, B.S.

Education

PH.D. IN CHEMISTRY, NORTHWESTERN UNIVERSITY, EVANSTON, IL

NOVEMBER 2008

Advisor: Professor Tobin J. Marks

GPA 3.9/4.0, Cumulative

B.S. IN CHEMISTRY, BILKENT UNIVERSITY, ANKARA, TURKEY

MAY 2004

Major: Chemistry (Ranked 1st, Honors in Chemistry)

GPA 4.0/4.0, Chemistry-Cumulative

RESEARCH EXPERIENCE

Graduate Research Assistant, Department of Chemistry, Northwestern University *2004 – Present*

- Designed, synthesized and characterized electron-deficient organic molecules and corresponding homo- and copolymers as air-stable and solution-processable *n*- and *p*-channel semiconductors
- Fabricated Organic Field Effect Transistors (OFETs) via vapor- and solution-phase fabrication techniques.
- Characterized OFET devices under ambient/inert conditions and evaluated electrical properties
- Designed and developed a new *n*-channel semiconducting molecule/polymer exhibiting one of the highest air-stable, solution-based FET device performance reported to date with excellent ambient stability
- Synthesized a new highly polarizable *Cyanine dye* and conducted a self-assembly study using the molecule as a nanodielectric for OFETs
- Collaborated with materials scientists, physicists on numerous projects
- Presented findings on projects at local and national conferences
- Supervised 2 undergraduate students for summer research, trained on organic synthesis and purification techniques

Undergraduate Research Assistant, Department of Chemistry, Texas A&M University *Summer 2002*

- Worked on the synthesis and characterization of a Truncated-*Pateamine A* derivative
- Presented findings in NSF-REU Program Meeting

Undergraduate Research Assistant, Department of Chemistry, Bilkent University *2002 – 2004*

- Performed theoretical calculations for copolymers TTP-Pyrrole (1:2) using Gaussian program.
- Investigated polaron formation in donor-acceptor polymeric systems.
- Assisted in the preparation of a manuscript.
- Presented findings in a departmental seminar and in a national meeting.

TEACHING EXPERIENCE

Teaching Assistant, Department of Chemistry, Northwestern University *2004 – 2006*

- Supervised, instructed, and evaluated undergraduate students in the organic chemistry laboratory, graded class exams.
- Tutored students with laboratory and course problems.

Teaching Assistant, Chicago Section of the U.S. National Chemistry Olympiad *2005 – 2006*

- Supervised and instructed students weekly on the National Chemistry Olympiads.

Teaching Assistant for the National/International Chemistry Olympiads, Turkey *2000 – 2004*

- Coached and instructed highly talented and exceptional students on the National and International Chemistry Olympiads.
- 20 of my students got medals in the National Chemistry Olympiads and 9 of them got medals in the International Chemistry Olympiads (2001-2005).

Teaching Assistant, Department of Chemistry, Bilkent University

2003 – 2004

- Tutored undergraduate students for general/organic chemistry courses.

Scientific Skills & Proficiencies

Chemical Synthesis: Multi-Step Organic Synthesis Including Inert-Atmosphere Cross-Coupling Reactions (Suzuki, Stille, Kumada, Sonogashira, Yamamoto, Heck) and Ambient Reactions. Solid Background in Dry Box and Air-Free/Schlenk-Line Techniques. Conventional/Microwave-Assisted Polymerization Reactions (Suzuki, Stille, Yamamoto) and Purifications.

Chemical Characterization: Spectroscopy (FT-IR, UV-Vis, Fluorescence, (VT-)NMR), Mass Spectrometry (GC-MS, MALDI, ESI-MS, (HT-)GPC), Thermal Analysis (TGA, DSC), Electrochemistry (CV)

Film Deposition: Chemical Vapor Deposition, Spin-Coating, Drop-Casting, Gravure-Printing, Solution-based Self-Assembly

Film Characterization: SEM, AFM, XRD, XRR, Profilometry

Device Characterization, & Stability Testing: FET Electrical Characterizations under ambient/vacuum using Keithley 6430 subfemtoammeter and a Keithley 2400 source meter, operated by a locally written Labview program and GPIB communication.

Selected Awards & Honors

Honorary Membership , Phi Lambda Upsilon Scholarship Society, Northwestern University	2006 - Present
Conference Travel Grant , Graduate School, Northwestern University	2007-2008
Allen S. Hussey Award , Excellence in Teaching, Organic Chemistry Division, Northwestern University	2006
Undergraduate Scholarship in Chemistry , The Scientific Research Council of Turkey	2000 - 2004
NSF-REU Scholarship , Texas A&M University, College Station, TX	2002
College Scholarship (Full) , Department of Chemistry, Bilkent University, Ankara, Turkey	2000 - 2004
Silver Medal , 32 nd International Chemistry Olympiad, Copenhagen, Denmark	2000
Bronze Medal , 31 st International Chemistry Olympiad, Bangkok, Thailand	1999
1st Place , 7 th National Chemistry Olympiad organized by TUBITAK, Ankara, Turkey	1999
Silver Medal , 8 th National Chemistry Olympiad organized by TUBITAK, Ankara, Turkey	1999
68th Place (Among 1,200,000 students) , Science High Schools Selection Examination, Turkey	1997

Selected Publications and Patents

Usta, H.; Risko, C.; Wang, Z.; Deliomeroğlu M. K.; Facchetti, A.; Marks, T. J. “Design, Synthesis, and Characterization of Ladder-Type Molecules and Polymers. Air-Stable, Solution-Processable *n*-Channel Semiconductors for Thin-Film Transistors via Experiment and Theory.”

Journal of the American Chemical Society, **2008**, to be submitted.

Usta, H.; Facchetti, A.; Marks, T. J. “Air-Stable, Solution-Processable *n*-Channel and Ambipolar Semiconductors for Thin-Film Transistors Based on the Indenofluorenebis(dicyanovinylene) Core”

Journal of the American Chemical Society, **2008**, *130*, 8580-8581.

Usta, H.; Facchetti, A.; Marks, T. J. “Synthesis and Characterization of Electron-Deficient and Highly Soluble (Bis)Indenofluorene Building Blocks for *n*-type Semiconducting Polymers”

Organic Letters, **2008**, *10*, 1385-1388.

Lu, G.; **Usta, H.**; Risko, C.; Wang, L.; Facchetti, A.; Marks, T. J. "Synthesis, Characterization, and Transistor Response of Semiconducting Silole Polymers with Substantial Hole Mobility and Air Stability. Experiment and Theory"
Journal of the American Chemical Society, **2008**, *130*, 7670–7685.

Wang, Z.; Kim, C.; **Usta, H.**; Lu, S.; Facchetti, A.; Marks, T. J. "N-Channel Organic Semiconductors Based on Anthracenedicarboximides for Organic Thin Film Transistors"
Chemistry of Materials, **2008**, to be submitted.

Usta, H.; Lu, G.; Facchetti, A.; Marks, T. J. "Silole-based Polymeric Semiconductors for Organic Thin Film Transistors"
PMSE Preprints, **2007**, *96*, 337-338.

Usta, H.; Lu, G.; Facchetti, A.; Marks, T. J. "Dithienosilole- and Dibenzosilole-Thiophene Copolymers as Semiconductors for Organic Thin-Film Transistors"
Journal of the American Chemical Society, **2006**, *128*, 9034-9035.
(Highlighted by the ACS: Chemical Innovation Heart Cut, August 21, 2006.)

Marks, T. J.; Facchetti, A.; Lu, G.; **Usta, H.**; Letizia, J.
"Silole-Containing π -Conjugated Polymers. Synthesis and Applications in Field-Effect Devices"
PCT Int. Appl. **2007**, **WO 2007133705**, **US2007282094-A1**

Marks, T. J.; Facchetti, A.; **Usta, H.**
"Ladder-Type Organic Molecules and Polymers as n-Channel Semiconductors for Organic Field-Effect Transistors" *USA Provisional*, **2007**, **NU27029**

Selected Presentations (*=talk, #=poster)

"Air-Stable, Solution-Processable n-Channel and Ambipolar Semiconductors for Thin-Film Transistors Based on the Indenofluorenebis(dicyanovinylene) Core." July 2008, *Gordon Research Conferences*, South Hadley, MA.

"Dithienosilole- and Dibenzosilole-Thiophene Copolymers as Semiconductors for Organic Thin-Film Transistors." March 2007, *Industrial Associates Meeting*, Evanston, IL.

"Silole-based Polymeric Semiconductors for Organic Thin-Film Transistors." March 2007, *233rd ACS National Meeting*, Chicago, IL.

"Synthesis and Characterization of AreneSilole-Thiophene Copolymers as New Semiconductors for Organic Thin-Film Transistors." May 2006, *38th Central Regional Meeting of the American Chemical Society*, Frankenmuth, MI.

* "Synthesis and Characterization of Electron-Deficient Monomers and Polymers as Air-Stable Semiconductors for OFETs" November 2007, *Departmental Seminar, Northwestern University*, Evanston, IL.

* "Silole-based Polymeric Semiconductors for OFETs" February 2007, *BIP, Northwestern University*, Evanston, IL.

* "Highly Soluble and Electron-Deficient Ladder-type (Bis)Indenofluorene building blocks for n-channel semiconductors for OFETs" December 2007, *BIP, Northwestern University*, Evanston, IL.

* "Investigation of the Polaron Formation in a Donor-acceptor System: TTP-Pyrrole (1:2) Copolymer" May 2004, *Senior Research Seminar at Bilkent University*, Ankara, Turkey.

* "Synthesis of a Truncated Pateamine A Derivative via a mediated ring-opening reaction" August 2002, *NSF-REU Seminar*, Texas A&M University, College Station, TX.